TU Delft

Delft University of Technology

Burial-related fracturing in sub-horizontal and folded reservoirs

Geometry, geomechanics and impact on permeability

Bisdom, Kevin

DOI
10.4233/uuid:f1b6f6e0-1542-4744-943e-04c7c551213b

Publication date
2016

Document Version
Final published version

Citation (APA)
Bisdom, K. (2016). *Burial-related fracturing in sub-horizontal and folded reservoirs: Geometry, geomechanics and impact on permeability*. [Dissertation (TU Delft), Delft University of Technology]. https://doi.org/10.4233/uuid:f1b6f6e0-1542-4744-943e-04c7c551213b

Important note
To cite this publication, please use the final published version (if applicable).
Please check the document version above.

Copyright
Other than for strictly personal use, it is not permitted to download, forward or distribute the text or part of it, without the consent of the author(s) and/or copyright holder(s), unless the work is under an open content license such as Creative Commons.

Takedown policy
Please contact us and provide details if you believe this document breaches copyrights.
We will remove access to the work immediately and investigate your claim.

This work is downloaded from Delft University of Technology.
For technical reasons the number of authors shown on this cover page is limited to a maximum of 10.

Burial-related fracturing in sub-horizontal and folded reservoirs

Geometry, geomechanics and impact on permeability

Burial-related fracturing in sub-horizontal and folded reservoirs

Geometry, geomechanics and impact on permeability

Proefschrift

ter verkrijging van de graad van doctor
aan de Technische Universiteit Delft,
op gezag van de Rector Magnificus prof. ir. K.C.A.M. Luyben,
voorzitter van het College voor Promoties,
in het openbaar te verdedigen op
29 november 2016 om 15:00 uur

door

Kevin BISDOM

Ingenieur Technische Aardwetenschappen,
Technische Universiteit Delft, Nederland
geboren te Alphen aan den Rijn, Nederland.

Dit proefschrift is goedgekeurd door de

promotor: Prof. dr. G. Bertotti

Samenstelling promotiecommissie:

Rector Magnificus	voorzitter
Prof. dr. G. Bertotti	promotor
Onafhankelijke leden:	
Prof. dr. J.D. Lamarche	CEREGE-Aix-Marseille Université
Prof. dr. P.W.M. Corbett	Heriot-Watt University Edinburgh
Prof. dr. W.R. Rossen	Technische Universiteit Delft
Dr. A. Barnhoorn	Technische Universiteit Delft
Prof. dr. J. Bruining	Technische Universiteit Delft, reserve lid
Overige leden:	
Dr. N.J. Hardebol	Technische Universiteit Delft
Dr. B.D.M. Gauthier	Total S.A.

Dr. B.D.M. Gauthier heeft in belangrijke mate aan de totstandkoming van het proefschrift bijgedragen.



TOTAL



Keywords: Natural fractures, aperture, equivalent permeability, deterministic modelling

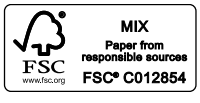
Printed by: Gildeprint

Front & Back: Design by K. Bisdom, pictures by R.D. Koster

Copyright © 2016 by K. Bisdom

ISBN 978-94-6186-740-7

An electronic version of this dissertation is available at http://repository.tudelft.nl/.



Contents

Summary ix

Samenvatting xi

1 Introduction 1
- 1.1 Rationale . . . 2
- 1.2 Scope of the Thesis . . . 3
- 1.3 Thesis outline . . . 4
- References . . . 7

2 Fracture network digitisation using a drone and photogrammetry 15
- 2.1 Introduction . . . 16
- 2.2 Image acquisition using a drone . . . 17
- 2.3 Image processing using photogrammetry . . . 18
  - 2.3.1 Image alignment . . . 18
  - 2.3.2 Point cloud generation . . . 20
  - 2.3.3 Surface generation . . . 21
  - 2.3.4 Fracture digitisation . . . 22
- 2.4 Discussion . . . 23
  - 2.4.1 Spatial accuracy and image quality . . . 23
  - 2.4.2 Comparison to other methods . . . 24
- 2.5 Conclusions . . . 25
- References . . . 26

3 Stress-induced discrete fracture aperture and fluid flow modelling 29
- 3.1 Introduction . . . 30
- 3.2 Barton-Bandis aperture . . . 32
  - 3.2.1 Initial intrinsic aperture . . . 32
  - 3.2.2 Mechanical aperture . . . 33
  - 3.2.3 Shearing and hydraulic aperture . . . 34
- 3.3 From fracture network to mechanical model . . . 35
  - 3.3.1 Meshing of discrete fracture networks . . . 35
  - 3.3.2 Boundary conditions and loads . . . 37
  - 3.3.3 Rheology and governing equations . . . 37
- 3.4 Equivalent permeability modelling . . . 38
- 3.5 Application . . . 40
  - 3.5.1 Aperture of a single fracture . . . 41
  - 3.5.2 Sensitivity analysis of aperture in fracture networks . . . 41
  - 3.5.3 Heterogeneous vs. constant aperture distributions . . . 47

3.6 Discussion . . . 49
3.6.1 Fracture aperture versus geometry . . . 49
3.6.2 2-D flow models as proxy for 3-D fractured reservoirs . . . 49
3.6.3 Scalability of the aperture-permeability workflow . . . 50
3.7 Conclusions . . . 50
References . . . 51

4 Geometry and reservoir permeability of burial-related fractures 57
4.1 Introduction . . . 58
4.1.1 Rationale . . . 58
4.1.2 Aperture definitions . . . 59
4.2 Geological setting . . . 60
4.2.1 Tectonics . . . 60
4.2.2 Stratigraphy . . . 61
4.2.3 Fracturing synthesis . . . 61
4.3 Quantitative fracture analysis . . . 62
4.3.1 Data acquisition and database . . . 62
4.3.2 Barren fractures . . . 64
4.3.3 Veins . . . 70
4.4 Implications for fractured reservoir permeability . . . 73
4.4.1 Methodology . . . 73
4.4.2 Variability in inter-well scale permeability . . . 74
4.4.3 Impact of exhumation . . . 75
4.4.4 Impact of aperture definition . . . 78
4.4.5 Impact of matrix flow and fracture connectivity . . . 80
4.5 Discussion . . . 82
4.6 Conclusions . . . 83
References . . . 85

5 Impact of burial-related fractures on hydraulic fracturing 89
5.1 Introduction . . . 90
5.2 Geological setting . . . 92
5.3 Regional natural fracturing . . . 92
5.3.1 Fracture characterisation . . . 92
5.3.2 Fracture infill . . . 94
5.3.3 Fracturing synthesis . . . 95
5.4 Stress-pore pressure modelling methodology . . . 97
5.4.1 Horizontal 2-D fracture model construction . . . 97
5.4.2 Vertical 2-D modelling . . . 100
5.5 Equivalent permeability of reactivated fractures . . . 101
5.6 Impact of hydraulic fracturing strategy on SRV . . . 102
5.6.1 Base case model . . . 102
5.6.2 Model calibration . . . 104
5.6.3 Impact of fracturing strategy on SRV . . . 105

5.7 Impact of mechanical stratigraphy . . . 108
5.7.1 Vertical pore pressure distribution . . . 108
5.7.2 Reactivation of beef . . . 109
5.7.3 Implications for 3-D . . . 110
5.8 Discussion . . . 110
5.9 Conclusions . . . 111
References . . . 112

6 Interplay between burial- and folding-related fracturing 117
6.1 Introduction . . . 118
6.2 Geological setting . . . 119
6.2.1 Structural setting . . . 119
6.2.2 Stratigraphy . . . 121
6.2.3 Geometry of the Alima fold . . . 121
6.3 Sub-seismic scale deformation . . . 122
6.3.1 Fracture digitisation . . . 122
6.3.2 Deformation types and sets . . . 124
6.3.3 Fracturing synthesis . . . 126
6.4 Fold-scale fracture distribution . . . 130
6.4.1 Methodology . . . 131
6.4.2 Results . . . 133
6.5 Pre-folding vs. syn-folding permeability . . . 137
6.5.1 Network geometry . . . 137
6.5.2 Permeability model set-up . . . 139
6.5.3 Results . . . 139
6.6 Discussion . . . 141
6.7 Conclusions . . . 141
References . . . 142

7 Conclusion 149

A Generating intersecting fracture seams in 2-D meshes 155

B A geometrically-based method for stress-induced aperture 165

C Fracture networks in the Jandaíra Fm. 181

Acknowledgements 191

Curriculum Vitæ 193

List of Publications 195

Summary

Improving our understanding of fluid flow patterns in subsurface rocks is essential for the recovery of oil and gas, development of geothermal energy, carbon capture and storage and underground nuclear waste storage. The development of these applications is strongly dependent on reservoir permeability and connectivity. While there are many sources of flow heterogeneity in rocks, natural fractures generally create the largest contrasts in flow. Fractures can increase or limit permeability, depending on fracture connectivity, hydraulic conductivity and cement infill. Wells are the only means for characterising fracture patterns in the subsurface, providing a 1-D analysis of 3-D fracture systems. To bridge the gap between 1-D and 3-D, outcrop analogues are used.

In this Thesis, we use outcrops to derive multiscale rules that relate subseismic-scale fracturing to regional stresses and deformation, which includes burial, regional shortening and folding, and study the impact of fractures on reservoir permeability. This requires large multiscale fracture patterns, which are digitised on images acquired using an Unmanned Aerial Vehicle (UAV) and processed using photogrammetry (Chapter 2). The size of these digitised outcrops approaches the inter-well scale of naturally fractured reservoirs. The potential permeability in these fracture networks is quantified using a novel workflow where the aperture distribution is determined through Finite Element (FE) modelling of the local stress state representative of reservoir conditions (Chapter 3).

We observe that natural fractures are abundant even in rocks that have experienced relatively little seismic-scale deformation, and that regional forces such as an increase in overburden can lead to significant fracturing. In Chapter 4, we describe the geometry of burial-related fractures and their relation with the regional stress field in carbonates outcropping in north-east Brazil. These rocks have had a simple deformation history, with limited burial and exhumation, no folding and limited seismic-scale faulting, and are therefore ideal for studying burial-related fractures. We digitise and analyse 13 000 outcropping fractures and find that a single regional tectonic phase can lead to a complex arrangement of opening-mode and sheared fractures with a scattered orientation. We take into account uncertainties that are often overlooked in outcrop analogue studies, such as the impact of exhumation, stress-induced variations in aperture and the role of matrix flow. We find that systems with similar fracture porosities can have significantly different permeabilities, as the connectivity of the hydraulically conductive fractures needs to be taken into account.

Even when fractures do not impact permeability at in-situ conditions, they can impact the mechanical behaviour of rocks. Using coupled stress-fluid pressure models, we explore the impact of a burial-related fracture network in the relatively undeformed rocks of the Vaca Muerta Fm. in the Neuquén Basin, Argentina, on

the propagation of hydraulic fractures and the resulting Stimulated Rock Volume (SRV; Chapter 5). High paleostress anisotropy created a network of burial-related bed-perpendicular mode I and mode II fractures in this basin. The stress-flow models show that these fractures are partly reactivated during hydraulic fracturing. However, the spatial distribution of the SRV is anisotropic, resulting from the preferential natural fracture orientation and high differential stress. Cemented sub-horizontal calcite fractures are common, and limit the vertical growth of hydraulic fractures, but this potentially leads to an increase in length and aperture of hydraulic fractures. By quantifying the mechanical impact of natural fractures using stress-flow models, the hydraulic fracturing strategy can be optimised even in an early phase of development, when limited well productivity data is available.

Third, the impact of pre-existing burial-related fractures on folding-related fracturing is studied in an outcropping fold in central Tunisia, where we observe a regional system of bed-perpendicular conjugate fractures formed at relatively shallow depth as a result of Layer-Parallel Shortening, in combination with hybrid mode I-mode II fractures formed during folding as a result of flexural slip (Chapter 6). The burial-related deformation controls the size and spatial distribution of more recent deformation, and provides potential reservoir connectivity in areas that are typically predicted to have a low connectivity when only folding is considered as a driver for fracturing. We develop a conceptual model using 3-D geomechanical restorations to quantify the folding-related fracture distribution combined with a pre-folding system, characterised from outcrops, to quantify relative permeability trends in different mechanical domains of the fold.

These three case studies illustrate that burial-related fractures are common in a range of compressional tectonic settings. The different modelling exercises illustrate that these features likely impact reservoir permeability, mechanical rock properties and the geometry of later natural and induced fracture systems. Recent deformation associated with exhumation complicates the identification and analysis of burial-related fractures in outcrops, but by using novel tools including a UAV and photogrammetry, we show that burial-related fracture systems can be characterised from outcrops to derive a representative geometrical, mechanical and fluid flow analysis.

The modelling workflow presented in this Thesis allows for constructing representative inter-well scale fracture-flow models that can be used to quantify uncertainties in fractured reservoir flow models. Although this Thesis does not cover all uncertainties, the presented framework does provide an integrated approach that seamlessly combines outcrop acquisition with geomechanical and fluid flow modelling in interwell-scale discrete fracture models, without need for upscaling. This approach can be easily extended to further reduce fracturing-related uncertainties in geothermal and hydrocarbon reservoirs.

Samenvatting

Voor succesvolle exploitatie van ondergrondse reservoirs voor winning van olie en gas, ontwikkeling van geothermie en opslag van CO_2 en radioactief afval is het noodzakelijk dat we begrijpen hoe water, olie en gas stromen in de ondergrond. Het voorspellen van stromingspatronen is ingewikkeld, omdat reservoirgesteente vaak heterogeen is. Natuurlijke breuken zijn een belangrijke bron van heterogeniteit die invloed hebben op de permeabiliteit. De grootste breuken kunnen worden geïdentificeerd op seismiek, maar kleinere breuken kunnen alleen deels gemeten worden in boorputten, waardoor slechts een 1-D beeld van de complexe 3-D netwerken ontstaat. Afhankelijk van de organisatie van het breuknetwerk en of de breuken open zijn of gecementeerd, kunnen deze kleine breuken de productiviteit in oliereservoirs verhogen of een risico voor lekkage vormen bij ondergrondse opslag van CO_2, afvalwater of radioactief afval. Ontsluitingen van gesteente aan het oppervlak zijn ideaal als analoog voor het bestuderen van deze kleinere breuken, om een beter idee te krijgen van hun 3-D distributie.

In dit proefschrift bestuderen we ontsluitingen om de relatie tussen grootschalige regionale deformatie en kleine breuken beter te begrijpen. Dit stelt ons in staat om de distributie van kleine breuken en hun invloed op stroming in reservoirs te voorspellen op basis van grootschalige deformatie die zichtbaar is op seismiek. Dit vereist 2-D of 3-D analyse van datasets met een groot aantal breuken. Wij presenteren een methode om deze datasets te verzamelen door middel van een drone en fotogrammetrie, waarmee 3-D ontsluitingsmodellen geconstrueerd kunnen worden (Hoofdstuk 2). De afmetingen van deze modellen zijn vergelijkbaar met de gebieden tussen boorputten in reservoirs, waar we de breuksystemen niet kunnen meten. Om te voorspellen wat de permeabiliteit van deze breuksystemen is, maken we gebruik van geomechanische- en stromingsmodellen om de lokale stressdistributie, breukopening en permeabiliteit te modelleren (Hoofdstuk 3).

Ons werk toont aan dat kleine breuken veel voorkomen, zelfs wanneer er geen intensieve regionale deformatie plaats heeft gevonden. Het begraven van gesteente tot een paar honderd meter diepte en minimale regionale verkorting zijn genoeg voor het vormen van kleine breuken. We beschrijven de geometrie van deze breuken en de link met regionale deformatie op basis van breuksystemen in kalksteen ontsluitingen in het noordoosten van Brazilië (Hoofdstuk 4). Gesteente in dit gebied ligt horizontaal en is nooit dieper dan een kilometer begraven geweest, waardoor het ideaal is voor analyse van kleinschalige breuksystemen. We verzamelen een database van 13 000 breuken en concluderen dat deze breuken zijn gevormd tijdens een constante fase van regionale deformatie, ondanks dat de dataset bestaat uit een mix van verschillende orientaties en verschillende types breuken. We gebruiken deze dataset om de rol van exhumatie, de relatie tussen lokale stress en breukopening en de rol van matrixpermeabiliteit te bestuderen. Een belangrijke

conclusie van dit werk is dat breuksystemen met een vergelijkbare porositeit niet per definitie een vergelijkbare permeabiliteit hebben, omdat de connectiviteit kan verschillen.

Afhankelijk van de druk in de ondergrond zijn niet alle breuken permeabel. Echter, de druk in een reservoir verandert tijdens het produceren van olie en gas of tijdens het injecteren van water of CO_2, waardoor breuken gereactiveerd kunnen worden of nieuwe breuken ontstaan en de permeabiliteit verandert. We bestuderen de invloed van drukveranderingen op natuurlijke breuken in schalies in het Neuquén Basin (Argentinië) door middel van modellen die veranderingen in druk en stroming koppelen (Hoofdstuk 5). Het natuurlijke breuksysteem in dit basin bestaat uit verticale en horizontale breuken, gevormd tijdens begraving van het gesteente. De modellen tonen aan dat door injectie van water ('hydraulic fracturing') een deel van het verticale breuksysteem gereactiveerd kan worden, waardoor permeabiliteit wordt verhoogd. Het horizontale breuksysteem is volledig gecementeerd, waardoor de verticale groei van hydraulische breuken beperkt wordt, maar tegelijkertijd kan dit leiden tot langere breuken met een grotere opening. Door deze effecten te modelleren kan de plaatsing van hydraulische breuken en de ontwikkeling van schaliegas geoptimaliseerd worden.

De derde studie richt zich op de rol die begravings-gerelateerde breuken hebben op latere breukvorming tijdens plooiing van gesteente (Hoofdstuk 6). Een regionaal systeem van verticale conjugaatpatronen, gevormd op ondiepe diepte tijdens horizontale verkorting, beinvloedt de grootte en positie van breuken gevormd tijdens plooiing. De plooiingsgerelateerde breuken staan haaks op de eerdere breuken, waardoor een breuksysteem ontstaat met een hoge connectiviteit en permeabiliteit. We analyseren de impact van deze combinatie van breuksystemen met een conceptueel model van de begravings-gerelateerde breuken gecombineerd met 3-D geomechanische restoraties van de deformatie tijdens plooiing. Deze modellen geven de relatieve verschillen in permeabiliteit aan in de verschillende delen van de plooi.

Wat deze drie studies gemeen hebben is dat ze allen aantonen dat kleine breuken veel voorkomen, zelfs als er geen zichtbare grootschalige deformatie is, en dat deze kleine breuken een significante invloed op permeabiliteit in reservoirs hebben. Daarnaast hebben de breuken invloed op de mechanische eigenschappen van gesteente en de groei van latere breuksystemen. Hoewel het bestuderen van breuken in ontsluitingen beperkingen heeft, kan met de methode uit dit proefschrift een deel van deze beperkingen omzeild worden. Daarnaast leent deze methode zich uitstekend voor het bestuderen van de vele onzekerheden die een rol spelen in stromingsmodellen van breuken in de ondergrond. Hoewel dit proefschrift slechts een deel van deze onzekerheden behandelt, is de gepresenteerde methode een goede basis voor verdere uitbreiding en analyse van breuksystemen die we normaliter niet kunnen analyseren in de ondergrond.

1

Introduction

1

1.1. Rationale

Natural fractures in subsurface rocks are discontinuities that affect rock strength and permeability, Fractures create local stress perturbations that control for example propagation of hydraulically induced fractures (Gale *et al.*, 2007, 2014; Weng *et al.*, 2016). Open natural fractures enhance fluid flow and are an important source of connectivity in hydrocarbon and geothermal reservoirs with low matrix permeability (Nelson, 2001; Narr *et al.*, 2006; Davatzes and Hickman, 2010; Singhal and Gupta, 2010). Cemented fractures, however, can limit fluid flow in reservoirs, as they form flow barriers (Gale *et al.*, 2007). In underground storage sites for CO_2 and nuclear waste, open fractures form a containment risk (Dershowitz *et al.*, 1999).

Optimised development of naturally fractured reservoirs requires an understanding of the 3-D fracture distribution, their geometrical attributes and their impact on permeability (Berkowitz, 2002; Bourbiaux *et al.*, 2002, 2005; Bourbiaux, 2010). We cannot fully characterise fractures using only subsurface data, as fractures are below the seismic resolution and well data is typically too sparse to capture the 3-D fracture distribution (Maerten *et al.*, 2006; Wilkins, 2007). Data that can be obtained from wells is sensitive to a range of artefacts. Fracture length, which strongly impacts connectivity, cannot be measured for fractures that exceed the borehole diameter, and orientation and spacing need to be corrected for orientation sampling bias using the Terzaghi correction (Terzaghi, 1965). Aperture measurements are often overestimated in BHI (Ponziani *et al.*, 2015), and can only be measured in cores if the core is not broken along fractures. Cores are often not oriented, which limits the analysis of the orientation distribution (Wu and Pollard, 2002). Well tests are the most important source for quantifying the flow potential of fractures and in some cases, they even provide an indication of fracture flow in between wells (Aguilera, 1987). However, fractures are typically not the only source of flow heterogeneity in the subsurface, and as a result there is no unique reservoir description for a single well test (Corbett *et al.*, 2010; Aljuboori *et al.*, 2015; Muhammad, 2016).

In fractured reservoir models, accurately sampled and corrected 1-D well data is used to populate a reservoir-scale 3-D model (Bourbiaux *et al.*, 2005; Makel, 2007; Bourbiaux, 2010). Seismic attributes including curvature, covariance and ant-tracking are used to define relative trends in fracture spacing and orientation, which requires high-resolution 3-D seismic (Gauthier *et al.*, 2002; Makel, 2007). In the absence of seismic as a driver for fracture attributes, multiscale geological and geomechanical rules are used that relate sub-seismic fracture patterns to regional deformation (Bourne *et al.*, 2000; Bergbauer, 2007). These rules are derived from outcropping analogues, where multiscale deformation patterns can be studied in 2-D or 3-D (e.g. Bergbauer and Pollard, 2004; Shackleton *et al.*, 2005; Stephenson *et al.*, 2007; Laubach *et al.*, 2009; Savage *et al.*, 2010; Lamarche *et al.*, 2012; Awdal *et al.*, 2016). Folding and faulting are typically considered as the main fracturing drivers, which has resulted in well-defined methods for modelling fractures related to those mechanisms (Sanders *et al.*, 2004; Stephenson *et al.*, 2007). However, fractures can be commonplace in rocks that experienced no or limited seismic-scale deformation, and although this is recognised qualitatively (Lacombe *et al.*, 2011;

Tavani *et al.*, 2011; Branellec *et al.*, 2015), there is a limited understanding of the quantitative relation between regional events such as shortening and burial on the one hand and fracturing on the other hand (e.g. Lorenz *et al.*, 1991). Moreover, the different mechanical conditions that lead to Mode I, Mode II and hybrid fractures are not understood, making it impossible to predict which fracture types to expect in fractured reservoirs (Bertotti and Barnhoorn, 2016).

The results from outcrop analogues are often used to supplement subsurface datasets, particularly to provide geometrical properties that cannot be fully sampled in wells (Pringle *et al.*, 2006; Agosta *et al.*, 2010; Gillespie *et al.*, 2011), such as length, abutting relations and spatial trends related to variations in lithology (Boro *et al.*, 2014; Lavenu *et al.*, 2014; Kleipool *et al.*, 2016), the definition of mechanical units (Wennberg *et al.*, 2006; Bertotti *et al.*, 2007; Laubach *et al.*, 2009; Lamarche *et al.*, 2012) and large-scale deformation (Bergbauer and Pollard, 2004; Bergbauer, 2007; Savage *et al.*, 2010). Often, outcropping fractures are analysed using scanlines (Mauldon and Mauldon, 1997), but scanlines have the same limitations and artefacts as well data (Bisdom *et al.*, 2014). In recent years, 3-D outcrop digitisation methods have become more commonplace (Rotevatn *et al.*, 2009; Wilson *et al.*, 2011; Hodgetts, 2013; Tavani *et al.*, 2014; Mahmud *et al.*, 2015), which provide multiscale quantitative fracture datasets, but at a high cost and limited flexibility (Hodgetts, 2013).

Another limitation of outcrop analogues is that they are not a direct proxy for reservoir flow, as stresses, apertures and fracture geometry change as a result of mechanical unloading during exhumation (English, 2012). Aperture is particularly difficult to quantify from outcrops, as exhumation and weathering enhances aperture and dissolves cement, creating barren fractures (Cacas *et al.*, 2001; Zeeb *et al.*, 2013), and aperture is highly sensitive to stress (Ghassemi and Suresh Kumar, 2007; Matsuki *et al.*, 2008; Lei *et al.*, 2015). Exhumation-related effects are however rarely taken into account in outcrop modelling (McGinnis *et al.*, 2015). Although outcrop analogues are essential to our understanding of natural fracture systems, particularly for deriving fundamental rules between fractures and geological and geomechanical properties, outcrop studies are only useful if data is acquired in an accurate and quantitative manner, and the impact of exhumation and stress changes on fracture geometry and permeability is taken into account. Too often, outcrop studies are limited to deriving statistical distributions for fracture attributes, often from limited datasets, for use in stochastic Discrete Fracture Network (DFN) modelling. Permeability in these outcrop-based DFNs is generally quantified by assuming that aperture is constant for individual fractures or entire sets. The resulting upscaled permeability does not capture the small-scale variability in permeability associated with natural fractures (Geiger and Matthäi, 2012).

1.2. Scope of the Thesis

In this Thesis, we develop an integrated workflow to efficiently acquire representative multiscale fracture datasets from outcrops, using an Unmanned Aerial Vehicle (UAV) to image outcrops and photogrammetry to construct high-resolution georeferenced 3-D models. This workflow permits fast data acquisition, resulting

in a unique database of fracture networks (Figure 1.1; Bertotti and Bisdom, 2013; Bisdom, 2015). We use these networks to study in detail, i.e. without upscaling, the stress-sensitive aperture and permeability of natural fractures, in particular regional fracture networks formed during burial (Figure 1.2). To obtain permeabilities representative of subsurface conditions, we develop a geomechanical modelling workflow that defines aperture as a function of in-situ stress, taking into account the combination of opening and shear displacement that is typically observed but rarely included in models (Figure 1.3; Barton, 2014; Lei *et al.*, 2014). This aperture definition predicts more heterogeneous distributions compared to the more typically used Mohr-Coulomb critically stressed aperture methods (Bisdom *et al.*, 2016). We use the combined workflow of quantitative data acquisition and geomechanical aperture and permeability modelling to focus specifically on the development of regional burial-related fractures and their impact on permeability in fractured reservoirs, as these fractures are often ignored, even though their abundance and importance for flow has been confirmed in several outcrop and subsurface studies (Lorenz *et al.*, 1991; Bergbauer and Pollard, 2004; Casini *et al.*, 2011).

Based on analysis of fractures in flat-lying carbonates with a straightforward burial and exhumation history, we characterise the geometry of outcropping burial-related fractures, and combined with isotope analysis of fluid inclusions we define relative fracture timing and regional stress conditions. We also study the interplay between pre- and syn-burial fractures, and the impact of burial-related fractures on the development of hydraulically induced fractures. For each case study, we use our modelling workflow to quantify uncertainties and derive general lessons for aperture and permeability modelling in fractured reservoirs. We focus specifically on the relation between stress and aperture as this is one of the most important factors impacting fracture porosity and permeability in the subsurface. In addition, we identify in each case study the different fracture types (e.g. Mode I, Mode II) and their relation with regional stress conditions.

1.3. Thesis outline

This Thesis starts with two chapters presenting the methodology, followed by three chapters that apply this methodology to study aspects of burial-related fractures in different case studies. The workflow for fast acquisition of a database of quantitative fracture patterns is presented in Chapter 2. This chapter discusses the advantages and disadvantages of fracture digitisation techniques including scanlines, laser scanning and UAVs, followed by the introduction of our method, which applies a rotary-wing UAV in combination with photogrammetry to generate high-resolution outcrop models. Rather than performing time-intensive 3-D interpretation of these models, we apply a fast 2-D digitisation technique to obtain the relevant fracture attributes.

Chapter 3 continues to discuss how the digitised networks are converted into geomechanical and fluid flow models where the fractures are represented as discrete features in all steps of the workflow. We implement the Barton-Bandis method for shear-induced aperture (Barton and Bandis, 1980; Barton, 1982) into a Finite El-

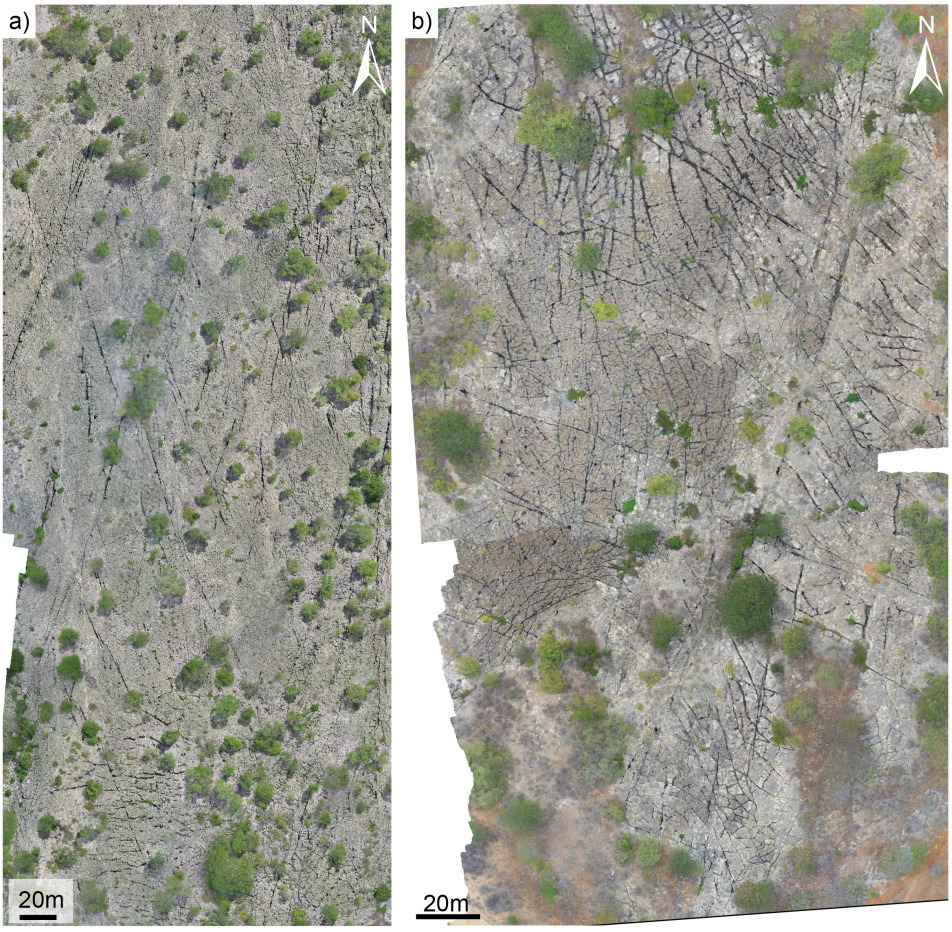


Figure 1.1: Two examples of sub-horizontal carbonate pavements containing predominantly burial-related fractures, digitised using a UAV (Unmanned Aerial Vehicle), where a) contains predominantly bed-perpendicular conjugates and N-S striking joints, and b) shows a more chaotic multiscale fracture pattern.

ement (FE) approach to model the translation of a far-field stress to local stress and aperture variations along fractures. We also quantify sensitivities and uncertainties associated with this approach, including an analysis of the impact of far-field stresses, rheology and geometrical properties on aperture.

The second part of this Thesis focuses on case studies involving burial-related regional fractures, emphasizing the role of stress on the development of fracture systems and their impact on permeability. In Chapter 4 we present the Jandaíra carbonates in the Potiguar basin, NE Brazil, where outcropping pavements with little large-scale deformation are intensely fractured. We digitise more than 13 000 fractures in pavements throughout this basin to study the relation between regional

1

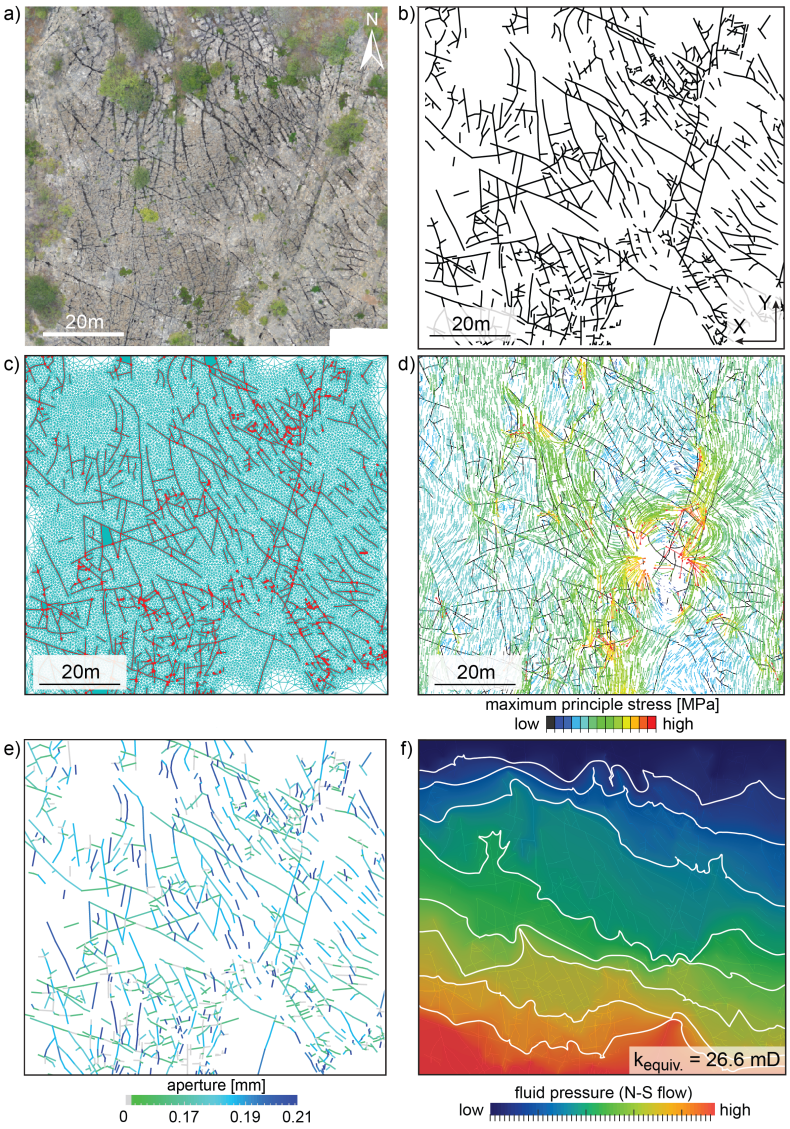


Figure 1.2: Illustration of the modelling workflow, using part of the outcrop shown in Figure 1.1b: a) High-resolution orthomosaic constructed from images obtained using a UAV; b) digitised fracture pattern; c) Meshed fracture model used for stress, aperture and permeability modelling; d) Maximum principle stress magnitude (indicated by the size of the arrows and colour scale) and orientation (indicated by arrow direction) under N-S compression; e) Stress-induced Barton-Bandis aperture derived from modelled shear and normal stresses; f) N-S fluid pressure gradient and contours (in white) based on flow through the fracture network from (e), assuming a 10 mD matrix permeability. The resulting equivalent permeability in N-S direction is 26.6 mD.



Figure 1.3: Example of an outcropping vein in the Jandaíra Fm. (Potiguar Basin, NE Brazil) showing opening and shear displacement.

stress and fracturing and define the attribute distributions. We then use the digitised database to model how permeability changed during burial and exhumation of the Jandaíra Fm. and to quantify uncertainties associated with different methods for defining fracture aperture in rocks with varying matrix properties.

Chapter 5 provides an example of sub-horizontal rocks with limited large-scale deformation where burial-related fractures impact the mechanical and flow properties. The shales of the Vaca Muerta Fm. have a high intensity of natural fractures that do not contribute to flow at in-situ stress conditions, but they are mechanical discontinuities that impact the growth and distribution of hydraulically induced fractures. Furthermore, part of the natural fracture network is reactivated during hydraulic fracturing, which increases equivalent permeability. Using coupled stress-fluid pressure models, we quantify these two aspects.

In Chapter 6, we present an outcrop study of a reservoir-scale fold in central Tunisia, that contains several carbonate formations with fractures associated with pre-folding Layer Parallel Shortening and syn-folding flexural slip. This study illustrates that even in folded reservoirs with folding-associated fractures, fracturing can take place prior to folding. We separate pre- and syn-folding fractures, and analyse how syn-folding fractures are affected by pre-folding deformation. We then use part of the methods from Chapter 3 to quantify the implications for permeability in different structural domains of folded reservoirs.

All case studies have in common that they show in a quantitative manner the impact of burial-related fractures on the mechanical and fluid flow properties of reservoir rocks.

References

J. F. W. Gale, R. M. Reed, and J. Holder, *Natural fractures in the Barnett Shale and their importance for hydraulic fracture treatments*, AAPG Bulletin **91**, 603 (2007).

J. F. Gale, S. E. Laubach, J. E. Olson, P. Eichhuble, and A. Fall, *Natural Fractures in shale: A review and new observations*, AAPG Bulletin **98**, 2165 (2014).

X. Weng, C.-E. Cohen, and O. Kresse, *Impact of Preexisting Natural Fractures on Hydraulic Fracture Simulation*, in *Unconventional Oil and Gas Resources Handbook* (Elsevier Inc., 2016) Chap. 10, pp. 289–331.

R. Nelson, *Geologic Analysis of Naturally Fractured Reservoirs*, in *Geologic Analysis of Naturally Fractured Reservoirs* (Gulf Professional Publishing, Woburn, MA, USA, 2001) 2nd ed., pp. 101–124.

W. Narr, D. S. Schechter, and L. B. Thompson, *Naturally Fractured Reservoir Characterization* (Society of Petroleum Engineers, Richardson, Texas, 2006) p. 112.

N. C. Davatzes and S. H. Hickman, *Stress, fracture, and fluid-flow analysis using acoustic and electrical image logs in hot fractured granites of the Coso geothermal field, California, U.S.A.* in *Dipmeter and borehole image log technology: AAPG Memoir 92*, edited by M. Poppelreiter, C. Garcia-Carballido, and M. Kraaijveld (AAPG, 2010) Chap. 15, pp. 259–293.

B. B. S. Singhal and R. P. Gupta, *Applied Hydrogeology of Fractured Rocks: Second Edition* (2010) pp. 1–408.

B. Dershowitz, T. Eiben, S. Follin, and J. Andersson, *Alternative models project*, Tech. Rep. (1999).

B. Berkowitz, *Characterizing flow and transport in fractured geological media: A review*, Advances in Water Resources **25**, 861 (2002).

B. Bourbiaux, R. Basquet, M.-C. Cacas, J.-M. Daniel, and S. Sarda, *An Integrated Workflow to Account for Multi-Scale Fractures in Reservoir Simulation Models: Implementation and Benefits*, in *Proceedings of Abu Dhabi International Petroleum Exhibition and Conference* (Society of Petroleum Engineers, Abu Dhabi, United Arab Emirates, 2002).

B. Bourbiaux, R. Basquet, J. M. Daniel, L. Hu, S. Jenni, G. Lange, and P. Rasolofosaon, *Fractured reservoirs modelling: a review of the challenges and some recent solutions*, First Break **23**, 33 (2005).

B. Bourbiaux, *Fractured Reservoir Simulation: a Challenging and Rewarding Issue*, Oil & Gas Science and Technology Revue de l'Institut Français du Pétrole **65**, 227 (2010).

L. Maerten, P. Gillespie, and J.-M. Daniel, *Three-dimensional geomechanical modeling for constraint of subseismic fault simulation*, AAPG Bulletin **90**, 1337 (2006).

S. J. Wilkins, *Fracture intensity from geomechanical models: application to the Blue Forest 3D survey, Green River Basin, Wyoming, USA*, Geological Society, London, Special Publications **292**, 137 (2007).

R. D. Terzaghi, *Sources of Error in Joint Surveys*, Géotechnique **15**, 287 (1965).

M. Ponziani, E. Slob, S. Luthi, R. Bloemenkamp, and I. Le Nir, *Experimental validation of fracture aperture determination from borehole electric microresistivity measurements*, GEOPHYSICS **80**, D175 (2015).

H. Q. Wu and D. D. Pollard, *Imaging 3-D fracture networks around boreholes*, AAPG Bulletin **86**, 593 (2002).

R. Aguilera, *Well Test Analysis of Naturally Fractured Reservoirs*, SPE Formation Evaluation **2**, 239 (1987).

P. Corbett, S. Geiger-Boschung, L. Borges, M. Garayev, J. Gonzalez, and C. Valdez, *Limitations in Numerical Well Test Modelling of Fractured Carbonate Rocks*, in *Proceedings of SPE EUROPEC/EAGE Annual Conference and Exhibition* (Society of Petroleum Engineers, 2010) pp. 1–10.

F. Aljuboori, P. Corbett, K. Bisdom, G. Bertotti, and S. Geiger, *Using Outcrop Data for Geological Well Test Modelling in Fractured Reservoirs*, in *77th EAGE Conference and Exhibition 2015* (2015).

F. Muhammad, *Geological well testing in fractured carbonate reservoir*, M.sc. thesis, Heriot Watt University (2016).

G. H. Makel, *The modelling of fractured reservoirs: constraints and potential for fracture network geometry and hydraulics analysis*, Geological Society, London, Special Publications **292**, 375 (2007).

B. Gauthier, M. Garcia, J.-M. J. Daniel, A. M. Zellou, A. Toublanc, M. Garcia, and J.-M. J. Daniel, *Integrated Fractured Reservoir Characterization: A Case Study in a North Africa Field*, SPE Reservoir Evaluation & Engineering **5**, 24 (2002).

S. J. Bourne, F. Brauckmann, L. Rijkels, B. J. Stephenson, A. Weber, J. M. Emanuel, S. International, T. Hague, and E. J. Willemse, *Predictive modelling of naturally fractured reservoirs using geomechanics and flow simulation*, in *Abu Dhabi International Petroleum Exhibition and Conference* (Society of Petroleum Engineers, Abu Dhabi, United Arab Emirates, 2000).

S. Bergbauer, *Testing the predictive capability of curvature analyses*, Geological Society, London, Special Publications **292**, 185 (2007).

S. Bergbauer and D. D. Pollard, *A new conceptual fold-fracture model including prefolding joints, based on the Emigrant Gap anticline, Wyoming*, Geological Society of America Bulletin **116**, 294 (2004).

J. R. Shackleton, M. L. Cooke, and A. J. Sussman, *Evidence for temporally changing mechanical stratigraphy and effects on joint-network architecture*, Geology **33**, 101 (2005).

B. J. Stephenson, A. Koopman, H. Hillgartner, H. McQuillan, S. Bourne, J. J. Noad, and K. Rawnsley, *Structural and stratigraphic controls on fold-related fracturing in the Zagros Mountains, Iran: implications for reservoir development*, Geological Society, London, Special Publications **270**, 1 (2007).

S. E. Laubach, J. E. Olson, and M. R. Gross, *Mechanical and fracture stratigraphy*, AAPG Bulletin **93**, 1413 (2009).

H. M. Savage, J. Ryan Shackleton, M. L. Cooke, and J. J. Riedel, *Insights into fold growth using fold-related joint patterns and mechanical stratigraphy*, Journal of Structural Geology **32**, 1466 (2010).

J. Lamarche, A. P. Lavenu, B. D. Gauthier, Y. Guglielmi, and O. Jayet, *Relationships between fracture patterns, geodynamics and mechanical stratigraphy in Carbonates (South-East Basin, France)*, Tectonophysics **581**, 231 (2012).

A. Awdal, D. Healy, and G. I. Alsop, *Fracture patterns and petrophysical properties of carbonates undergoing regional folding: A case study from Kurdistan, N Iraq*, Marine and Petroleum Geology **71**, 149 (2016).

C. Sanders, M. Bonora, D. Richards, E. Kozlowski, C. Sylwan, and M. Cohen, *Kinematic structural restorations and discrete fracture modeling of a thrust trap: a case study from the Tarija Basin, Argentina*, Marine and Petroleum Geology **21**, 845 (2004).

O. Lacombe, N. Bellahsen, and F. Mouthereau, *Fracture patterns in the Zagros Simply Folded Belt (Fars, Iran): constraints on early collisional tectonic history and role of basement faults*, Geological Magazine **148**, 940 (2011).

S. Tavani, F. Storti, B. Soleimany, M. Fallah, J. A. Muñoz, and R. Gambini, *Geometry, kinematics and fracture pattern of the Bangestan anticline, Zagros, SW Iran*, Geological Magazine **148**, 964 (2011).

M. Branellec, J. P. Callot, B. Nivière, and J. C. Ringenbach, *The fracture network, a proxy for mesoscale deformation: Constraints on layer parallel shortening history from the Malargüe fold and thrust belt, Argentina*, Tectonics **34**, 623 (2015).

J. C. Lorenz, L. W. Teufel, and N. R. Warpinski, *Regional fractures I: a mechanism for the formation of regional fractures at depth in flat-lying reservoirs,* (1991).

G. Bertotti and A. Barnhoorn, *Geology of Mode I , Hybrid and Mode II Fractures - What Do we Really Know ?* in *78th EAGE Conference and Exhibition 2016* (EAGE, Vienna, Austria, 2016).

J. K. Pringle, J. A. Howell, D. Hodgetts, A. R. Westerman, and D. M. Hodgson, *Virtual outcrop models of petroleum reservoir analogues: a review of the current state-of-the-art*, First Break **24** (2006), 10.3997/1365-2397.2006005.

F. Agosta, M. Alessandroni, M. Antonellini, E. Tondi, and M. Giorgioni, *From fractures to flow: A field-based quantitative analysis of an outcropping carbonate reservoir*, Tectonophysics **490**, 197 (2010).

P. Gillespie, E. Monsen, L. Maerten, D. Hunt, J. Thurmond, and D. Tuck, *Fractures in carbonates: from digital outcrops to mechanical models*, Society for Sedimentary Geology **10**, 137 (2011).

H. Boro, E. Rosero, and G. Bertotti, *Fracture-network analysis of the Latemar Platform (northern Italy): integrating outcrop studies to constrain the hydraulic properties of fractures in reservoir models*, Petroleum Geoscience **20**, 79 (2014).

A. P. Lavenu, J. Lamarche, R. Salardon, A. Gallois, L. Marié, and B. D. Gauthier, *Relating background fractures to diagenesis and rock physical properties in a platform-slope transect. Example of the Maiella Mountain (central Italy)*, Marine and Petroleum Geology **51**, 2 (2014).

L. Kleipool, J. Reijmer, N. Hardebol, G. Bertotti, M. Aurell, and B. Bádenas, *Fracture distribution along an Upper Jurassic carbonate ramp, NE Spain*, Marine and Petroleum Geology **70**, 201 (2016).

O. P. Wennberg, T. Svana, M. Azizzadeh, A. M. M. Aqrawi, P. Brockbank, K. B. Lyslo, and S. Ogilvie, *Fracture intensity vs. mechanical stratigraphy in platform top carbonates: the Aquitanian of the Asmari Formation, Khaviz Anticline, Zagros, SW Iran*, Petroleum Geoscience **12**, 235 (2006).

G. Bertotti, N. Hardebol, J. Koppen, and S. M. Luthi, *Toward a quantitative definition of mechanical units: New techniques and results from an outcropping deep-water turbidite succession (Tanqua-Karoo Basin, South Africa)*, AAPG Bulletin **91**, 1085 (2007).

M. Mauldon and J. G. Mauldon, *Fracture sampling on a cylinder: From scanlines to boreholes and tunnels*, Rock Mechanics and Rock Engineering **30**, 129 (1997).

K. Bisdom, B. Gauthier, G. Bertotti, and N. Hardebol, *Calibrating discrete fracture-network models with a carbonate three-dimensional outcrop fracture network: Implications for naturally fractured reservoir modeling*, AAPG Bulletin **98**, 1351 (2014).

A. Rotevatn, S. J. Buckley, J. A. Howell, and H. Fossen, *Overlapping faults and their effect on fluid flow in different reservoir types: A LIDAR-based outcrop modeling and flow simulation study*, AAPG Bulletin **93**, 407 (2009).

C. E. Wilson, A. Aydin, M. Karimi-Fard, L. J. Durlofsky, S. Amir, E. E. Brodsky, O. Kreylos, and L. H. Kellogg, *From outcrop to flow simulation: Constructing discrete fracture models from a LIDAR survey*, AAPG Bulletin **95**, 1883 (2011).

D. Hodgetts, *Laser scanning and digital outcrop geology in the petroleum industry: A review*, Marine and Petroleum Geology **46**, 335 (2013).

S. Tavani, P. Granado, A. Corradetti, M. Girundo, A. Iannace, P. Arbués, J. Muñoz, and S. Mazzoli, *Building a virtual outcrop, extracting geological information from it, and sharing the results in Google Earth via OpenPlot and Photoscan: An example from the Khaviz Anticline (Iran)*, Computers & Geosciences **63**, 44 (2014).

K. Mahmud, G. Mariethoz, P. C. Treble, and A. Baker, *Terrestrial LiDAR Survey and Morphological Analysis to Identify Infiltration Properties in the Tamala Limestone, Western Australia*, IEEE Journal of Selected Topics in Applied Earth Observations and Remote Sensing **8**, 4871 (2015).

J. M. English, *Thermomechanical origin of regional fracture systems*, AAPG Bulletin **96**, 1597 (2012).

M. C. Cacas, J. M. Daniel, and J. Letouzey, *Nested geological modelling of naturally fractured reservoirs*, Petroleum Geoscience **7**, S43 (2001).

C. Zeeb, E. Gomez-Rivas, P. D. Bons, and P. Blum, *Evaluation of sampling methods for fracture network characterization using outcrops*, AAPG Bulletin **97**, 1545 (2013).

A. Ghassemi and G. Suresh Kumar, *Changes in fracture aperture and fluid pressure due to thermal stress and silica dissolution/precipitation induced by heat extraction from subsurface rocks*, Geothermics **36**, 115 (2007).

K. Matsuki, E. Wang, A. Giwelli, and K. Sakaguchi, *Estimation of closure of a fracture under normal stress based on aperture data*, International Journal of Rock Mechanics and Mining Sciences **45**, 194 (2008).

Q. Lei, J.-p. Latham, J. Xiang, and C.-F. Tsang, *Polyaxial stress-induced variable aperture model for persistent 3D fracture networks*, Geomechanics for Energy and the Environment **1**, 34 (2015).

R. N. McGinnis, D. a. Ferrill, K. J. Smart, A. P. Morris, C. Higuera-Diaz, and D. Prawica, *Pitfalls of using entrenched fracture relationships: Fractures in bedded carbonates of the Hidden Valley Fault Zone, Canyon Lake Gorge, Comal County, Texas*, AAPG Bulletin **99**, 2221 (2015).

S. Geiger and S. Matthäi, *What can we learn from high-resolution numerical simulations of single- and multi-phase fluid flow in fractured outcrop analogues?* Geological Society, London, Special Publications **374**, 125 (2012).

G. Bertotti and K. Bisdom, *Fracture patterns in the Jandaira Fm. (NE Brazil)*, (2013).

K. Bisdom, *Natural fracture patterns in carbonate rocks*, (2015).

N. Barton, *Non-linear behaviour for naturally fractured carbonates and frac-stimulated gas-shales*, First Break **32**, 51 (2014).

Q. Lei, J.-P. Latham, J. Xiang, C.-F. Tsang, P. Lang, and L. Guo, *Effects of geomechanical changes on the validity of a discrete fracture network representation of a realistic two-dimensional fractured rock*, International Journal of Rock Mechanics and Mining Sciences **70**, 507 (2014).

K. Bisdom, G. Bertotti, and H. M. Nick, *The impact of different aperture distribution models and critical stress criteria on equivalent permeability in fractured rocks*, Journal of Geophysical Research: Solid Earth **121**, 4045 (2016).

G. Casini, P. a. Gillespie, J. Verges, I. Romaire, N. Fernandez, E. Casciello, E. Saura, C. Mehl, S. Homke, J.-C. Embry, L. Aghajari, and D. W. Hunt, *Sub-seismic fractures in foreland fold and thrust belts: insight from the Lurestan Province, Zagros Mountains, Iran*, Petroleum Geoscience **17**, 263 (2011).

N. Barton and S. Bandis, *Some effects of scale on the shear strength of joints*, in *International Journal of Rock Mechanics and Mining Sciences & Geomechanics Abstracts*, Vol. 17 (Pergamon Press Ltd., 1980) pp. 69–73.

N. Barton, *Modelling rock joint behaviour from in situ block tests: Implications for nuclear waste repository design*, Tech. Rep. (Office of Nuclear Waste Isolation, Columbus, OH, 1982).

2

Outcropping fracture network digitisation using a drone and photogrammetry

Outcrop analogues provide the 2-D or 3-D fracture geometry that cannot be characterised from subsurface data. To obtain a representative characterisation of geometry, fracture datasets obtained from outcrops need to include at least several hundred fractures covering several orders of magnitude in length and spacing after correction for truncation and censoring artefacts. Until recently, scanlines and laser scanning methods such as LiDAR were the preferred tools for fracture analysis, but scanlines provide limited data whereas LiDAR is relatively expensive and inflexible. Unmanned Aerial Vehicles (UAVs) are a more flexible and inexpensive alternative to LiDAR, as they can image any type of outcrop geometry at a fraction of the cost. The outcrop images are processed into georeferenced photorealistic 3-D models using photogrammetry, which is computationally fast compared to LiDAR point cloud processing. We present an integrated workflow for outcrop imaging using UAVs, 2-D and 3-D outcrop modelling using photogrammetry and 2-D fracture interpretation in a georeferenced environment using DigiFract software. This workflow provides maximum flexibility in terms of required resolution and digitised outcrop geometry with minimum censoring and truncation artefacts. Moreover, the method is fast, as the quality of the acquired dataset can be checked immediately after image acquisition, and the outcrop model is generated and interpreted within hours after acquisition.

2.1. Introduction

Natural fracture networks are multiscale systems that develop through a combination of mechanical and chemical processes, that are only partly understood (Philip *et al.*, 2005; Olson *et al.*, 2009). Outcrops are the only source to obtain realistic descriptions of fracture networks, as no models exist that can create realistic fracture networks on the scale of fractured reservoirs. Deriving lessons for subsurface fracture modelling requires outcropping datasets containing at least several hundred fractures covering several orders of magnitude in spacing and length, corrected for censoring and truncation artefacts (Bonnet *et al.*, 2001; Ortega *et al.*, 2006). Such datasets are not easily obtained from conventional outcrop photographs or scanline studies, as these methods capture only a limited number of scales. To obtain multiscale datasets of at least several hundred fractures, satellite imagery and Light Detection And Ranging (LiDAR) are used (e.g. Rotevatn *et al.*, 2009; Reif *et al.*, 2011; Wilson *et al.*, 2011; Strijker *et al.*, 2012; Hodgetts, 2013; Tavani *et al.*, 2014; Mahmud *et al.*, 2015; Kleipool *et al.*, 2016). However, the use of satellite imagery is limited to sub-horizontal pavements and the resolution is typically limited (Jones *et al.*, 2016). LiDAR provides a higher resolution and accuracy, but acquisition and processing is relatively costly and time-intensive (Hodgetts, 2013).

Photogrammetry, particularly Structure from Motion (SfM) Multiview stereo (MVS) is an inexpensive and fast alternative to reconstruct the 3-D outcrop geometry (James and Robson, 2012). Photogrammetry aligns partly overlapping images by identifying and extracting common points, which are positioned in 3-D space to reconstruct the outcrop geometry. Using the camera position and orientation, calibrated with georeferenced markers on the outcrop, the 3-D model is accurately georeferenced. This 3-D reconstruction of a geometry from 2-D images is referred to as stereophotogrammetry (James and Robson, 2012; Bemis *et al.*, 2014). As this approach requires that the outcrop is fully covered by images with an overlap of at least 50%, Unmanned Aerial Vehicles (UAVs or drones), equipped with a camera and positioning sensors such as GNSS (Global Navigation Satellite Systems), are best suited to acquire the images required for photogrammetry modelling (e.g. James and Robson, 2012; Hodgetts, 2013; Bemis *et al.*, 2014; Tavani *et al.*, 2014; Vasuki *et al.*, 2014; Bond *et al.*, 2015; Vollgger and Cruden, 2016).

The main bottleneck of this approach is the digitisation and extraction of geological features such as fractures from the photogrammetry models. Automatic extraction techniques are still in early development (Vasuki *et al.*, 2014; Lin *et al.*, 2015), and most geological modelling tools are not optimised for displaying these models and extracting features from them, with some exceptions (Tavani *et al.*, 2014). We present an integrated workflow for extracting 2-D fracture patterns from relatively large pavements (e.g. up to 250×800 m), imaged using a UAV and processed through photogrammetry. The aim of this workflow is to rapidly obtain a quantitative 2-D fracture network from which geometrical properties can be extracted that are relevant for naturally fractured reservoir characterisation. Second, the digitised patterns are direct input for geomechanical and fluid flow models (Chapter 3).

2.2. Image acquisition using a drone

We use a multi-rotor type UAV (md4-200®, Microdrones GmbH®; Figure 2.1), which is able to hover at fixed positions to take photographs and is more flexible in manoeuvring close to objects such as cliffs compared to fixed-wing UAVs. The disadvantage compared to fixed-wing UAVs is the limited flight time and speed, limiting the area that can be photographed during a single flight. The md4-200 weighs 0.8 kg and can carry up to 0.3 kg of additional payload. Its horizontal dimensions without rotors are 54 × 54 cm, with a height of 23 cm. These small dimensions allow for easy transport and deployment. The UAV can be used in a wide range of conditions, including high-altitude regions (up to 4000 m), heavy rain and wind speeds up to 8 $m s^{-1}$.

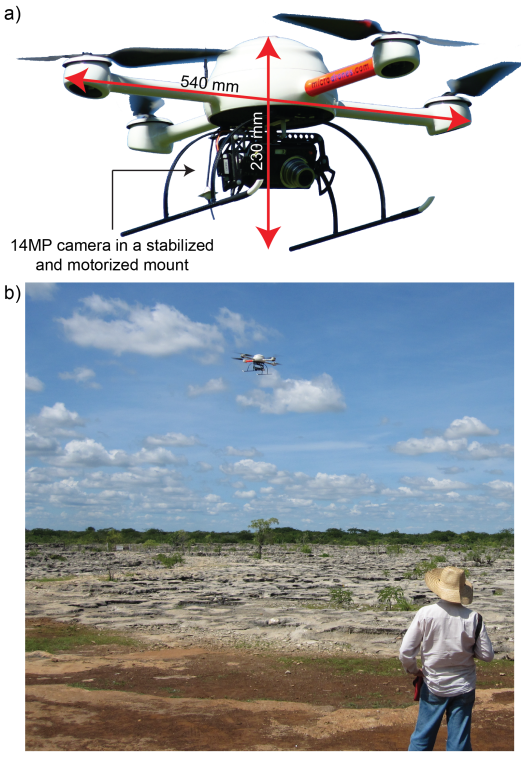


Figure 2.1: Outcrop imaging using a UAV: a) The md4-200 UAV equipped with a compact camera; b) Imaging fractured pavements in the Potiguar Basin, NE Brazil (Chapter 4).

To ensure that an area is fully covered by images with constant overlap, flight paths are programmed prior to flights using mdCockpit® software, where the flight path, altitude, velocity, UAV position, imaging targets and image overlap are specified (Figure 2.2). It uses a Digital Elevation Model (DEM) to allow for adjusting the UAV altitude on slopes, ensuring a constant distance from the ground and a

constant image resolution. The programmed flights are automatically executed and controlled using the GNSS sensor (2 m accuracy) for horizontal positioning and a temperature-compensated barometer (dm-accuracy) for vertical positioning. Accuracy of the GNSS signal is monitored continuously and used to quantify the accuracy of each flight and subsequent georeferenced image dataset. A magnetic compass provides the absolute heading while accelerometers and a gyroscope further control the position of the UAV and ensure stable operation. Flight and environment conditions are continuously monitored. Furthermore, within a range of approximately 300 m from the operator, the UAV transmits live video and diagnostic data to a base station that is equipped with a downlink decoder, which projects the live flight details and video feed to a regular laptop equipped with mdCockpit (Figure 2.3).

Outcrop images are taken with a compact camera (OPTIO® S1) in a motorised mount attached to the UAV. The resulting image resolution is a function of altitude:

$$H = \frac{w_i \cdot R \cdot F_r}{w_s \cdot 100} \tag{2.1}$$

where H is the distance between the camera and the object (in meters), which is a function of the image width w_i (in pixels), the image resolution R (in cm/pixel), the camera sensor width w_s (in mm) and the real focal length F_r (in mm):

$$F_R = \frac{F_{35}\, w_s}{34.6} \tag{2.2}$$

with $F35$ as the focal length in a 35 mm equivalent. For the OPTIO S1, the relation between flying altitude and image resolution is:

$$R = \frac{H}{34.70} \tag{2.3}$$

From this it follows that an altitude of 50 m yields a resolution of 1.44 cm/pixel. Depending on outcrop size and required resolution, most flights are between 20–100m altitude, corresponding to resolutions of 0.6–2.9cm/pixel respectively. For each image, the corresponding UAV position (horizontal coordinates and altitude) and orientation are stored. We also position brightly marked GCPs (Ground Control Points) on the outcrop surface, which are georeferenced using (differential) GNSS and a hand-held laser range finder.

2.3. Image processing using photogrammetry

Using Agisoft PhotoScan®, we process the UAV images and location data into georeferenced 3-D outcrop models. This workflow consists of image alignment, point cloud generation, surface meshing and texturing.

2.3.1. Image alignment

The approximate GNSS position from where each image is taken is used to identify the image pairs that are likely to overlap. Next, common points are identified that help to determine the exact position of one image with respect to surrounding images. These points are extracted and positioned in 3-D in a *sparse point*

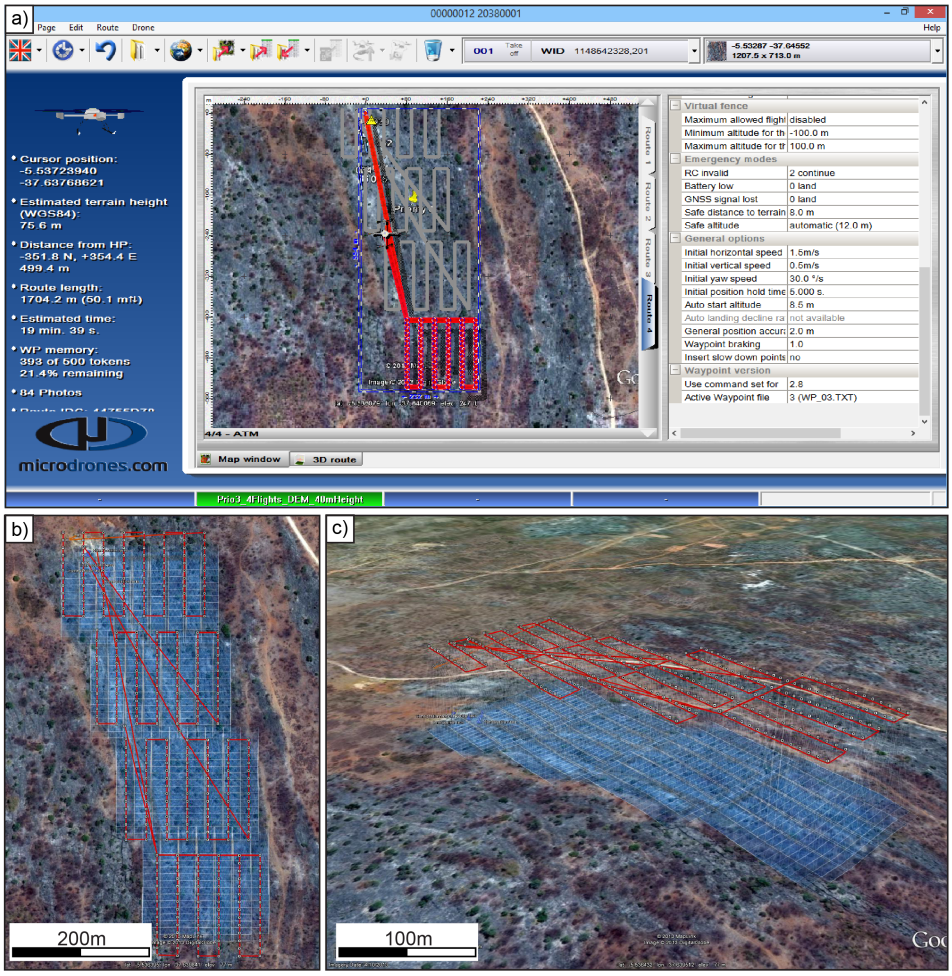


Figure 2.2: Programming and visualising GNSS-steered flights: a) In mdCockpit, flight paths can be programmed in detail using a georeferenced backdrop from Google Earth as reference; b) The resulting flight paths (red lines) and imaged areas (blue rectangles) can be exported to Google Earth for quality checking; c) In Google Earth, flight paths are visualised in 3-D, allowing for checking the programmed flight altitude with respect to ground level.

cloud (Figure 2.4a). The vertical position of a point is determined from the relative change in position in the partly overlapping images, where one point is imaged from different angles. Without location data, image alignment remains possible, although the alignment process will take significantly longer. If the alignment is not successful, e.g. because of limited overlap or poor image quality, common points can be identified manually in the different images to assist the alignment process.

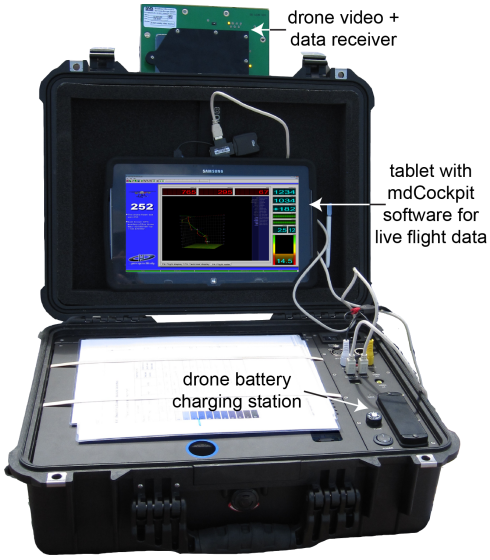


Figure 2.3: Base station used to receive and visualise flight and video data during flights.

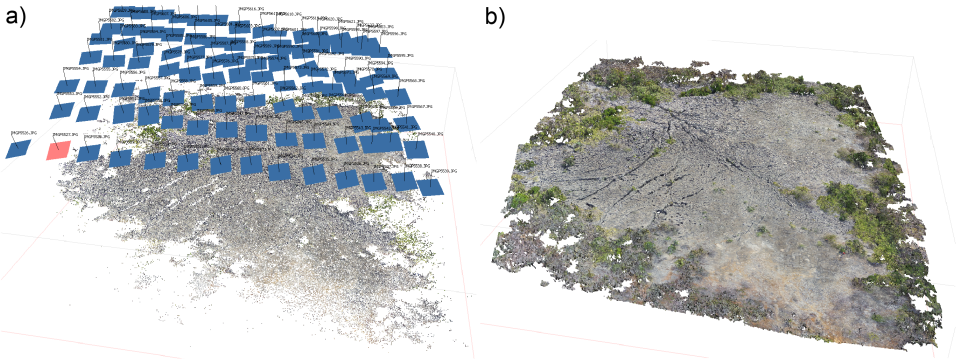


Figure 2.4: Generating a 3-D outcrop model from georeferenced photographs using photogrammetry: a) Alignment of the images (rectangles) based on their GNSS position and common points extracted from the images; b) 3-D high-resolution dense point cloud.

2.3.2. Point cloud generation

After image alignment, all points are extracted from the images to generate a *dense point cloud* (Figure 2.4b). Resolution depends on flight altitude but it can approximate the resolution of LiDAR data for low-altitude flights. A single flight at 50 m altitude, capturing 100 images covering an area of 200 × 200 m, results in a dense point cloud of 1.4×10^7 points (35 points per m^2). Datasets captured from an altitude of 3 m yield point clouds of 8.6×10^7 points for an area of 20 × 30 m (1.4×10^4 points per m^2; Figure 2.5).

The dense point cloud is an accurate 3-D representation of the outcrop geometry

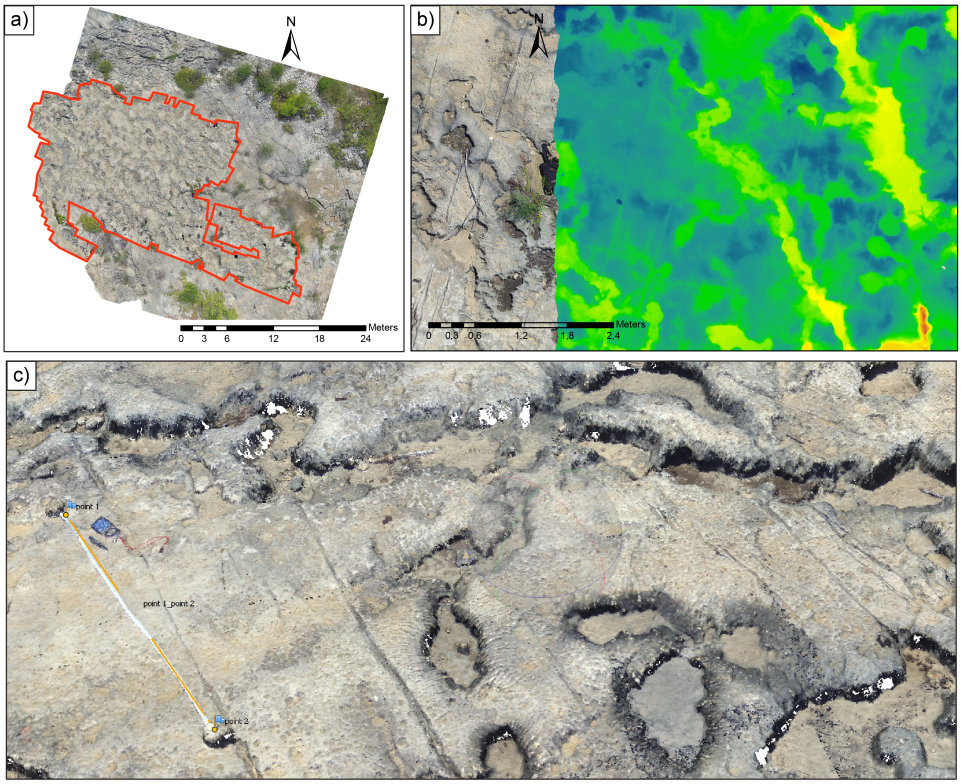


Figure 2.5: High-resolution dataset of a pavement: a) Top view of the 2-D orthophoto. The area within the red boundary has a resolution of 0.6 mm per pixel; b) Detail of the outcrop, showing partly the orthophoto (left) and partly the Digital Elevation Model. From the Digital Elevation Model, closed fractures and weathering patterns can be identified. Warm colours indicate relatively low elevation, cold colours is higher elevation; c) Oblique view detail of the high-density point cloud. The measuring tape in the lower left corner is 1.5 m. White areas are sub-vertical parts of the outcrop that were not sufficiently covered by the photographs.

(Figure 2.5). When the images are georeferenced, aligning and dense point cloud generation are relatively fast processes (less than 3 hours for up to 200 images on a mid-range laptop). These steps can already be completed during a fieldwork campaign, providing an almost immediate data check to analyse whether data acquisition was successful or additional flights are required. Furthermore, having already a high-resolution aerial overview image in the field can be useful in identifying interesting features or sections of the outcrop that warrant further inspection, or additional higher-resolution flights.

2.3.3. Surface generation

Interpretation of outcropping features requires converting the point cloud into a meshed surface (Figure 2.6). The meshed surface can have the same resolution

as the dense point cloud, but as this creates large datafiles, we downsample the meshes for planar pavement models, where the 3-D geometry is less important. For the example in Figure 2.6, the point cloud consists of 8.6×10^7 points whereas the resulting surface is downsampled to 2×10^6 elements (Figure 2.6b). This surface has a sufficiently high resolution for fracture interpretation (Figure 2.6c).

The 3-D surface model can be exported to Google Earth® or most reservoir modelling software tools, including Gocad/SKUA®, JewelSuite® and Petrel®. Alternatively, 2-D orthomosaic photos can be exported for interpretation in GIS-based tools such as ArcGIS®, QGIS® or DigiFract (Hardebol and Bertotti, 2013).



Figure 2.6: Constructing a 3-D meshed surface from the point cloud: a) Detail view of the point cloud, showing the compass and pen that can also be seen in Figure 2.5c; b) Triangular mesh constructed for the area from (a). The mesh has a lower resolution than the point cloud; c) Texture extracted from the original photographs, projected onto the mesh.

2.3.4. Fracture digitisation

For fracture digitisation we load the 2-D orthomosaic images into the GIS-based interpretation software DigiFract (Hardebol and Bertotti, 2013). For each fracture, the trajectory is manually digitised in a 2-D environment, and attributes including orientation and infill are assigned. This approach is designed to be fast and user-friendly such that fractures can be rapidly digitised, such that it can be used on tablet PCs in the outcrop. Manual interpretation is time-intensive, but automatic tracking methods are not sufficiently sophisticated to replace manual interpretation, and require time-intensive quality-checking and manual corrections (Lin *et al.*, 2015; Vasuki *et al.*, 2014; de Callatay, 2016).

After digitisation, orientation, spacing and length distributions can be calculated and visualised using stereoplots, rose diagrams and frequency distributions (Figure 2.7). Fracture spacing is calculated using a combination of methods, where P_{10} intensity, which is the 1-D fracture density measured along a line (Dershowitz, 1985), is calculated using a large amount of closely-spaced scanlines projected along the entire height or length of an outcrop. Alternatively, spacing is defined by P_{21} intensity, which is the total fracture length versus outcrop area, calculated by summing the total length or height of fractures within the entire outcrop or in individual beds as a function of outcrop area (Dershowitz, 1985; Wu and Pollard, 2002).

The full spacing distribution is analysed using box-counting methods, where the outcrop is either divided into boxes with a constant area, in which P_{21} intensity is calculated (Figure 2.7e), or the P_{21} intensity is calculated within a circle with a fixed centre and an increasing radius (Bonnet *et al.*, 2001; Reith, 2015). The latter

method also provides a means for characterising the Representative Elementary Area, which indicates the optimal grid cell size for upscaled fracture flow modelling (Long and Witherspoon, 1985; Dershowitz and Doe, 1997). The analysis of spacing and size distributions using these methods helps to identify the scaling behaviour of fracture systems, to test for example if the fracture networks follow power-law scaling trends (Davy *et al.*, 1990; Bour and Davy, 1997; Bonnet *et al.*, 2001).

The size and spacing distributions are corrected for censoring artefacts, which result from fractures that are not fully captured in the model such that their true length or height is unknown (e.g. Ortega *et al.*, 2006). We correct for this by filtering all fractures that intersect the user-defined outcrop boundaries and by manually identifying and excluding areas obscured by for example trees. Truncation artefacts, which are related to the resolution limit of the outcrop model such that the smallest fractures are typically under-represented (e.g. Bonnet *et al.*, 2001; Ortega *et al.*, 2006), cannot be corrected automatically. Truncated length and spacing scales need to be identified by the user, based on the image resolution limit.

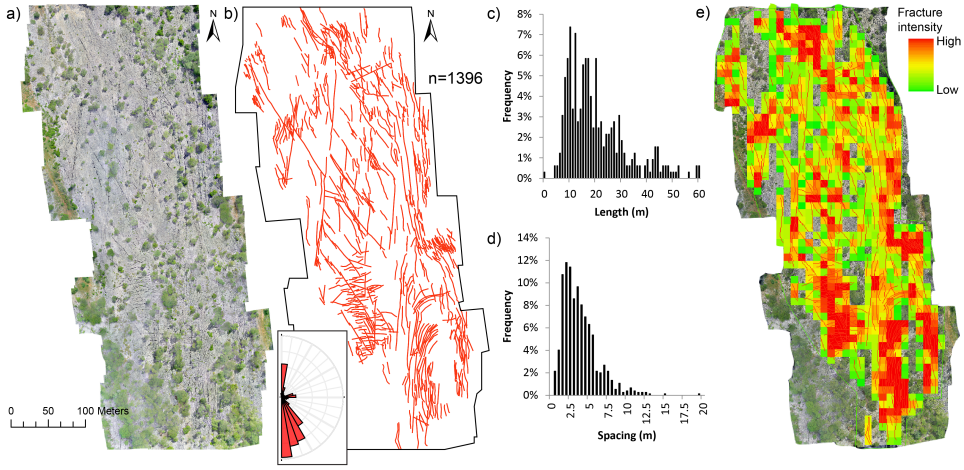


Figure 2.7: Fracture digitisation and analysis in DigiFract using a 2-D orthomosaic of a carbonate pavement, constructed from 400 photographs taken from an altitude of 50 m, resulting in a orthomosaic resolution of 1 cm/px: a) The orthomosaic used for fracture digitisation; b) The digitised fracture network; c) Fracture length distribution; d) Fracture spacing distribution calculated using a box-counting method; e) Spatial fracture intensity calculated using box-counting.

2.4. Discussion

2.4.1. Spatial accuracy and image quality

Although the digital outcrop models constructed using photogrammetry have a high accuracy when calibrated with GCPs measured using differential GNSS (Harwin and Lucieer, 2012), not all outcrops can be accessed to position and measure these GCPs. In the absence of differential GNSS, the model can be accurately

scaled by positioning several scale bars with known lengths on the outcrop before image acquisition, or by measuring distances between easily recognisable points using a laser range finder. A sensitivity analysis of a pavement model covering 250×250 m, imaged from a 100 m altitude, shows an error in horizontal scaling of 0.5% when no ground control points are used. This indicates that models of areas that could not be accessed for placement of ground control points can still be assumed to have an error margin of less than 1%, although this error increases with increasing flight altitude. Potential distortion of the x and y axes of an image are no issue when using photogrammetry, as the exact position, which includes also the orientation of the camera, is reconstructed in the alignment process, and corrected for when extracting and positioning points in 3-D.

Whereas positioning of the image is relatively accurate, ensuring a high image quality is more challenging as our UAV supports only light-weight compact cameras. Although these cameras have a relatively high resolution, they are sensitive to movement and poor light conditions, increasing the probability of blurry images. Even in good weather conditions, i.e. wind speeds of less than $3\,\mathrm{m\,s^{-1}}$, minor movements and UAV vibrations result in up to 20% of blurry images. This percentage increases rapidly for higher wind speeds. This can be partly compensated by increasing the hover time allocated for taking an image and by taking multiple images at the same location. A more significant improvement is achieved by using small sports cameras (e.g. GoPro®), which are optimised for taking sharp images while moving. Our tests indicate that this decreases the amount of blurred images to less than 1%.

2.4.2. Comparison to other methods

Aside from photogrammetry, scanlines and LiDAR are the most commonly used tools to characterise fractures in outcrops. Scanlines are fast and easy to use, particularly in small outcrops, but they only provide a 1-D characterisation of fracture spacing, orientation and aperture, and typically only one orientation set can be measured at a time. Scanlines are suited to analysing datasets of small veins in outcrops of several square meters, but they are not suited to quantitative acquisition of a statistically significant dataset of fractures covering multiple orders of magnitude in spacing and length, required for quantitative fracture analysis (e.g. Bonnet *et al.*, 2001).

Prior to the advancement of UAVs, LiDAR was the preferred method for acquiring quantitative fracture datasets. However, its usage is limited to airborne application or easily accessible outcrops that can be imaged from ground level such as cliffs. Usability is further limited by high equipment costs and the computationally expensive processing of the point clouds (Hodgetts, 2013). Outcrop imaging with UAVs is more flexible than LiDAR, as UAVs can hover close to any outcrop, including cliffs, pavements and dipping or folded surfaces. Small UAVs such as the md4-200 used in this study are easily transported to and deployed in the fieldwork area, and the live video feed during flights combined with pre-programmed flight paths permits imaging of outcrops that are inaccessible by foot. It is however the combination of UAV image acquisition and photogrammetry processing that positions

this methodology perfectly in between the flexible but qualitative scanline method and the inflexible but quantitative LiDAR methods, as photogrammetry provides almost instantaneous quantitative results. Within an hour after image acquisition, the individual image quality and overlap between images can be checked, and a high-resolution 3-D point cloud can be constructed within hours using a conventional laptop. This 3-D point cloud can be used directly during the fieldwork for initial fracture interpretation and positioning in the field.

The resolution and image quality of photogrammetry is slightly lower compared to LiDAR datasets, but for fracture interpretation LiDAR tends to provide too much detail that requires some degree of downsampling to be able to interpret the 3-D models using conventional hardware. For the photogrammetry workflow, the required combination of area covered and minimal image resolution can be determined prior to deploying the UAV, and the flying altitude can be adjusted accordingly. This way, the ideal amount of detail is captured directly, without need for later downsampling. Although the initial spatial error of the photogrammetry models is higher than for LiDAR, the use of accurate GCPs, for example measured using differential GNSS, significantly decrease the spatial error.

2.5. Conclusions

The presented workflow combines outcrop image acquisition using a UAV with 3-D outcrop modelling using photogrammetry followed by 2-D fracture digitisation in DigiFract. The UAV and photogrammetry software are readily available commercial tools, but by combining these with fast 2-D interpretation in DigiFract, we present a complete workflow aimed at fast but accurate digitisation of outcropping fracture networks and generating fracture datasets for sound statistical analysis. Compared to alternative outcrop digitisation and fracture interpretation techniques, this workflow has several advantages:

i) The UAV can image any outcrop, irrespective of the outcrop geometry, and the use of pre-programmed flights ensures complete coverage and sufficient overlap between images.
ii) High-resolution 2-D and 3-D outcrop models can be created with UAV image acquisition combined with photogrammetry processing that bridge the gap between conventional outcrop measurements made in the field and satellite imagery.
iii) The required resolution and covered area can be customised for each individual outcrop, to avoid generating large datasets that need subsequent downsampling.
iv) By extracting and interpreting 2-D orthomosaics from 3-D outcrop models, while storing the original 3-D view parameters, fracture interpretation is fast and the resulting dataset can be projected back onto the 3-D outcrop models if needed.

References

Z. G. Philip, J. W. Jennings, J. E. Olson, S. E. Laubach, and J. Holder, *Modeling Coupled Fracture-Matrix Fluid Flow in Geomechanically Simulated Fracture Networks*, SPE Reservoir Evaluation & Engineering **8**, 300 (2005).

J. E. Olson, S. E. Laubach, and R. H. Lander, *Natural fracture characterization in tight gas sandstones: Integrating mechanics and diagenesis*, AAPG Bulletin **93**, 1535 (2009).

E. Bonnet, O. Bour, N. E. Odling, P. Davy, I. Main, P. Cowie, and B. Berkowitz, *Scaling of fracture systems in geological media*, Reviews of Geophysics **39**, 347 (2001).

O. J. Ortega, R. A. Marrett, and S. E. Laubach, *A scale-independent approach to fracture intensity and average spacing measurement*, AAPG Bulletin **90**, 193 (2006).

A. Rotevatn, S. J. Buckley, J. A. Howell, and H. Fossen, *Overlapping faults and their effect on fluid flow in different reservoir types: A LIDAR-based outcrop modeling and flow simulation study*, AAPG Bulletin **93**, 407 (2009).

D. Reif, B. Grasemann, and R. H. Faber, *Quantitative structural analysis using remote sensing data: Kurdistan, northeast Iraq*, AAPG Bulletin **95**, 941 (2011).

C. E. Wilson, A. Aydin, M. Karimi-Fard, L. J. Durlofsky, S. Amir, E. E. Brodsky, O. Kreylos, and L. H. Kellogg, *From outcrop to flow simulation: Constructing discrete fracture models from a LIDAR survey*, AAPG Bulletin **95**, 1883 (2011).

G. Strijker, G. Bertotti, and S. M. Luthi, *Multi-scale fracture network analysis from an outcrop analogue: A case study from the Cambro-Ordovician clastic succession in Petra, Jordan*, Marine and Petroleum Geology **38**, 104 (2012).

D. Hodgetts, *Laser scanning and digital outcrop geology in the petroleum industry: A review*, Marine and Petroleum Geology **46**, 335 (2013).

S. Tavani, P. Granado, A. Corradetti, M. Girundo, A. Iannace, P. Arbués, J. Muñoz, and S. Mazzoli, *Building a virtual outcrop, extracting geological information from it, and sharing the results in Google Earth via OpenPlot and Photoscan: An example from the Khaviz Anticline (Iran)*, Computers & Geosciences **63**, 44 (2014).

K. Mahmud, G. Mariethoz, P. C. Treble, and A. Baker, *Terrestrial LiDAR Survey and Morphological Analysis to Identify Infiltration Properties in the Tamala Limestone, Western Australia*, IEEE Journal of Selected Topics in Applied Earth Observations and Remote Sensing **8**, 4871 (2015).

L. Kleipool, J. Reijmer, N. Hardebol, G. Bertotti, M. Aurell, and B. Bádenas, *Fracture distribution along an Upper Jurassic carbonate ramp, NE Spain*, Marine and Petroleum Geology **70**, 201 (2016).

R. Jones, S. Kokkalas, J. Long, and S. Daniels, *Prediction of fracture networks in structural traps: Insights from outcrop characterisation of four-way closing anticlines in reservoir analogues*, in *International Conference and Exhibition, Barcelona, Spain,*

3-6 April 2016 (Society of Exploration Geophysicists and American Association of Petroleum Geologists, 2016) pp. 271–271.

M. R. James and S. Robson, *Straightforward reconstruction of 3D surfaces and topography with a camera: Accuracy and geoscience application*, Journal of Geophysical Research: Earth Surface **117**, 1 (2012).

S. P. Bemis, S. Micklethwaite, D. Turner, M. R. James, S. Akciz, S. T. Thiele, and H. A. Bangash, *Ground-based and UAV-Based photogrammetry: A multi-scale, high-resolution mapping tool for structural geology and paleoseismology*, Journal of Structural Geology **69**, 163 (2014).

Y. Vasuki, E.-J. Holden, P. Kovesi, and S. Micklethwaite, *Semi-automatic mapping of geological Structures using UAV-based photogrammetric data: An image analysis approach*, Computers & Geosciences **69**, 22 (2014).

C. E. Bond, J. R. Shackleton, and T. Wild, *From Field Fractures to Reservoir Prediction: Utilizing Drones, Virtual Outcrop and Digital Data Analysis to Input Into Discrete Fracture Network (DFN) Models*, in *AAPG Annual Convention and Exhibition* (Denver, Colorado, 2015).

S. A. Vollgger and A. R. Cruden, *Mapping folds and fractures in basement and cover rocks using UAV photogrammetry, Cape Liptrap and Cape Paterson, Victoria, Australia*, Journal of Structural Geology **85**, 168 (2016).

Y. Lin, M. Jiang, Y. Yao, L. Zhang, and J. Lin, *Use of UAV oblique imaging for detection of individual trees in residential environments*, Urban Forestry & Urban Greening **14**, 404 (2015).

N. Hardebol and G. Bertotti, *DigiFract: A software and data model implementation for flexible acquisition and processing of fracture data from outcrops*, Computers & Geosciences **54**, 326 (2013).

G. de Callatay, *Digitization and representation of natural fracture networks based on drone imagery using the Hough transform*, M.sc. thesis, Delft University of Technology (2016).

W. Dershowitz, *MIT*, Ph.d. thesis, Massachusetts Institue of Technology, Cambridge, MA. (1985).

H. Q. Wu and D. D. Pollard, *Imaging 3-D fracture networks around boreholes*, AAPG Bulletin **86**, 593 (2002).

D. F. H. Reith, *Analysis of the different impacts influencing the value of the fractal dimension regarding the Whitby Mudstone formation (UK) & Jandaira formation (Brazil)*, B.sc. thesis, Delft University of Technology (2015).

J. C. S. Long and P. A. Witherspoon, *The relationship of the degree of interconnection to permeability in fracture networks*, Journal of Geophysical Research **90**, 3087 (1985).

W. Dershowitz and T. Doe, *Analysis of heterogeneously connected rock masses by forward modeling of fractional dimension flow behavior*, International Journal of Rock Mechanics and Mining Sciences **34**, 61.e1 (1997).

P. Davy, A. Sornette, and D. Sornette, *Some consequences of a proposed fractal nature of continental faulting*, Nature **348**, 56 (1990).

O. Bour and P. Davy, *Connectivity of random fault networks following a power law fault length distribution*, Water Resources Research **33**, 1567 (1997).

S. Harwin and A. Lucieer, *Assessing the accuracy of georeferenced point clouds produced via multi-view stereopsis from Unmanned Aerial Vehicle (UAV) imagery*, Remote Sensing **4**, 1573 (2012).

3

Stress-induced discrete fracture aperture and fluid flow modelling

Aperture controls fracture permeability in naturally fractured reservoirs, but not all fractures are observed to be hydraulically conductive. Mohr-Coulomb is typically used to define which fractures are critically stressed under in-situ stress conditions, and only critically stressed fractures are expected to contribute to flow. However, fracture flow has also been observed in reservoirs where according to Mohr-Coulomb fractures are not critically stressed. Cement bridges can keep fractures open even under unfavourable stress conditions, but cement bridges are not always present or sufficiently strong to stay intact under in-situ stress. The Barton-Bandis method predicts that in the absence of cement bridges and critical stress conditions, fractures can have sub-millimetre apertures associated with the intrinsic surface roughness. We present an implementation of this method in geomechanical Finite Element simulations to model aperture and permeability in multiscale deterministic fracture patterns covering areas of up to $2.5 \times 10^5 \mathrm{m}$ *to quantify the impact of these small apertures on permeability in reservoirs that are not critically stressed. The results show that these apertures increase equivalent permeability and that the angle between fracture strike and maximum horizontal stress has a controlling impact on aperture and permeability, where hydraulic opening is largest for an angle of 15°. At this angle, the fracture experiences a minor amount of shear displacement that allows it to remain open in non-critically stressed conditions. Averaging the modelled heterogeneous aperture distribution to scale up permeability can result in an underestimation of flow, indicating the need to incorporate full aperture distributions rather than averaged constant apertures in reservoir-scale flow models.*

This chapter is based on: K. Bisdom, G. Bertotti, H.M. Nick. The impact of in-situ stress and outcrop-based fracture geometry on hydraulic aperture and upscaled permeability in fractured reservoirs. Tectonophysics, **In Press**.

3.1. Introduction

Outcrop analogue studies provide an improved understanding of the spatial distribution of fractures in naturally fractured reservoirs, but network geometry alone is not sufficient to characterise fluid flow in fractured reservoirs. At depth, flow is a function of aperture, which is partly controlled by in-situ stress (Zoback, 2007; Baghbanan and Jing, 2008; Tao *et al.*, 2009; Lei *et al.*, 2015), but during exhumation these apertures are changed due to pressure relief. Outcropping apertures are therefore not representative, unless it can be proven that apertures have been preserved during exhumation. This is typically assumed to be the case for veins (e.g. Hooker *et al.*, 2014), but preserved veins are relatively rare and often limited to small fractures.

Whether a fracture contributes to flow at in-situ stress conditions in reservoir models is typically defined using the Mohr-Coulomb critical stress method (Barton *et al.*, 1995; Rogers, 2003). If shear stresses acting on a fracture exceed normal stresses, it becomes critically stressed, forming a conduit for flow (Figure 3.1). Fracture orientation with respect to the maximum and minimum principle stresses is the main variable controlling the critical stress potential (e.g. Crampin, 1987; Teufel *et al.*, 1991). Cement bridges, observed in outcrops and some reservoirs, are considered as a potential mechanism for conductive fractures in areas that are not predicted to be critically stressed (Laubach, 2003; Laubach *et al.*, 2004; Becker *et al.*, 2010; Laubach *et al.*, 2016), but others argue that at depth, the cement is not strong enough to keep the fracture open (e.g. Yasuhara, 2004).

An additional complication lies in the aperture definition of a single fracture. Studies focusing on the relation between in-situ stress and permeability in fractured reservoirs find that the relation between stress and aperture is heterogeneous, with partial opening and closing within a single fracture orientation family or even along a single fracture (e.g. Nemoto *et al.*, 2009; Lei *et al.*, 2015). Although models and outcrop descriptions of heterogeneous apertures of individual fractures exist, they are rarely included in Discrete Fracture Networks (DFNs), which more typically consider a constant aperture per fracture or even per orientation set, with some notable exceptions (Philip *et al.*, 2005; Olson *et al.*, 2009; Nick *et al.*, 2011; de Dreuzy *et al.*, 2012; Lei *et al.*, 2014).

The empirical Barton-Bandis model quantifies the heterogeneous aperture that remains when irregular mismatching fracture walls are partly closed under in-situ stress (Barton, 1982; Bandis *et al.*, 1983). Whereas the critical stress model requires high fluid pressures (Barton *et al.*, 1995; Rogers, 2003; Zoback, 2007), Barton-Bandis predicts that fractures can remain hydraulically open in the absence of high fluid pressures (Figure 3.1; Olsson and Barton, 2001). Under low fluid pressure conditions, kinematic aperture variations that result from for example length-aperture relations do not play a role, as the fracture is 'macroscopically' (i.e. mm-scale or larger) closed by the surrounding stresses. The model quantifies 'microscopic' aperture (i.e. less than 0.5 mm) associated with minor asperities and irregularities along fracture walls on a smaller scale than that of critically stressed fracture planes described by Mohr-Coulomb, assuming that there are no partial cement bridges that prop fractures open. Barton-Bandis furthermore takes into account horizontal

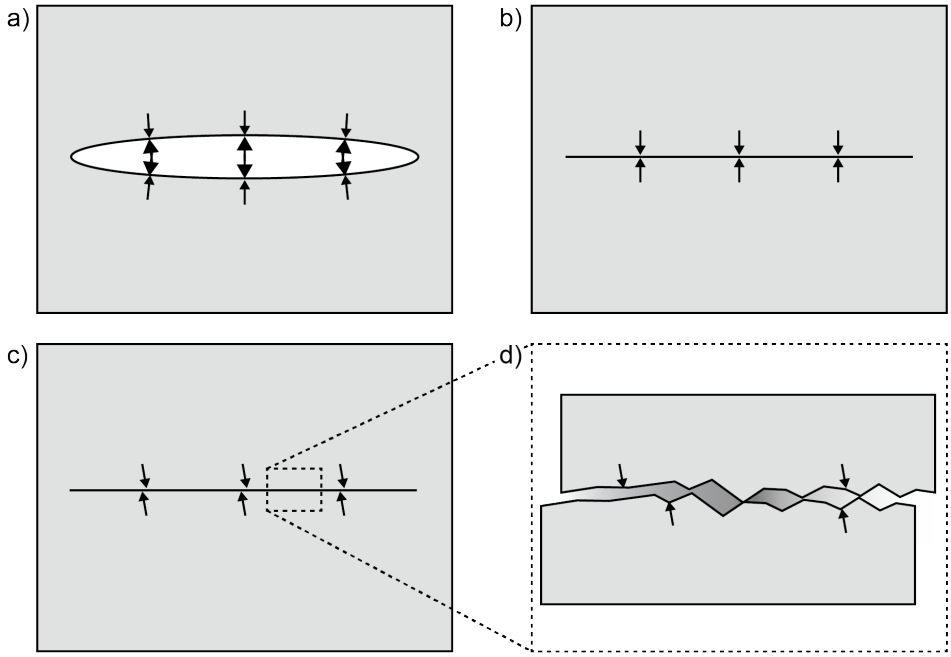


Figure 3.1: Hydraulic fracture aperture under different stress conditions: a) A fracture is open and conductive as the fluid pressure within the fracture is larger than the minimum principle stress acting on the fracture; b) Without high fluid pressures, the fracture is closed macroscopically; c) A fracture with low internal fluid pressure that experiences some shear stress remains macroscopically closed; d) Assuming that fractures are not planar surfaces but have an intrinsic roughness and that experience some shear, a microscopic aperture remains, creating a conductive fracture.

stress anisotropy during production and the subsequent heterogeneous flow behaviour along fracture walls, where local stress conditions may prevent flow along some fractures (Olsson and Barton, 2001; Matsuki *et al.*, 2008).

Barton-Bandis aperture is based on laboratory-scale mechanical experiments on a range of rough fracture surfaces (Barton and Choubey, 1977; Barton and Bandis, 1980; Barton, 1982). It assumes that fractures at in-situ conditions have an aperture that is only controlled by local fracture wall roughness, shape and the local normal stress and shear displacement (Barton, 1982; Bandis *et al.*, 1983; Barton *et al.*, 1985). It defines an initial mechanical aperture, which is a function of roughness and strength in an uncemented fracture, that experiences a certain amount of closing given the local normal and shear stress. If the fracture experiences sufficient shearing, it will remain hydraulically open even if the internal fluid pressure is low, albeit with small hydraulic apertures (Olsson and Barton, 2001).

Aperture and permeability predicted by Barton-Bandis has been studied before, but mainly in synthetic fracture networks with simplified geometries or deterministic models with small dimensions (e.g. Nemoto *et al.*, 2009; Tao *et al.*, 2009; Lei *et al.*, 2014), as implementation of the method requires an accurate definition of the

local stress acting on each fracture segment, which needs to be obtained from Finite Element (FE) models. We present a novel workflow for modelling of Barton-Bandis apertures using digitised 2-D fracture patterns from relatively large outcrops (e.g. up to 250 × 250 m) and model the stress-aperture relation and fluid flow patterns through these deterministic patterns, to better understand the fluid flow response of realistic fracture networks.

For the stress-aperture relation, we use conditions for which fractures are not critically stressed as predicted by Mohr-Coulomb, and quantify the permeability related to poorly interlocking rough fractures as predicted by the Barton-Bandis model. As we are ultimately interested in the hydraulic apertures of present-day fractures in the subsurface and not in the conditions for creating new fractures, we do not consider fracture initiation and propagation. Cement is also not considered as we focus on how an uncemented fracture with irregular fracture walls can contribute to flow through an aperture associated with the roughness of the fracture.

The impact on permeability is modelled using a hybrid Finite-Element Finite-Volume (FEFV) approach that models single-phase incompressible flow through discrete fractures and a permeable matrix (Matthäi and Belayneh, 2004; Matthäi *et al.*, 2007; Paluszny *et al.*, 2007). We illustrate the relative impact of Barton-Bandis aperture on permeability using a set of fracture networks digitised from an outcrop in central Tunisia.

3.2. Barton-Bandis aperture

The aperture described by Barton-Bandis is that of a fracture that is closed according to Mohr-Coulomb, i.e. the fluid pressure within the fracture is smaller than the surrounding stress. Under these conditions, intrinsic fracture roughness combined with limited shear displacement can still result in a small aperture that is typically less than 0.5 mm, depending on the roughness and strength of the fracture and local normal and shear stresses (Barton and Choubey, 1977; Barton and Bandis, 1980; Barton, 1982, 2014). The relation between local stress, shear displacement and aperture is described using a set of empirical functions defined by Barton and Bandis (1980); Barton (1982).

The model assumes an initial intrinsic aperture that is only dependent on roughness and strength of the fracture walls (Figure 3.2). Local stress conditions in the subsurface partly reduce this aperture. The resulting stress-induced aperture is defined as mechanical aperture. The amount of shear displacement that the fracture experiences then defines the hydraulic aperture as a function of mechanical aperture (Olsson and Barton, 2001; Barton, 2014). The parameters used to calculate aperture are listed in Table 3.1. We acknowledge that cement precipitation impacts aperture (Laubach *et al.*, 2004; Philip *et al.*, 2005; Hooker *et al.*, 2012), but for the sake of modelling purposes we only consider mechanical behaviour.

3.2.1. Initial intrinsic aperture

The initial aperture E_0 (in mm), associated with the opening between irregular fracture walls that can no longer fully close, is defined by the *Joint Roughness*

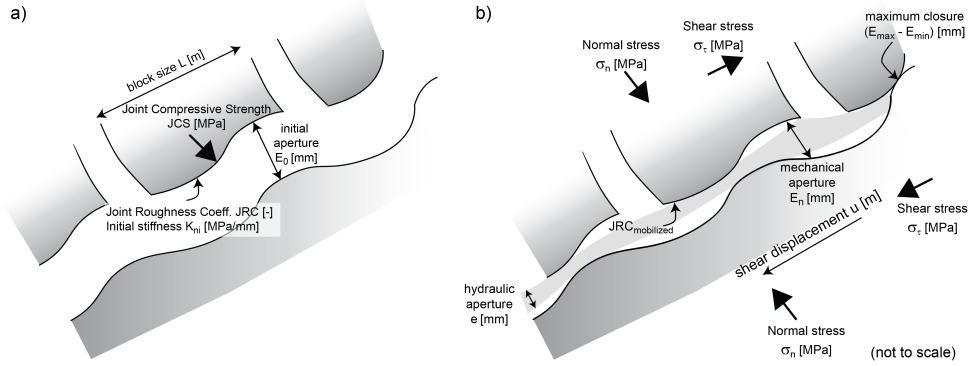


Figure 3.2: Overview of the parameters used to calculate the mechanical and hydraulic apertures: a) The initial aperture which is laterally consistent and a function of fracture roughness and strength; b) Following the application of in-situ stress, the fracture experiences limited shear displacement and partial closure.

Coefficient (*JRC*, dimensionless) and the *Joint Compressive Strength* (*JCS*, in MPa), which are derived from empirical data (Barton and Choubey, 1977; Barton, 2014):

$$E_0 = \frac{JRC}{5}\left(0.2\frac{\sigma_c}{JCS} - 0.1\right) \tag{3.1}$$

In the case of un-weathered joints, where $\sigma_c = JCS$, the initial aperture is a function of the *JRC* only (Barton *et al.*, 1985):

$$E_0 = \frac{JRC}{50} \tag{3.2}$$

The *JRC* can be measured in outcrops using a Barton comb, calculated by the ratio between the amplitude and length of the fracture wall asperities, or estimated from a chart of roughness profiles (Barton, 2014). The *JCS* is measured with for example a Schmidt hammer (Barton, 2014). Throughout this Thesis, we use $JRC = 15$ and $JCS = 120$ MPa, resulting in $E_0 = 0.3$ mm.

3.2.2. Mechanical aperture

By applying stress, the initial intrinsic aperture E_0 becomes stress-dependent mechanical aperture E_n, defined by a hyperbolic function of the normal stress acting on fracture planes, maximum closure and stiffness (Barton and Bandis, 1980; Barton *et al.*, 1985):

$$E_n = E_0 - \left(\frac{1}{v_m} + \frac{K_{ni}}{\sigma_n}\right)^{-1} \tag{3.3}$$

The maximum closure v_m, which is the difference between maximum opening and the smallest aperture along the fracture, depends on *JRC* and *JCS* (Bandis *et al.*, 1983). For irregular fracture walls with a high roughness coefficient, the maximum closure is:

$$v_m = -0.1032 - 0.0074JRC + 1.135\left(\frac{JCS}{E_0}\right)^{-0.251} \tag{3.4}$$

Symbol	Definition	Units
JRC	Joint Roughness Coefficient	–
JCS	Joint Compressive Strength	MPa
σ_c	Uni-axial compressive strength	MPa
E_0	Initial intrinsic aperture	mm
E_n	Mechanical aperture	mm
E_s	Shear component of aperture	mm
Δu_s	Shear displacement	mm
u_{peak}	Peak shear displacement	mm
d_{nmob}	Mobilised dilation angle	°
L	Block size	m
e and $\bar{e}$	Hydraulic aperture and averaged hydraulic aperture	mm
v_m	Maximum closure	mm
K_{ni}	Initial stiffness	MPa/mm
E	Young's modulus	GPa
ν	Poisson's ratio	-
σ_n, σ_1 and σ_3	Normal, maximum and minimum horizontal stress	MPa
δ_{ij}	Kronecker delta	-
ϵ	Strain	-
τ	Shear stress	MPa
c	Cohesion	MPa
ϕ	Internal friction angle	°
q	Darcy flow	m/s
k, k_{eq}, k_m, k_f	Permeability (equivalent, matrix, fracture)	m^2 or mD
μ	Viscosity	Pa s
p	Pressure	Pa

Table 3.1: Overview of parameters used in the Barton-Bandis model

When fracture walls are mismatched during closing, a maximum closure is generated that is larger than zero. The initial stiffness is a constant defined by Bandis *et al.* (1983) as:

$$K_{ni} = -7.15 + 1.75JRC + 0.02\frac{JCS}{E_0} \tag{3.5}$$

Changes in E_n are a direct result of changes in normal stress. We use equation (3.3) to define the relation between normal stresses and the subsequent apertures, where aperture ranges from 0.3 (i.e. initial aperture) to 0.17 mm (i.e. maximum closure) for $JRC = 15$ and $JCS = 120$MPa.

3.2.3. Shearing and hydraulic aperture

To quantify the conductive behaviour of fractures, the Barton-Bandis model defines a hydraulic aperture, which is a function of shear-induced dilation E_s, defined by shear displacement and a modified version of JRC, the mobilised JRC_{mob} (Barton, 1982; Barton *et al.*, 1985; Olsson and Barton, 2001). Shear-induced dilation is defined as (Olsson and Barton, 2001):

$$E_s = \Delta u_s \tan d_{nmob} \tag{3.6}$$

where d_{nmob} is the mobilised dilation angle assuming shear under high normal stress (Barton, 1982; Barton *et al.*, 1985):

$$d_{nmob} = \frac{1}{2}JRC_{mob}\log_{10}\left(\frac{JCS}{\sigma_n}\right) \tag{3.7}$$

and JRC_{mob} is the empirically defined change in joint roughness that occurs at the onset of shearing (Olsson and Barton, 2001). The peak displacement can be described by (Asadollahi *et al.*, 2010):

$$u_{peak} = \frac{L_n}{500}\left[\frac{JRC_n}{L_n}\right]^{0.33} \tag{3.8}$$

where L_n is the effective length or block size and JRC_n the JRC of fracture segment n (Barton, 1982). For fracture networks, L_n is the spacing between the fractures that intersect the fracture of interest (Barton, 1982).

To calculate the hydraulic aperture e that defines the effective aperture for fluid flow, we use a function that relates it to mechanical aperture E_n:

$$e = \begin{cases} \frac{{E_n}^2}{JRC^{2.5}} \text{for} \frac{u_s}{u_{peak}} \leq 0.75 \\ \sqrt{E_n} JRC_{mob} \text{for} \frac{u_s}{u_{peak}} \geq 1 \end{cases} \tag{3.9}$$

where by definition $E \geq e$ (Olsson and Barton, 2001). This takes into account the shearing described by equations (3.6) and (3.7), using the ratio between shear and peak shear displacement. The domain in between $0.75 \leq u_s/u_{peak} \leq 1.0$ is interpolated linearly (Olsson and Barton, 2001). When shear displacement approaches peak shear displacement, shearing has a significant positive effect on hydraulic aperture. Mechanical and hydraulic aperture are calculated along the entire length of a fracture, where block size varies along a fracture if it is intersected by multiple other fractures, and where normal and shear stresses vary along the length of a fracture, as a result of local stress perturbations.

3.3. From fracture network to mechanical model

To calculate the normal stress and shear displacement acting on each fracture segment, the Barton-Bandis approach is implemented into a geomechanical FE model where the fracture network is represented explicitly. The model is subjected to a far-field stress, which is translated into local stress perturbations around the fracture network. We implement the Barton-Bandis calculations directly into the simulation workflow to model aperture for each geomechanical fracture network in two steps:

i) Represent fractures as mechanical discontinuities in a FE mesh, defined as 'seams', that create local stress perturbations (Figure 3.3). This is done using a set of functions written in `Python` (Appendix A).
ii) Use the local normal stress and shear displacement that act on the fracture walls in the FE model to calculate the local aperture for each fracture segment during each simulation step.

3.3.1. Meshing of discrete fracture networks

Accurate representation of fracture connectivity is essential, particularly when the matrix is close to impermeable (Hardebol *et al.*, 2015; Sanderson and Nixon,

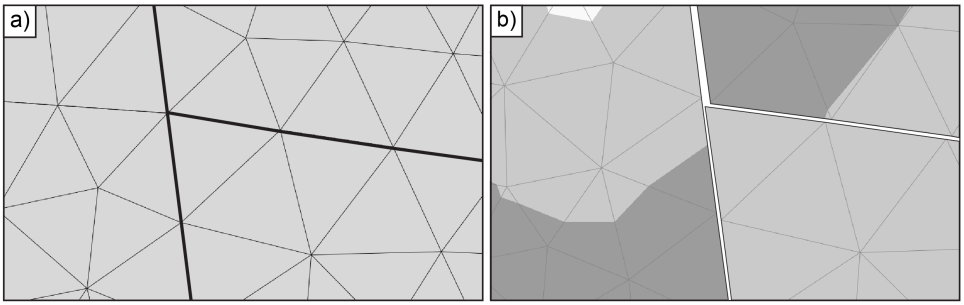


Figure 3.3: Aperture in the FE models is modelled by representing the fractures as seams in the mesh, which can open or close as a function of local stress: a) Input mesh with 2 fractures indicated by the thick lines; b) Result after simulation, showing the stresses in the mesh and the resulting fracture opening along the seams.

2015). In an impermeable matrix, even a cm-scale gap in between two fractures forms a flow barrier. We therefore ensure that the topology is accurately represented in our digitised fracture network, focusing on fracture terminations and intersections (Figure 3.4).

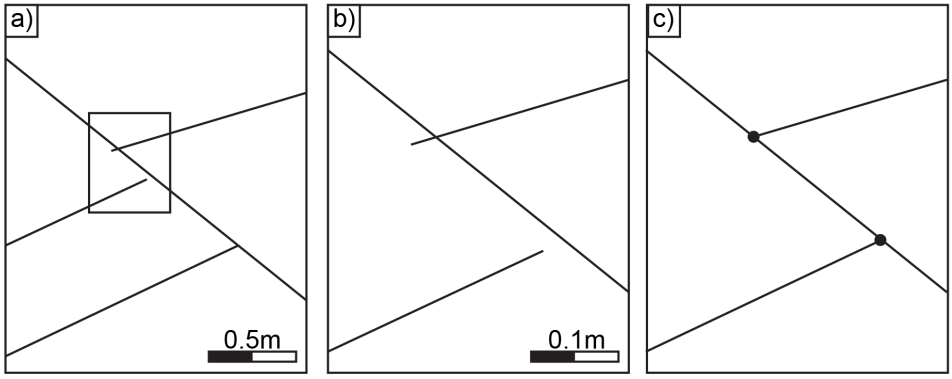


Figure 3.4: Removal of minor gaps and overlaps to accurately represent the network topology: a) Three small fractures terminating against one larger fracture, with incorrect connections; b) Detail showing one overlapping segment and one segment with a gap; c) Correct fracture network interpretation using snapping.

For meshing the geometry in 2-D we use ABAQUS CAE® (Dassault Systèmes®). Compared to other meshing tools, we find that for our application, ABAQUS successfully meshes complex geometries with minimal pre-processing. An unstructured triangulated mesh with quadratic elements is used to represent the fracture network. At this point, the fractures are not yet represented explicitly, but the mesh is conformable around the network geometry (Figure 3.5). The element size is non-uniform with refinements near fracture segments and further refinements around the crack tips to avoid simulation convergence errors related to singularity issues.

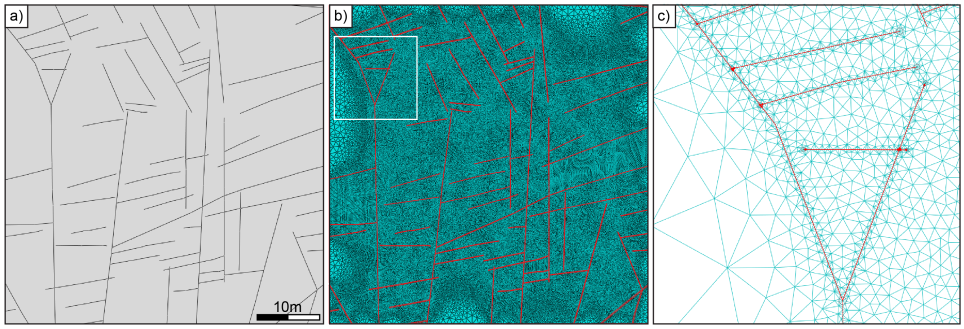


Figure 3.5: Converting a deterministic fracture network into a triangular mesh: a) 50×50 m section extracted from an outcropping carbonate pavement; b) Meshed fracture network geometry; c) detail of the mesh showing refinement around the fractures.

3.3.2. Boundary conditions and loads

We apply maximum and minimum horizontal principle stresses to the boundaries, with displacement conditions that ensure symmetry and prevent model rotations (Figure 3.6). In this example, a maximum horizontal stress σ_1 (e.g. tectonic stress) is applied in the y direction, which results in a Poisson's stress (σ_3) in the x direction. Within each element, the principle stresses are used to calculate normal stress σ_n (Zoback, 2007):

$$\sigma_n = 0.5\left(\sigma_1 + \sigma_3\right) + 0.5\left(\sigma_1 - \sigma_3\right)\cos 2\beta \tag{3.10}$$

where β is the angle between σ_1 and fracture strike. The models are 2-D, representing the scenario of a 2-D horizontal cross-section under horizontal stresses. The model dimensions are significantly larger than the fracture network, ensuring that the stress field around the fractures is not affected by boundary effects (Figure 3.6).

3.3.3. Rheology and governing equations

Stress and strain is modelled using the ABAQUS Standard (i.e. implicit) simulator, using geostatic conditions (Dassault Systemes, 2013). Deformation is applied in small incremental steps, allowing for non-linear behaviour of aperture as predicted by Barton-Bandis (Barton, 2014). The equilibrium equations are solved using a non-linear Newton method for plane-strain models (Table 3.1):

$$\sigma_{ij} = \frac{E}{1+\nu}\varepsilon_{ij} + \frac{E\nu}{(1+\nu)(1-2\nu)}\delta_{ij}\varepsilon_{kk} \tag{3.11}$$

For elastoplastic materials a linear Mohr-Coulomb criterion is used (Table 3.1):

$$\tau = c - \sigma\tan\phi \tag{3.12}$$

The transition from the elastic to the plastic domain is defined by the cohesion yield stress. Using this model set-up, the local stress distribution is calculated around all fractures for any given far-field stress configuration (Figure 3.7). The local stress state is then used to calculate the Barton-Bandis aperture distribution.

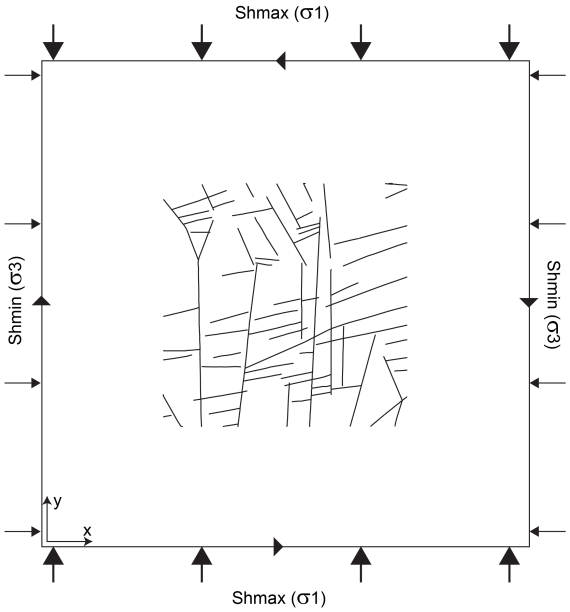


Figure 3.6: Set-up of an elastic mechanical fracture network, using the model from Figure 3.5. Maximum horizontal stress σ_1 (30 MPa) is applied in the y direction, resulting in a σ_3 of 10 MPa in the x direction, for a Poisson's ratio of 0.3. We apply displacement boundary conditions on the centre points of each boundary to ensure symmetrical deformation.

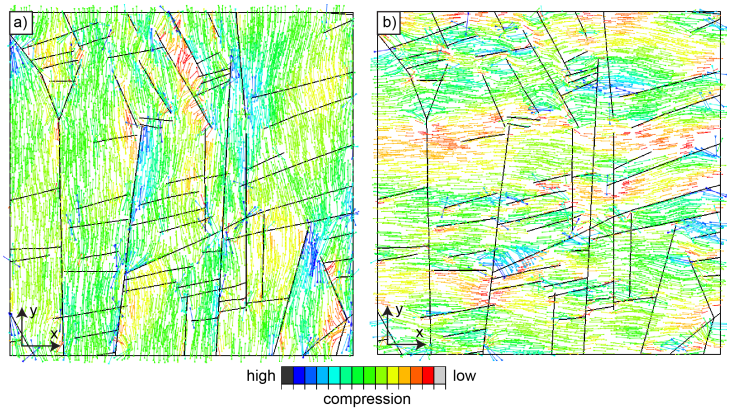


Figure 3.7: Maximum **(a)** and minimum **(b)** principle stress directions and magnitudes for the model from Figure 3.6, taking into account the fracture seams. As σ_1 is applied in the y direction, maximum horizontal compression is in the same direction, with variations in both magnitude and direction around the fractures. Minimum horizontal stress σ_3 (i.e. Poisson's stress) is predominantly oriented in the x direction.

3.4. Equivalent permeability modelling

Permeability is modelled using the geomechanical FE mesh with discrete fractures represented by 1-D line elements, using single-phase fluid pressure sim-

ulations. There is hence no upscaling of effective flow properties. To solve the flow equations, we use a hybrid Finite-Element Finite-Volume (FEFV) approach implemented in the Complex Systems Modelling Platform (CSMP++; Matthäi *et al.*, 2007).

We calculate the equivalent permeability, which is a function of combined matrix and fracture permeability (Matthäi *et al.*, 2009), by numerically solving the steady state continuity equation,

$$\nabla q = 0 \tag{3.13}$$

using CSMP++, with q being the Darcy velocity in $\mathrm{m\,s^{-1}}$:

$$q = -\frac{k}{\mu}\nabla p \tag{3.14}$$

with fluid pressure p in Pa, viscosity μ in $\mathrm{Pa\,s^{-1}}$ and intrinsic permeability k in $\mathrm{m^2}$ (Matthäi *et al.*, 2007). A far field pressure gradient of 10 kPa is applied in either the N-S or E-W direction of the model, after which equation (3.13) is solved (Paluszny and Matthäi, 2010; Nick and Matthäi, 2011).

Matrix permeability k_m is assumed constant. Intrinsic fracture permeability k_f is calculated for each element that has a positive hydraulic aperture. Note that the hydraulic aperture calculated for all nodes is mapped along the fracture onto its centre line (see Figure 1 in Nick *et al.*, 2011). Assuming laminar flow between two parallel plates, intrinsic fracture permeability is a function of hydraulic aperture e in meters (Snow, 1969):

$$k_f = \frac{e^2}{12} \tag{3.15}$$

with k_f in $\mathrm{m^2}$. In networks with heterogeneous apertures, this function will yield a heterogeneous k_f, where each fracture node has a local permeability value. The fractures are discretised using lower dimensional line elements, to which the hydraulic aperture values calculated using the Barton-Bandis method are assigned (Figure 3.8a-b Juanes *et al.*, 2002; Matthäi *et al.*, 2009). The mesh conversion is done using ANSYS ICEM®, as the required input file format for CSMP++ cannot be created directly using ABAQUS.

Similar to Matthäi and Nick (2009), equivalent permeability in the N-S and E-W directions is calculated through equation (3.14) by integrating the fluid flux across the model boundaries. The equivalent permeability describes the capability of the fractured formations to permit the flow of fluid through the porous rock matrix and open fractures in each direction from one boundary to the opposite one, assuming no-flow boundary conditions at the other two boundaries parallel to the far field pressure gradient (e.g. Matthäi and Belayneh, 2004).

Using CSMP++, the velocity and pressure fields are calculated in the x and y directions of the rectangular 2-D models (Figure 3.8c-d). Optionally, the full pressure tensor fields can be modelled, but here we focus only on relative trends in permeability From the pressure fields in the x and y directions, equivalent permeabilities are calculated. Intrinsic permeability is large even for small aperture values (i.e. 833 Darcy for a 0.1 mm aperture), but a high intrinsic permeability does not necessarily result in a significant increase in equivalent permeability, as this depends on

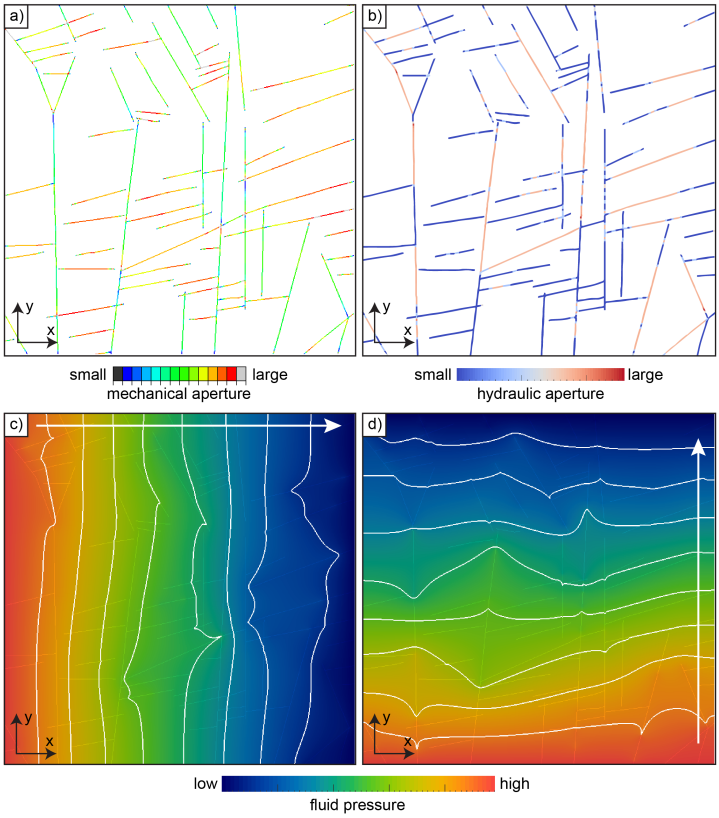


Figure 3.8: Fracture aperture and flow analysis in CSMP++: a) Mechanical aperture defined by Barton-Bandis; b) Subsequent hydraulic aperture, assuming 30 MPa bulk shortening in the y direction; c) Fluid pressure distribution in the x direction; d) Fluid pressure distribution in the y direction. The contour lines (white) and colour gradient show the fluid pressure distribution.

the contrast between matrix and intrinsic permeability, as well as fracture network intensity and connectivity.

3.5. Application

The aperture and permeability distributions predicted by the presented workflow are analysed using a synthetic single-fracture model and four models with geometries extracted from a fractured pavement. The single-fracture model is only analysed in terms of aperture, to quantify how mechanical and hydraulic aperture change as a function of orientation. The four outcrop models are used to illustrate in more detail the impact of different fracture geometrical parameters, far-field stress conditions and rock properties on the modelled aperture and equivalent permeability.

3.5.1. Aperture of a single fracture

We analyse changes in aperture as a function of normal stress and orientation in the single-fracture model. The σ_1, applied in the y direction (i.e. σ_y), is 30 MPa, which results in a Poisson's stress (i.e. σ_x) of 10 MPa. The model set-up and boundary conditions are similar to those in Figure 3.6, covering 100 × 100 m, but instead of a fracture network, we only consider a single 40 m long fracture striking parallel to σ_1 in the centre. In all models, we assume a JRC of 15 and a JCS of 120 MPa, resulting in an initial aperture of 0.3 mm. The rock is fully elastic with a Young's Modulus of 50 GPa and a Poisson's ratio of 0.3.

Mechanical aperture as defined by equation (3.3) decreases for increasing normal stress (Figure 3.9), as the model is compressed on all sides and the initially open fracture is the only void space in an otherwise elastic rock mass. Hydraulic aperture increases with increasing compression once the shear displacement along the fracture surfaces approaches or exceeds the peak shear displacement (Figure 3.9b). Mechanical aperture is largest for a fracture parallel to the σ_1 and decreases with an increasing angle up to 30°, after which aperture remains approximately constant (Figure 3.9c). Hydraulic aperture is nearly zero for a fracture parallel to σ_1, but increases when the fracture strike becomes oblique, with a maximum at 15°. The strong dependency of orientation and aperture results from the small amounts of shear displacement, resulting in poor interlocking fracture walls, creating relatively large hydraulic apertures.

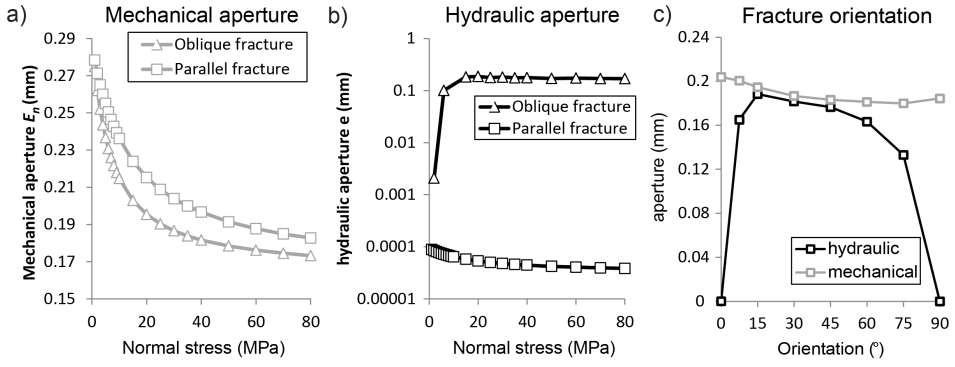


Figure 3.9: Relation between mechanical opening (E_n) and hydraulic aperture (e) for a fracture that is striking parallel to the direction of σ_1, compared to that of a fracture striking at 30°: a) Mechanical aperture; b) Hydraulic aperture; c) Mechanical and hydraulic apertures as a function of fracture orientation.

3.5.2. Sensitivity analysis of aperture in fracture networks

Aperture and permeability in more realistic natural fracture networks is analysed using four 50 × 50 m patterns digitised from a pavement (Figure 3.10). These patterns are converted to fracture meshes of 100 × 100 m, to prevent boundary stress effects. The geometry of each model is summarised in Table 3.2. The structural setting and regional geology of this outcrop are discussed in Chapter 6. As these models are extracted from the same pavement, they have similar, but not

identical, fracture geometrical distributions. We quantify how these small differences affect aperture and permeability. These models assume the same stress conditions, initial apertures and rock properties as the synthetic single-fracture model. Equivalent permeability is quantified in N-S and E-W directions for a σ_1 oriented either N-S or E-W (Figure 3.11).

	model 1	model 2	model 3	model 4
# fset 1 (N-S)	19	20	9	22
spacing fset 1 [m]	6.8	6.4	9.2	9.2
length fset 1 [m]	13.2	15.6	18.5	14.8
# fset 2 (E-W)	50	38	34	52
spacing fset 2 [m]	5.6	7.2	8.8	5.1
length fset 2 [m]	7.8	9.0	8.8	5.1
# total	69	58	43	74
spacing [m]	3.3	3.6	4.9	3.5
average length [m]	9.5	11.6	10.1	9.0
maximum length [m]	42.2	48.5	37.7	28.5
# intersections	48	41	16	43
N-S pathways	1	1	1	0
E-W pathways	1	0	0	0

Table 3.2: Summary of fracture geometry in each model

Impact of spacing

Spacing, defined as the inverse of P_{21} (Dershowitz and Einstein, 1988), has no strong impact on equivalent permeability, as for a N-S oriented σ_1, the outcrops with the smallest spacing (i.e. highest intensity) have the lowest permeability (model 1), whereas the model with the largest spacing (model 3) has the highest equivalent permeability (Figure 3.11a,c). The spacing distributions of the different sub-models are similar, with relatively small variations in average spacing (except for model 3), whereas variations in permeability are relatively large. In terms of spacing per orientation set, the N-S system has a larger spacing than the E-W system (Table 3.2), but the higher-intensity E-W system has a lower permeability, even when maximum compression is oriented E-W (Figure 3.11b).

Impact of connectivity

Fracture connectivity is not representative of equivalent permeability, as the model with the lowest connectivity, expressed as the number of fracture intersections, has the highest permeability for a N-S oriented σ_1 (model 3 in Figure 3.11a). Model 1, which has the highest connectivity, has the lowest permeability when σ_1 is in N-S direction. Models 2 and 4 do have high permeabilities as well as a high connectivity, but it is lower than that of model 3, which has 50% fewer intersections compared to the other models.

With the exception of model 4, three of the four models have percolating pathways of connected fractures (Figure 3.10 and Table 3.2). However, in terms of hydraulic aperture, there is no fully connected pathway in any of the models, so the connected fractures in model 4 do not form a percolating pathway in terms of fluid flow.

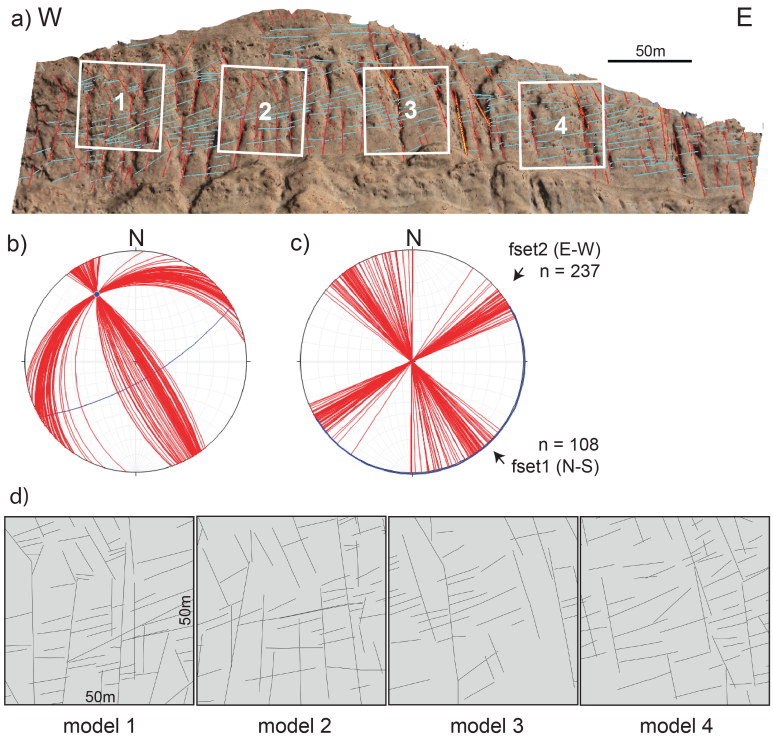


Figure 3.10: Outcrop model with interpreted fractures, from which the four sub-models are extracted: a) Digitised outcrop model of the complete pavement with the position of the four outcrop windows; b) Lower hemisphere stereoplot of 345 digitised fractures (red) and bedding (blue); c) Stereoplot with back-rotated fracture orientations; d) The four fracture models.

Impact of fracture length

The large contrast in N-S versus E-W equivalent permeability is mainly related to the maximum and average fracture lengths (Table 3.2 and Figure 3.11d). Average fracture length of the N-S trending system is more than 50% larger than that of the E-W fracture system (Table 3.2). The longest fractures in each model are part of the N-S system. Moreover, when ranking the outcrops from large to small average length of N-S sets, the ranking is identical to the ranking of N-S equivalent permeability (Figure 3.11a).

Average and maximum length better describe the resulting equivalent permeability trends, compared to spacing, even though spacing is defined as a function of length (i.e. inverse of P_{21}). However, the P_{21} intensity does not distinguish between many small fractures or a few large fractures.

Impact of orientation

Although length correlates to some extent with equivalent permeability, it does not explain the relatively high N-S permeability in model 3. Orientation, however, does have a positive impact on fluid flow in this network. Fracture strike with respect

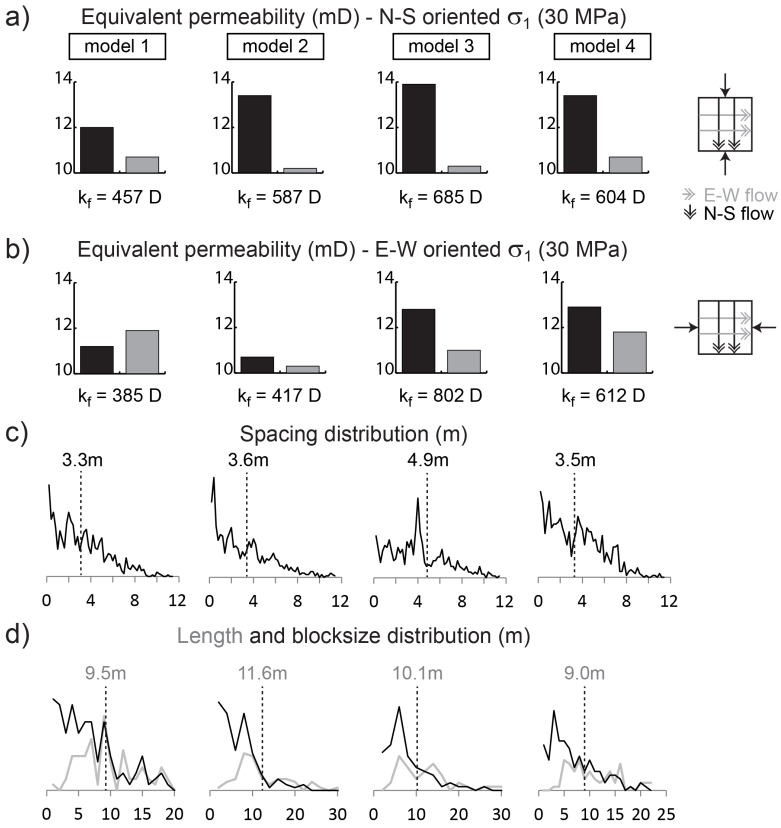


Figure 3.11: Equivalent permeability in N-S (black bars) and E-W directions (grey bars) for each outcrop model as a function of maximum horizontal stress oriented in: a) N-S direction; b) E-W direction. The k_f indicated for each plot is the average intrinsic fracture permeability calculated using the cubic law; c) Average spacing and spacing distribution for each sub-model; d) Length (grey) and block size distributions (black) for each sub-model, with the average length indicated in each plot.

to the direction of σ_1 is key for hydraulic aperture and subsequent permeability. The average strike in model 3 is 17°, which corresponds approximately to the ideal angle between shortening direction and strike observed in the synthetic models (Figure 3.9c). The other three models contain more fractures, but a smaller subset of these fractures is ideally oriented with respect to the shortening direction (i.e. 15°; Figure 3.12). The length-weighted orientation distribution of model 4 is similar to model 3, resulting in a similar permeability, but models 1 and 2 have fewer ideally oriented fractures, resulting in lower permeabilities.

Impact of stress

We quantify the change in aperture as a function of increasing regional stress σ_1 and changing stress orientation (N-S vs. E-W). In the single-fracture model it was shown that an increase in stress may lead to an increase in permeability, depending

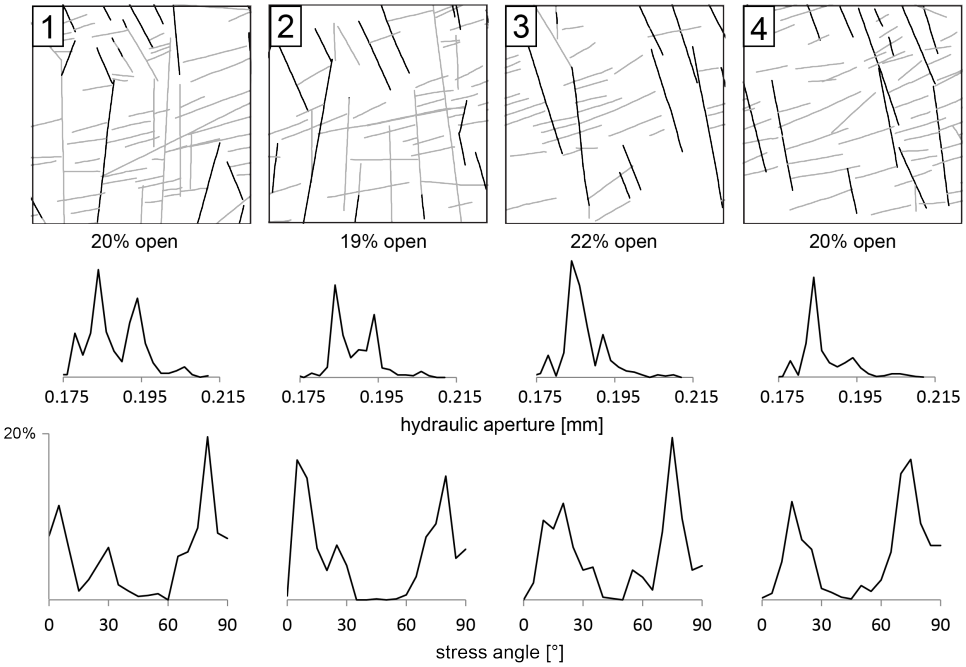


Figure 3.12: Fracture orientation per model, highlighting in black all fractures that strike at an angle of 10-30° with respect to the direction of maximum horizontal stress. The percentage of hydraulically open fracture segments, the hydraulic aperture distribution and length-weighted orientation distribution, defined by the stress angle, are shown below each outcrop model.

on whether the fracture experiences shear stress (Figure 3.9). In the four networks, changing the far-field stress leads to more heterogeneous aperture and permeability distributions (Figure 3.13).

We identify three equivalent permeability domains for N-S compression (Figure 3.13a). These trends are similar for E-W compression (Figure 3.13b), but as the contribution of fractures to flow is small, the domains are less easily observed. Focusing on N-S compression, the first domain (up to 5 MPa differential stress) is characterised by a lack of change in permeability. Between 5–20MPa, permeability increases, and flattens again for differential stresses above 20 MPa. The flattening results from the definition of hydraulic aperture, which cannot exceed mechanical aperture.

A second factor strongly impacting aperture and permeability is the direction of σ_1. When σ_1 is applied in the N-S direction, most E-W striking fractures experience maximum closure, resulting in lower E-W equivalent permeability (Figure 3.13a). However, when σ_1 is in the E-W direction, N-S permeability in three of the four models remains larger than permeability in the E-W direction, indicating that the direction of highest permeability is not only a function of stress direction, but also of other factors, such as geometry (Figure 3.13).

The irregular increase in permeability, most notably in the domain between 5–

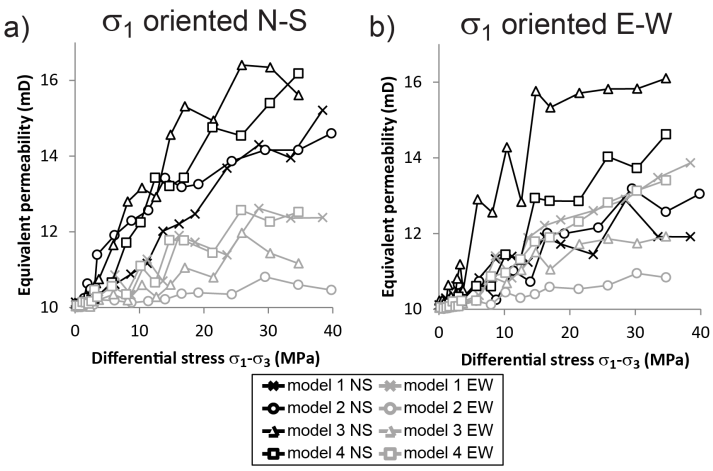


Figure 3.13: Equivalent permeability in N-S direction (black curves) and E-W direction (grey curves) for each sub-model as a function of increasing stress: a) Maximum horizontal stress in N-S direction; b) Maximum horizontal stress in E-W direction.

15MPa differential stress, is primarily dependent on the ratio between shear displacement and peak shear displacement, as a small change in shear may result in changing from one hydraulic aperture domain to another, as determined by equation (3.9).

Impact of rock properties

Compressive stress and the subsequent aperture and permeability distributions are functions of the mechanical behaviour of the rock matrix. We analyse a range of values for the Young's modulus and Poisson's ratio, and compare the elastic model with an elastoplastic model. In all models, the applied σ_1 is constant (30 MPa). We do not consider the effect of deformation on matrix porosity and permeability, and assume that fracture properties remain constant.

For an elastic rheology, the equivalent permeability decreases with increasing Young's modulus and Poisson's ratio, irrespective of the direction of σ_1 (Figure 3.14). A higher Young's modulus results in a decrease in shear displacement and shear-induced hydraulic aperture and flow. Since we only consider compression, a high Poisson's ratio increases σ_3 and decreases mechanical and subsequent hydraulic opening. This effect is clearest in Figure 3.14d, where for N-S shortening without the possibility of E-W extension, the E-W trending fractures are almost immediately closed when the Poisson's ratio starts to increase, resulting in a large contrast in permeability in the E-W direction versus the N-S direction.

Plasticity lowers the shear displacement acting on fracture surfaces and subsequently lowers the hydraulic aperture (Figure 3.14c,f). The relative impact of fractures on equivalent permeability decreases, resulting in smaller differences in permeability between the sub-models. For the applied stress conditions, the elastic properties have a stronger impact on permeability than the plastic properties. For

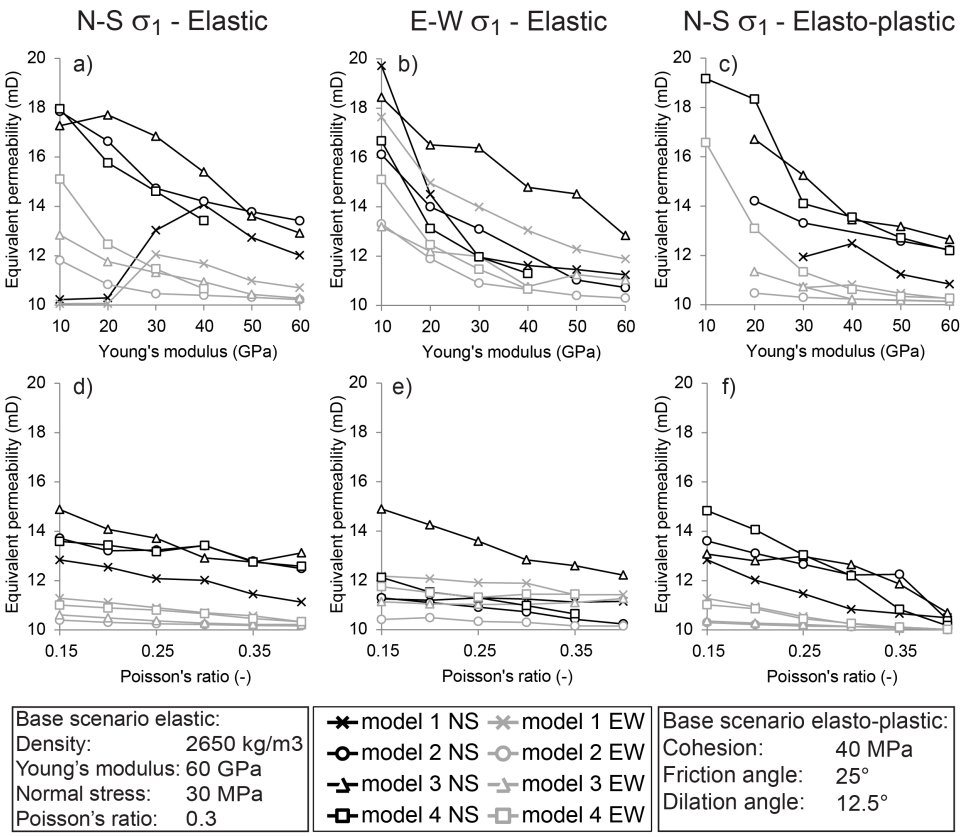


Figure 3.14: Equivalent permeability as a function of rheology: a) N-S (black curves) and E-W (grey curves) permeability as a function of the Young's modulus for a N-S σ_1; b) The impact of Young's modulus on permeability when σ_1 is oriented E-W; c) Changes in permeability as a function of Young's modulus in an elastoplastic model; d) Relation between permeability and Poisson's ratio (N-S σ_1); e) Relation between permeability and Poisson's ratio (E-W σ_1); f) Impact of Poisson's ratio in an elasto-plastic model.

a higher differential stress, the plastic domain may become the controlling factor, and its properties may have a larger impact relative to the elastic properties.

3.5.3. Heterogeneous vs. constant aperture distributions

The aperture distributions of the 50 × 50 m models are heterogeneous, even along single fractures. In most fractured reservoir models, aperture is constant per fracture, or even per orientation set as creating a reservoir-scale 3-D fracture model with mechanically controlled heterogeneous aperture distributions is a complex task (Geiger and Matthäi, 2012). Alternatively, the high-resolution aperture and permeability, calculated per fracture node, of explicit fracture permeability models can be upscaled through arithmetic or harmonic averaging (Jonoud and Jackson, 2008; Cottereau *et al.*, 2010). We test the accuracy of averaging aperture in terms of

permeability using our permeability modelling workflow.

For each of the four models, we calculate the weighted average aperture $\bar{e}$ as a function of the summed apertures of fracture segments with length l_e:

$$\bar{e} = \frac{\sum e * l_e}{\sum l_e} \tag{3.16}$$

The average is a function of both open and closed fracture parts, including those that are practically closed by the first part of equation 3.9, and is assigned as a constant aperture to the entire fracture network. The equivalent permeability resulting from the averaged aperture distributions is modelled for elastic (N-S and E-W oriented σ_1) and elastoplastic (N-S oriented σ_1) models (Figure 3.15).

The average aperture yields an upward trend in permeability for increasing differential stress that is similar to that of the heterogeneous distributions, with model 3 having the highest equivalent permeability in N-S direction (Figure 3.15a). The permeability in the E-W direction, however, has changed significantly, and is similar to the N-S permeability, as all fractures in all directions have the same aperture (Figure 3.15b). Permeability resulting from average aperture in an elastoplastic model is lower, similar to that which was observed for heterogeneous apertures (Figure 3.15c). Compared to the heterogeneous aperture distributions, the averaged distributions underestimate in N-S permeability and overestimate E-W permeability (Figure 3.15).

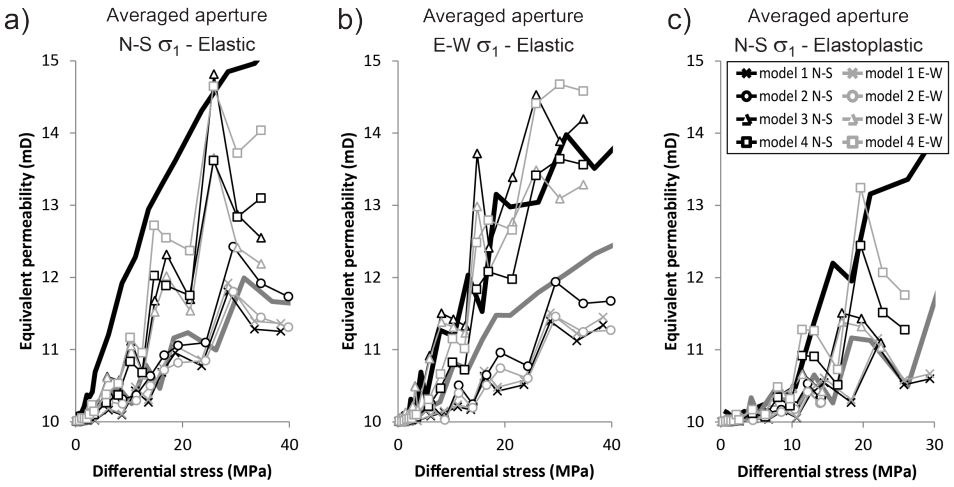


Figure 3.15: N-S (black curves) and E-W (grey curves) equivalent permeability for all four models, calculated using an average aperture. For comparison with heterogeneous aperture, the thick black and grey curves show the N-S and E-W heterogeneous aperture averaged for all sub-models; a) N-S compression; b) E-W compression; c) Elastoplastic rheology under N-S compression.

3.6. Discussion

3.6.1. Fracture aperture versus geometry

The amount of shear displacement and the resulting hydraulic aperture distributions in the presented models are partly driven by fracture orientation. For maximum hydraulic aperture, Barton-Bandis predicts that fractures should ideally strike at a small angle (i.e. close to 15°) with respect to σ_1 (Figure 3.9). As a result, model 3, which has the largest spacing and smallest fracture intersection count, but ideally oriented fractures for large hydraulic apertures, has a larger equivalent permeability than the other models. Figures similar to Figure 3.9 may be useful for defining the relation between fracture orientation and hydraulic aperture. When in-situ stress data are available and the mechanical rock properties are relatively homogeneous, such that fracture attributes are only influenced by stress, the impact of fracture orientation can be incorporated into DFN modelling workflows to define hydraulic aperture without the need of geomechanical modelling of aperture (Appendix B).

In the studied outcrop-based models, the fracture orientation and associated hydraulic aperture have a stronger impact on equivalent permeability than length or spacing. Spacing does not significantly impact equivalent permeability, even though we have defined spacing as a function of length using P_{21}. We do find that for constant spacing, equivalent permeability is higher for a fracture system consisting of few large fractures rather than many small fractures. This distinction is however not made by the P_{21} definition.

In terms of network connectivity, the number of pathways in both horizontal directions has no direct impact on permeability, as these pathways are not necessarily hydraulically open under the given stress conditions. Percolation studies often assume that all fractures are conductive and that the matrix is impermeable, such that disconnected fractures do not contribute to flow. This yields a binary response in permeability, where breaking up a fracture network by removing a single fracture may yield a large change in permeability (i.e. the percolation threshold; Long and Witherspoon, 1985; Berkowitz and Balberg, 1993). We do not observe this effect in our permeability analysis, where 10 mD matrix flow is included and fracture aperture is relatively small. Other studies that take into account coupled fracture-matrix flow find that even with matrix permeability, connectivity has a larger impact than aperture (Philip *et al.*, 2005; Olson *et al.*, 2009). However, the contrast between matrix and fracture permeability is large in most of these models, resulting in an equivalent permeability that is controlled by intrinsic fracture permeability (Matthäi and Belayneh, 2004). For low matrix permeability (i.e. less than 10 mD), network connectivity controls fluid flow, whereas for a more permeable matrix, absolute apertures define flow (Bisdom *et al.*, 2016).

3.6.2. 2-D flow models as proxy for 3-D fractured reservoirs

The studied models are limited to fracture lengths in 2-D, representing a horizontal section through a bed-perpendicular fracture network, capturing the horizontal equivalent permeabilities, without considering vertical permeability. In 3-D

bed-perpendicular fracture systems, the stress-induced variations in aperture predicted by Barton-Bandis may become relatively insignificant compared to mesoscopic rotation of fractured rock segments resulting from slip along bedding planes (e.g. Lei *et al.*, 2015). Slip along bedding planes may also result in increased opening of fractures that is not described by the Barton-Bandis model. This process is observed through microseismic for hydraulic fractures, but may also affect natural fractures (Gu *et al.*, 2008).

In natural fracture networks, where fractures commonly have scattered orientations resulting in highly-connected networks, the consideration of 3-D connectivity significantly increases permeability magnitude and anisotropy (de Dreuzy *et al.*, 2012). At the fracture scale, these 3-D models show that heterogeneous aperture along single fractures results in flow bottlenecks that decrease permeability, which is also observed in our 2-D models.

3.6.3. Scalability of the aperture-permeability workflow

Conversion of a digitised fracture network to a fracture mesh for mechanical and flow modelling works for even the most complex 2-D fracture geometries, including high-density models (e.g. with a P_{21} of 2.5 or higher) and large-scale models (e.g. 300×300 m), provided that the network topology is accurately mapped. The equivalent permeability models are also capable of handling large meshes with only limited computation times. The mechanical stress-aperture models in ABAQUS, however, may form a bottleneck in the presented workflow when fracture networks become too complex, especially when there are many complex fracture intersections, such as intersecting sub-parallel fractures. In those cases, even in a fine mesh, there are convergence issues when modelling the stress distribution.

To be able to define stress-induced aperture in the more complex fracture networks, we derive empirical functions that relate far-field stresses to local stress acting on fracture surfaces and to fracture aperture, as defined by the Barton-Bandis model (Appendix B). These functions are derived from a range of FE models of synthetic fracture networks with a range of complexities, in which the relation between fracture geometrical parameters, such as orientation, spacing and size, are related to aperture of the Barton-Bandis model.

3.7. Conclusions

We have presented a workflow that applies the Barton-Bandis method to model stress-sensitive mechanical and hydraulic aperture in fracture networks that are not critically stressed, resulting in sub-millimetre heterogeneous aperture distributions even along single fractures. This method predicts that fractures can have small apertures (i.e. less than 0.3 mm) related to roughness even if fractures are not critically stressed according to Mohr-Coulomb. The impact of Barton-Bandis aperture on flow is quantified in terms of equivalent permeability, modelling the fractures with heterogeneous apertures explicitly in a permeable matrix.

We show that this workflow can be used to study equivalent permeability in

real fracture networks, using deterministic fracture patterns from outcrops to obtain realistic geometries. The studied networks have relatively simple geometries compared to what is commonly observed in outcrops, but this enables us to study the impact of each individual geometrical attribute on the aperture distribution along single fractures. However, the presented workflow can be applied to larger multi-scale discrete fracture networks (Appendix B). Our main findings are:

i) The Barton-Bandis model predicts that in the absence of high fluid pressures within the fracture, the hydraulic aperture of fractures with minor amounts of shear under compression is highly heterogeneous, even along a single fracture. This results in a disconnected fracture network where a small fraction of the network controls equivalent permeability. In our models, the angle between σ_1 and the fracture strike has the largest impact on hydraulic aperture and equivalent permeability. Fractures that strike slightly oblique to σ_1 experience a combination of dilation and a small amount of shear displacement, creating poorly interlocking fractures with a relatively large hydraulic aperture.
ii) In the studied models, fracture block size and spacing have a relatively small impact on equivalent permeability. From the four sub-models studied, the model with the lowest fracture density and lowest connectivity showed the highest equivalent permeability as most fractures were oriented ideally with respect to σ_1.
iii) Upscaling of the heterogeneous aperture distribution to a single averaged aperture may provide the same equivalent permeability as the heterogeneous model when there is no large contrast between flow in different directions. Averaging and upscaling equivalent permeability of small-scale fracture models can provide an accurate description of permeability when flow is relatively homogeneous, i.e. most fractures contribute to flow. Otherwise, the small-scale models may underestimate equivalent permeability.

The stress-based aperture and permeability modelling workflow, with heterogeneous apertures along single fractures, provides more representative heterogeneous aperture distributions for fractures that are not critically stressed. The resulting equivalent permeability can be assigned to grid cells in reservoir-scale fracture flow models. By applying this methodology to realistic multiscale fracture systems digitised from outcrops, combined with in-situ stress models, the flow behaviour of naturally fractured reservoirs can be better understood.

References

M. D. Zoback, *Reservoir Geomechanics* (Cambridge University Press, Cambridge, 2007) p. 449.

A. Baghbanan and L. Jing, *Stress effects on permeability in a fractured rock mass with correlated fracture length and aperture*, International Journal of Rock Mechanics and Mining Sciences **45**, 1320 (2008).

Q. Tao, C. A. Ehlig-Economides, and A. Ghassemi, *Investigation of Stress-Dependent Permeability in Naturally Fractured Reservoirs Using a Fully Coupled Poroelastic Displacement Discontinuity Model*, in *SPE Annual Technical Conference and Exhibition* (Society of Petroleum Engineers, New Orleans, Louisiana, 2009).

Q. Lei, J.-p. Latham, J. Xiang, and C.-F. Tsang, *Polyaxial stress-induced variable aperture model for persistent 3D fracture networks*, Geomechanics for Energy and the Environment **1**, 34 (2015).

J. N. Hooker, S. E. Laubach, and R. Marrett, *A universal power-law scaling exponent for fracture apertures in sandstones*, Geological Society of America Bulletin **126**, 1340 (2014).

C. A. Barton, M. D. Zoback, and D. Moos, *Fluid flow along potentially active faults in crystalline rock*, Geology **23**, 683 (1995).

S. F. Rogers, *Critical stress-related permeability in fractured rocks*, Geological Society, London, Special Publications **209**, 7 (2003).

S. Crampin, *Geological and industrial implications of extensive-dilatancy anisotropy*, Nature **328**, 491 (1987).

L. W. Teufel, D. W. Rhett, and H. E. Farrell, *Effect of Reservoir Depletion And Pore Pressure Drawdown On In Situ Stress And Deformation In the Ekofisk Field, North Sea*, in *The 32nd U.S. Symposium on Rock Mechanics (USRMS)* (1991).

S. E. Laubach, *Practical approaches to identifying sealed and open fractures*, AAPG Bulletin **87**, 561 (2003).

S. E. Laubach, J. E. Olson, and J. F. Gale, *Are open fractures necessarily aligned with maximum horizontal stress?* Earth and Planetary Science Letters **222**, 191 (2004).

S. P. Becker, P. Eichhubl, S. E. Laubach, R. M. Reed, R. H. Lander, and R. J. Bodnar, *A 48 m.y. history of fracture opening, temperature, and fluid pressure: Cretaceous Travis Peak Formation, East Texas basin*, Geological Society of America Bulletin **122**, 1081 (2010).

S. E. Laubach, A. Fall, L. K. Copley, R. A. Marrett, and S. J. Wilkins, *Fracture porosity creation and persistence in a basement-involved Laramide fold, Upper Cretaceous Frontier Formation, Green River Basin, USA*, Geological Magazine , 1 (2016).

H. Yasuhara, *Evolution of permeability in a natural fracture: Significant role of pressure solution*, Journal of Geophysical Research **109**, B03204 (2004).

K. Nemoto, N. Watanabe, N. Hirano, and N. Tsuchiya, *Direct measurement of contact area and stress dependence of anisotropic flow through rock fracture with heterogeneous aperture distribution*, Earth and Planetary Science Letters **281**, 81 (2009).

Z. G. Philip, J. W. Jennings, J. E. Olson, S. E. Laubach, and J. Holder, *Modeling Coupled Fracture-Matrix Fluid Flow in Geomechanically Simulated Fracture Networks*, SPE Reservoir Evaluation & Engineering **8**, 300 (2005).

J. E. Olson, S. E. Laubach, and R. H. Lander, *Natural fracture characterization in tight gas sandstones: Integrating mechanics and diagenesis*, AAPG Bulletin **93**, 1535 (2009).

H. M. Nick, A. Paluszny, M. J. Blunt, and S. K. Matthai, *Role of geomechanically grown fractures on dispersive transport in heterogeneous geological formations*, Physical Review E **84**, 056301 (2011).

J.-R. de Dreuzy, Y. Méheust, and G. Pichot, *Influence of fracture scale heterogeneity on the flow properties of three-dimensional discrete fracture networks (DFN)*, Journal of Geophysical Research **117**, B11207 (2012).

Q. Lei, J.-P. Latham, J. Xiang, C.-F. Tsang, P. Lang, and L. Guo, *Effects of geomechanical changes on the validity of a discrete fracture network representation of a realistic two-dimensional fractured rock*, International Journal of Rock Mechanics and Mining Sciences **70**, 507 (2014).

N. Barton, *Modelling rock joint behaviour from in situ block tests: Implications for nuclear waste repository design*, Tech. Rep. (Office of Nuclear Waste Isolation, Columbus, OH, 1982).

S. Bandis, A. Lumsden, and N. Barton, *Fundamentals of rock joint deformation*, International Journal of Rock Mechanics and Mining Sciences & Geomechanics Abstracts **20**, 249 (1983).

R. Olsson and N. Barton, *An improved model for hydromechanical coupling during shearing of rock joints*, International Journal of Rock Mechanics and Mining Sciences **38**, 317 (2001).

K. Matsuki, E. Wang, A. Giwelli, and K. Sakaguchi, *Estimation of closure of a fracture under normal stress based on aperture data*, International Journal of Rock Mechanics and Mining Sciences **45**, 194 (2008).

N. Barton and V. Choubey, *The shear strength of rock joints in theory and practice*, Rock Mechanics Felsmechanik Mecanique des Roches **10**, 1 (1977).

N. Barton and S. Bandis, *Some effects of scale on the shear strength of joints*, in *International Journal of Rock Mechanics and Mining Sciences & Geomechanics Abstracts*, Vol. 17 (Pergamon Press Ltd., 1980) pp. 69–73.

N. Barton, S. Bandis, and K. Bakhtar, *Strength, deformation and conductivity coupling of rock joints*, International Journal of Rock Mechanics and Mining Sciences & Geomechanics Abstracts **22**, 121 (1985).

S. K. Matthäi and M. Belayneh, *Fluid flow partitioning between fractures and a permeable rock matrix*, Geophysical Research Letters **31** (2004), 10.1029/2003GL019027.

S. K. Matthäi, S. Geiger, S. G. Roberts, A. Paluszny, M. Belayneh, A. Burri, A. Mezentsev, H. Lu, D. Coumou, T. Driesner, and C. A. Heinrich, *Numerical simulation of multi-phase fluid flow in structurally complex reservoirs*, Geological Society, London, Special Publications **292**, 405 (2007).

A. Paluszny, S. K. Matthäi, and M. Hohmeyer, *Hybrid finite element-finite volume discretization of complex geologic structures and a new simulation workflow demonstrated on fractured rocks*, Geofluids **7**, 186 (2007).

N. Barton, *Non-linear behaviour for naturally fractured carbonates and frac-stimulated gas-shales*, First Break **32**, 51 (2014).

J. N. Hooker, L. A. Gomez, S. E. Laubach, J. F. W. Gale, and R. Marrett, *Effects of diagenesis (cement precipitation) during fracture opening on fracture aperture-size scaling in carbonate rocks*, Geological Society, London, Special Publications **370**, 187 (2012).

P. Asadollahi, M. C. a. Invernizzi, S. Addotto, and F. Tonon, *Experimental Validation of Modified Barton's Model for Rock Fractures*, Rock Mechanics and Rock Engineering **43**, 597 (2010).

N. J. Hardebol, C. Maier, H. Nick, S. Geiger, G. Bertotti, and H. Boro, *Multiscale fracture network characterization and impact on flow: A case study on the Latemar carbonate platform*, Journal of Geophysical Research: Solid Earth **120**, 8197 (2015).

D. J. Sanderson and C. W. Nixon, *The use of topology in fracture network characterization*, Journal of Structural Geology **72**, 55 (2015).

Dassault Systemes, *ABAQUS v6.13 documentation*, (2013).

S. K. Matthäi, H. M. Nick, C. Pain, and I. Neuweiler, *Simulation of Solute Transport Through Fractured Rock: A Higher-Order Accurate Finite-Element Finite-Volume Method Permitting Large Time Steps*, Transport in Porous Media **83**, 289 (2009).

A. Paluszny and S. K. Matthäi, *Impact of fracture development on the effective permeability of porous rocks as determined by 2-D discrete fracture growth modeling*, Journal of Geophysical Research **115**, B02203 (2010).

H. M. Nick and S. K. Matthäi, *Comparison of Three FE-FV Numerical Schemes for Single- and Two-Phase Flow Simulation of Fractured Porous Media*, Transport in Porous Media **90**, 421 (2011).

D. T. Snow, *Anisotropic Permeability of Fractured Media*, Water Resources Research **5**, 1273 (1969).

R. Juanes, J. Samper, and J. Molinero, *A general and efficient formulation of fractures and boundary conditions in the finite element method*, International Journal for Numerical Methods in Engineering **54**, 1751 (2002).

S. K. Matthäi and H. M. Nick, *Upscaling two-phase flow in naturally fractured reservoirs*, AAPG Bulletin **93**, 1621 (2009).

W. S. Dershowitz and H. H. Einstein, *Characterizing rock joint geometry with joint system models*, Rock Mechanics and Rock Engineering **51**, 21 (1988).

S. Geiger and S. Matthäi, *What can we learn from high-resolution numerical simulations of single- and multi-phase fluid flow in fractured outcrop analogues?* Geological Society, London, Special Publications **374**, 125 (2012).

S. Jonoud and M. D. Jackson, *Validity of Steady-State Upscaling Techniques*, SPE Reservoir Evaluation & Engineering **11**, 405 (2008).

N. Cottereau, M. H. Garcia, O. R. Gosselin, and L. Vigier, *Effective Fracture Network Permeability: Comparative Study of Calculation Methods*, in *SPE EUROPEC/EAGE Annual Conference and Exhibition* (Society of Petroleum Engineers, Barcelona, Spain, 2010).

J. C. S. Long and P. A. Witherspoon, *The relationship of the degree of interconnection to permeability in fracture networks*, Journal of Geophysical Research **90**, 3087 (1985).

B. Berkowitz and I. Balberg, *Percolation theory and its application to groundwater hydrology*, Water Resour. Res. **29**, 775 (1993).

K. Bisdom, G. Bertotti, and H. M. Nick, *The impact of different aperture distribution models and critical stress criteria on equivalent permeability in fractured rocks*, Journal of Geophysical Research: Solid Earth **121**, 4045 (2016).

H. Gu, E. Siebrits, and A. Sabourov, *Hydraulic Fracture Modeling With Bedding Plane Interfacial Slip*, in *SPE Eastern Regional/AAPG Eastern Section Joint Meeting* (Society of Petroleum Engineers, 2008).

4

Geometry and reservoir permeability of burial-related fracture systems

Fractures and stylolites in the carbonate Jandaíra Fm. in the Potiguar basin (north-east Brazil) are formed during early burial at shallow depth, creating high-density fracture networks even though there is relatively little seismic-scale deformation, aside from limited faulting. We quantify the geometrical and spatial distribution of the burial-related fractures in the Jandaíra Fm. through mapping of barren fractures from aerial imagery combined with the analysis of veins at the outcrop surface, which results in a multiscale database of more than 13 000 digitised fractures and veins in ten pavements throughout the basin. Most fractures are linked to regional N-S to NNE-SSW shortening during burial. Fracture length and spacing follows power-law relations. In addition to the regional trends, we observe a scatter in the spatial distribution in between pavements, resulting in heterogeneous connectivity even though the fracture network is formed by a single regional tectonic phase. This results in significant variations in permeability at the inter-well scale (i.e. less than 1 km*) that are not captured by any seismic-scale geological or geomechanical drivers. We quantify these permeability variations using discrete fracture-matrix flow models derived from deterministic networks digitised in outcrops, taking into account uncertainties associated with aperture and matrix permeability. Uncertainties associated with aperture can lead to orders of magnitude differences in equivalent permeability. We find that percolation parameters are only representative of modelled permeability when matrix permeability is low, and when the impact of hydraulic conductivity variations are taken into account through discrete fracture-matrix flow models. Fracture porosity is not representative of permeability, as network connectivity strongly controls permeability.*

This chapter is based on: K. Bisdom, G. Bertotti, F.H. Bezerra. Inter-well scale natural fracture geometry and permeability variations in low-deformation carbonate rocks. **Submitted**.

4.1. Introduction

4.1.1. Rationale

In Naturally Fractured Reservoir (NFR) modelling, trends in attributes such as spacing, length and orientation are related to large-scale strain events such as folding and faulting (Price, 1966; Bergbauer and Pollard, 2004; Hudleston and Treagus, 2010; Anders *et al.*, 2014). A wide range of studies have used outcrop analogues to quantify the multiscale relation between seismic-scale deformation and subseismic fracture attributes, as this allows for predicting of fracture attribute trends in domains where no direct measurements are available, i.e. in between wells in subsurface fractured reservoirs (e.g. Fischer and Jackson, 1999; Bellahsen *et al.*, 2006; Stephenson *et al.*, 2007; Tavani *et al.*, 2011). However, an increasing number of studies now recognise that burial and Layer-Parallel Shortening (LPS) can also create regional fracture systems (Lacombe *et al.*, 2011; Tavani *et al.*, 2011; Branellec *et al.*, 2015). The multiscale relation between these tectonic forces and fracture attributes and the implications for flow in naturally fractured reservoirs are less well constrained compared to folding- or faulting-related fracturing.

Fractures in the Jandaíra Fm. (Potiguar basin, NE Brazil) have been characterised as regional fractures, formed during shallow burial (Bertotti *et al.*, subm; de Graaf *et al.*, subm). The studied outcrops in this basin have undergone relatively limited faulting and no folding, but fractures are nonetheless abundant and likely impact fluid flow in subsurface NFR analogues. We extend the qualitative analysis by de Graaf *et al.* (subm) and Bertotti *et al.* (subm) with a quantitative analysis of fracture geometry, to characterise orientation, length, spacing and connectivity of the regional fracture network. This analysis is based on a database of 13 000 digitised fractures in ten pavements, with individual pavement sizes of up to 250 × 800 m, supplemented by smaller observations at the outcrop scale. We study barren fractures, i.e. outcropping fractures whose cements have fully dissolved, veins and stylolites. Here, barren refers to the outcrop conditions, as these features may have been veins prior to exhumation.

The aim of this analysis is to assess the impact of regional fractures on horizontal permeability and well productivity in NFRs. By combining the large database of realistic regional fracture patterns with discrete fracture and matrix flow modelling, we investigate the impact of a range of uncertainties associated with fracture flow modelling that cannot be investigated in subsurface reservoirs, because of a limited understanding of network geometry and the limited detail that can be incorporated into conventional dual-permeability models (e.g. Muhammad, 2016). In these models, fracture flow is modelled explicitly, using heterogeneous apertures derived from geomechanical stress-aperture relations (Chapter 3). Using this approach, we investigate the implications for permeability modelling related to the following uncertainties:

i) We characterise the natural variability of fracture patterns that can be expected at the inter-well scale by comparing variations in geometry and permeability in between adjacent pavements;
ii) We separate burial- and exhumation-related deformation to characterise how

permeability changes during exhumation.

iii) As the barren fractures have been reactivated during exhumation, the outcropping apertures are not representative of reservoir conditions. Instead, we compare three methods for defining aperture and analyse their implications for reservoir permeability.

iv) Percolation and fracture connectivity studies typically assume that the matrix is impermeable, such that disconnected fractures are not considered to contribute to flow during upscaling. We consider a range of matrix permeabilities to investigate the interplay between fractures and matrix.

4.1.2. Aperture definitions

The studied sensitivities are mainly related to uncertainties associated with aperture, as outcropping apertures are typically not representative of subsurface conditions. Subsurface veins can become barren fractures during exhumation and unloading during exhumation typically enhances apertures (e.g. Gale *et al.*, 2014). Subsurface apertures can be measured using borehole image logs (BHI), but absolute apertures are typically overestimated as the stresses near the wellbore are affected by the drilling process and drilling fluids (e.g. Makel, 2007). Rather than measuring apertures, we use the digitised fracture patterns in the Jandaíra Fm. to study the differences in permeability associated with different aperture models, using the three most commonly used definitions:

i) Barton-Bandis shear-induced aperture for irregular fracture walls that have experienced normal and shear displacement (Barton and Bandis, 1980; Barton, 1982);

ii) (Sub)linear length-aperture scaling predicted by Linear Elastic Fracture Mechanics (LEFM) (Lawn and Wilshaw, 1975; Pollard and Segall, 1987; Olson, 2003);

iii) Power-law frequency scaling trends derived from scanline aperture measurements (Hooker *et al.*, 2012, 2014).

The Barton-Bandis method is an empirical approach derived from mechanical experiments on natural fractures (Barton and Bandis, 1980; Barton, 1982). This method defines an aperture that results from shear displacement on irregular fracture surfaces, such that fracture walls are not perfectly interlocking and a hydraulic aperture remains, even if fluid pressures within the fracture are lower than the stresses acting on the fracture (Lei *et al.*, 2014). Aperture is mainly controlled by the intrinsic roughness and strength of the fracture walls and the local normal and shear stress, whereas spacing and length have smaller impacts (Bisdom *et al.*, 2016a).

(Sub)linear length-aperture scaling assumes that after initiation of a fracture, it grows incrementally when fluid pressure within the fracture increases and eventually exceeds the rock stresses (Atkinson, 1984; Vermilye and Scholz, 1995; Olson, 2003; Anders *et al.*, 2014). This results in propagation along the crack terminations, which subsequently increases the maximum aperture along the entire fracture through length-displacement scaling (Olson, 2003). Depending on how parts

of the method are interpreted, this relation between length and aperture is either linear (Scholz, 2010, 2011) or sublinear (Olson, 2003; Olson and Schultz, 2011).

Whereas Barton-Bandis and (sub)linear fracture scaling are functions of local stresses, power-law scaling is not related to stress. Vein apertures measured in outcrops and cores using scanlines are observed to follow power-law frequency scaling, where smaller apertures are more common than larger apertures (Hooker *et al.*, 2012, 2013, 2014).

As most preserved veins in the Jandaíra Fm. show a combination of shear and normal opening (Bertotti *et al.*, subm), we use the Barton-Bandis method as the main method to define aperture, but compare the aperture and permeability distributions from this method to the other two methods.

4.2. Geological setting

The Potiguar basin is a rift basin in NE Brazil, formed during the crustal breakup of Gondwana in the Early Cretaceous (H. A. O. Ojeda, 1982; de Matos, 1992). The onshore part of the basin has a width of 350 km, measured along the coast, and consists of two NE-SW trending grabens that extend 200 km land inwards, with an individual width of 100 km (Figure 4.1; Reis *et al.*, 2013).

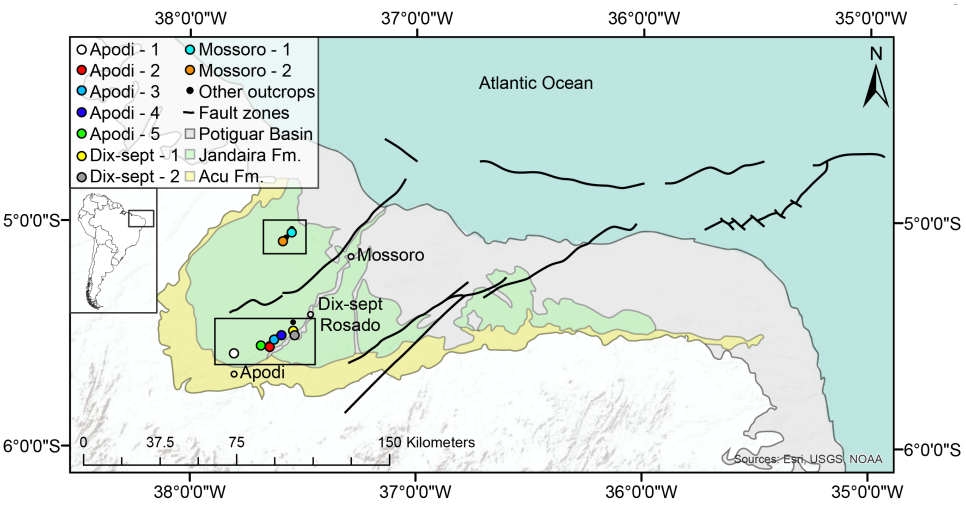


Figure 4.1: The Potiguar basin, containing NE-SW faults part of the graben system.

4.2.1. Tectonics

The basin is part of the Equatorial Atlantic, a shear margin that connects the south and central Atlantic (de Matos, 1992). It is one of three NE-SW trending intra continental basins in NE Brazil, which are bounded by transfer faults (de Brito Neves *et al.*, 1984). Rifting started and continued into the Albian and was followed by a phase of post-rift deposition.

The basin experienced NNE-SSW oriented reactivation from the Middle Campanian to Miocene, followed by a NW-SE reactivation phase from the Miocene to present-day (Assumpção, 1992; Reis *et al.*, 2013). During this compressional stage the carbonates were exhumed and partly eroded. Aside from limited faulting, there is little seismic-scale deformation, and layers in the basin dip sub-horizontal (3°).

4.2.2. Stratigraphy

Post-rift deposition started with the Albian Açu Fm., which consists of fluvial-estuarine sandstones and mudstones (Figure 4.2; H. A. O. Ojeda, 1982). This non-marine phase was followed by transgression and deposition of the Jandaíra carbonate platform from the Turonian to Campanian (de Matos, 1992). Depositional thickness is up to 700 m. There is a subtle mechanical stratigraphy, but the lithology is constant in the different beds, indicating that the mechanical units were potentially formed more recently, for example along burial-related horizontal stylolites when these rocks were exhumed.

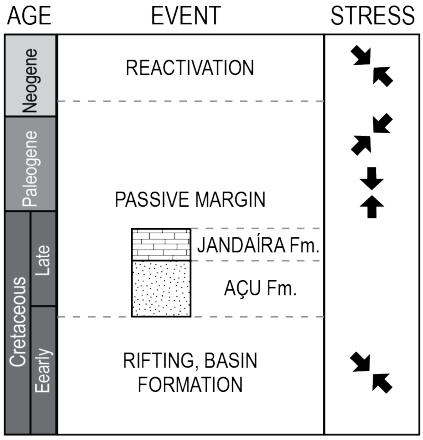


Figure 4.2: Simplified chart of the main tectonic events and the associated stress fields since the Early Cretaceous, compiled from Assumpção (1992); de Matos (1992); Reis *et al.* (2013); Bertotti *et al.* (subm).

4.2.3. Fracturing synthesis

Sets of barren fractures, veins and stylolites and their fracturing mechanisms have been characterised through an integrated study of structural deformation patterns and vein cement isotope and fluid inclusion analysis (Bertotti *et al.*, subm; de Graaf *et al.*, subm). The structural analysis focused on fracturing types, orientation and abutment relations. The cement analysis focused on the type of cements and their growth patterns, as well as the analysis of isotopes of fluid inclusions within the cement to identify pressure and temperature conditions at the time of cementation and the type of fluids that circulated through the system.

The fracturing synthesis is based on Bertotti *et al.* (subm); de Graaf *et al.* (subm).

The integrated study has found that the majority of present-day barren fractures were veins at depth, whose cements were dissolved during exhumation. These features are bed-perpendicular joints and conjugate sets, with a predominantly N-S orientation (Figure 4.3a), and are interpreted to have formed during burial, related to N-S to NNE-SSW horizontal compression during Middle Campanian and Miocene times, in an overall strike-slip tectonic regime (Assumpção, 1992; Reis *et al.*, 2013).

In addition to the N-S oriented features, a high-intensity system of E-W striking bed-perpendicular features is observed, which are interpreted as reactivated stylolites formed under the same stress field (Figure 4.3b). Stress release during reactivation resulted in preferential reactivation of these stylolites as barren fractures. As as result, we observe orthogonal patterns of barren fractures in the outcrops, which were initially veins and stylolites formed in one N-S to NNE-SSW stress field (Figure 4.3c).

The bed-perpendicular and bedding-parallel stylolites and bed-perpendicular veins are formed during burial. Horizontal stylolites are observed to cross-cut the vertical features, indicating that compression-related fracturing occurred during early burial, when σ_2 was vertical (Figure 4.3d). This is also supported by the high intensity of bed-perpendicular conjugate pairs and the isotope analysis (Figure 4.3a). Based on estimates of regional paleostress magnitudes and mechanical rock properties, fracturing occurred at a depth between 450–850m (Figure 4.4). Burial then continued, during which burial-related horizontal stylolites were formed under a vertical σ_1. The burial-related joints and conjugates were fully cemented shortly after fracturing, removing all porosity and permeability. Cements were mostly dissolved during exhumation, although many of the smaller veins (i.e. shorter than 1 m) were preserved (Figure 4.3e,f).

4.3. Quantitative fracture analysis

We extend the analysis from de Graaf *et al.* (subm) and Bertotti *et al.* (subm) with a quantitative analysis of geometry and connectivity using a database of 13 000 digitised barren fractures and close to 500 preserved veins, with the aim of providing an accurate characterisation of fracture geometry as a basis for permeability modelling. We analyse barren fractures separate from preserved veins, and further separate the barren fractures into two sets:

i) N-S to NNE-SSW striking bed-perpendicular conjugates and joints formed during burial (*set 1*);
ii) E-W striking bed-perpendicular joints formed along burial-related stylolites during exhumation (*set 2*).

4.3.1. Data acquisition and database

Data acquisition and interpretation was done through a multiscale approach combining large-scale mapping of the barren network using an Unmanned

The quantitative analysis is based on data from M.Sc. theses by van Eijk (2014); van der Voet (2015) and B.Sc. theses by Wever (2015); Paulides (2013).

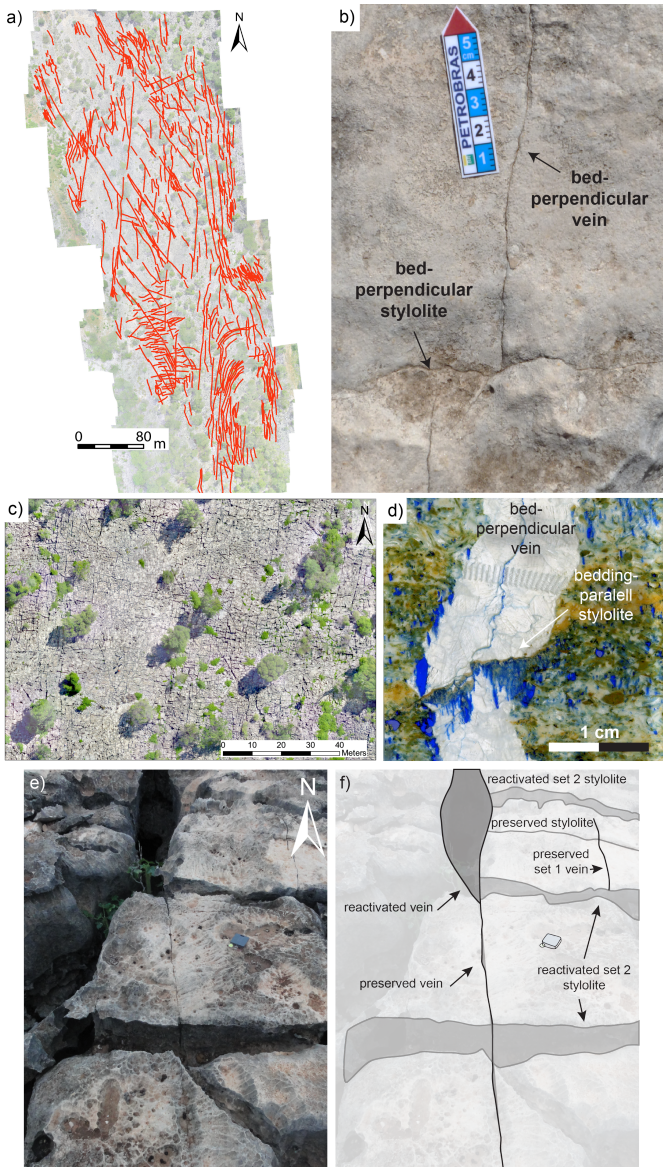


Figure 4.3: Examples of structural indicators of the relation between veins and stylolites and their relation to the regional stress field: a) Barren fractures digitised in a pavement, showing conjugates with a N-S to NNW-SSE bisector as well as N-S striking fractures interpreted as joints; b) Bed-perpendicular N-S striking veins displaced by an E-W striking bed-perpendicular stylolite; c) Aerial view of a section of pavement with N-S and E-W striking barren fractures. The N-S features are interpreted as reactivated veins, whereas the E-W striking features are reactivated bed-perpendicular stylolites; d) Bed-perpendicular vein pre-dating a bedding-parallel stylolite, adapted from de Graaf *et al.* (subm); e) Detail of a pavement showing bed-perpendicular veins and stylolites that have been partly reactivated; f) Interpretation of (e).

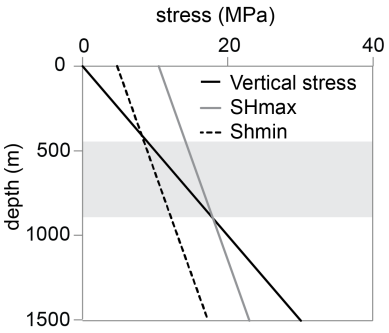


Figure 4.4: Simplified burial plot showing the changes in vertical and horizontal stresses with increasing depth, based on a maximum horizontal stress of 10 MPa, that increases with depth as a function of Poisson's stress, constant rock density of 2300 kg m^{-3} and a Poisson's ratio of 0.3. The highlighted interval indicates the depth where σ_2 is the maximum horizontal stress and bed-perpendicular conjugate fractures can form. Adapted from Bertotti *et al.* (subm).

Aerial Vehicle (UAV; Chapter 2) with measuring and sampling veins and stylolites at the outcrop and in cross-sections (Figure 4.5). From images obtained with the UAV we digitised fractures with lengths between 1–300m. Observations at the outcrops captured scales between 0.1–10m, and thin sections provided sub-millimetre observations. The UAV images were used to capture the barren fractures, whereas the outcrop and thin section observations focused on veins and stylolites.

Using UAV image acquisition and DigiFract for fracture interpretation (Chapter 2), barren fractures in nine pavements covering an area of 88 hectares were digitised. These pavements are located in two parts of the basin, towards the centre (*Apodi* and *Dix-sept* outcrops) and further towards the western edge (*Mossoró* outcrops; Figure 4.1). Most images were taken at an altitude of 50 m, resulting in a resolution of 1.4 cm/px. The pavements contain at least several hundred fractures covering several length and spacing scales, which makes these pavements suitable for quantitative analysis of geometrical and spatial distributions (Figure 4.1; Bonnet *et al.*, 2001).

Preserved veins and stylolites were studied in 33 locations within the pavements by imaging and digitising small sections at a 0.5 mm/px resolution and by drilling plug-size (37 mm diameter) samples of veins and stylolites which were used for thin-section analysis (de Graaf *et al.*, subm). Quantitative analysis was performed on 446 veins digitised in a 30 × 20 m preserved section of a pavement containing exclusively veins and stylolites. Aperture was not measured, as the aperture of exhumed barren fractures is not representative of in-situ aperture.

4.3.2. Barren fractures

The geometrical and spatial distribution of the barren fractures is analysed per pavement, and for all nine pavements combined, separating *set 1* from *set 2* features. For the barren fractures, we focus on the present-day outcropping geometry, irrespective of whether features were veins or stylolites prior to exhumation. We

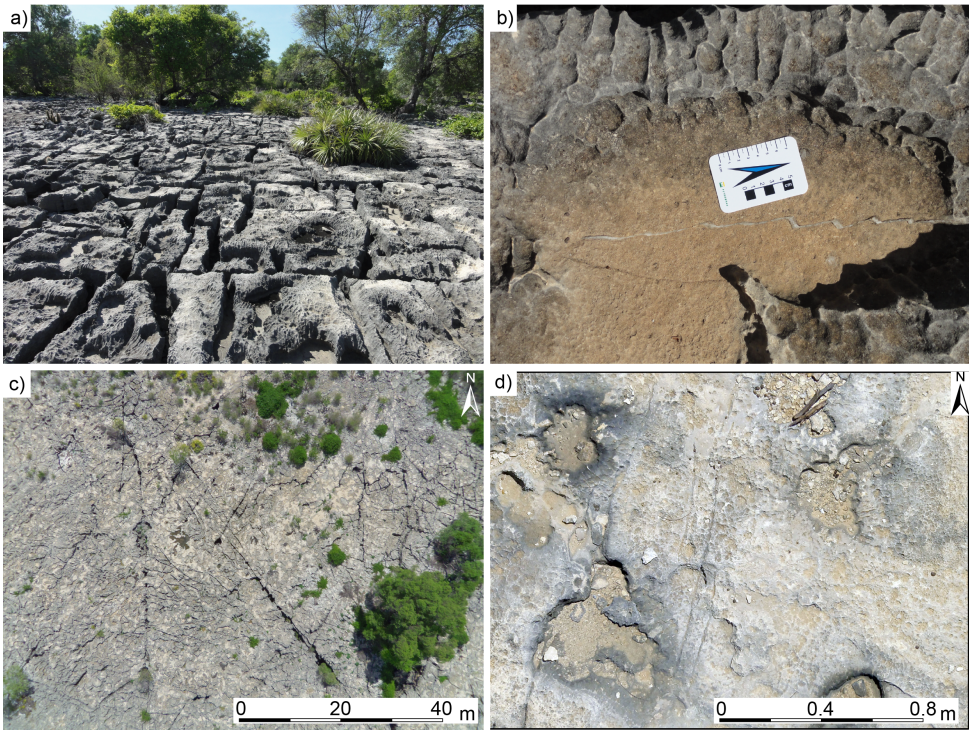


Figure 4.5: Examples of the fracture types and scales that are studied quantitatively: a) View from the outcrop surface of the barren fracture network with large apertures enhanced by reactivation and recent weathering; b) Bed-perpendicular hybrid vein preserved during exhumation; c) Aerial view (100 m altitude) of the barren network; d) Detail view (2 m altitude) of a preserved section with NNE-SSW bed-perpendicular veins.

refer to all digitised features in this section as 'fractures'. The pavement images and digitised networks for all nine pavements are shown in Appendix C.

Orientation

The strike of digitised barren fractures is plotted for each individual pavement and all pavements combined in length-weighted rose diagrams (Figure 4.6). There are two distinct N-S and E-W striking trends in the outcrops, as well as more scattered orientations (Figure 4.6a). Five out of nine pavements contain predominantly fractures with the N-S and E-W orientations (*Apodi3-5*, *Dix-sept 1* and *Mossoró 2*), but the distribution is more scattered in the other pavements. Spatially, there is no trend in orientation between the different pavements, and in some cases we find pavements with clear orientation trends close to pavements with scattered orientations (e.g. *Dix-sept 1* and *2*).

Length

Fracture length, expressed by the average, standard deviation and minimum and maximum digitised lengths, varies strongly throughout the pavements (Figure 4.7).

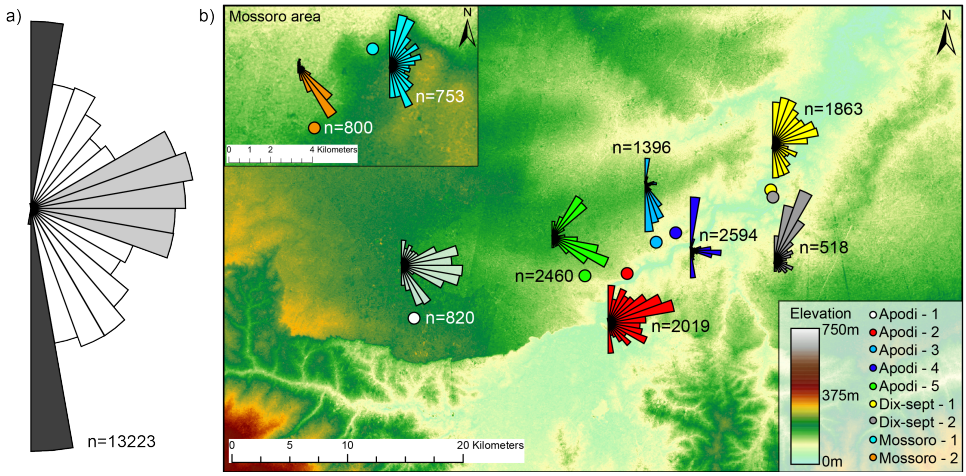


Figure 4.6: Length-weighted orientation distribution of barren fractures: a) Rose diagram of all 13 223 barren fractures digitised in ten outcrops, highlighting the two main N-S and E-W striking orientation trends; b) False-colour map of a detail of the basin, showing the *Apodi* and *Dix-sept* outcrops, with the *Mossoró* outcrops in the top left inset. For each pavement, the fracture orientations digitised are shown in the rose diagrams, in addition to the number of digitised fractures.

In most pavements the maximum length is smaller than the outcrop dimensions, indicating that censoring has only a small impact on the dataset (Appendix C).

Average length varies from 3.5 m (*Mossoró 2*) to 17.4 m (*Apodi 1*; Figure 4.7). Fractures are smaller in the *Mossoró* outcrops, which is not related to outcrop size, as these outcrops have similar dimensions as other pavements with larger fractures (e.g. *Dix-sept 1-2*). This trend in length is possibly related to the position in the basin, as the *Mossoró* outcrops are closer to the edge of the basin. For the other seven pavements, which are several hundred meters to several kilometres apart, there are no clear spatial trends, even though variations in length are large.

Length is further analysed using frequency and cumulative frequency distributions (Figure 4.7b-e). Where we have sufficient data, we use the density frequency distribution as it is more accurate compared to the cumulative frequency distribution (Bonnet *et al.*, 2001). The length distribution is analysed per pavement (Figure 4.7b,c) and for all pavements combined (Figure 4.7d), as well as for the two main orientation sets (Figure 4.7e). In most pavements, barren fractures are mutually crosscutting, and in the absence of any mechanical or lithological control, our hypothesis is that fracture length follows power-law scaling functions (Bonnet *et al.*, 2001). This hypothesis is tested by plotting the frequency length distributions on log-log plots and analysing their fit to power-law scaling functions.

The cumulative length frequency distribution for individual pavements indicates that a power-law function best fits the data (Figure 4.7b,c). Note that these plots cover all digitised length scales, where the lower and upper bounds suffer from limited censoring and truncation artefacts. The individual exponents are close to 2.0, with the exceptions of *Apodi 3* and *Mossoró 1-2*, which have exponents be-

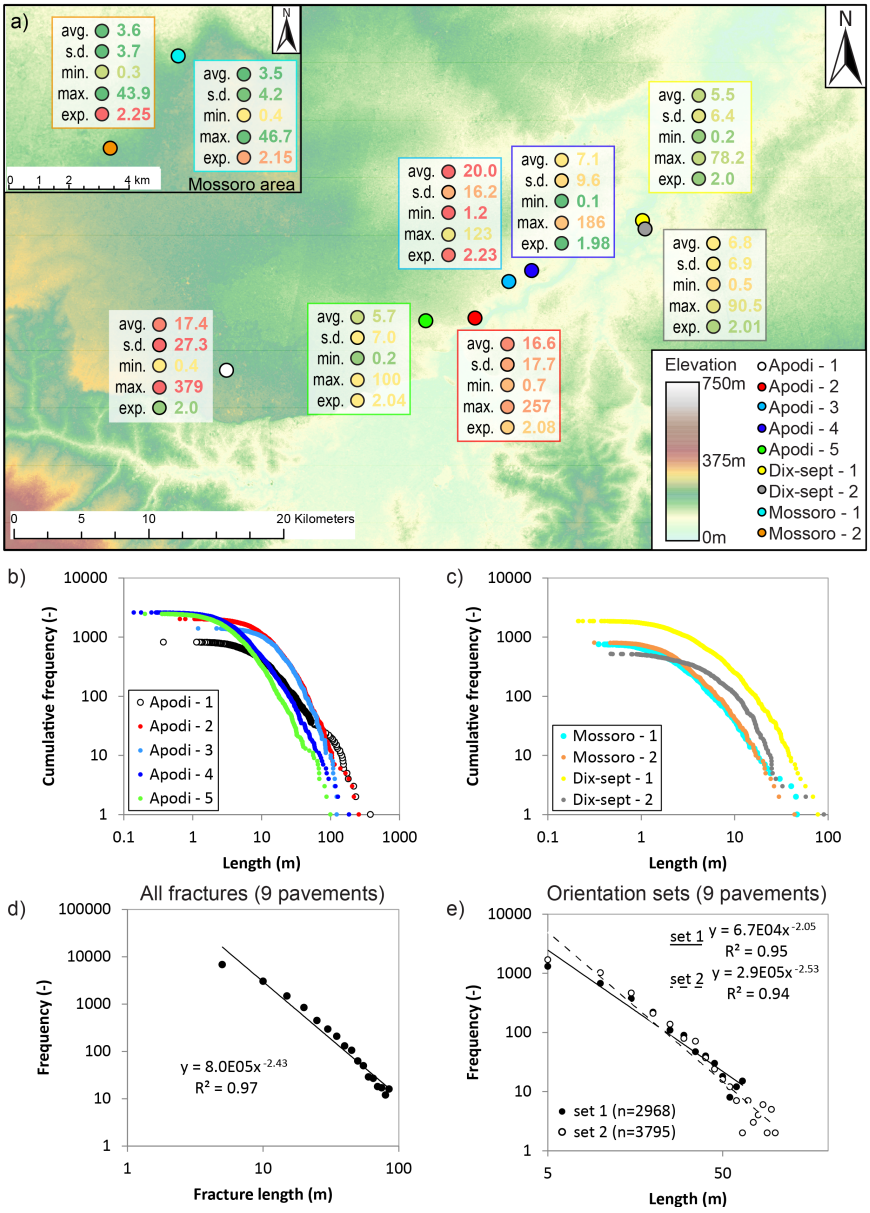


Figure 4.7: Analysis of fracture length: a) Spatial variations in length attributes (average length, standard deviation, minimum and maximum digitised lengths, and the power-law scaling exponent) in the individual pavements, where the bar plots indicate relative trends in between the pavements; b) Cumulative frequency distributions for the *Apodi* pavements; c) Cumulative frequency for the *Mossoró* and *Dix-sept* pavements; d) Combined frequency distribution for fractures from all pavements; e) Frequency distributions for the two main orientation sets (N-S *set 1* and E-W *set 2*), derived from all pavements.

tween 2.15 and 2.25 (Figure 4.7a). An exponent of 2.0 indicates that the length distribution is scale-independent (Odling *et al.*, 1999; Bonnet *et al.*, 2001; Bour, 2002), whereas the higher exponents indicate that the distribution lacks large fractures. In *Apodi 3*, we observe that particularly in the SW corner of the pavement, E-W striking fractures have small lengths as they abut against a N-S striking conjugate system. As a result, the distribution is not fully scale-independent. The higher exponent in the *Mossoró* pavements corresponds to the observed low average fracture lengths in those pavements (Figure 4.7a). The small scatter in the exponent in the other pavements is likely related to the natural variability of fracture systems.

The frequency distribution of all measured fractures in the basin, corrected for censoring and truncation artefacts, follows a power-law scaling distribution with a relatively high exponent of 2.43 (Figure 4.7d). Removal of censored and truncated fractures has limited the length scales and changed the shape of the distribution. Separating the data based on orientation sets shows that the higher exponent is related to E-W striking *set 2* fractures, whereas the distribution of *set 1* is close to scale-independent, with an exponent of 2.05 (Figure 4.7e). As observed in for example *Apodi 3*, the E-W striking fractures often abut against *set 1* fractures, resulting in a skewed length distribution. Average length of *set 1* fractures is also larger compared to *set 2* (10.7 m versus 9.6 m respectively).

Spacing

The spatial distribution is defined by P_{21} intensity (Dershowitz and Einstein, 1988), which is the inverse of fracture spacing defined by the cumulative length of fractures within a given area. Intensity is relatively homogeneous throughout most of the pavements, with an average close to $0.19\,m^{-1}$ (Figure 4.8a). Intensity is lowest in *Apodi 5* and highest in *Dix-sept 1*, which are the main outliers. Intensity of all other pavements is between $0.13–0.21 m^{-1}$, with no spatial trends in between pavements in different parts of the basin.

We use the box-counting method (Bonnet *et al.*, 2001) to define the spatial distribution within individual pavements, where each pavement is discretised by a rectangular grid where each cell dimension is 2–10% of the outcrop dimensions, resulting in 100–4000 cells per outcrop. Areas with low image quality or censoring effects related to trees or other objects are manually mapped and excluded prior to the analysis. The P_{21} intensity is calculated within each cell and the resulting distribution is plotted using frequency and cumulative frequency distributions (La Pointe, 1988; Walsh and Watterson, 1993; Bonnet *et al.*, 2001; Darcel, 2003). In all pavements, the cumulative spacing distribution follows power-law scaling trends, with scaling exponents between 1.69 and 2.23 (Figure 4.8a). The cumulative distributions follow similar trends in all pavements, with relatively small variations in scaling exponents (Figure 4.8b-d). This exponent is representative of the degree of network saturation, where a higher exponent indicates a higher degree of network saturation. For the cumulative spacing distributions we find no correlation between exponents and the maximum and average intensity, although defining an average intensity is not representative for distributions that follow power-law scaling. Alternatively, the exponents may be affected by limited sampling and truncation artefacts.

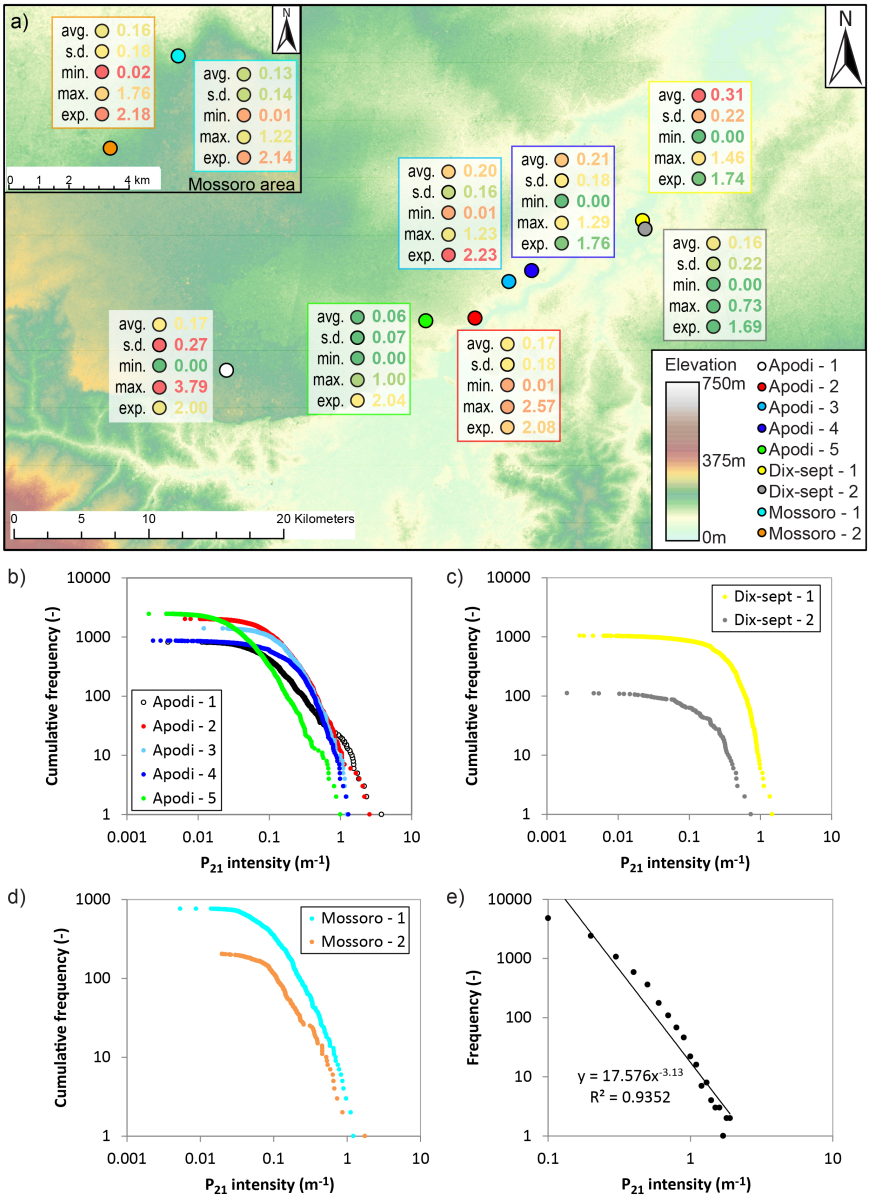


Figure 4.8: Analysis of fracture intensity: a) Spatial variations in P_{21} intensity attributes (average, standard deviation, minimum and maximum, and the power-law scaling exponent), where the bar plots indicate relative trends in between the pavements; b) Cumulative frequency distributions for the *Apodi* pavements; c) Cumulative frequency for the *Dix-sept* pavements; d) Cumulative frequency for the *Dix-sept* pavements; e) Frequency distribution derived from intensity measurements from all pavements.

To further investigate power-law scaling behaviour we plot the intensity distribution for all pavements combined (Figure 4.8e). Intensity follows a power-law trend across two orders of magnitude with a scaling exponent of 3.1, indicating a high degree of fracture network saturation (Darcel, 2003). This is higher than the exponents derived from the cumulative distributions of individual pavements, and the large difference between exponents may be an indication that even for such a large multiscale dataset, an accurate spacing distribution cannot be derived as a result of censoring and truncation artefacts in the individual pavements. Removing fractures that suffer from these artefacts results in a distribution covering less than two orders of magnitude (Figure 4.8).

Connectivity

Compared to P_{10}, which is typically used to define intensity in cores and along scanlines, the P_{21} intensity is more representative of the spatial fracture distribution. However, both definitions do not consider the spatial arrangement of fractures and whether the fractures form a percolating network for flow, or whether they are organised in a disconnected network. Instead, we use the percolation parameter defined by Robinson (1983) to define the connectivity of the network as a proxy for fracture permeability in an impermeable matrix. This parameter is a function of the ratio between the number of intersections and the number of fractures, normalised for the outcrop area, where a higher value indicates a higher degree of percolation (Robinson, 1983, 1984). This parameter does not explicitly take fracture orientation into account, so any connectivity anisotropy is not recognised.

The percolation probability is relatively high in pavements with scattered orientation distributions (e.g. *Apodi 1-2* and *Dix-sept 1*), as a larger scatter in orientation increases the likelihood of fractures intersecting. This likelihood is also increased when fractures are relatively long, such as in *Apodi 1* and *Apodi 2*. Percolation is highest in *Apodi 5*, which also has the highest intensity (Figure 4.9). On the other hand, *Dix-sept 2* and *Mossoró 2* have the lowest percolation parameters but average intensities compared to other pavements (Figures 4.8 and 4.9). We observe that percolation is controlled by a combination of the three main geometrical parameters (i.e. orientation, length and intensity).

4.3.3. Veins

The quantitative vein analysis is based on a single pavement containing 446 veins, as this is the only section of pavement in which there are sufficient veins and no barren fractures (Figure 4.10).

Orientation

The orientation of the veins is NNE-SSW (N020), with a small scatter (15°; Figure 4.10), which is similar to the reactivated *set 1* barren fracture orientation, although the scatter in orientation is smaller for the veins. This difference is likely a sampling artefact, as *set 1* barren fractures are studied in large areas in different outcrops, where we capture the natural variability in the system, whereas the veins are only sampled in one small area. Bertotti *et al.* (subm) measured orienta-

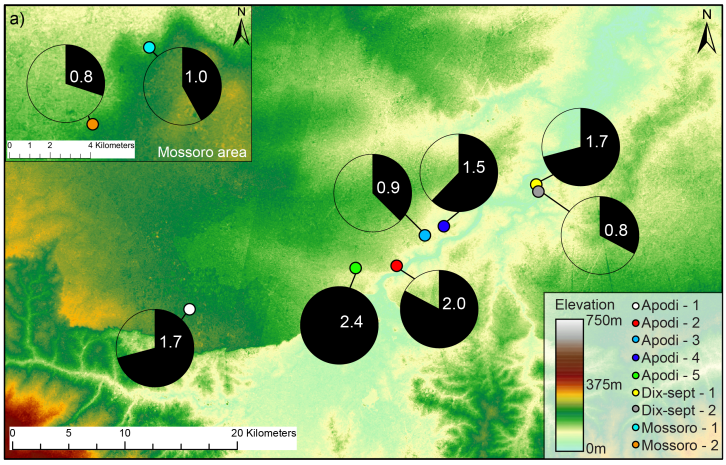


Figure 4.9: Percolation parameters (intersections versus fracture count) for all pavements. The absolute percolation parameter is listed within the pie charts. The pie charts show the normalised percolation parameter, based on the maximum (observed in *Apodi 5*).

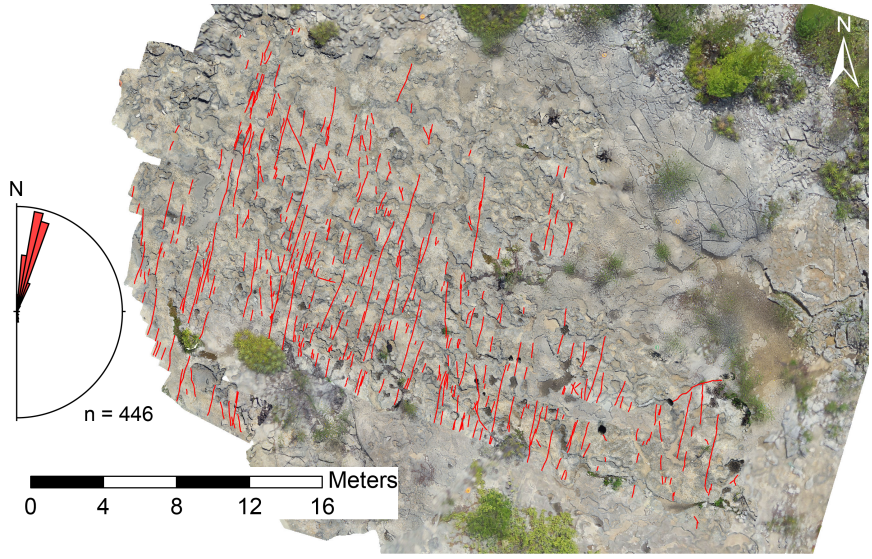


Figure 4.10: High-resolution (0.6 mm/px) image of a 30 × 20 m pavement that has been preserved during exhumation. Within this pavement, 446 veins have been digitised.

tions of veins in some of the other studied outcrops, and found a wider range of orientations.

Length

The largest digitised vein length is smaller than 7 m, even though the outcrop dimensions are larger, so the limited length is not related to censoring artefacts (Fig-

ure 4.11a). This limit is attributed to exhumation, where longer veins have a higher probability of reactivation as they form larger planes of weakness that are more prone to mechanical failure, such that only small veins are preserved (Bertotti *et al.*, subm). In other nearby pavements we observe veins that have been partly preserved and partly reactivated, further confirming this observation (Figure 4.3e,f).

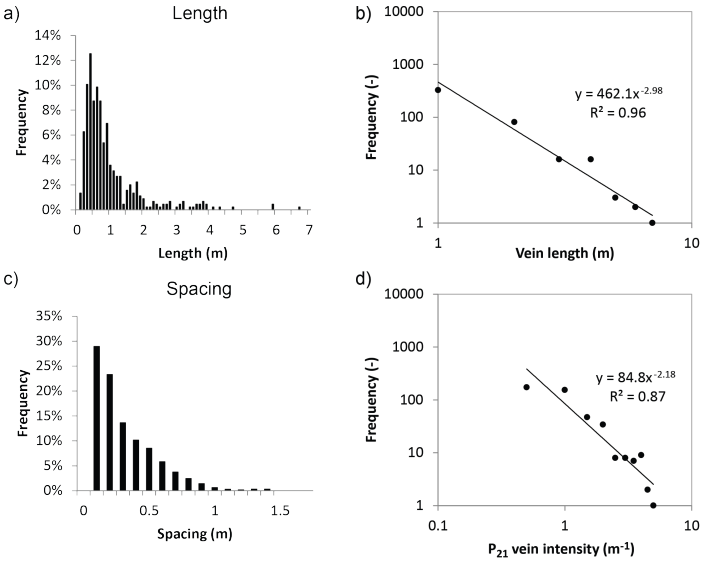


Figure 4.11: Geometrical analysis of outcropping veins: a) Histogram of the length distribution. The decrease for veins shorter than 0.4 m is related to truncation artefacts; b) Frequency distribution for the length domain that does not suffer from truncation artefacts, plotted on a log-log plot; c) Histogram of vein spacing, defined as the inverse of P_{21}; d) Frequency distribution for the intensity domain that does not suffer from truncation artefacts, plotted on a log-log plot.

Vein length in the small pavement follows a power-law scaling trend over nearly two orders of magnitude (Figure 4.11b). The power-law exponent is 3.0, indicating that the distribution lacks large fractures compared to the self-similar case, which is related to the limited vein length scale. This exponent is larger than that of the barren *set 1* fractures.

Spacing and connectivity

Spacing in the pavement is characterised using the P_{21} box-counting method and plotted as a spacing distribution and P_{21} frequency distribution (Figure 4.11c,d). The resulting density frequency distribution, corrected for truncation artefacts, covers less than two orders of magnitude (Figure 4.11d). The power-law exponent of this trend is 2.2, indicating a lower degree of saturation compared to the barren fractures, but as the power-law fit is relatively low ($R^2 = 0.87$), this exponent may not be representative.

In terms of percolation, the vein network is fully disconnected, as fewer than ten veins out of 446 are found to be intersecting other veins. The horizontal percolation

probability is less than 0.1.

4.4. Implications for fractured reservoir permeability

The digitised geometries of the barren network form a unique database covering several orders of magnitude of spacing and length over areas that approach dimensions of inter-well spacing in fractured reservoirs. Aside from their infill and aperture, the geometries have been mostly preserved during exhumation (Bertotti *et al.*, subm). We use this unique dataset of burial-related geometries to quantify the implications for permeability in NFR flow modelling, focusing on uncertainties related to:

i) Subseismic scale natural variations in network geometry;
ii) Changes in aperture, infill and permeability during (partial) exhumation;
iii) The definition of aperture;
iv) The extent to which the matrix contributes to fluid flow.

We extract patterns from four of the pavements that contain barren fractures and part of the preserved pavement containing veins for aperture and permeability modelling (Appendix C). To ensure that permeability is not affected by sampling artefacts, rectangular sections of pavements are used that have a minimum of internal censoring artefacts related to for example trees. Each model contains at least several hundred fractures, and the spatial distribution varies strongly between models and sometimes within a model. The resulting models are:

i) *Apodi 2*, which contains N-S, NE-SW and NW-SE striking fractures;
ii) *Apodi 3*, with large partly intersecting fractures striking approximately N-S, and smaller E-W striking fractures that are mostly limited to the SW part of the outcrop;
iii) *Apodi 4*, with an orthogonal fully percolating fracture system striking N-S and E-W;
iv) *Dix-sept 1*, with a multiscale system with scattered orientations where many small fractures are abutting against lower-intensity larger fractures;
v) *Apodi 6*, a section of NNE-SSW striking veins preserved during exhumation.

4.4.1. Methodology

Aperture modelling

The digitised present-day geometries are used as deterministic patterns for geomechanical aperture and flow modelling (Chapter 3), as these patterns better capture the natural variability observed in fracture patterns compared to Discrete Fracture Network (DFN) models based on purely stochastic distributions (Bisdom *et al.*, 2014). As aperture of the outcropping barren network is not representative of subsurface conditions, we use the Barton-Bandis model for shear-induced apertures. This model assumes that fractures are non-planar surfaces with varying degrees of

The permeability models are partly based on Bisdom, K., Bertotti, G., Nick, H.M., 2016. The impact of different aperture distribution models and critical stress criteria on equivalent permeability in fractured rocks. J. Geophys. Res. Solid Earth 121 (5), 4045-4063.

roughness, which corresponds to the geometry of the preserved hybrid veins in the Jandaíra Fm (Bertotti *et al.*, subm). This method is used to define aperture for all barren fractures, including those that were stylolites prior to exhumation, without taking into account cement. We also apply this method to define the aperture of digitised veins.

Barton-Bandis aperture is a function of fracture roughness (Joint Roughness Coefficient, JRC) and strength (Joint Compressive Strength, JCS) and the local normal and shear stresses (Chapter 3). We use a constant JRC of 15, representative of somewhat irregular fracture walls, and a JCS of 120 MPa. We approximate local stress using a geometrically-based method (Appendix B). For all networks, constant stress boundary conditions and mechanical rock properties are used, with a σ_1 of 30 MPa applied from the north. For a fully elastic rock with a Young's modulus of 50 GPa and a Poisson's ratio of 0.3, the E-W Poisson's stress is 10 MPa.

Permeability modelling

To model flow through the discrete fracture network we generate a mesh that is conformable to the fracture geometry using ABAQUS CAE® (Dassault Systèmes®). Each network is meshed using 2-D triangular elements representing the matrix and 1-D line elements representing fractures (Chapter 3). Intrinsic fracture permeability is calculated using the cubic law, assuming flow between parallel plates (Snow, 1969). To take into account potential flow from disconnected fractures, we assume a matrix permeability of 1 mD, and calculate along each fracture element the flow exchange between fracture and matrix. In a subset of models we vary matrix permeability to quantify the impact of matrix flow.

Flow is modelled using the Complex Systems Modelling Platform (CSMP++; Matthäi *et al.*, 2007), which models the fluid pressure distribution for single-phase incompressible flow through fractures and matrix (e.g. Matthäi and Belayneh, 2004). A fluid pressure gradient is applied in the directions parallel to the model edges (e.g. E-W and N-S). This does not necessarily capture the maximum permeability, but our aim is to characterise relative permeability trends between different networks and different aperture methods. From the fluid pressure gradient we derive the equivalent permeability in the two horizontal directions, which is the permeability representative of combined fracture and matrix flow within the model. Since the studied fracture networks are 2-D patterns obtained from horizontal pavements, we only consider 2-D horizontal permeability, representative of horizontal reservoir flow in between horizontal wells with a spacing of several hundred meters. The impact of well placement, assuming vertical wells, is investigated in (Egya *et al.*, 2016).

4.4.2. Variability in inter-well scale permeability

For the applied boundary conditions, Barton-Bandis apertures range between 0–0.28mm (Figure 4.12). The corresponding equivalent permeability in a 1 mD matrix is quantified as the ratio between equivalent permeability and matrix permeability in the E-W and N-S directions (Figure 4.13a). Except for *Apodi 2*, permeability is anisotropic and highest in the N-S flow direction. Anisotropy is highest in

the veins pavement, as this pavement contains only N-S striking lineaments, and in *Apodi 3*, which contains predominantly long N-S striking conjugates and joints. The limited E-W striking lineaments in this pavement have a small length resulting in low E-W connectivity. Permeability is nearly isotropic in *Apodi 4*, which has an orthogonal system of N-S and E-W striking fractures with a homogeneous intensity, and *Dix-sept 1*, which has a scattered distribution resulting in no preferential flow direction. In *Apodi 2*, only a small fraction of fractures strikes N-S, resulting in a higher E-W permeability.

The increase in equivalent permeability with respect to matrix flow, averaged over the two flow directions, ranges between 3.5–8 (Figure 4.13b). These large permeability variations further illustrate the impact of natural fracture variability on permeability in the absence or regional drivers. Note that the aperture distribution predicted by Barton-Bandis is relatively narrow, and that the permeability contrasts between outcrops likely increases for other aperture models (Bisdom *et al.*, 2016b). Without regional drivers, fracture geometry and permeability is typically considered relatively homogeneous, but we observe that outcrops *Apodi 3* and *4*, which are less than 2 km apart, have the largest contrast in permeability, whereas the other two outcrops have comparable permeabilities although they are nearly 20 km apart.

We observe no relation between geometry, specifically length and intensity, and permeability (Figure 4.13b). The outcrop with the highest permeability does have the highest P_{21} intensity (*Apodi 4*), but a small average fracture length, whereas *Apodi 3*, which has a similar intensity and significantly larger average length, has the lowest permeability. Although particularly intensity is generally considered to determine permeability, we find no correlation between permeability and intensity for these networks in a 1 mD permeable matrix.

4.4.3. Impact of exhumation

In the previous section, all barren features were assumed to contribute to permeability. However, the barren network is the result of exhumation, where the E-W striking features are reactivated stylolites (Bertotti *et al.*, subm). Although the permeability models help to illustrate the natural variability of flow in fracture networks, they are not representative of subsurface flow conditions. To better estimate the subsurface flow conditions and quantify the differences related to exhumation, we compare the results from the previous section with aperture and permeability models for networks with only *set 1* fractures, prior to cementation. We filter *set 1* fractures based on orientation (NNW to NNE striking features) and model their aperture using Barton-Bandis with the same mechanical rock properties and stress conditions as used in the previous models.

In all fracture networks, we observe a decrease in the ratio between equivalent and matrix permeability when considering only flow through *set 1* fractures (Figure 4.14). The decrease is largest in the E-W direction (Figure 4.14a), as mostly E-W striking features are removed from the networks. However, this removal results in a decrease in overall connectivity that also affects N-S permeability (Figure 4.14b,c). The decrease is smallest in *Apodi 3*, as the impact of E-W lineaments was limited

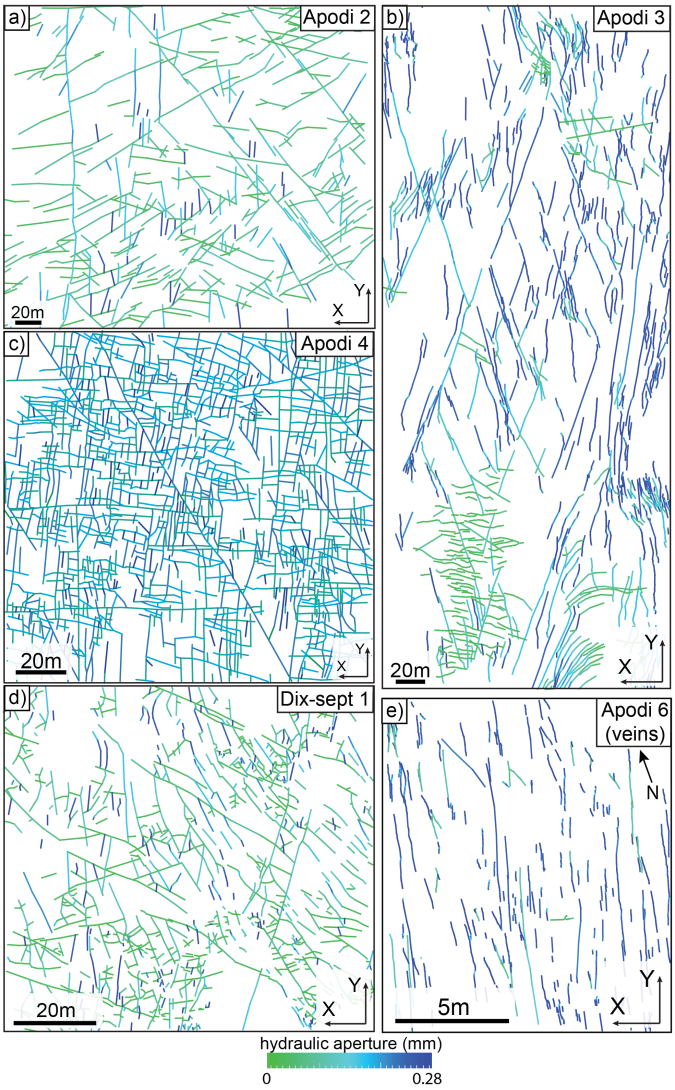


Figure 4.12: The hydraulic aperture distribution calculated using the Barton-Bandis shear aperture model, applied to the exhumed fracture networks. Adapted from Bisdom *et al.* (2016b).

in the exhumed network. In all networks, E-W permeability related to fractures is negligible when only considering burial-related fractures.

In the N-S direction, i.e. sub-parallel to the dominant fracture strike, the decrease in the ratio between equivalent and matrix permeability is smaller compared to E-W permeability, but the differences between pavements ARE large. The decrease in *Dix-sept 1* is similar to that of *Apodi2,4* as fractures in the burial-related network increase equivalent permeability with a factor 2–3, compared to 4–9 in the

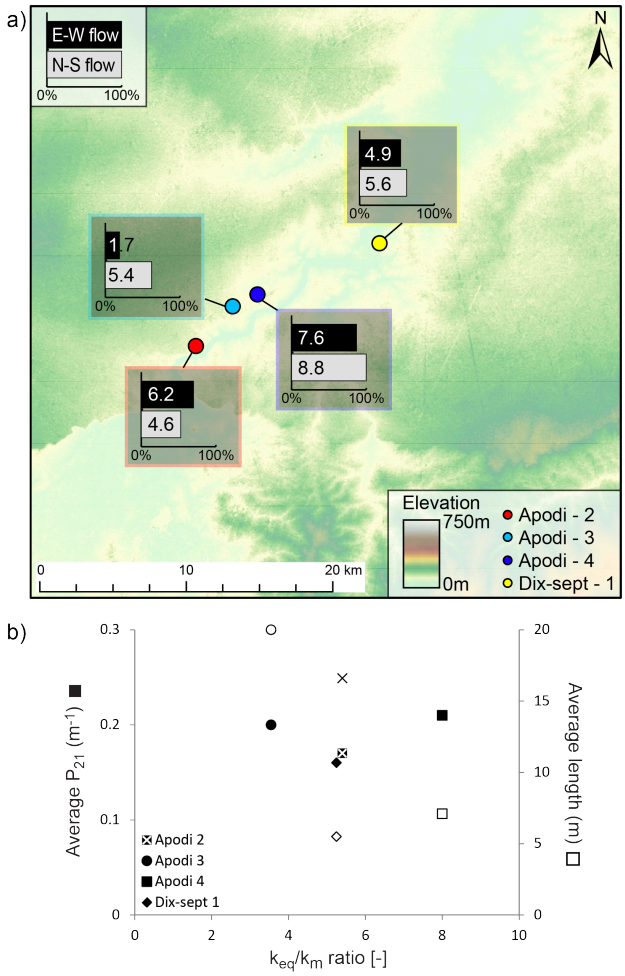


Figure 4.13: a) Ratio between equivalent permeability and matrix permeability in the E-W and N-S directions for four outcrops with barren fractures. The bar plots show the relative differences in different outcrops and different directions, normalised for the largest permeability; b) Relation between the permeability ratio for each outcrop (average of the two directions) and average length (open symbols) and P_{21} intensity (filled symbols).

exhumed networks (Figure 4.14b). This decrease is smaller in *Apodi 3*, as this pavement has a high ratio of N-S striking fractures. Averaged for both directions, the horizontal equivalent permeability of the burial-related fracture network is only 1.5–2.5 times higher than matrix permeability. However, this is based on apertures modelled using the Barton-Bandis method, which typically predicts small apertures (i.e. smaller than 0.3 mm), and may be larger for other aperture methods.

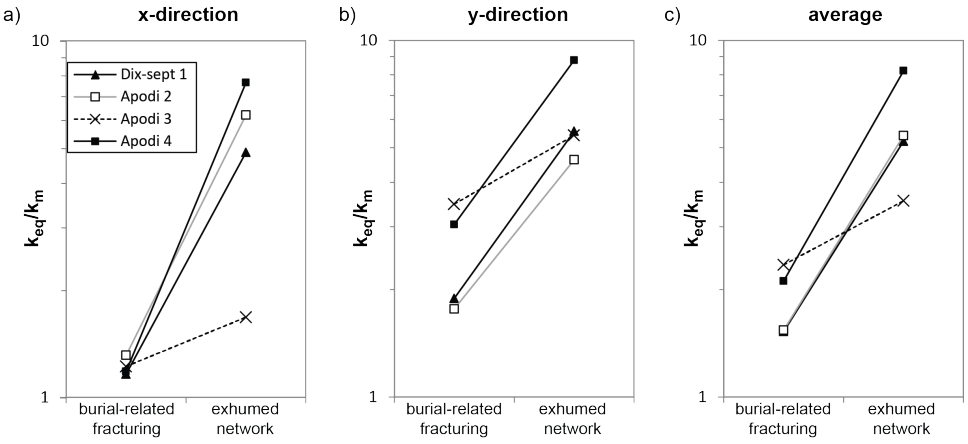


Figure 4.14: Differences in the ratio between equivalent (k_{eq}) and matrix (k_m) permeability associated with reactivation of stylolites. We compare equivalent permeability of the burial-related N-S striking fractures, prior to cementation, to permeability in the exhumed network, where stylolites are reactivated and cements are assumed to be fully dissolved: a) Permeability ratio in the *x* direction (E-W); b) *y* direction (N-S); c) Averaged permeability ratio. Matrix permeability is 1 mD.

4.4.4. Impact of aperture definition

We quantify the impact of aperture on equivalent permeability by comparing the results from the Barton-Bandis method with power-law scaling and (sub)linear length-aperture scaling. We use the present-day outcropping network geometry, which has a high connectivity and therefore creates larger contrasts in permeability. The matrix permeability in these models is 10 mD. For (sub)linear length-aperture scaling we use the same mechanical boundary conditions as for Barton-Bandis. For power-law apertures, we use a scaling exponent of 0.8, as this exponent is often observed for apertures in carbonates (Hooker *et al.*, 2013, 2014).

The spatial variations in hydraulic aperture resulting from each method and the implications for permeability are illustrated for pavement *Dix-sept 1* (Figure 4.15). Absolute apertures modelled using power-law scaling and Barton-Bandis are similar in magnitude, as aperture is mostly smaller than 0.5 mm (Figure 4.15a,c). The linear length-aperture method predicts larger apertures, with a maximum of 40 mm in this pavement (Figure 4.15b).

For power-law and linear length-aperture scaling, we use Mohr-Coulomb with a 0.6 friction coefficient to define which fractures are hydraulically conductive under N-S compression, not considering vertical stresses. Fracture orientation with respect to N-S shortening defines which fractures are critically stressed, and hence considered conductive (Barton *et al.*, 1995). Application of Mohr-Coulomb hydraulically closes on average 50% of fractures in the studied pavements, which reduces the porosity and percolation probability of the networks. For power-law scaling, the 50% decrease in conductivity combined with small apertures results in a low percolation parameter (Figure 4.15a), and almost no increase in equivalent permeability compared to matrix flow (Figure 4.15d,g). Although apertures are as-

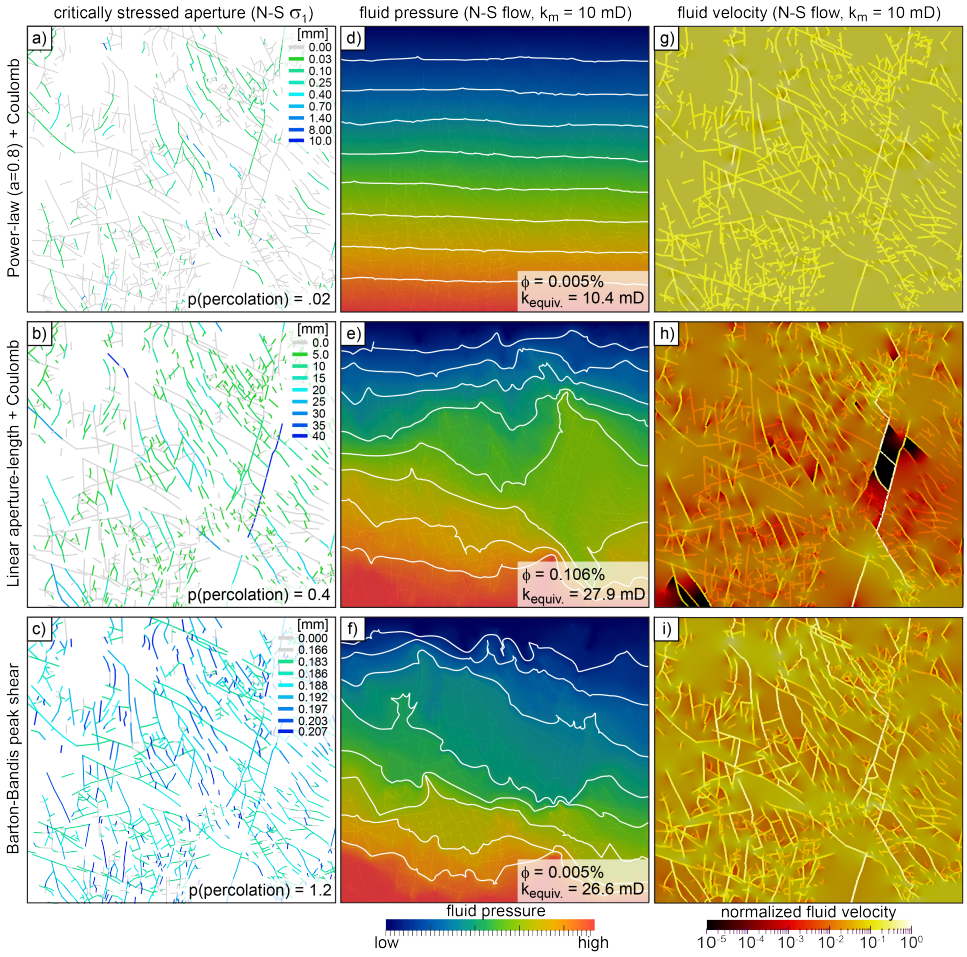


Figure 4.15: Critically stressed aperture and subsequent fluid pressure for the three main aperture methods, applied to *Dix-sept 1*. Critical stress analysis assumes a N-S maximum horizontal stress: a) Power-law aperture based on an exponent of 0.8; b) Linear length-aperture scaling; c) Barton-Bandis aperture. The corresponding percolation parameter is shown in the inset of a-c (the percolation probability of the entire network, assuming all fractures are open, is 1.7); d-f) N-S fluid pressure for the critically stressed aperture models from a-c, using a 10 mD matrix. White lines are fluid pressure contour lines. The equivalent permeability is listed in each image; g-i) N-S fluid velocity magnitude field, showing which fractures contribute most to the increase in equivalent permeability. Adapted from Bisdom *et al.* (2016b).

signed randomly and are not stress-dependent, there are only minor variations in permeability in different realisations.

Connectivity also decreases for linear length-aperture scaling when we apply a critical stress criterion, but as absolute apertures are large, the increase in equivalent permeability is larger compared to power-law scaling (27.9 mD; Figure 4.15e). The increase is mainly related to several long fractures with large apertures, whereas

smaller fractures do not contribute significantly to flow (Figure 4.15h).

The Barton-Bandis method uses an alternative definition for hydraulic aperture, which is strongly controlled by orientation, but also depends on fracture geometry and particularly the spatial distribution (Bisdom *et al.*, 2016a). The transition from a conductive to non-conductive fracture is more continuous compared to Mohr-Coulomb, resulting in a ratio of 80% conductive fractures on average, albeit with small absolute apertures (Figure 4.15c). Regardless of the small apertures, the high connectivity results in a N-S equivalent permeability of 26.6 mD, which is close to the permeability resulting from linear length-aperture scaling (Figure 4.15e,f).

The differences in permeability resulting from the three aperture methods emphasize the importance of connectivity, in addition to aperture and subsequent fracture porosity. The power-law and Barton-Bandis models have identical fracture porosities, defined by the summed product of aperture and length, but different permeabilities (Figure 4.15d,f). The model derived from linear length-aperture scaling has a significantly higher fracture porosity compared to the Barton-Bandis model, but only a marginally higher permeability (Figure 4.15e,f).

4.4.5. Impact of matrix flow and fracture connectivity

In the previous models we have assumed a constant matrix permeability of 1 mD (Figures 4.13 and 4.14) and 10 mD (Figure 4.15) to allow for flow from disconnected fractures. In the 1 mD matrix, the relative impact of Barton-Bandis apertures on permeability is larger compared to the 10 mD matrix. To further quantify the relative impact of the matrix, we model equivalent permeability for a range of matrix permeabilities between 1–1000mD (Figure 4.16).

For power-law scaling with an exponent of 0.8, the contribution of fractures to permeability is low even in a low-permeability matrix (e.g. 1 mD) and decreases to nearly zero for higher matrix permeabilities (Figure 4.16a). As aperture is not related to geometry, the differences in permeability between the pavements are directly related to fracture intensity. The 30 × 20 m section with veins has a high fracture intensity (Figure 4.11), resulting in a high permeability when using randomly assigned power-law apertures, even though connectivity is low.

For a matrix permeability below 100 mD, the increase in permeability related to fracture flow is larger for Barton-Bandis apertures compared to power-law scaling (Figure 4.16b). As Barton-Bandis aperture depends on a combination of geometrical and spatial parameters, there is no straightforward relation between geometry and permeability. Furthermore, the relative differences in permeability between pavements change with changing matrix permeability. In a low-permeability matrix (i.e. less than 5 mD), equivalent permeability is higher in models with a higher percolation parameter (Figure 4.9). When matrix permeability increases, aperture controls equivalent permeability. The pavement with veins has the largest average aperture, resulting from an optimal fracture orientation (Figure 4.12), creating the highest equivalent permeability in a high-permeability matrix even though connectivity is lower compared to the other networks (Figure 4.16b).

Apertures modelled using linear length-aperture scaling are one to two orders of magnitude larger than Barton-Bandis and power-law scaling apertures, resulting

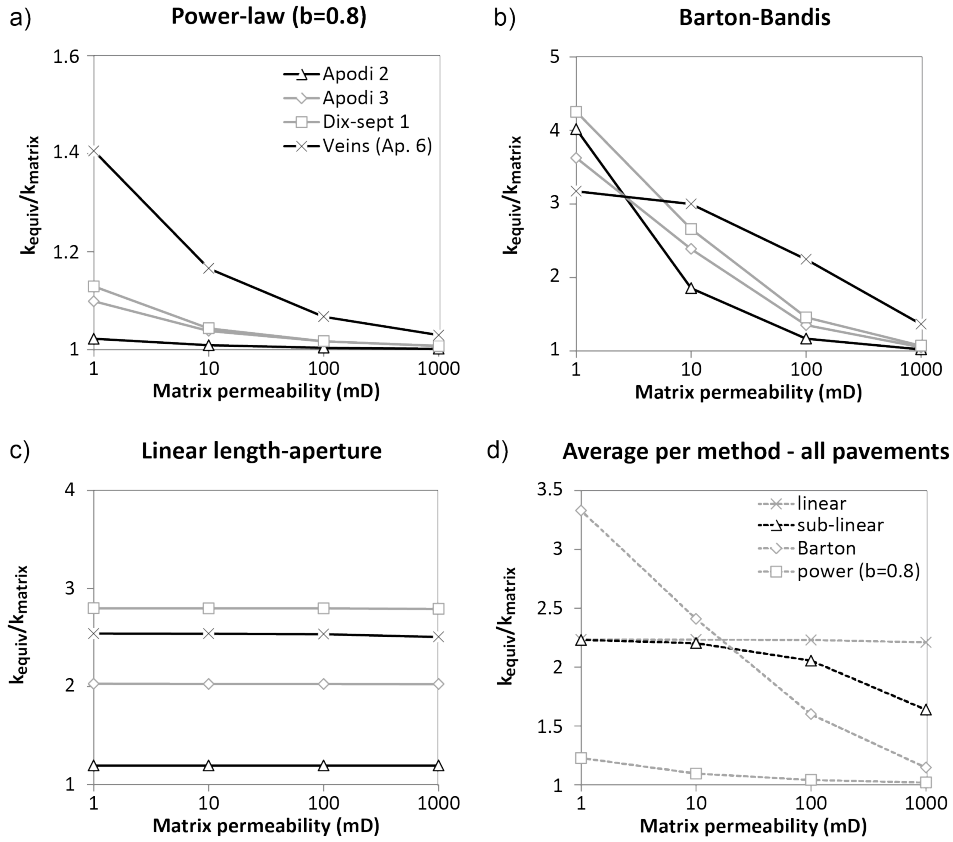


Figure 4.16: Ratio between equivalent and matrix permeability (average of N-S and E-W flow) as a function of increasing matrix permeability for the three different aperture methods: a) Power-law scaling with an exponent of 0.8; b) Barton-Bandis aperture; c) Linear length-aperture scaling; d) Average permeability ratio from all pavements for each method. Adapted from Bisdom *et al.* (2016b).

in a relatively large increase in equivalent aperture, irrespective of matrix permeability (Figure 4.16c). This method defines aperture as a function of intensity and length, as well as local stress perturbations, and since length and intensity vary strongly between pavements, permeability is also highly variable. For networks with an identical intensity, permeability is higher when the network consists of fewer but longer fractures compared to a large amount of short fractures.

When matrix permeability is high (i.e. >15 mD) in the studied networks, linear length-aperture scaling predicts the largest permeability (Figure 4.16d). Apertures modelled by this method are large, but as on average only 50% of the network is conductive for the given stress conditions, connectivity is low. As a result, the relative impact of fractures on flow does not increase when matrix permeability decreases. The Barton-Bandis method predicts that up to 80% of fractures are conductive, which results in a significant increase in equivalent permeability when

matrix permeability is low (i.e. lower than 15 mD).

4.5. Discussion

The horizontal equivalent permeability has been quantified in a subset of the pavements, taking into account a range of uncertainties in matrix permeability and aperture. For these pavements, we have a detailed analysis of the geometrical and spatial distributions, which we compare with permeability to assess to what extent geometrical parameters such as connectivity and spacing can be used to approximate flow behaviour.

Definitions of percolation aim to characterise the network connectivity as a proxy for permeability, but we observe no relation between the percolation parameter defined by Robinson (1983) and equivalent permeability, independent of the applied aperture definition (Figure 4.17a). Only for Barton-Bandis apertures we find for four out of five pavements a linear relation between percolation parameter and equivalent permeability, but *Apodi 4*, which has the highest permeability but a lower percolation parameter, does not fit this trend. For power-law aperture scaling, which is not related to fracture geometry or in-situ stress, equivalent permeability was observed to scale with P_{21} intensity, but permeability modelled using the other aperture definitions is related to a combination of geometrical parameters and in-situ stress conditions.

One reason for the poor correlation between permeability and connectivity is that connectivity is only based on network geometry, without considering aperture variations and hydraulically closed segments. On average 50% of apertures are hydraulically closed when using power-law or linear length-aperture scaling combined with Mohr-Coulomb, resulting in a poor correlation between permeability and connectivity compared to the Barton-Bandis model, where 80% of the network is conductive on average (Figure 4.17a). Defining percolation based on the hydraulically conductive network slightly improves the relation, but the example of the *Dix-sept 1* pavement shows that networks with a different conductive percolation parameter can have similar equivalent permeabilities (Figure 4.15b,c).

Second, the percolation parameter implicitly takes into account intensity, length and orientation through the intersection count. However, the intersection count can also be high when fractures are short and clustered, but if these fractures do not form a connecting network from one side of the model to the other side, permeability will be low even though the percolation parameter is high.

To better capture the impact of the spatial distribution on permeability, we use network saturation as an alternative definition of percolation. The network saturation is defined as the ratio between the area of clustered fractures and total outcrop area. The cluster analysis is done in FracMan® (Golder Associates®). For the Barton-Bandis method, network saturation is a representative proxy for equivalent permeability in a 1 mD matrix (Figure 4.17b). However, as the cluster analysis is only based on geometry, the correlation remains low for permeability derived from length-aperture and power-law scaling. Since percolation assumes that the matrix is impermeable, we also observe that the correlation between connectivity and permeability only holds for a low matrix permeability (i.e. less than 1 mD).

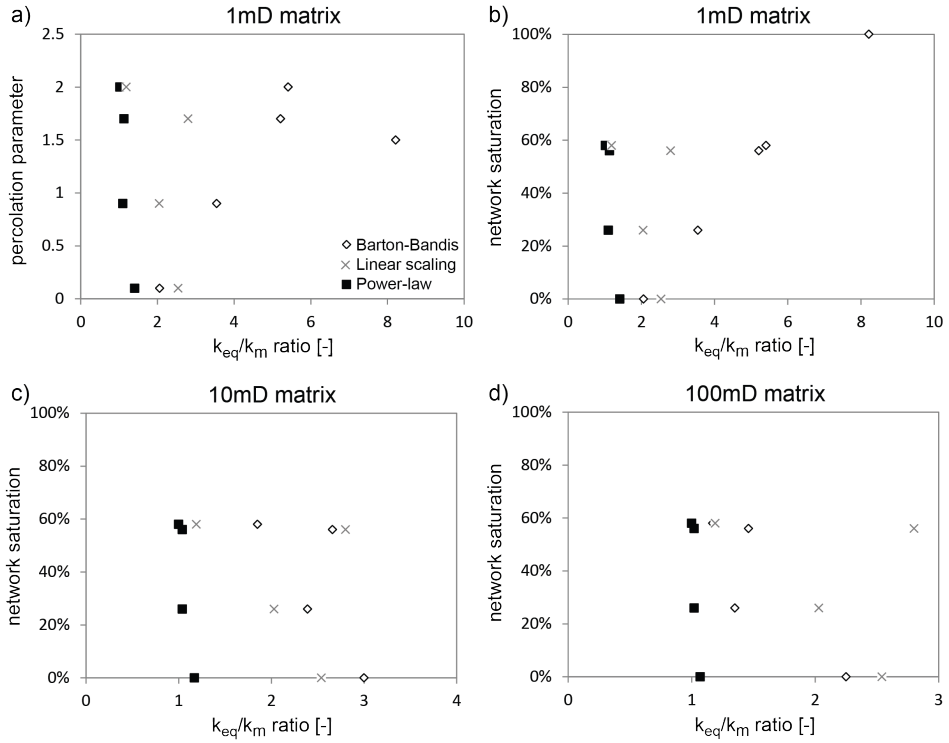


Figure 4.17: Relation between connectivity and the ratio between equivalent permeability k_{eq} and matrix permeability k_m, derived from three aperture methods for the individual pavements: a) Percolation parameter as defined by Robinson (1983) versus equivalent permeability in a 1 mD matrix; b) The degree of network saturation derived from cluster analysis versus the equivalent permeability ratio in a 1 mD matrix; c) Network saturation versus permeability ratio for a 10 mD matrix; d) Network saturation versus permeability ratio for a 100 mD matrix.

For a more permeable matrix, where flow from disconnected fractures also contributes to equivalent permeability, there is no relation between connectivity and permeability, irrespective of the connectivity definition or aperture method (Figure 4.17c,d).

4.6. Conclusions

The geometrical and spatial distribution of burial-related veins and stylolites in the Jandaíra Fm. (Potiguar bain, NE Brazil) is characterised from high-resolution images taken by a UAV, supported by smaller-scale observations at the outcrop. From the UAV images we digitise predominantly barren fractures, but based on findings from de Graaf *et al.* (subm) and Bertotti *et al.* (subm) we can reconstruct the type and infill of these features prior to exhumation. Most sub-seismic structural deformation in the Jandaíra Fm. is the result of regional N-S to NNE-SSW shortening during burial, creating approximately N-S striking bed-

perpendicular veins and conjugate fractures and E-W striking bed-perpendicular stylolites, followed by the formation of horizontal stylolites during continued burial (Bertotti *et al.*, subm).

We have quantified the geometrical and spatial distributions of over 13 000 barren fractures in nine pavements and nearly 500 veins in a pavement that was preserved during exhumation. We observe power-law scaling for the spacing and length distributions in all pavements with relatively constant scaling exponents. However, within each pavement and between different pavements there are large differences in the spatial arrangement and length of barren fractures. The percolation parameter, defined as the ratio between the amount of intersections and the fracture count, varies strongly even between closely-spaced pavements.

Within and between pavements we observe variations in permeability magnitude and anisotropy, which correlate to the observed variations in geometry and spacing. To quantify the equivalent permeability of burial-related fractures, we model flow through the N-S striking system for assumed stress conditions prior to cementation at depths between 450–850m. This system has a decreased connectivity and permeability compared to the exhumed system with reactivated stylolites, but burial-related fractures do increase equivalent permeability up to three times compared to matrix permeability, even if the networks are largely disconnected.

We quantify the uncertainties in permeability associated with unknown in-situ apertures by comparing the Barton-Bandis aperture method for conductive shear fractures to power-law and linear length-aperture scaling. Linear length-aperture scaling predicts large apertures (up to 40 mm) but on average only 50% of the network is hydraulically conductive, based on the principles of Mohr-Coulomb. For power-law scaling we find the same ratio of conductive fractures, but absolute apertures are typically smaller than 0.5 mm. Barton-Bandis apertures are equally small, but on average 80% of the network is conductive, resulting in equivalent permeabilities that are similar to those resulting from linear length-aperture scaling. In a tight matrix, Barton-Bandis apertures result in higher equivalent permeabilities compared to the other methods, but for a permeable matrix where disconnected fractures can contribute to flow, linear length-aperture scaling has a larger impact on permeability.

We find that even though fractures in the different pavements are related to a single regional shortening event, there is a large scatter in particularly the spatial distribution and length between the pavements. The distance between pavements is comparable to well spacing in large fractured carbonate reservoirs in for example the Middle East, and the results illustrate that even in reservoirs with relatively little seismic-scale deformation, fracture permeability varies strongly on an inter-well scale. Percolation parameters observe this scatter, but we find that percolation is only representative of permeability when matrix permeability is less than 1 mD and when hydraulic conductivity is taken into account. Fracture porosity is also not representative in itself, as models with equal porosities but different hydraulic aperture distributions have significantly different equivalent permeabilities.

References

N. J. Price, *Fault and Joint Development in Brittle and Semi-Brittle Rock* (Pergamon, 1966) p. 192.

S. Bergbauer and D. D. Pollard, *A new conceptual fold-fracture model including prefolding joints, based on the Emigrant Gap anticline, Wyoming*, Geological Society of America Bulletin **116**, 294 (2004).

P. J. Hudleston and S. H. Treagus, *Information from folds: A review*, Journal of Structural Geology **32**, 2042 (2010).

M. H. Anders, S. E. Laubach, and C. H. Scholz, *Microfractures: A review*, Journal of Structural Geology **69**, 377 (2014).

M. P. Fischer and P. B. Jackson, *Stratigraphic controls on deformation patterns in fault-related folds: a detachment fold example from the Sierra Madre Oriental, northeast Mexico*, Journal of Structural Geology **21**, 613 (1999).

N. Bellahsen, P. Fiore, and D. D. Pollard, *The role of fractures in the structural interpretation of Sheep Mountain Anticline, Wyoming*, Journal of Structural Geology **28**, 850 (2006).

B. J. Stephenson, A. Koopman, H. Hillgartner, H. McQuillan, S. Bourne, J. J. Noad, and K. Rawnsley, *Structural and stratigraphic controls on fold-related fracturing in the Zagros Mountains, Iran: implications for reservoir development*, Geological Society, London, Special Publications **270**, 1 (2007).

S. Tavani, F. Storti, B. Soleimany, M. Fallah, J. A. Muñoz, and R. Gambini, *Geometry, kinematics and fracture pattern of the Bangestan anticline, Zagros, SW Iran*, Geological Magazine **148**, 964 (2011).

O. Lacombe, N. Bellahsen, and F. Mouthereau, *Fracture patterns in the Zagros Simply Folded Belt (Fars, Iran): constraints on early collisional tectonic history and role of basement faults*, Geological Magazine **148**, 940 (2011).

M. Branellec, J. P. Callot, B. Nivière, and J. C. Ringenbach, *The fracture network, a proxy for mesoscale deformation: Constraints on layer parallel shortening history from the Malargüe fold and thrust belt, Argentina*, Tectonics **34**, 623 (2015).

G. Bertotti, S. de Graaf, K. Bisdom, H. Vonhof, J. Reijmer, F. Bezerra, and C. Cazarin, *Fracturing and flow during post-rift subsidence in carbonate rocks of the Jandaira Formation (NE Brazil)*, (subm).

S. de Graaf, G. Bertotti, J. Reijmer, F. Bezerra, C. Cazarin, K. Bisdom, and H. Vonhof, *Fracture-controlled fluid circulation and calcite vein cementation during early burial in shallow water carbonates (Jandaíra Formation, northeast Brazil)*, Marine and Petroleum Geology (subm).

F. Muhammad, *Geological well testing in fractured carbonate reservoir*, M.sc. thesis, Heriot Watt University (2016).

J. F. Gale, S. E. Laubach, J. E. Olson, P. Eichhuble, and A. Fall, *Natural Fractures in shale: A review and new observations*, AAPG Bulletin **98**, 2165 (2014).

G. H. Makel, *The modelling of fractured reservoirs: constraints and potential for fracture network geometry and hydraulics analysis*, Geological Society, London, Special Publications **292**, 375 (2007).

N. Barton and S. Bandis, *Some effects of scale on the shear strength of joints*, in *International Journal of Rock Mechanics and Mining Sciences & Geomechanics Abstracts*, Vol. 17 (Pergamon Press Ltd., 1980) pp. 69–73.

N. Barton, *Modelling rock joint behaviour from in situ block tests: Implications for nuclear waste repository design*, Tech. Rep. (Office of Nuclear Waste Isolation, Columbus, OH, 1982).

B. Lawn and T. Wilshaw, *Fracture of brittle solids* (Cambridge University Press, 1975) p. 204.

D. D. Pollard and P. Segall, *Theoretical displacements and stresses near fractures in rock: with applications to faults, veins, dikes, and solution surfaces*, in *Fracture Mechanics of Rock* (Elsevier, 1987) Chap. 8, pp. 277–349.

J. E. Olson, *Sublinear scaling of fracture aperture versus length: An exception or the rule?* Journal of Geophysical Research: Solid Earth **108**, 2413 (2003).

J. N. Hooker, L. A. Gomez, S. E. Laubach, J. F. W. Gale, and R. Marrett, *Effects of diagenesis (cement precipitation) during fracture opening on fracture aperture-size scaling in carbonate rocks*, Geological Society, London, Special Publications **370**, 187 (2012).

J. N. Hooker, S. E. Laubach, and R. Marrett, *A universal power-law scaling exponent for fracture apertures in sandstones*, Geological Society of America Bulletin **126**, 1340 (2014).

Q. Lei, J.-P. Latham, J. Xiang, C.-F. Tsang, P. Lang, and L. Guo, *Effects of geomechanical changes on the validity of a discrete fracture network representation of a realistic two-dimensional fractured rock*, International Journal of Rock Mechanics and Mining Sciences **70**, 507 (2014).

K. Bisdom, G. Bertotti, and H. M. Nick, *The impact of in-situ stress and outcrop-based fracture geometry on hydraulic aperture and upscaled permeability in fractured reservoirs*, Tectonophysics (2016a), 10.1016/j.tecto.2016.04.006.

B. K. Atkinson, *Subcritical crack growth in geological materials*, Journal of Geophysical Research **89**, 4077 (1984).

J. M. Vermilye and C. H. Scholz, *Relation between vein length and aperture*, Journal of Structural Geology **17**, 423 (1995).

C. H. Scholz, *A note on the scaling relations for opening mode fractures in rock*, Journal of Structural Geology **32**, 1485 (2010).

C. H. Scholz, *Reply to comments of Jon Olson and Richard Schultz*, Journal of Structural Geology **33**, 1525 (2011).

J. E. Olson and R. A. Schultz, *Comment on A note on the scaling relations for opening mode fractures in rock by C.H. Scholz*, Journal of Structural Geology **33**, 1523 (2011).

J. Hooker, S. Laubach, and R. Marrett, *Fracture-aperture sizefrequency, spatial distribution, and growth processes in strata-bounded and non-strata-bounded fractures, Cambrian Mesón Group, NW Argentina*, Journal of Structural Geology **54**, 54 (2013).

H. A. O. Ojeda, *Structural Framework, Stratigraphy, and Evolution of Brazilian Marginal Basins*, AAPG Bulletin **66**, 732 (1982).

R. M. D. de Matos, *The Northeast Brazilian Rift System*, Tectonics **11**, 766 (1992).

Á. F. C. Reis, F. H. R. Bezerra, J. M. Ferreira, A. F. Do Nascimento, and C. C. Lima, *Stress magnitude and orientation in the Potiguar Basin, Brazil: Implications on faulting style and reactivation*, Journal of Geophysical Research: Solid Earth **118**, 5550 (2013).

B. de Brito Neves, R. Fuck, U. Cordani, and A. Thomaz F, *Influence of basement structures on the evolution of the major sedimentary basins of Brazil: A case of tectonic heritage*, Journal of Geodynamics **1**, 495 (1984).

M. Assumpção, *The regional intraplate stress field in South America*, Journal of Geophysical Research **97**, 11889 (1992).

M. van Eijk, *Analysis of the fracture network in carbonate rocks of the Jandaira Formation in northeast Brazil*, M.sc. thesis, VU University Amsterdam (2014).

E. van der Voet, *Fracture networks in carbonate rocks of the Potiguar Basin, northeast Brazil*, M.sc. thesis, VU University Amsterdam (2015).

E. Wever, *Discrete Fracture Network modelling of carbonate pavements in Brazil*, B.sc. thesis, Delft University of Technology (2015).

C. Paulides, *Statistical analysis of 2D trace-line maps of fracture networks in carbonate rocks of the Jandeíra Formation in Brazil*, Ph.D. thesis, Delft University of Technology (2013).

E. Bonnet, O. Bour, N. E. Odling, P. Davy, I. Main, P. Cowie, and B. Berkowitz, *Scaling of fracture systems in geological media*, Reviews of Geophysics **39**, 347 (2001).

N. E. Odling, P. Gillespie, B. Bourgine, C. Castaing, J. P. Chiles, N. P. Christensen, E. Fillion, A. Genter, C. Olsen, L. Thrane, R. Trice, E. Aarseth, J. J. Walsh, and J. Watterson, *Variations in fracture system geometry and their implications for fluid flow in fractures hydrocarbon reservoirs*, Petroleum Geoscience **5**, 373 (1999).

O. Bour, *A statistical scaling model for fracture network geometry, with validation on a multiscale mapping of a joint network (Hornelen Basin, Norway)*, Journal of Geophysical Research **107**, 2113 (2002).

W. S. Dershowitz and H. H. Einstein, *Characterizing rock joint geometry with joint system models*, Rock Mechanics and Rock Engineering **51**, 21 (1988).

P. La Pointe, *A method to characterize fracture density and connectivity through fractal geometry*, International Journal of Rock Mechanics and Mining Sciences & Geomechanics Abstracts **25**, 421 (1988).

J. Walsh and J. Watterson, *Fractal analysis of fracture patterns using the standard box-counting technique: valid and invalid methodologies*, Journal of Structural Geology **15**, 1509 (1993).

C. Darcel, *Stereological analysis of fractal fracture networks*, Journal of Geophysical Research **108**, 2451 (2003).

P. C. Robinson, *Connectivity of fracture systems-a percolation theory approach*, Journal of Physics A: Mathematical and General **16**, 605 (1983).

P. C. Robinson, *Numerical calculations of critical densities for lines and planes*, Journal of Physics A: Mathematical and General **17**, 2823 (1984).

K. Bisdom, B. Gauthier, G. Bertotti, and N. Hardebol, *Calibrating discrete fracture-network models with a carbonate three-dimensional outcrop fracture network: Implications for naturally fractured reservoir modeling*, AAPG Bulletin **98**, 1351 (2014).

D. T. Snow, *Anisotropic Permeability of Fractured Media*, Water Resources Research **5**, 1273 (1969).

S. K. Matthäi, S. Geiger, S. G. Roberts, A. Paluszny, M. Belayneh, A. Burri, A. Mezentsev, H. Lu, D. Coumou, T. Driesner, and C. A. Heinrich, *Numerical simulation of multi-phase fluid flow in structurally complex reservoirs*, Geological Society, London, Special Publications **292**, 405 (2007).

S. K. Matthäi and M. Belayneh, *Fluid flow partitioning between fractures and a permeable rock matrix*, Geophysical Research Letters **31** (2004), 10.1029/2003GL019027.

D. Egya, S. Geiger, P. Corbett, K. Bisdom, G. Bertotti, and H. Bezerra, *Assessing the Validity and Limitations of Dual- porosity Models Using Geological Well Testing for Fractured Formations*, in *78th EAGE Conference & Exhibition* (EAGE, Vienna, Austria, 2016).

K. Bisdom, G. Bertotti, and H. M. Nick, *The impact of different aperture distribution models and critical stress criteria on equivalent permeability in fractured rocks*, Journal of Geophysical Research: Solid Earth **121**, 4045 (2016b).

C. A. Barton, M. D. Zoback, and D. Moos, *Fluid flow along potentially active faults in crystalline rock*, Geology **23**, 683 (1995).

5

Impact of burial-related fractures on hydraulic fracturing in sub-horizontal shales

The shales of the Vaca Muerta Fm. (Neuquén Basin, Argentina) are intensely fractured, but these natural fractures are closed at in-situ stress conditions. However, varying hydraulic fracture height and an anisotropic Stimulated Rock Volume (SRV) indicate that natural fractures impact hydraulic fracturing. Understanding this impact can lead to optimised reservoir development. We use a subsurface dataset of natural fractures obtained from three wells in a pilot area to quantify the role of natural fractures on hydraulic fracturing. Natural fractures are characterised as bed-perpendicular conjugates and joints, formed through Layer-Parallel Shortening related to the ongoing Andean compression, and bedding-parallel fractures filled with calcite cement (beef), formed during burial. Using coupled stress-fluid pressure models, we quantify the vertical and horizontal distribution of the SRV. The potential flow properties of the reactivated natural fractures are modelled using a Discrete Fracture Network model with a stress-induced aperture distribution. Our models show that the SRV is controlled by natural fracture corridors, which have a reactivated permeability of up to 40 mD. *Equivalent permeability is up to 30 times higher in the direction sub-parallel to regional shortening, compared to the perpendicular direction. The models show that the beef features limit vertical growth of hydraulic fractures, which in turn leads to an increase in fracture length and aperture. The burial-related natural fractures in the Vaca Muerta Fm. significantly impact the stimulation strategy and post-stimulation permeability.*

This chapter is based on: K. Bisdom, E. Baud, S. Estrada, Y. Sanz-Perl, B. Gauthier, G. Bertotti (2016). Coupled Stress-fluid Pressure Modelling of Stimulated Rock Volume in Shale - Impact of Natural Fractures and Beef. 78th EAGE Conference & Exhibition, 30 May - 2 June, Vienna, Austria.

5.1. Introduction

Subsurface rocks can be intensely fractured even in the absence of seismic-scale deformation events (Chapter 4). This indicates that natural fractures can be expected in most rocks in the deeper subsurface, including in hydrocarbon reservoirs. However, these natural fractures do not necessarily impact fluid flow, so not all fractured rocks act as fractured reservoirs (Nelson, 2001). Fracture permeability is greatly reduced when fractures are cemented (e.g. Ahr, 2008), and even in the absence of cement, unfavourable stress conditions may limit permeability (Barton *et al.*, 1995; Rogers, 2003). Furthermore, natural fracture networks can change from an impermeable cemented system to a permeable network of open fractures or vice versa through geological times (Bertotti *et al.*, subm).

The Vaca Muerta Fm. in the central part of the Neuquén Basin (Argentina) is an example of a sub-horizontal calcareous shale formation with limited seismic-scale faulting, that is nonetheless highly fractured, as indicated by core data and outcrop analogues (Cobbold *et al.*, 2013; Sagasti *et al.*, 2014). At in-situ stress conditions these fractures do not contribute to fluid flow (Padin *et al.*, 2014; Sagasti *et al.*, 2014). Observations from cores and outcrop analogues indicate that part of the fractures are fully cemented (Cobbold *et al.*, 2013; Padin *et al.*, 2014). The uncemented fractures are not conductive, as in-situ fluid pressures are not sufficiently high to reactivate natural fractures, even though the rocks are overpressured (Padin *et al.*, 2014).

Although there is no in-situ permeability in the Vaca Muerta Fm., it contains significant volumes of hydrocarbons (e.g. Garcia *et al.*, 2013). Induced hydraulic fracturing is used to increase permeability in the vicinity of wells to unlock these reserves (e.g. Padin *et al.*, 2014). During hydraulic fracturing, microseismic and pressure interference tests indicate that the Stimulated Rock Volume (SRV) is laterally larger and more heterogeneous than what is commonly observed in shales (Moos *et al.*, 2011; Osorio and Muzzio, 2013). Microseismic shows that the vertical growth of hydraulic fractures varies, even though the completion strategy is constant (Figure 5.1a). Second, pressure interference data from two wells 400 m away from a stimulated well indicates pressure interference between one well and the stimulated well, but there is no interference in the other nearby well (Figure 5.1b).

These observations are attributed to the impact of pre-existing natural fracture network. The impact of natural fractures and other structural heterogeneities on hydraulic fracture propagation has been identified qualitatively (Gale *et al.*, 2007, 2014; Gasparrini *et al.*, 2014) and quantitatively (Smart *et al.*, 2014). In settings of low differential stress, hydraulic fractures link up with natural fractures, forming complex networks of induced and natural fractures with varying orientations (Gale *et al.*, 2007; Weng *et al.*, 2016). Cemented natural fractures can limit hydraulic fracture growth and decrease the recoverable volumes (Fisher and Warpinski, 2012; Gasparrini *et al.*, 2014). One unique feature of the Vaca Muerta Fm. is its high density of bedding-parallel calcite veins ('beef'), which can be laterally continuous over several hundred meters, potentially limiting hydraulic fracture growth (Rodrigues *et al.*, 2009; Gale *et al.*, 2014; Sagasti *et al.*, 2014).

Our aim is to quantify the impact of core- and FMI-scale natural fractures in the

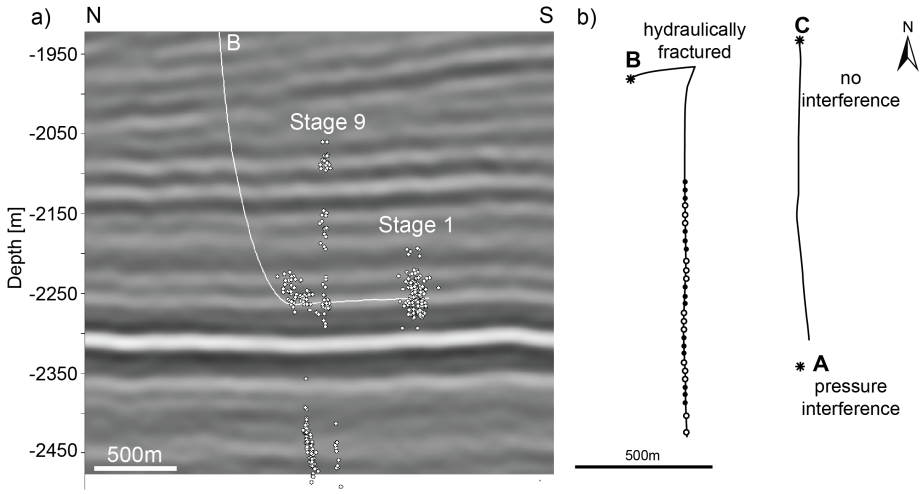


Figure 5.1: Indicators of heterogeneity within the Vaca Muerta Fm.: a) Vertical section showing horizontal well B with two hydraulic fracturing stages with identical set-ups, but different hydraulic fracture height, as indicated by induced seismicity events; b) Map view of two horizontal wells B and C and a vertical well A. During hydraulic fracturing of well B, pressure interference is observed in well A, but not in well C.

sub-horizontal Vaca Muerta Fm. on hydraulic fracturing and the resulting permeability change, focusing on:

i) Changes in equivalent permeability in the natural fracture network associated with reactivation during hydraulic fracturing;
ii) Impact of natural fractures and corridors on the shape and size of the SRV;
iii) Impact of beef on the height and elongation of hydraulic fractures.

The potential for reactivating natural fractures and the subsequent increase in permeability is modelled using a coupled geomechanical-fluid flow approach. We calculate the potential equivalent permeability of the natural fractures which is then used to model the change in in-situ pressure resulting from fluid injection during hydraulic fracturing. Based on the pressure distribution, areas are identified in which pressure is sufficiently high to reactivate natural fractures. Furthermore, the elevated pressure is a proxy for quantifying the SRV.

The fluid pressure models are generated using 2-D Finite Element (FE) models that couple geomechanics and fluid flow (e.g. Smart *et al.*, 2014). Vertical 2-D models of cross-sections along wells are used to model the vertical and horizontal growth of hydraulic fractures. The mechanical rock properties and in-situ stresses required for these models are obtained from an extensive high-resolution subsurface dataset including three closely-spaced wells. Microseismic and pressure interference data are available to calibrate and constrain the models. These geomechanical models provide a means for capturing inter-well-scale mechanical discontinuities in the absence of well production data.

5.2. Geological setting

The Vaca Muerta Fm. is a calcareous shale deposited the Neuquén basin in Argentina (northern Patagonia; Figure 5.2a). Basin development started in the Triassic and Early Jurassic, related to first NE and later NW extension resulting from the break-up of Gondwana and the Atlantic opening, creating graben structures (Vergani *et al.*, 1995; Howell *et al.*, 2005). During the Mesozoic, the basin transformed into a back-arc basin behind a volcanic arc (Vergani *et al.*, 1995; Messager *et al.*, 2010). This was followed by compression from the west resulting from the Andean orogeny, which is still active today (Messager *et al.*, 2010).

The present-day stress is characterised by a horizontal σ_H striking N110, associated with the ongoing Andean compression. At reservoir depth in the study area, the overburden stress σ_v is slightly smaller than the horizontal maximum stress σ_H, such that $\sigma_H > \sigma_v > \sigma_h$. These stresses are accurately mapped using breakout data and induced tensile fractures for σ_H and leak-off tests and Instantaneous Shut-In Pressure (ISIP) measurements during hydraulic fracturing for the minimum horizontal stress σ_h. The Vaca Muerta Fm. is overpressured.

The basin is filled with up to 7000 m of predominantly Mesozoic strata (Rodrigues *et al.*, 2009). The Vaca Muerta Fm. is part of the lower Mendoza Group, deposited during a Late Jurassic-Early Cretaceous marine transgression (Figure 5.2b; Cobbold and Rossello, 2003). It is part of a series of transgressional cycles during post-rift thermal subsidence, where deposition of Kimmeridgian fluvial sands of the Tordillo Fm. was followed by the deposition of deep marine mudstones of the Vaca Muerta Fm. (Vergani *et al.*, 1995; Rodrigues *et al.*, 2009). We focus on the lowermost 200 m, representing the 'high-TOC' section with an average Total Organic Content (TOC) of 12%, whereas the shallower half of the Vaca Muerta Fm. has a TOC of less than 2% (Figure 5.2d).

We focus on an area in the south-western edge of the basin, north of the Huincul Arch, where the total thickness of the Vaca Muerta Fm. is 400 m, with 2400 m overburden (Figure 5.2b,c). Average matrix porosity is 8%, but there is no matrix permeability, resulting in no economical production from conventional wells. Within this area, we use data from two horizontal wells and a vertical well that are all in an area of 1.5×1.2 m. For this area, a 3-D Discrete Fracture Network (DFN) is constructed.

5.3. Regional natural fracturing

5.3.1. Fracture characterisation

Fractures in the Vaca Muerta Fm. are characterised using Formation MicroImaging (FMI) data of the two horizontal wells and one vertical well and core data for the vertical well, supplemented by outcrop analogues (Rodrigues *et al.*, 2009). The resolution of FMI data is relatively low and suffers from a range of artefacts such as drilling-induced fractures. The section of the vertical well for which both FMI and core data are available shows that FMI under-samples fracture intensity, as the smallest fractures are missed. To correct for the under-sampling, an intensity multiplier is derived from the sections of FMI for which cores are avail-

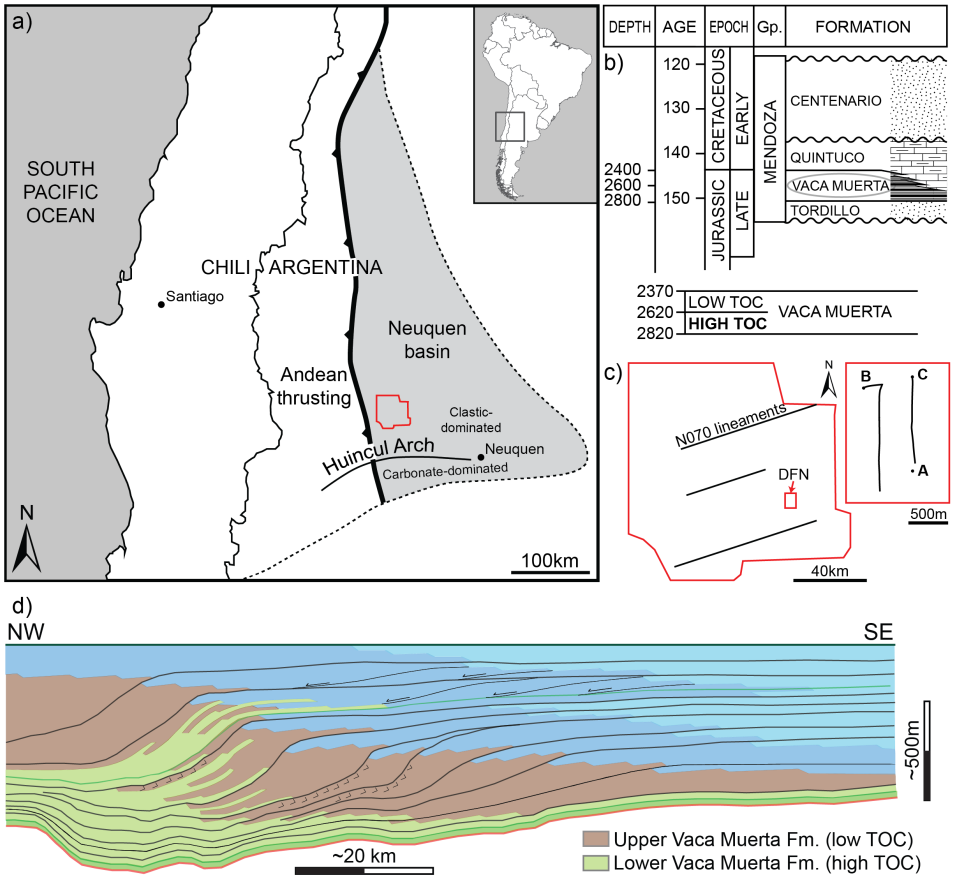


Figure 5.2: Regional setting of the Neuquén basin: a) Location of the area of interest in the west of the Neuquén basin, in an area dominated by clastic facies. Adapted from Vergani *et al.* (1995); Witte *et al.* (2012); Branellec *et al.* (2015); b) Stratigraphic chart focusing on the Mendoza Group, adapted from Vergani *et al.* (1995); Cobbold and Rossello (2003); c) Detail of the block of interest, showing several large-scale N070 shear zones mapped from seismic, and an inset with the wells of interest. The area of the DFN is far from the shown shear zones; d) NW-SE cross-section showing the thickness of the Vaca Muerta, adapted from Pose *et al.* (2014).

able, and applied to the FMI data where no core data is available (Total Austral S.A., 2015).

Four sets of subvertical natural fractures are identified, striking N010, N070, N110 and N140, with a scatter of 30–40° in each set (Figure 5.3; Total Austral S.A., 2015). These clusters are identified using in-house statistical clustering software. Low-angle features in this distribution are bedding-parallel calcite layers and small faults. Average fracture intensity (P_{10}) at the landing depth of the wells of interest is 0.28 m^{-1}, but intensity can be up to 1 m^{-1} for some intervals (Figure 5.4). Vertically, fracture intensity decreases with increasing depth and TOC (Total Austral S.A.,

2015). The higher-intensity zones are interpreted as fracture corridors.

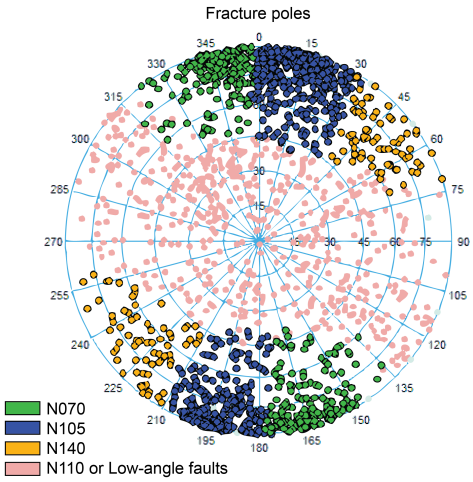


Figure 5.3: Lower hemishpere stereoplot showing the poles of all fractures measured using FMI (horizontal and vertical wells).

Fracture length cannot be obtained from subsurface data, and no outcrop analogue with quantitative data is available for this study. Qualitative observations from outcrops along the western edge of the basin indicate that fracture sets are mutually crosscutting, forming highly connected networks (Figure 5.5). However, these outcrops are in a slightly folded domain on the western edge of the basin and fracture orientations only partly match those observed in wells, as the outcrops show two orthogonal sets striking N-S and E-W, instead of the three families with smaller angles observed in the subsurface. For the subsurface, we assume that fractures are mutually cross-cutting with lengths following power-law distributions. This type of distribution is common for regional diffuse fractures in a homogeneous lithology with no nearby large-scale folds or faults (e.g. Anders *et al.*, 2014). Maximum fracture length is 200 m, inferred from seismic attribute maps. Height is not considered, as we focus on 2-D models of fracture length.

5.3.2. Fracture infill

Core data indicates that 14% of the bed-perpendicular fractures are open and filled with traces of bitumen. Another 20% are partly cemented and the remaining 66% are closed, either because fractures are fully cemented or fracture walls are interlocking with no remaining pore space. As the cores are not oriented and contain only a relatively small number of features, no distinction can be made as to whether different orientation sets have different infill.

In addition to bed-perpendicular fractures, cores and outcrops indicate a system of bedding-parallel veins (beef; Rodrigues *et al.*, 2009) throughout the entire interval of the Vaca Muerta Fm., with intensities ranging from 1–6 veins per meter. The intensity decreases in the shallower carbonate-rich sequences, but here beef is

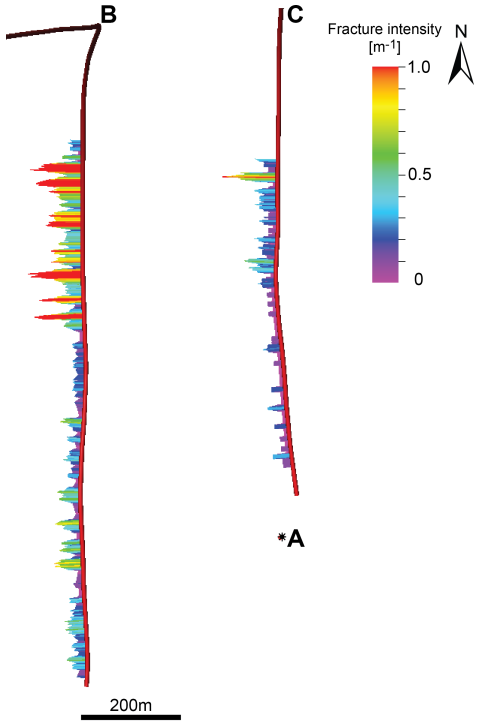


Figure 5.4: Fracture intensity logs for the two horizontal wells, derived from FMI and corrected for the mismatch between core and FMI observed in the vertical well.

thicker (i.e. more than 10 cm), whereas in the deeper higher-intensity parts beef is less than a cm thick. Outcrop studies indicate that beef may be laterally continuous over more than 100 m, and a length-to-thickness ratio of 20:1 is observed (Rodrigues *et al.*, 2009). The beef contains traces of bitumen in the centre and calcite growing from the fracture walls (Figure 5.6).

5.3.3. Fracturing synthesis

Based on the intersection angles, the N070 and N140 sets are interpreted as a conjugate system with a bisector striking N105, which is sub-parallel to σ_H. The N110 set is interpreted to consist of joints striking parallel to σ_H. The conjugate fractures were formed in conditions similar to the present-day stress field, with a horizontal σ_1. The joints were formed under similar stress conditions or under a vertical maximum principle stress, which could have been the stress field prior to or at the early onset of the E-W horizontal shortening related to the Andean compression.

The N010 set has a lower intensity than the other sets, and its orientation does not correspond to any known present-day or paleostress field. An outcrop study along the edge of the basin has found four fracture sets with similar orientations,



Figure 5.5: Outcrop of the Vaca Muerta Fm. on the western edge of the basin, showing two mutually cross-cutting sets of natural fractures. Courtesy of S. Estrada.

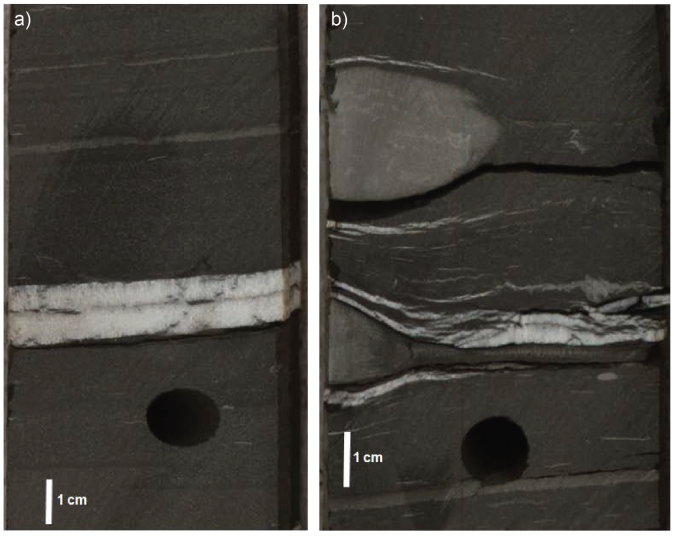


Figure 5.6: Core photographs from well A of bedding-parallel calcite features: a) Cm-thick beef layer with bitumen traces in the centre; b) Thinner beef features filled with calcite and traces of bitumen.

including a N-S striking set (Branellec *et al.*, 2015). This set is interpreted as folding-related, but in our study area bedding measurements from wells indicate that the layers are sub-horizontal, and there are no indications of seismic-scale folding. The

other three sets, which correspond approximately to the N070, N110 and N140 sets, are related to regional Layer-Parallel Shortening (LPS). We do not include the N010 set in our models, as we cannot confirm whether these fractures are regional, and following Mohr-Coulomb this set is unlikely to be reactivated in the present-day stress field, even during hydraulic fracturing (Figure 5.3).

The beef features are sub-horizontal, indicating they were formed under low vertical stress. Generally, this requires shallow depths corresponding to early burial or high pore pressure related to kerogen production (Rodrigues *et al.*, 2009), although a discussion remains on the exact conditions under which beef can form (Gale *et al.*, 2014). Although absolute timing is not known, the beef is observed to have experienced at least two cementation phases (Rodrigues *et al.*, 2009).

On a larger scale, curvature maps derived from seismic indicate the presence of N070 striking strike-slip fault zones. These fault zones have a consistent spacing of approximately 5 km, but there is no fault zone present near or within the study area.

5.4. Stress-pore pressure modelling methodology

We use two types of 2-D FE models to model the change in pore pressure during hydraulic fracturing:

i) Horizontal models capturing lateral changes in pore pressure related to hydraulic fracturing and reactivation of natural fractures;
ii) Vertical sections along a vertical well to quantify the impact of beef and mechanical stratigraphy on pore pressure and hydraulic fracture growth.

Permeability of the reactivated natural fracture network is taken into account through geomechanical aperture and equivalent permeability models (Chapter 3). These models are based on a DFN of the regional natural fractures, from which we extract horizontal 2-D slices to capture the well-to-well permeability.

5.4.1. Horizontal 2-D fracture model construction

Based on the geometrical characterisation, a 3-D DFN has been constructed of the regional fractures (Figure 5.7). The DFN covers an area of 1.5×1.2 km, with a vertical thickness of 400 m, and includes the three wells from which fracture and stress data are derived: one vertical well (A) and two horizontal wells (B and C). Several N070 corridors were identified based on high fracture intensity in image logs, which are represented in the DFN as zones with a high density of regional fractures.

From the 3-D DFN, we extract a horizontal 600×600 m slice that captures fracture lengths in 2-D at the landing depth of wells B and C, at a depth of 2744 m (Figure 5.7c). The 2-D model contains 680 fractures with an average P_{21} fracture intensity of $0.28\,\mathrm{m}^{-1}$ (Figure 5.7c). The spatial distribution of the DFN is modelled stochastically, which creates variability in the network geometry. However, as the orientation and size distributions are constant and network intensity and connectivity are high, different realizations have no significant impact on the flow potential of the model.

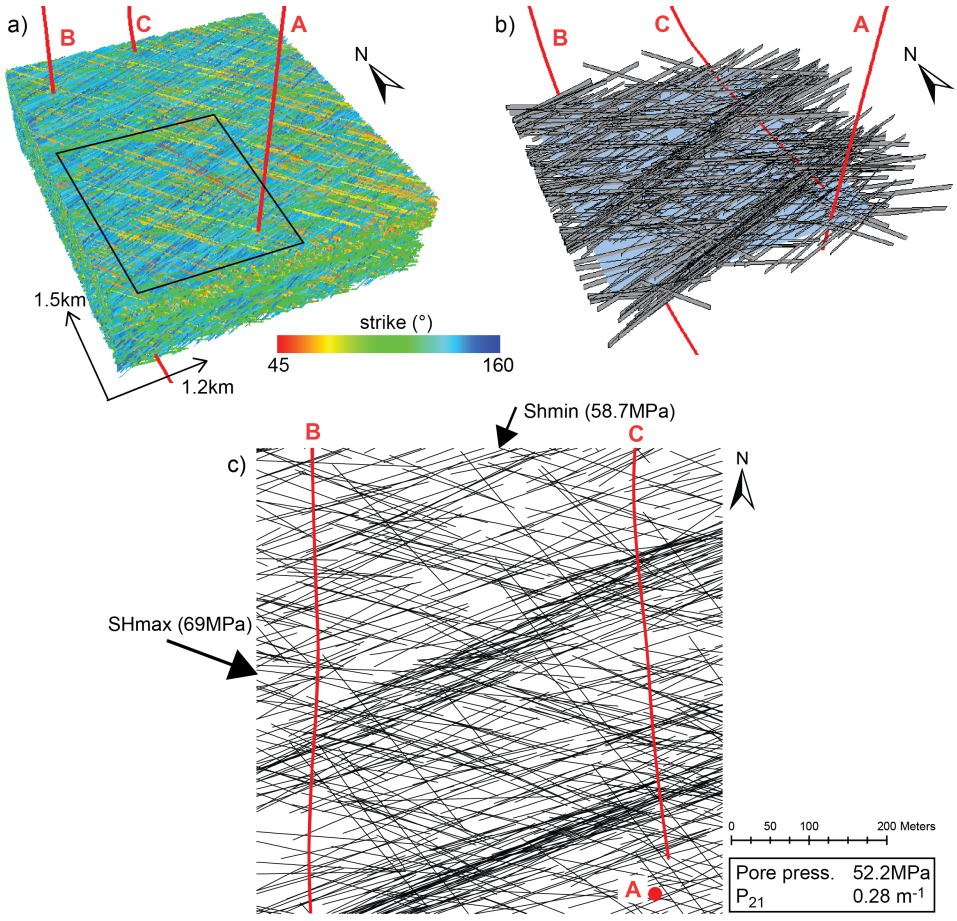


Figure 5.7: Extrapolation of a representative 2-D fracture pattern from the 3-D DFN: a) The DFN constructed around wells A, B and C, confined to a volume of 1.5 × 1.2 × 0.4 km; b) A 600 × 600 m surface positioned at the landing depth of wells B and C, with all fractures that intersect this surface; c) Top view of the 2-D surface with all intersecting fracture segments.

Stress-pore pressure model set-up

We use ABAQUS CAE® (Dassault Systèmes®) to mesh the fracture model (Chapter 3) and to solve the coupled stress-pore pressure response of the model. This code includes a *Damaged Plasticity* model, which is similar to an elastoplastic rheology, but in addition it models the breakdown of the rock in the plastic domain, i.e. implicit fracturing of the rock, where porosity increases with increasing damage. Although the method is designed for modelling of concrete failure, it has been used successfully to represent rocks failing as a result of hydraulic fracturing (Smart *et al.*, 2014).

The elastic component of the model is represented using a Poisson's ratio and Young's modulus measured using scratch tests in the vertical well. For the horizon-

tal 2-D model, we use a Poisson's ratio of 0.2 (Poisson's ratio), a Young's modulus of 25 GPa and a rock density of 2380 kgm^{-3}. For vertical models representing the mechanical stratigraphy, we use the log measurements from the vertical well. For the plastic domain, values of a stiff rock are obtained from Smart *et al.* (2014), as no direct measurements are available.

The coupled pore fluid diffusion/stress analysis procedure in ABAQUS is used to model single-phase fully or partly saturated flow through porous media (Dassault Systemes, 2013). This method considers transient or steady-state conditions that are either linear or non-linear. For the horizontal 2-D models, we consider fully saturated flow with a combination of transient and steady-state modelling steps. The transient step considers time-dependent changes in stress and pore pressure, and is used to simulate the injection stages. After each injection stage, the pore pressure distribution is allowed to reach an equilibrium using a steady-state step, where equilibrium is reached when the change in pore pressure in all elements is less than a defined tolerance value.

The in-situ stresses measured in well A are used as boundary conditions. As the model is 2-D, only the horizontal differential stress is considered, i.e. overburden stress is not included. The rock matrix has an average porosity of 8% and no initial permeability. Permeability is defined as conductivity, assuming that the rock is fully saturated with water with a density of 1000 kgm^{-3}. The in-situ pore pressure is assigned to the matrix, creating an effective stress of 16.8 MPa in the direction of σ_H and 6.5 MPa in the direction of σ_h (Figure 5.7c).

Hydraulic fracturing set-up

The two horizontal wells were hydraulically fractured, with 29 perforations in well B, divided into ten stages, and 20 perforations in well C, divided into five stages (Figure 5.8). The stages are regularly spaced along the wells. The average pumping time is six hours for each stage, with varying average pumping pressures (Figure 5.8). Each stage is modelled by increasing the fluid pressure at the location of the perforation using the transient modelling steps.

The simulated injected fluid is water, without gels or proppants, as our aim is to quantify to what extent the injected fluids increase the pore pressure and reactivate natural fractures. We quantify the potential impact of the reactivated natural fractures on flow, but we do not predict the absolute change in permeability related to hydraulic fracturing, which depends on the combined induced and natural fracture network that remains open because of the proppants once the injected fluids have been recovered (Novotny, 1977).

During a pumping phase, the absolute pore pressure is increased locally, at the point of injection, and with increasing time the spread in elevated pore pressure expands laterally, away from the injection point. The absolute and lateral increases are functions of injection pressure and matrix permeability. However, for an impermeable matrix, pore pressure increases only at the injection point, as the injected fluids cannot spread through the matrix, similar to what is observed in the drilled wells before hydraulic fracturing.

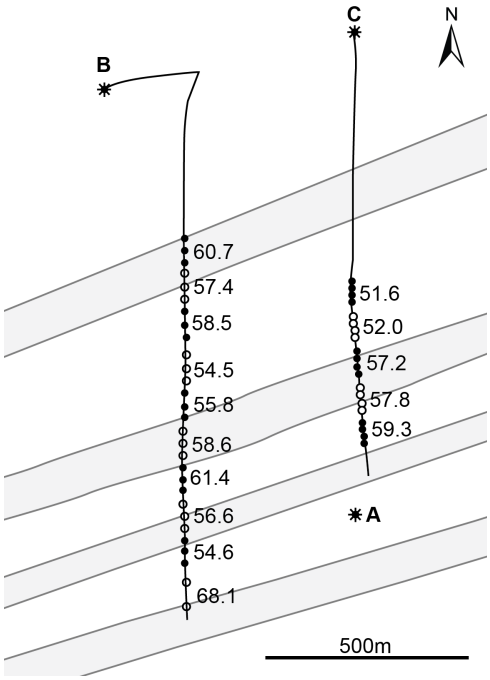


Figure 5.8: Map view of the trajectories of the two horizontal wells, with the locations of all hydraulic fractures placed in each well. The alternating white and black points indicate the different stages in which multiple hydraulic fractures are created. The average injection pressures used during each pumping stage is listed next to each stage. The light grey areas indicate the zones in which fracture corridors have been observed from image logs.

5.4.2. Vertical 2-D modelling

To quantify the role of beef on induced fracture growth we model the pore pressure change in a vertical section of rock intersecting vertical well A. The section is 200 m wide, 20 m high and located at the depth of the landing zone of the horizontal wells.

The depth interval of interest contains a number of beef layers and ash beds. The ash beds are up to 20 cm thick layers with a larger stiffness than the calcareous shale 'matrix'. The corresponding mechanical properties are also derived from the log data. Core analysis indicates that the interfaces in between adjacent shale layers are strong, as the core is generally intact along these interfaces and often the contacts are formed by a gradual change, increasing the mechanical bond. The core is however typically broken along the beef interfaces, which form a sharp contact with the surrounding rock. The calcite infill of the beef forms a low-friction surface. The beef interfaces are therefore modelled as nearly frictionless contacts, whereas the other interfaces have a high friction coefficient. To capture the vertical variations in mechanical properties, we use a non-uniform high-resolution layering in which individual ash beds and beef features with distinct mechanical properties

can be accurately represented. A lower resolution can result in over-estimation of the lateral change in pore pressure (Figure 5.9).

Accurate measurements of the overburden stress and the horizontal stress ratios are available from well data, and applied as gradients from the top to the bottom of the vertical interval. The rock matrix has a homogeneous low conductivity. The hydraulic fracturing process is simulated by injecting water at the injection points of well A using the actual injection pressures and durations.

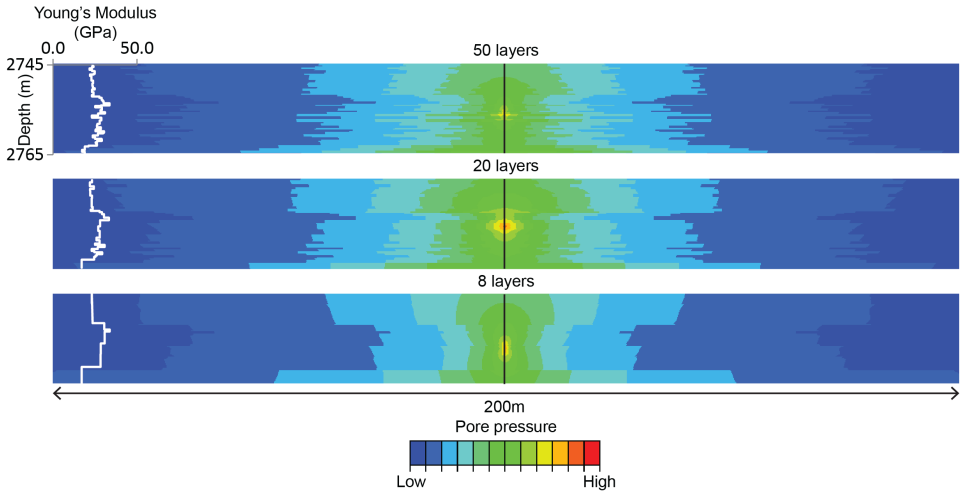


Figure 5.9: Geomechanical model of a 20 m thick vertical section along a vertical well with a single fluid injection point. We use three different resolutions for the mechanical layering of a single section. The highest resolution model (top) fully captures the heterogeneity observed in the mechanical logs (the Young's modulus is shown to illustrate this). The lower-resolution models (middle and bottom) are based on averaged log properties. The lowest resolution model over-estimates the lateral spread in elevated pore pressure.

5.5. Equivalent permeability of reactivated fractures

The equivalent permeability of the regional fracture network after reactivation is quantified using the meshing and geomechanical modelling approach from Chapter 3 (Figure 5.10a). The 2-D horizontal fracture model presented in the previous section provides fracture geometry, and the rock properties and stress boundary conditions are derived from well data. During hydraulic fracturing, the pore pressure near wells increases to 61 MPa. At this pressure, partial reactivation of natural fractures is assumed, based on a post-stimulation permeability that is higher than what is expected from the contribution of hydraulic fractures.

To identify which natural fractures are reactivated at these elevated pore pressure conditions and what their contribution to permeability is, we model stress-dependent aperture and equivalent permeability using the Barton-Bandis workflow (Chapter 3). This approach has been successfully applied to other shale studies (Dusseault, 2013; Barton, 2014). The aperture in this model is predominately

a function of stresses at the boundaries, which are obtained from wells, and the fracture roughness profile, which we estimate from veins and fractures in core and limited thin sections. Most fractures have a high roughness (i.e. $JRC = 15$), resulting in an initial unstressed aperture of 0.3 mm.

To consider the impact of cement, we apply the ratios of partly and fully cemented and open fractures observed in cores to the aperture models to close part of the network. For in-situ stress conditions before hydraulic fracturing, the modelled aperture is less than 0.05 mm on average. When applying the cement ratios, there is no flow through the model, which corresponds to the observed lack of production from wells prior to hydraulic fracturing. Under elevated pore pressure conditions, average aperture increases to 0.1 mm (Figure 5.10b).

Using the workflow based on CSMP++ (Chapter 3), we model the equivalent permeability through the natural fracture network, using the modelled aperture distribution. The resulting equivalent permeability is up to 40 mD in the N070 striking corridors (Figure 5.10c). Permeability is anisotropic, with 7 mD in the E-W direction (outside corridors) compared to 0.5 mD in the N-S direction. This anisotropy is the combined effect of the fracture orientation, which is between N070 and N140, and the N110 direction of σ_H, as the Barton-Bandis aperture model predicts the highest apertures in the direction sub-parallel to σ_H (Chapter 3 and Appendix B).

This approach gives an indication of the equivalent permeability of the reactivated natural fracture network. The equivalent permeability is used to capture the change in permeability in the hydraulic fracturing models, where after each fracturing stage, the pore pressure distribution is used to determine in which areas the in-situ permeability should be updated to match the reactivated fracture network permeability.

5.6. Impact of hydraulic fracturing strategy on SRV

Based on the equivalent permeability of natural fractures as a function of elevated pore pressure and the hydraulic fracturing parameters, we simulate the change in SRV during hydraulic fracturing to understand the impact of natural fractures and corridors on the SRV distribution. We calibrate this model using microseismic and pressure interference data. This will subsequently allow us to optimise the hydraulic fracturing strategy, by varying parameters such as well spacing or injection pressure and quantify the resulting SRV distribution.

5.6.1. Base case model

The base case model uses the real injection pressures and times, with six-hour injection periods followed by a time of shut-in (Figure 5.8). Diffuse fracture and corridor permeabilities are derived from the equivalent permeability models (Figure 5.10c). We model the change in pore pressure in the reservoir around wells B and C, honouring the original injection strategy regarding hydraulic fracture position and the order of fracturing.

The resulting elevated pore pressure profile is anisotropic, with the largest in-

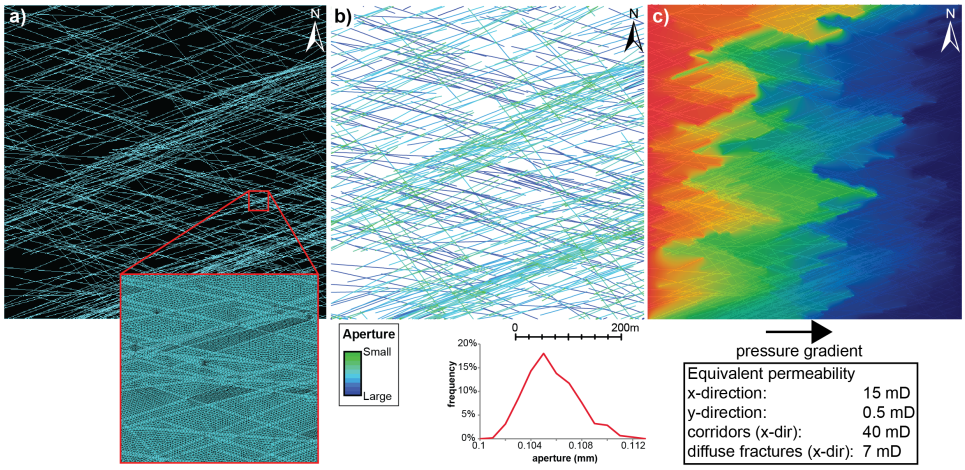


Figure 5.10: Workflow for quantifying fracture aperture and equivalent permeability for a constant far-field stress and a constant pore pressure: a) Meshing the 600 × 600 m fracture network to represent the fractures explicitly as 1-D line elements in a 2-D unstructured mesh. The inset shows a detailed view of the mesh in a 50 × 50 m section; b) Aperture distribution modelled using the Barton-Bandis method, with a histogram of the entire distribution; c) Resulting fluid pressure distribution for an E-W pressure gradient, with the resulting equivalent permeabilities listed below.

crease parallel to σ_H (Figure 5.11). The N070 striking corridors included in the model introduce more anisotropy into the system, as injected fluids move at higher velocity through these higher-permeability zones. The increase of in-situ pore pressure is largest in a small zone around the wells, with an increase of up to 5 MPa for one stimulated well (Figure 5.11a) and 8 MPa when stimulating both wells (Figure 5.11b). Quantifying the lateral extent of the area with an increased pore pressure provides a better understanding of the SRV, although it is not a direct proxy. The area with perturbed pore pressure in Figure 5.11b exceeds 1.5 × 2.5 km, but the area in which pore pressure is high enough to reactivate part of the natural fracture network is less than 600 × 600 m.

The increase in pore pressure in different parts of the reservoir can be quantified as a function of injection time and distance from each well. A pressure-time plot for different locations near the wells shows that pressures vary strongly depending on the distance to the wells and the permeability anisotropy created by the natural fractures and corridors (Figure 5.12). The dashed and solid grey trends are both measured 200 m east of well C, but one point is aligned with the N110 stress direction, resulting in a pore pressure that is 2.5 MPa higher compared to the other location. Figures 5.11 and 5.12 illustrate the two components that we use to quantify the SRV, which are the change in pore pressure at given locations and the area in which in-situ pore pressure is elevated. Using these two parameters, the impact on well placement and hydraulic fracturing strategy can be quantified.

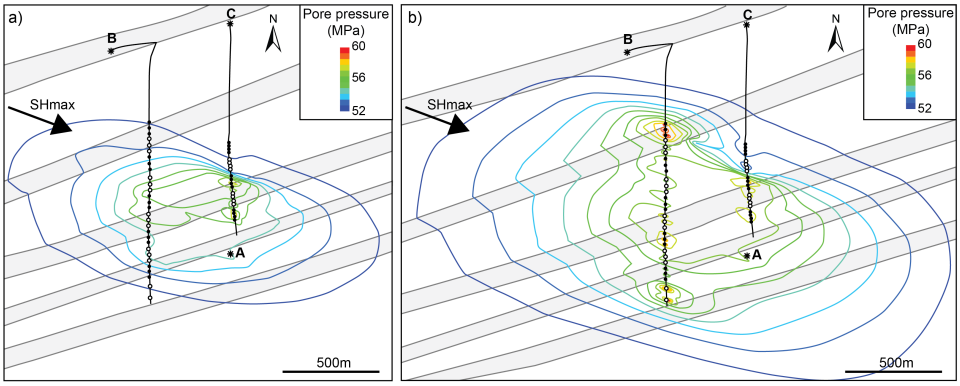


Figure 5.11: Map view of the pore pressure contour lines showing the area in which the pore pressure is elevated as a result of hydraulic fracturing (i.e. the SRV), with the three wells as reference. The grey areas are natural fracture corridors which act as higher-permeability zones; a) Elevated pore pressure after five fracturing stages in well C; Pore pressure after hydraulic fracturing in wells B and C. In both models the SRV is oriented along the σ_H direction (N110).

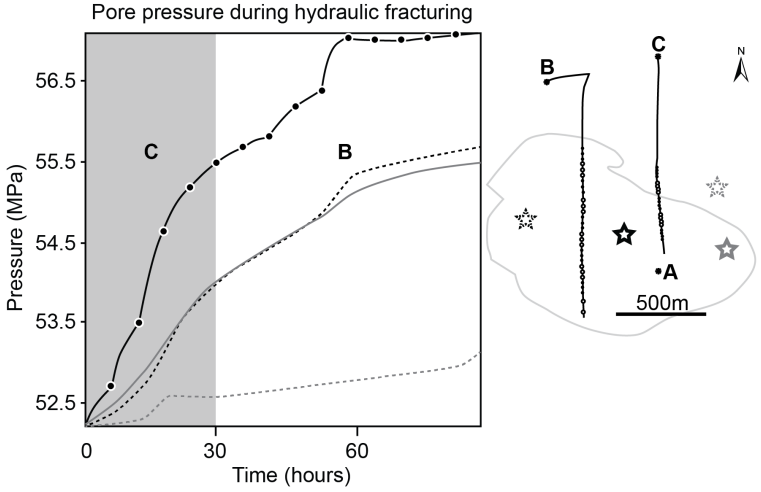


Figure 5.12: Change in pore pressure as a function of time, measured in four locations in between and around horizontal wells B and C. Hydraulic fracturing starts in C, with five stages that each last six hours, followed by ten stages in well B. The start of each stage is indicated by the black points along the black curve. The map view shows the location of each pressure curve. For reference, the 55 MPa contour from Figure 5.11b is shown.

5.6.2. Model calibration

The base case model is based on the actual completion strategy (i.e. injection locations, times and pressures), but the reactivated natural fracture permeability is based on a DFN constructed from limited well data, with an estimated length distribution. To constrain the uncertainties associated with the natural fracture

network in between the wells, we use microseismic and pressure interference data.

Microseismic was acquired using downhole and surface receivers in nearby wells during pumping and provides the direction of hydraulic fracture growth and zones where shear reactivation occurs, either along the natural fracture surfaces or along bedding planes (Warpinski *et al.*, 2013). Downhole pressure gauges monitor pressure communication, and hence connectivity, between wells during hydraulic fracturing.

Microseismic indicates a fracture half-length of 200–280m (Figure 5.13a). The spatial alignment of the microseismic events corresponds to the regional σ_H direction, as well as the average natural fracture strike. Microseismic events for each pumping stage have a similar spatial distribution and size, indicating that the length of different hydraulic fractures is relatively homogeneous. However, pressure interference is only observed in well A but not in well C, even though this horizontal well is at the same landing depth as B, with the same 400 m spacing as between A and B (Figure 5.13b). This indicates that hydraulic fracture growth and natural fracture reactivation are heterogeneous, even within this small pilot area. The hydraulic fracturing stages in well B have approximately constant injection times and pressures, so hydraulic fracture growth is assumed to be constant along this well. The hydraulic fracturing strategy was designed to create fractures with a half-length of 220–280m, which corresponds to the observations from microseismic and the lack of pressure interference in well C.

The interference in well A is thus not explained by hydraulic fracture growth, but more likely related to natural fracture reactivation. Several fracture corridors have been interpreted based on density trends in FMI, which are correlated across the three wells (Figure 5.8). Although there is no corridor in well A, this well is in between two corridors that are interpreted to extend to well B. The lack of connectivity between wells B and C suggests heterogeneous reactivation of corridors, where these corridors have a lower density and subsequent inter-well connectivity than the corridors near well A. Log data indicates that intensity is lower in the northern corridors compared to the corridors near well A. We therefore double the equivalent permeability in the corridor connecting wells B and A. This difference in permeability better captures the observed pressure interference trends (Figure 5.13c).

5.6.3. Impact of fracturing strategy on SRV

The impact of changing hydraulic fracturing parameters on the SRV is quantified using the pressure increase, measured in between the two horizontal wells, and the lateral extent of the SRV (Figure 5.14). The considered parameters are the injection times, the number of hydraulic fractures per stage and spacing between the wells. These parameters are important variables for optimising the SRV, and are strongly dependent on the mechanical properties of the rock. Strategies that produce best results in other basins therefore do not necessarily apply to the Vaca Muerta shales. The geometry of the natural fracture network is a large uncertainty in these models, as fracture length and connectivity is unknown. However, the base case model shows that the corridors have a controlling impact on flow, whereas

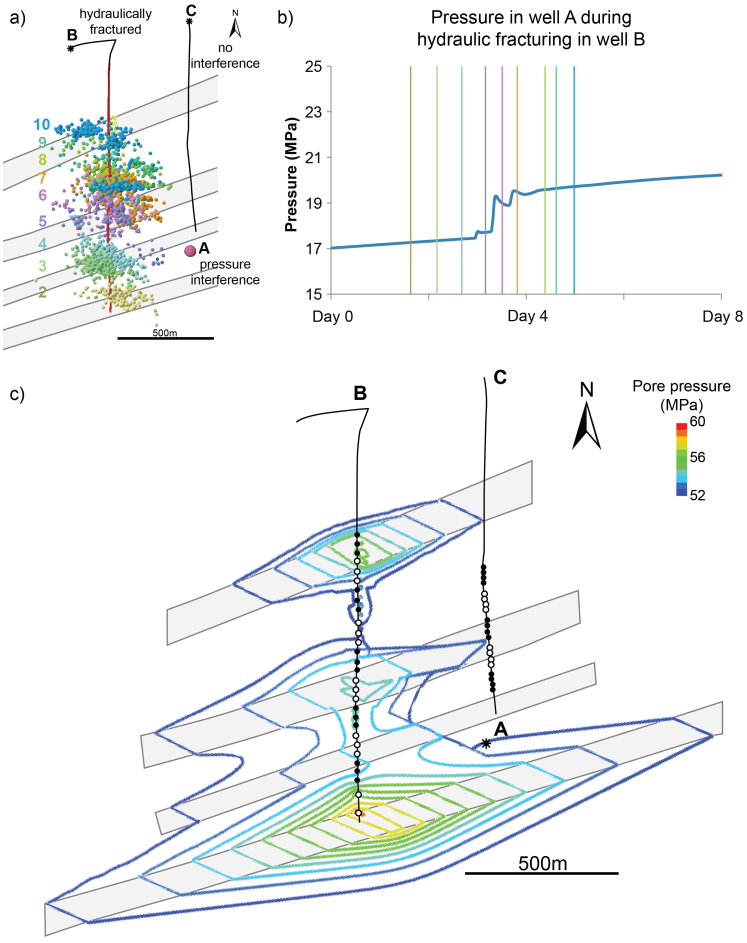


Figure 5.13: Calibration of the reactivated equivalent permeability model, using microseismic and pressure interference: a) Microseismic events corresponding to each fracturing stage in well B, showing a fracture half-length of 200 m; b) Pressure interference observed in well C during the 5th stage. Coloured bars indicate the start of each stage, where the colour corresponds to the event colours in (a); c) Pore pressure distribution after hydraulic fracturing in well B, showing an elevated pore pressure around well A but not in C.

the diffuse fractures have a relatively small impact. Without representative outcrop analogues, we cannot decrease the uncertainties associated with network geometry, but since the base case model is calibrated to microseismic and pressure interference data, we assume the network geometry is representative.

Decreasing the injection time for each stage from six to three hours does not change the pore pressure in between the wells, as in both models the increase in pore pressure is 4.8 MPa (Figure 5.14a). With shorter pumping times, the 4.8 MPa pressure increase is achieved faster. However, the 50% decrease in pumping time

also decreases the pumped volumes by 50%, as it is assumed that injection rates are always at a maximum. This results in an approximately 50% decrease in the lateral extent of the SRV (Figure 5.14b).

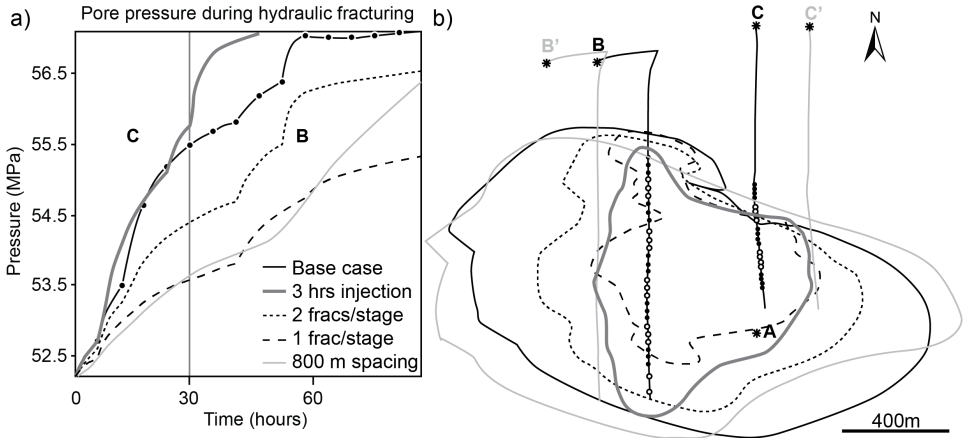


Figure 5.14: Change in pressure and distribution of the SRV as a function of different fracturing strategies: the original strategy (solid black) is compared to 50% shorter injection times ("3 hrs injection", a decreased number of perforations per stage ("2 fracs/stage" and "1 frac/stage") and larger well spacing (800 m instead of 400 m). The results are quantified by: a) Pore pressure, measured in between the two wells, as a function of time; b) Distribution of the SRV, quantified by plotting the 55 MPa contour. The grey well trajectories of wells B and C show the locations of the wells for the 800 m well spacing model.

In the base case model, the number of perforations per stage is three in well B and four in well C, with a stage spacing of 100 m and a perforation spacing of 25 m. This completion strategy is relatively costly, so we investigate the impact of decreasing the number of perforations on the SRV. The number of perforations is decreased first to two in well B and three in well C ("2 fracs/stage"; Figure 5.14) and then to one in well B and two in well C ("1 frac/stage"). The injection rates are the same as in the base case model, so the total volume of injected fluids decreases linearly with the number of perforations per stage.

Decreasing the number of perforations per stage by one results in a pressure increase of 4.3 MPa, compared to 4.8 MPa for the base case. This difference is relatively small, but the SRV does decrease with approximately 30% (Figure 5.14b). Decreasing the number of perforations further decreases the SRV, as well as the pressure increase in between both wells (2.9 MPa). Decreasing the perforations per stage by one leads to a relatively small decrease in pressure, but a further decrease significantly decreases not only the SRV but also the absolute pressure in between wells.

Third, the spacing between wells is considered. The base case model has a well spacing of 400 m, which results in reasonable communication between the wells, as microseismic indicates an hydraulic fracture half-length of 220–280m. This half-length is predominantly a function of the injected volume, which is constant for most simulations except when we change the injection time. For 800 m spacing, the

increase in pore pressure in between wells is 4 MPa, compared to 4.8 MPa for 400m well spacing, but the lateral extent of the SRV is larger (Figure 5.14). Moreover, the pressure increase for the 400 m case is decreasing before the end of the injection phase of the second well, but for the 800 m case the pressure is still increasing. Extending the injection time for the 800 m scenario can increase the maximum pore pressure and the extent of the SRV, provided that fracture corridor length exceeds well spacing.

5.7. Impact of mechanical stratigraphy

Microseismic indicates variations in induced fracture height, which is likely related to the presence of beef, which forms the main mechanical discontinuity in an otherwise relatively homogeneous lithology. We quantify the role of beef on hydraulic fracture growth and permeability using FE models of vertical sections of rock along the vertical well.

5.7.1. Vertical pore pressure distribution

To model the role of beef during hydraulic fracturing, we use a 2-D model of a vertical section intersecting vertical well A (Figure 5.15). The section is 30 m thick, with a 0.2 m thick horizontal beef layer in the middle. Fluids are injected via a single point 2 m below the beef layer. The rock properties of this section are derived from log data. To quantify the difference in pressure resulting from beef, we compare a vertical section with and without beef (Figure 5.15a-b).

In a model with no beef, injection of fluids results in a radial increase in pore pressure (Figure 5.15a). Although gravity and overburden stress are included, they have a relatively small impact as in-situ permeability is low. When pumping fluids near a beef layer, the pore pressure distribution changes significantly, as the beef acts as a partial barrier to flow (Figure 5.15b). The limiting impact of beef on fluid flow is a function of the friction coefficient, as a low coefficient results in slip along the interface between beef and rock. Increasing the friction coefficient decreases the mechanical contrast between rock and beef, creating a more homogeneous distribution of pore pressure, i.e. similar to the model without beef.

The beef features control the vertical spread of pumped fluids, and subsequently limit growth of hydraulic fractures, as fluid pressure is not sufficiently high to propagate hydraulic fractures through the beef. Simultaneously, the injected fluids may have a larger lateral spread in the direction of σ_H in thin shale layers confined by beef. The limited induced fracture height can thus translate in an extended fracture length. In addition, slip along beef can increase the aperture of hydraulic fractures, similar to what is observed with bedding-plane slip (Gu *et al.*, 2008). If a hydraulic fracture terminates against beef, the low friction coefficient allows the fracture walls to open more easily in the direction of σ_h (Figure 5.15). The limited vertical growth of hydraulic fractures that terminate against beef may thus be offset by increased length and aperture, increasing horizontal permeability.

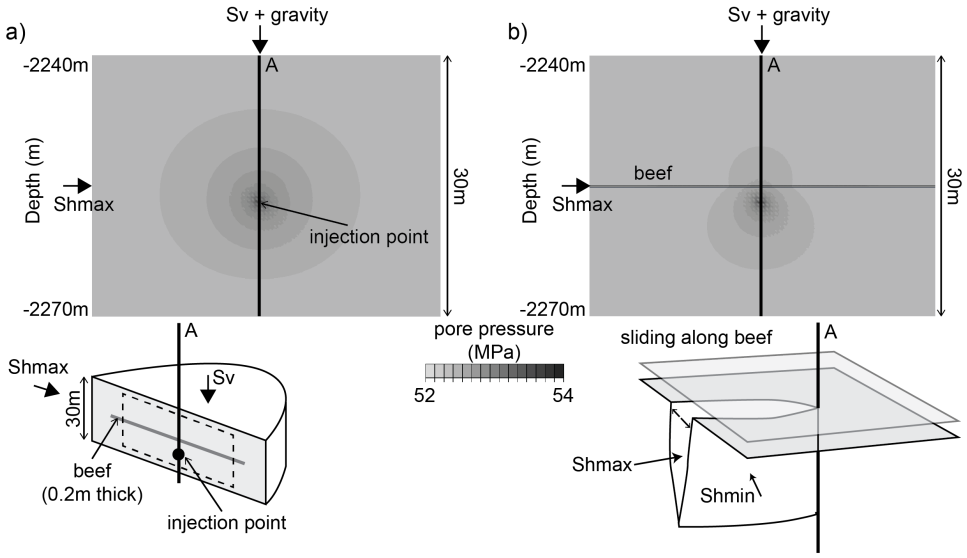


Figure 5.15: Pore pressure distribution in vertical sections of rock intersecting vertical well A. The rock section is 30 m high, with overburden stress and σ_H as far-field stresses and a constant pore pressure. Fluids are pumped into the reservoir through an injection point 2 m below the centre of the model. The 3-D sketch of the well illustrates the model set-up. After injection, the pore pressure distribution is compared for models with: a) a homogeneous rock; b) homogeneous rock with a 0.2 m thick layer of beef along the middle, with a low friction surface interaction between beef and rock. While this sliding surface limits vertical propagation of pumped fluids, it enhances local fracture aperture as illustrated in the 3-D sketch of a fracture opening along the well.

5.7.2. Reactivation of beef

Outcrops indicate that the horizontal extent of a beef layer may exceed 200 m (Rodrigues *et al.*, 2009). If beef is reactivated during hydraulic fracturing, it forms a horizontal flow pathway that potentially connects to a large system of natural fractures in the overlying and underlying beds.

As only the elastic properties of beef have been sampled, the stress conditions required for reactivating beef are unknown. However, a qualitative assessment can be made using available data. All beef sampled in the Vaca Muerta Fm. consists of calcite cement, which is relatively weak compared to the calcareous mudstones. Furthermore, the calcite could be dissolved by injecting acids into the reservoir, although the combination of acids and large volumes of clay may result in blockage of flow near the well. Although injecting acids in clay-rich formations typically results in a decrease in permeability, it may be an effective method in the more carbonate-rich shales of the Vaca Muerta Fm. (Garcia *et al.*, 2013; Wu and Sharma, 2015).

From a mechanical point of view, the vertical stress is the intermediate principle stress, whereas the minimum principle stress is horizontal. In a network of vertical fractures and horizontal beef, the vertical fractures will have a higher reactivation probability, since they open up in the direction of σ_h. Dissolving the calcite in beef

is therefore a more likely option compared to mechanically reactivating the beef.

5.7.3. Implications for 3-D

Gravity has no significant impact on the SRV in the 30 m thick vertical models. However, the Vaca Muerta Fm. is up to 400 m thick, and microseismic events related to some of the hydraulic fractures span a vertical thickness of up to 300 m. In these thicker intervals, gravity potentially has a larger impact. The role of gravity is also strongly dependent on the mechanical stratigraphy. Layers with a high intensity of beef may act as individual mechanical units that not only control hydraulic fracture growth but also gravitational effects. If beef indeed controls the mechanical stratigraphy, then the modelled SRV in 2-D models may be representative of the 3-D distribution within these layers, as the SRV is confined to a thin layer. However, when mechanical units reach a thickness of tens of meters, gravity flow may become more important, and the horizontal extent of the SRV decreases.

We study this effect by comparing the SRV in a 2-D model with two 3-D models with different mechanical unit thicknesses. The models have a single horizontal well with hydraulic fractures considering only permeability from background fractures. The 3-D models have a thickness of 400 m, with either no mechanical stratigraphy (i.e. a homogeneous low-permeability unit) or a series of 20 m thick layers confined by laterally continuous strong mechanical interfaces (Figure 5.16).

When the mechanical stratigraphy is homogeneous, the SRV is laterally limited in size, and there is a significant gravity effect. Alternatively, when there is no distinct mechanical stratigraphy, the lateral extent of the SRV in 3-D is similar to that of the 2-D models.

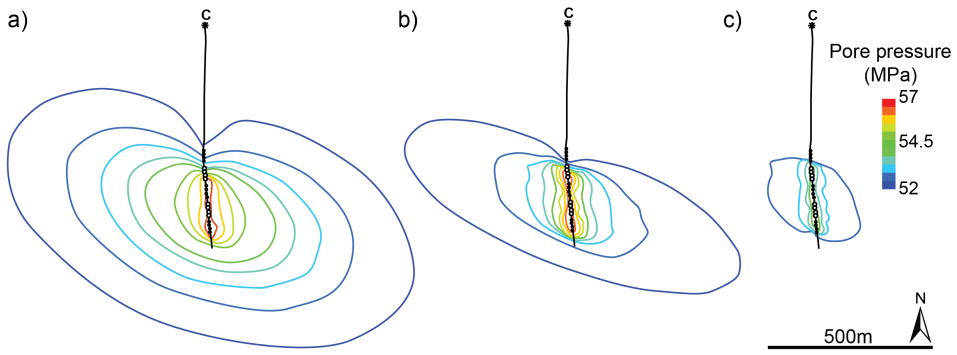


Figure 5.16: Horizontal pore pressure distribution in a 2-D model versus 3-D models, considering a simplified model with five fracturing stages in well C, in a homogeneous rock matrix (i.e. no corridors): a) 2-D model; b) 3-D model with a heterogeneous mechanical stratigraphy (i.e. low vertical permeability); c) 3-D model with no distinct mechanical stratigraphy (i.e. high vertical permeability).

5.8. Discussion

The horizontal and vertical stress-fluid pressure models indicate that natural heterogeneities impact the development of hydraulic fractures, as well as the

spread in elevated pore pressure during fracturing and the potential permeability after treatment. Taking into account natural fractures and corridors results in a more heterogeneous SRV, corresponding with observations from pressure interference and results from other studies of the Vaca Muerta Fm. (Garcia *et al.*, 2013; Padin *et al.*, 2014).

As this is a pilot project, the permeability after hydraulic fracturing has not been fully quantified. However, we provide an estimate by modelling to what extent the natural fracture network is reactivated when pore pressure is increased during hydraulic fracturing. The magnitude and anisotropy of the equivalent permeability models correspond to initial permeability measurements after hydraulic fracturing.

For the horizontal geomechanical models, we use the pore pressure as a proxy for the SRV, and optimise the hydraulic fracturing strategy based on the SRV. Pore pressure is indicative of where natural fractures are reactivated, but we cannot derive any absolute permeability or well productivity values from these models, as we do not consider proppants, so the aperture and permeability of the induced fractures is unknown. However, the Barton-Bandis aperture model that we use for the permeability of natural fractures considers that a small aperture (i.e. smaller than 0.3 mm) can remain, even if fractures are not critically stressed and no proppants are used. If natural fractures experience sufficient shear, asperities along the fracture walls can prevent the fractures from fully closing after the injected fluids are recovered (Barton, 2014; Tezuka, 2005).

All geomechanical models in this study are based on measured stresses and elastic properties (Young's modulus and Poisson's ratio), but we have no experimental data regarding the plastic behaviour of the Vaca Muerta Fm., which is likely to have a strong impact on the permeability evolution of the rock and natural fracture reactivation potential (e.g. Smart *et al.*, 2014; Stone and Zoback, 2011).

5.9. Conclusions

The Vaca Muerta Fm. in the Neuquén basin is a thick carbonate-rich shale with little large-scale deformation. Seismic indicates no major folding and the presence of limited strike-slip fault zones, with a spacing of several kilometres. The area of interest for this study is far from the strike-slip zones, and consists of up to 400 m of sub-horizontal shales.

Even though the Vaca Muerta Fm. has experienced little seismic-scale folding, active compression related to Andean thrusting has resulted in a regional system of bed-perpendicular background fractures. The natural fracture distribution is characterised using a rich dataset of FMI and cores. The bed-perpendicular fractures are organised in a joint set striking parallel to the regional σ_H of N110 with several higher-intensity corridors, and two conjugate sets striking N070 and N140. Even though the present-day minimum principle stress is horizontal, there is an abundance of bedding-parallel calcite fractures (beef), formed during burial.

The natural fractures and beef do not contribute to permeability at in-situ stress conditions. However, these features do have an impact on hydraulic fracturing and the SRV. Microseismic indicates that even along a single horizontal well, the height

of induced fractures varies. Pressure interference data from several wells furthermore indicates that natural fractures may be reactivated, albeit in a heterogeneous pattern.

We use 2-D geomechanical Finite Element models to quantify the role of regional fractures and beef on the horizontal SRV distribution and the vertical hydraulic fracture growth. In these models, regional stresses, mechanical stratigraphy and pore pressure variations are considered during the injection phases of the hydraulic fracturing process. These models use real well data and hydraulic fracturing parameters, and are calibrated to observations from microseismic and pressure interference. The models show that:

i) Although natural fractures do not contribute to flow at in-situ stress conditions, they are reactivated during hydraulic fracturing, increasing the SRV and permeability. Natural fracture orientation and stress anisotropy control the shape of the SRV.
ii) The area in which pore pressure is sufficiently increased for natural fracture reactivation is heterogeneous, and strongly controlled by fracture corridors. Along these corridors, the SRV may extend up to 400 m from the wells, based on pressure interference observations. However, in the background fracture network, pore pressure may only be high enough for fracture reactivation within a 50 m radius of the well.
iii) If shearing occurs during reactivation of natural fractures, the Barton-Bandis aperture model predicts that natural fractures can remain hydraulically open after hydraulic fracturing, even if no proppants are injected. Depending on fracture roughness, network connectivity and orientation, the equivalent permeability of the reactivated natural fracture network is between 0.5–15mD. In the natural fracture corridors, permeability may be two to five times higher. However, these findings strongly depend on the geometry and connectivity of the natural fracture network, for which no static data is available. Outcrop analogues are essential for decreasing these uncertainties.
iv) The bedding-parallel beef acts as a low-friction surface that limits vertical propagation of hydraulic fractures. However, sliding of fracture walls along the low-friction surface enhances hydraulic fracture aperture, and where vertical growth is limited, horizontal growth will be increased. Furthermore, if beef can be reactivated, it can act as a horizontal flow pathway.

References

R. Nelson, *Geologic Analysis of Naturally Fractured Reservoirs*, in *Geologic Analysis of Naturally Fractured Reservoirs* (Gulf Professional Publishing, Woburn, MA, USA, 2001) 2nd ed., pp. 101–124.

W. Ahr, *Geology of carbonate reservoirs: the identification, description and characterization of hydrocarbon reservoirs in carbonate rocks* (John Wiley & Sons, Inc., Hoboken, New Jersey, USA, 2008) p. 296.

C. A. Barton, M. D. Zoback, and D. Moos, *Fluid flow along potentially active faults in crystalline rock*, Geology **23**, 683 (1995).

S. F. Rogers, *Critical stress-related permeability in fractured rocks*, Geological Society, London, Special Publications **209**, 7 (2003).

G. Bertotti, S. de Graaf, K. Bisdom, H. Vonhof, J. Reijmer, F. Bezerra, and C. Cazarin, *Fracturing and flow during post-rift subsidence in carbonate rocks of the Jandaira Formation (NE Brazil)*, (subm).

P. R. Cobbold, A. Zanella, N. Rodrigues, and H. Løseth, *Bedding-parallel fibrous veins (beef and cone-in-cone): Worldwide occurrence and possible significance in terms of fluid overpressure, hydrocarbon generation and mineralization*, Marine and Petroleum Geology **43**, 1 (2013).

G. Sagasti, M. Foster, D. Hryb, A. Ortiz, and V. Lazzari, *Understanding Geological Heterogeneity to Customize Field Development: An Example from the Vaca Muerta Unconventional Play, Argentina*, in *Proceedings of the 2nd Unconventional Resources Technology Conference* (American Association of Petroleum Geologists, Tulsa, OK, USA, 2014).

A. Padin, A. N. Tutuncu, and S. Sonnenberg, *On the Mechanisms of Shale Microfracture Propagation*, in *SPE Hydraulic Fracturing Technology Conference*, February (Society of Petroleum Engineers, 2014) pp. 4–6.

M. N. Garcia, F. Sorenson, J. C. Bonapace, F. Motta, C. Bajuk, and H. Stockman, *Vaca Muerta Shale Reservoir Characterization and Description: The Starting Point for Development of a Shale Play with Very Good Possibilities for a Successful Project*, in *Unconventional Resources Technology Conference, Denver, Colorado, 12-14 August 2013* (Society of Petroleum Engineers, 2013).

D. Moos, G. Vassilellis, R. Cade, J. Franquet, A. Lacazette, E. Bourtembourg, and G. Daniel, *Predicting Shale Reservoir Response to Stimulation in the Upper Devonian of West Virginia*, in *SPE Annual Technical Conference and Exhibition* (Society of Petroleum Engineers, Denver, Colorado, 2011).

J. Osorio and M. Muzzio, *Correlation Between Microseismicity and Geomechanics Factors Affecting the Hydraulic Fracturing Performance in Unconventional ReservoirsA Field Case in Neuquén, Argentina*, in *47th US Rock Mechanics/Geomechanics Symposium* (American Rock Mechanics Association, San Francisco, California, 2013).

J. F. W. Gale, R. M. Reed, and J. Holder, *Natural fractures in the Barnett Shale and their importance for hydraulic fracture treatments*, AAPG Bulletin **91**, 603 (2007).

J. F. Gale, S. E. Laubach, J. E. Olson, P. Eichhuble, and A. Fall, *Natural Fractures in shale: A review and new observations*, AAPG Bulletin **98**, 2165 (2014).

M. Gasparrini, W. Sassi, and J. F. W. Gale, *Natural sealed fractures in mudrocks: A case study tied to burial history from the Barnett Shale, Fort Worth Basin, Texas, USA*, Marine and Petroleum Geology **55**, 122 (2014).

K. J. Smart, G. I. Ofoegbu, A. P. Morris, R. N. McGinnis, and D. A. Ferrill, *Geomechanical modeling of hydraulic fracturing: Why mechanical stratigraphy, stress state, and pre-existing structure matter*, AAPG Bulletin **98**, 2237 (2014).

X. Weng, C.-E. Cohen, and O. Kresse, *Impact of Preexisting Natural Fractures on Hydraulic Fracture Simulation*, in *Unconventional Oil and Gas Resources Handbook* (Elsevier Inc., 2016) Chap. 10, pp. 289–331.

M. K. Fisher and N. R. Warpinski, *Hydraulic-Fracture-Height Growth: Real Data*, SPE Production & Operations **27**, 8 (2012).

N. Rodrigues, P. R. Cobbold, H. Loseth, and G. Ruffet, *Widespread bedding-parallel veins of fibrous calcite ('beef') in a mature source rock (Vaca Muerta Fm, Neuquen Basin, Argentina): evidence for overpressure and horizontal compression*, Journal of the Geological Society **166**, 695 (2009).

G. D. Vergani, A. J. Tankard, H. J. Belotti, and H. J. Welsink, *Tectonic Evolution and Paleogeography of the Neuquén Basin, Argentina*, in *Petroleum basins of South America: AAPG Memoir 62*, edited by A. J. Tankard, R. Suarez, and H. J. Welsink (1995) pp. 383–402.

J. A. Howell, E. Schwarz, L. A. Spalletti, and G. D. Veiga, *The Neuquen Basin: an overview*, Geological Society, London, Special Publications **252**, 1 (2005).

G. Messager, B. Nivière, J. Martinod, P. Lacan, and J.-P. Xavier, *Geomorphic evidence for Plio-Quaternary compression in the Andean foothills of the southern Neuquén Basin, Argentina*, Tectonics **29** (2010), 10.1029/2009TC002609.

J. Witte, M. Bonora, C. Carbone, and O. Oncken, *Fracture evolution in oil-producing sills of the Rio Grande Valley, northern Neuquén Basin, Argentina*, AAPG Bulletin **96**, 1253 (2012).

M. Branellec, J. P. Callot, B. Nivière, and J. C. Ringenbach, *The fracture network, a proxy for mesoscale deformation: Constraints on layer parallel shortening history from the Malargüe fold and thrust belt, Argentina*, Tectonics **34**, 623 (2015).

P. Cobbold and E. Rossello, *Aptian to recent compressional deformation, foothills of the Neuquén Basin, Argentina*, Marine and Petroleum Geology **20**, 429 (2003).

F. Pose, A. Gangui, and S. Galeazzi, *Estratigrafia secuencial del sistema Quintuco-Vaca Muerta en el engolfamiento neuquino, Cuenca Neuquina, argentina*, in *IX Congreso de Exploraci{ó}n y Desarrollo de Hidrocarburos IAPG, Mendoza, Argentina* (2014).

Total Austral S.A., *DFN model documentation - internal report*, Tech. Rep. (2015).

M. H. Anders, S. E. Laubach, and C. H. Scholz, *Microfractures: A review*, Journal of Structural Geology **69**, 377 (2014).

Dassault Systemes, *ABAQUS v6.13 documentation*, (2013).

E. Novotny, *Proppant Transport*, in *SPE Annual Fall Technical Conference and Exhibition* (Society of Petroleum Engineers, 1977).

M. Dusseault, *Geomechanical aspects of shale gas development*, in *Rock Mechanics for Resources, Energy and Environment* (CRC Press, 2013) pp. 39–56.

N. Barton, *Non-linear behaviour for naturally fractured carbonates and frac-stimulated gas-shales*, First Break **32**, 51 (2014).

N. R. Warpinski, M. Mayerhofer, K. Agarwal, and J. Du, *Hydraulic-Fracture Geomechanics and Microseismic-Source Mechanisms*, SPE Journal **18**, 766 (2013).

H. Gu, E. Siebrits, and A. Sabourov, *Hydraulic Fracture Modeling With Bedding Plane Interfacial Slip*, in *SPE Eastern Regional/AAPG Eastern Section Joint Meeting* (Society of Petroleum Engineers, 2008).

W. Wu and M. M. Sharma, *Acid Fracturing Shales: Effect of Dilute Acid on Properties and Pore Structure of Shale*, in *SPE Hydraulic Fracturing Technology Conference* (Society of Petroleum Engineers, 2015).

K. Tezuka, *Numerical simulation of hydraulic shearing in fractured reservoir*, in *Proceedings World Geothermal Congress*, April (2005) pp. 24–29.

H. Stone and M. D. Zoback, *Visco-plastic Properties of Shale Gas Reservoir Rocks*, in *45th U.S. Rock Mechanics / Geomechanics Symposium* (San Francisco, California, 2011).

6

Interplay between burial- and folding-related fracturing and implications for reservoir flow

As fractures are typically below the seismic resolution, multiscale relations between seismic-scale folding and subseismic-scale fracturing have been derived to predict natural fracture and flow patterns in folded reservoirs. These relations focus predominantly on seismic-scale folding and faulting, but analyses of fracture patterns around outcropping folds indicates that pre-existing fractures sets are also common. These constrain syn-folding fractures and impact fluid flow patterns in naturally fractured reservoirs. This is however rarely taken into account in fractured reservoir modelling. To quantify the impact of pre-folding fractures on permeability, we identify and characterise fractures in an outcropping carbonate fold in central Tunisia. We identify the pre-folding fractures based on their orientation, crosscutting relations and spatial distribution. These are predominantly hybrid conjugates formed during regional shortening at depths of less than 1 km. *Folding-related deformation mostly consists of obliquely-dipping stylolites, Riedel shears and bed-perpendicular veins, which are limited in size by the pre-folding fractures. We correlate relative fracture intensity throughout the fault-propagation fold with 3-D strain models, constructed using geomechanical restorations, as kinematic restorations are not able to capture the interplay between horizontal shortening related to fault movement and vertical movements related to evaporites. Using fracture patterns digitised from outcrops, we model equivalent permeability in fracture systems representative of the different structural domains identified from the strain models to quantify how permeability varies across a fold containing pre- and syn-folding fractures. The resulting permeability is highest in the direction perpendicular to the fold axis, sub-parallel to pre-folding fractures, as these are longer and have a higher connectivity compared to syn-folding fractures striking parallel to the fold axis.*

6.1. Introduction

Natural fractures are common in folded structures, and fractured folds in the subsurface are often prolific reservoirs as the fold provides a structural reservoir closure and fractures can create additional porosity and permeability (e.g. folds in the Zagros and Ghadames-Illizi basins; Stephenson *et al.*, 2007; Dixon *et al.*, 2010; Casini *et al.*, 2011; Lacombe *et al.*, 2011; Tavani *et al.*, 2011). Syn-folding fracturing has been studied extensively in outcrops (Price, 1966; Hudleston and Treagus, 2010; Anders *et al.*, 2014), as understanding the multiscale relation between seismic-scale folding and subseismic-scale fracturing allows for extrapolation of 1-D well data to 3-D fractured reservoir models (e.g. Bergbauer and Pollard, 2004; Sanders *et al.*, 2004; Makel, 2007). Price (1966) presented the first conceptual model for fold-related fracturing, variations of which are still commonly used (e.g. Couples and Lewis, 1998; Fischer and Jackson, 1999; Bellahsen *et al.*, 2006; Savage *et al.*, 2010; Awdal *et al.*, 2016). Salvini and Storti (2001) presented conceptual models of different folding mechanisms, focusing on types of active-hinge folding, and the relative deformation intensities in different parts of the fold.

More recently, the presence and importance for flow of pre-folding fractures in folded structures is recognised (Bergbauer and Pollard, 2004; Casini *et al.*, 2011; Tavani *et al.*, 2011; Branellec *et al.*, 2015). Pre-folding burial-related fractures are related Layer Parallel Shortening (LPS), overpressured fluids or simply overburden stresses (Lorenz *et al.*, 1991; Roberts and Nunn, 1995; Bergbauer and Pollard, 2004; Shackleton *et al.*, 2011; Fall *et al.*, 2015; Bertotti *et al.*, subm). Burial-related fractures have been characterised in sub-horizontal reservoirs and outcrops (e.g. Lorenz *et al.*, 1991; Arlegui and Simón, 2001; Bertotti *et al.*, subm), but since their geometry and orientation can be similar to folding-related fractures, they are more rarely identified and studied in folds (Shackleton *et al.*, 2005).

Syn-folding fractures are modelled using curvature maps or kinematic restorations (e.g. Olson, 1997; Ericsson *et al.*, 1998; Ormand and Hudleston, 2003; Sanders *et al.*, 2004; Wilkins, 2007; Ukar *et al.*, 2016), but these methods do not consider pre-folding deformation. Furthermore, kinematic restorations require a complete understanding of the kinematic evolution of structures and are not suited for more complex deformation related to for example ductile evaporite movements. Alternatively, geomechanical restorations can be used to capture stress and strain associated with more complex structures (Vidal-Royo *et al.*, 2012).

We aim to identify and characterise pre- and syn-folding fractures in an outcropping fold in central Tunisia, which serves as an analogue for folded and fractured carbonate reservoirs in the subsurface, using a combination of structural fracture interpretation and isotope analysis of the fracture cements. We quantify the geometrical distributions, fracturing mechanisms, spatial distribution and relative timing of each fracture system. The present-day fold geometry is constructed in 3-D using a combination of outcropping and subsurface data. The spatial fracture distributions derived from outcrops are compared to strain patterns in different domains of the fold, modelled using geomechanical restoration of the present-day fold geometry to the pre-folding conditions. Based on the strain distribution, we characterise the spatial distribution of syn-folding and reactivated pre-folding frac-

tures throughout the fold, and model the associated variations in permeability using the equivalent permeability modelling workflow from Chapter 3.

6.2. Geological setting

6.2.1. Structural setting

The Gafsa basin in central Tunisia is host to several outcropping folds with predominantly naturally fractured carbonate facies. The largest of these folds is the Alima structure, which is the focus of this study. The basin is part of the Southern Atlas Fold and Thrust Belt (SAFTB), which is an active foreland fold-thrust belt in the southern half of the Atlasic domain (Figure 6.1a). The Atlasic domain forms the foreland basin of the Tellian Alpine Chain (Bouaziz *et al.*, 2002). The Gafsa basin is bounded by the Gafsa fault and Orbata-Bou Hedna range in the north, the Tozeur fault in the west, the Chotts range in the south, and the Sahel block in the east (Bouaziz *et al.*, 2002; Riley *et al.*, 2011; Saïd *et al.*, 2011a) (Figure 6.2).

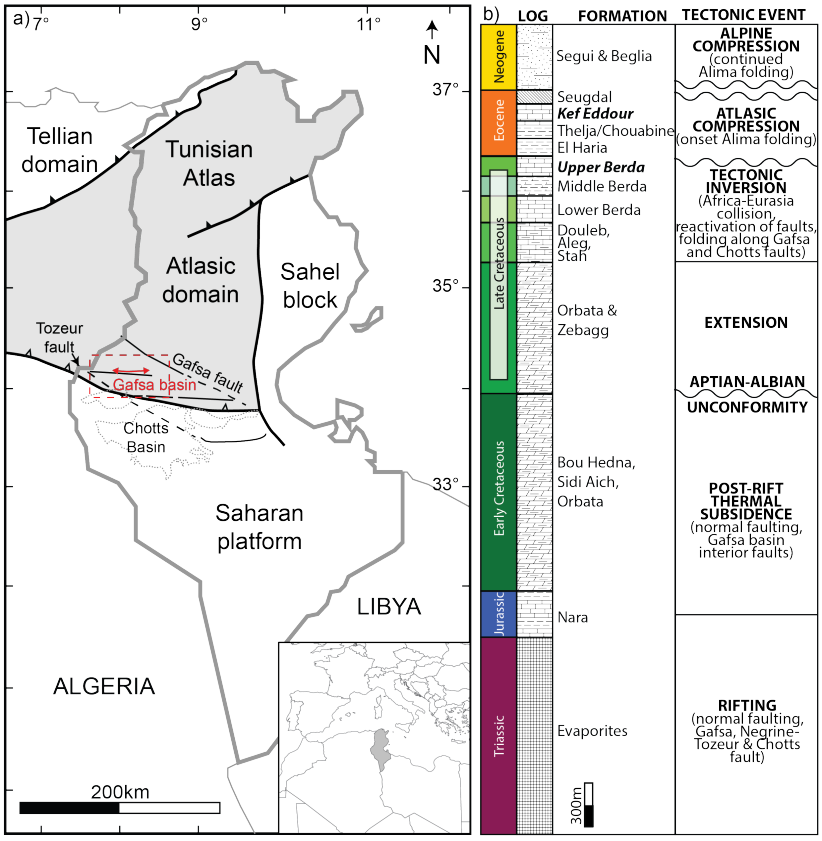


Figure 6.1: Setting and stratigraphy: a) Regional setting of the Gafsa basin, bordered by the Tozeur and Gafsa faults. The red fold axis shows the Alima fold. Adapted from Bouaziz *et al.* (2002); b) Simplified tectono-stratigraphic chart of the Gafsa basin. Adapted from Saïd *et al.* (2011b).

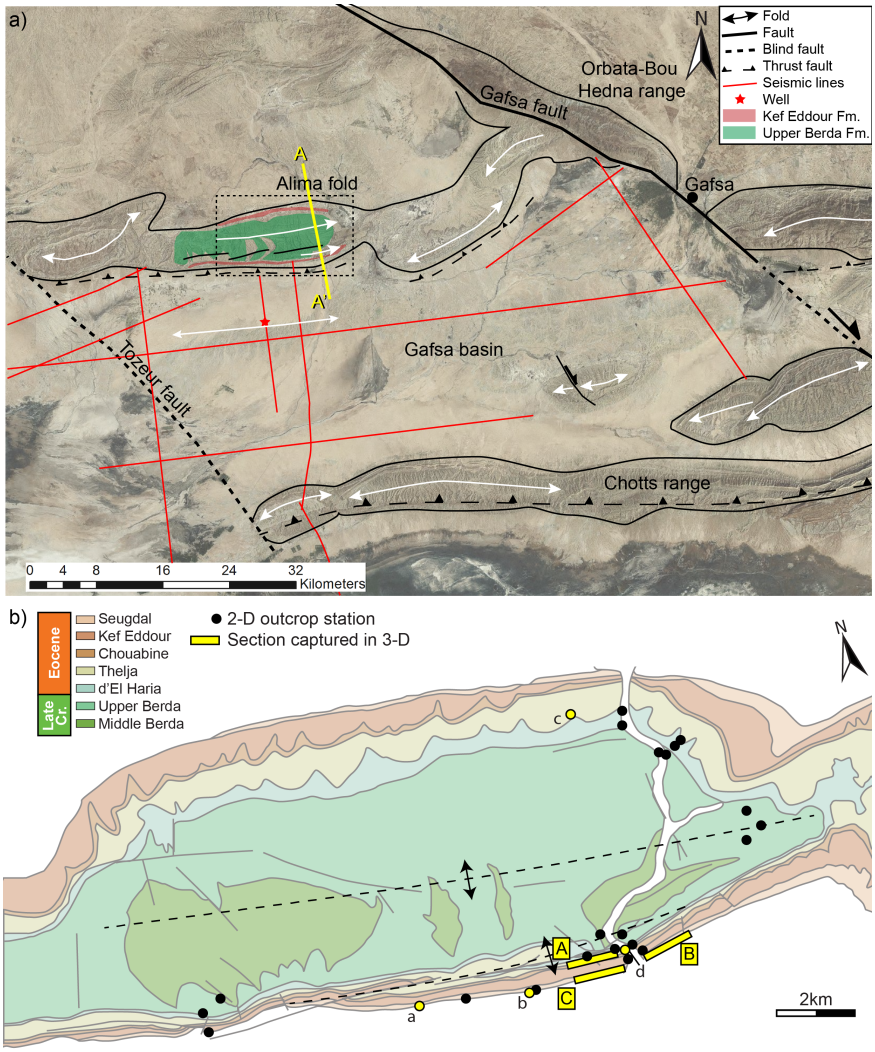


Figure 6.2: a) Overview of the Gafsa basin. The available seismic lines and well data used for constraining the 3-D geometry of the Alima fold are indicated in red. Adapted from Bouaziz *et al.* (2002); Saïd *et al.* (2011a); b) Simplified geological map of the eastern part of the Alima fold, with the locations where fractures were digitised in 2-D and 3-D (indicated by capital letters). The small letters a-d indicate the locations of the examples shown in Figure 6.5.

Formation of the basin coincided with the opening of the Neothethys during the Late Triassic-Early Cretaceous, creating the E-W striking Chotts and NW-SE striking Gafsa normal faults (Figure 6.1b; Riley *et al.*, 2011). These faults were reactivated during Atlasic and Alpine events, where the Gafsa fault became an oblique right-lateral strike-slip fault and the Chotts fault a transpressional fault (Riley *et al.*, 2011; Saïd *et al.*, 2011b,a). Folding occurred along these faults, creating the Chotts

and Orbata ranges along the southern and northeastern edges of the basin (Riley *et al.*, 2011).

Folding within the basin itself started during Alpine compression (Riley *et al.*, 2011). This phase, which included folding of the Alima structure, started in the Paleogene and is still active today (Outtani *et al.*, 1995; Bouaziz *et al.*, 2002). Small E-W striking normal faults were reactivated as thrust faults under NNW-SSE to NW-SE compression. The development and present-day geometry of the folds is at least partly driven by upward movement of underlying evaporites, although the quantitative contributions of horizontal shortening and upward movements are not fully understood (Outtani *et al.*, 1995; Hlaiem, 1999; Riley *et al.*, 2011).

6.2.2. Stratigraphy

The basin stratigraphy is analysed based on outcrops and a vertical well 7 km south of the outcropping Alima fold (Saïd *et al.*, 2011a). The oldest sediments are 1500 m thick Triassic and Jurassic evaporites, deposited during rifting and post-rift thermal subsidence. Deposition continued in the Jurassic with the Nara Fm., which consists of 350–500m of limestones and marls (Figure 6.1b). Above the Nara Fm., we find Lower Cretaceous limestones, dolomites and sandstone intervals with a total thickness of 1500 m. Following the Aptian-Albian reactivation, 2000 m of Upper Cretaceous dolomites and limestones were deposited, alternated by marly and shaly intervals, including the Upper Cretaceous Upper Berda Fm. (also referred to as Abiod Fm.), which is a fractured carbonate.

Following a minor unconformity and deposition of Paleogene shales and marls, carbonates of the Eocene Kef Eddour (or Metlaoui) Fm. were deposited, with a thickness of 50 m. The Kef Eddour Fm. is overlain by a layer of gypsum, the Seugdal Fm., which is the youngest Eocene formation. After the Oligocene-Miocene Alpine unconformity, deposition continued mostly in the form of sandstone and shale, followed by Quaternary alluvium (Swezey, 1996). This study focuses on fractures in the Upper Berda and Kef Eddour formations.

6.2.3. Geometry of the Alima fold

The E-W striking Alima fold is an asymmetrical fold with an outcropping area of 18 × 8 km (Figures 6.2 and 6.3). The northern limb dips at a gentle angle (10–20°), whereas the southern limb is relatively steep in most areas (50–70°). In the south east, a tightly folded anticline is superposed on the southern flank of the main fold, with a nearly overturned southern flank dipping at 70°.

Seismic lines indicate that the structure is a fault-propagation fold, with the main detachment in the Triassic evaporites and additional detachments in Cretaceous layers (Outtani *et al.*, 1995). The main folding mechanism is the regional shortening related to the Atlasic and Alpine compressional events, although the underlying evaporites likely contributed to the present-day shape and height of the fold (Outtani *et al.*, 1995; Hlaiem, 1999; Riley *et al.*, 2011). The Late Eocene Kef Eddour Fm. and the Neogene deposits are syn-folding and show slight variations in thickness and wedge-shaped structures on seismic lines, which indicates that folding was gentle (Hlaiem, 1999; Riley *et al.*, 2011). The thickness variations are

strongest in the Miocene Beglia Fm., indicating that the most prominent stage of folding was recent.

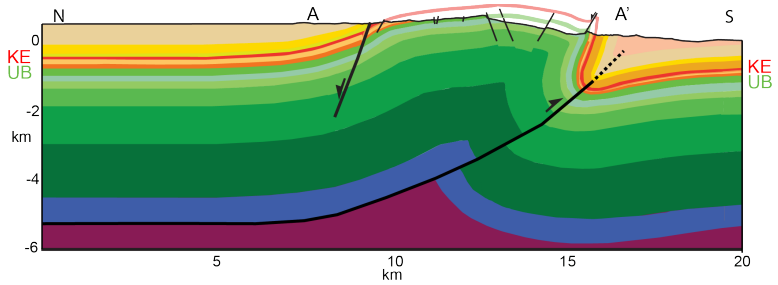


Figure 6.3: Cross-section of the Alima fold (see Figure 6.2 for location) showing the restored Kef Eddour ('KE') and Upper Berda ('UB') Fms., constructed from seismic, well data, a Digital Elevation Model and a fieldwork cross-section. The colours of the formations correspond to the stratigraphy in Figure 6.1b.

6.3. Sub-seismic scale deformation

We analyse the pre- and syn-folding fracture systems in outcrops in different domains of the Alima fold (Figure 6.2b) and other parts of the basin, including other folds and areas that have not experienced significant folding (Bekkers, 2013; Boeser, 2014). We digitised fractures and the mechanical stratigraphy and collect rock samples and plugs for petrophysical and cement analyses, from which mechanical and acoustic properties including rock density, porosity, Poisson's ratio and Young's Modulus were measured (Toby, 2013). In addition, cements of sampled veins were analysed in thin sections and isotopes of fluid inclusions within the veins were measured to analyse fracture timing and conditions (Vaughan, 2015). The methodology and results for the mechanical and fluid inclusion analyses are discussed in Toby (2013) and Vaughan (2015). Here, the main conclusions from those studies are used to support the fracture geometrical analysis.

6.3.1. Fracture digitisation

Fracture data was acquired in 49 locations along the southern flank of the Alima fold, south of the fold and along a N-S transect through the fold close to its eastern termination (Figure 6.2). The dimensions of the studied outcrops are between 1×10^1–$2.5 \times 10^4 m^2$, containing tens to several hundreds of fractures. With the exception of three large dipping pavements, fractures and bedding interfaces were digitised at the outcrop, by taking georeferenced photographs and loading them into DigiFract on a tablet PC (Hardebol and Bertotti, 2013). Digitising the fractures directly in the field allows for accurately measuring orientation and size. This method is as fast as conventional scanlines, but contrary to scanlines, the collected dataset is an accurate representation of the 2-D geometry and spatial distribution of the fracture patterns, which can be used to quantify length and spacing

The fracture analysis is partly based on the M.Sc. theses of Bekkers (2013); Toby (2013); Boeser (2014); Vaughan (2015).

distributions and investigate relations between bedding units and fracture height (e.g. Bisdom *et al.*, 2014).

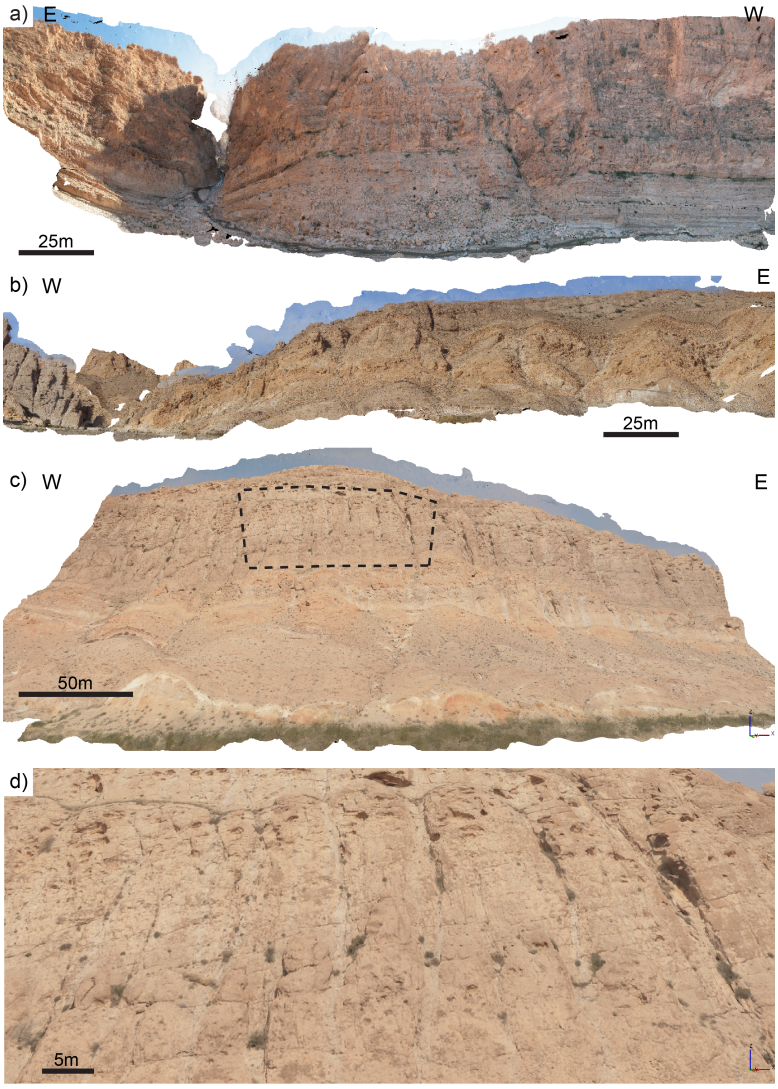


Figure 6.4: Overview of the 3-D outcrop models. The locations of these models are indicated by the A, B and C labels in Figure 6.2b: a) Vertical section showing steeply dipping beds and vertical fracture segments of the Upper Berda Fm., along the south flank of the fold; b) Partial exposures of fractured pavements of the Kef Eddour Fm.; c) Large dipping pavement of the Kef Eddour Fm.; d) Detail of (c).

There are several large sections of steeply dipping pavements along the southern flank of the fold, which cannot be captured in a single photograph or a conventional panorama picture, as these sections are several hundred meters wide

with varying dips. Instead, photogrammetry was used to create accurately high-resolution 3-D models of these outcrops. Brightly coloured georeferenced markers were positioned along the outcrops, after which we photographed the surfaces from different positions and a range of distances, ensuring at least 50% overlap between images. Agisoft Photoscan® was used to merge the images and markers into georeferenced 3-D outcrop models (Chapter 2).

Fractures in these 3-D outcrop models were digitised using OpenPlot by Tavani *et al.* (2014) and Gocad/SKUA® (Paradigm®). These models were constructed and interpreted after the fieldwork, but the 3-D geometry of the outcrop permitted capturing the full orientation of most large fractures. One model captures fracture height in a steeply dipping vertical section of the Upper Berda Fm. (Pengel, 2014), and the other two models cover a large dipping pavement of the Kef Eddour Fm., in which fracture length is digitised (Figure 6.4; Althuis, 2014).

In each of the three 3-D outcrop models, several hundred barren fractures were digitised, covering at least two to three orders of magnitude of length and spacing, required for quantitative analysis of fracture attributes (Bonnet *et al.*, 2001). The minimum length that is fully captured, i.e. without truncation artefacts, in the large models is 6 m. Most of the other digitised outcrops do not contain a sufficiently large amount of fractures for quantitative analysis, and these are only used for qualitative analysis, which includes identification of orientation sets, abutment and bedding relations, fracture type and infill. In these outcrops, we digitise veins, barren fractures and stylolites and analyse each type separately.

6.3.2. Deformation types and sets

Outcrops were studied along the northern and southern flanks of the main fold, as there were no exposures along the crest. Unless explicitly mentioned, we describe the fracture orientation relative to the present-day bedding orientation.

Southern flank

Along the steeply dipping southern flank of the superpositioned fold and the southern limb of the main Alima fold, bed-perpendicular conjugate fractures, striking perpendicular to the fold axis, are observed in the Kef Eddour and Upper Berda Fms. (Figure 6.5a). These fractures are interpreted as conjugates, as small-scale observations show shearing and fractures typically intersect at angles of 20–30°. The bisection of the conjugates is NNW-SSE, perpendicular to the present-day fold axis. Fibrous calcite infill is sometimes observed, with evidence of shear during cement precipitation (Vaughan, 2015). There are no fully cemented conjugates, but we do observe cemented tension gashes and barren Riedel shears (Figure 6.6a).

In the same structural domain, we observe fractures that dip oblique to bedding with a strike that is perpendicular to the bed-perpendicular conjugates, if beds are returned to their horizontal position. Within this set, the angle between fractures is 10–30°. The majority of these fractures are interpreted as conjugates where the small angle indicates a σ_1 striking parallel to the present-day fold axis (Figure 6.5b). In some outcrops, we observe small fractures with the same orientation which are fully cemented veins with blocky calcite cement that lack any indication of shear,

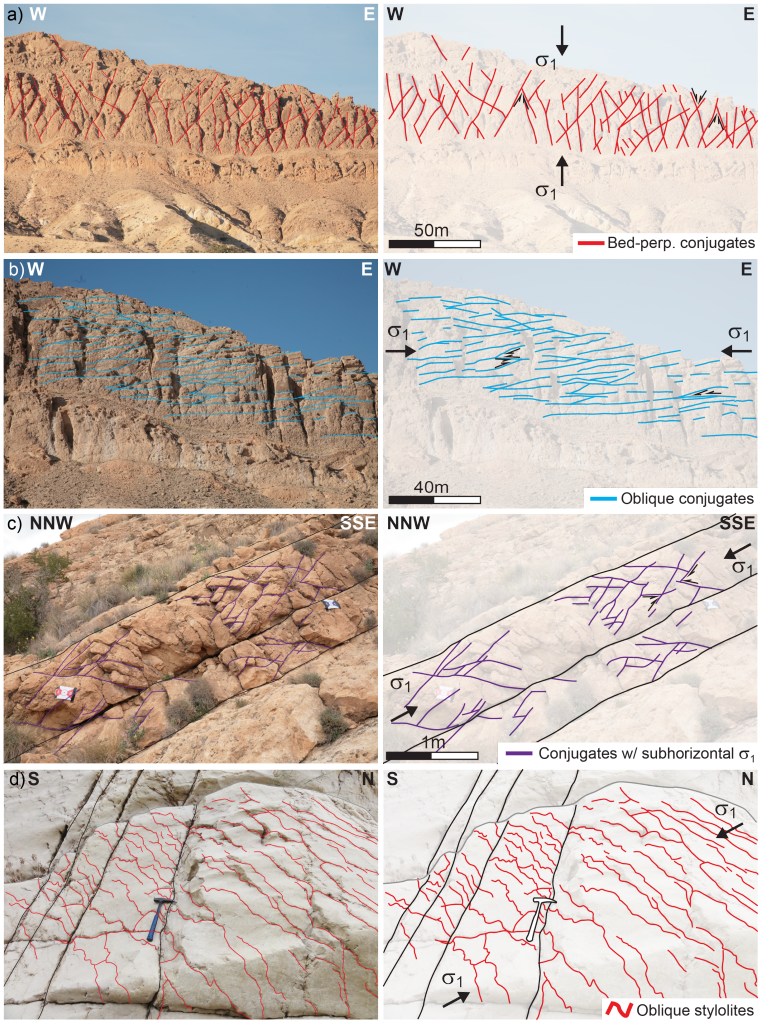


Figure 6.5: Examples of the main fracture and stylolite families in the Alima fold. The locations of these four examples are indicated in Figure 6.8: a) Large-scale bed-perpendicular conjugate fracturing along the steeply dipping southern flank (Kef Eddour Fm.); b) Large-scale oblique-dipping fractures along the southern flank (Kef Eddour Fm.); c) Bed-confined fracturing along the northern flank (Kef Eddour Fm.); d) Oblique stylolites in steeply dipping layers of the Upper Berda Fm. (southern flank).

aligned with stylolites (Figure 6.7; Vaughan, 2015). These stylolites are observed in most outcrops along the southern flank, with a present-day dip that is steeply towards the north (Figure 6.5d). In contrast to the fracture observations, which show no significant differences between the two formations, the Upper Berda Fm. has a significantly higher stylolite intensity.

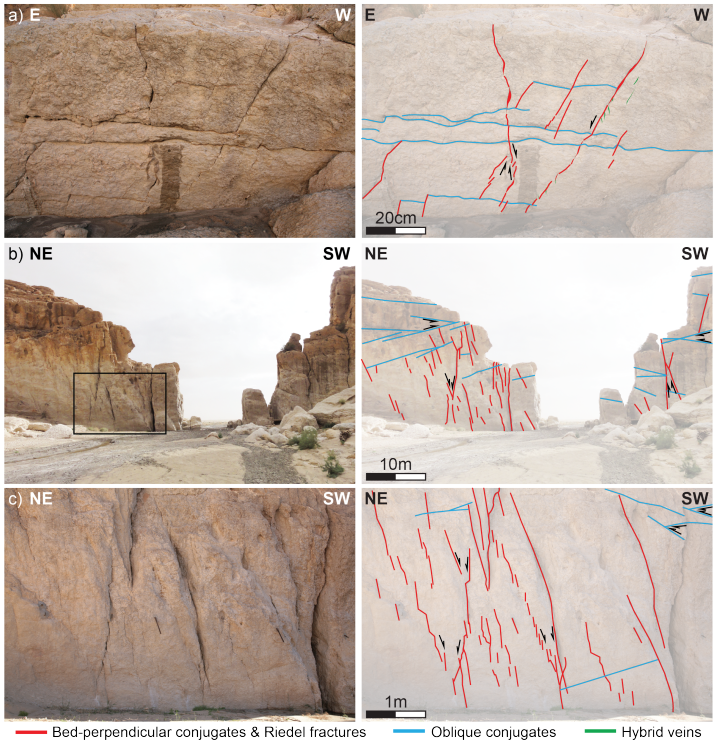


Figure 6.6: Multiscale examples of the interactions between bed-perpendicular and oblique conjugates: a) Detail of the base of a steeply dipping layer of the Upper Berda Fm., along the southern flank of the main fold, with coeval bed-perpendicular conjugates, Riedel shears, tension veins and oblique-dipping conjugates and veins; b) Parts of the base of a steeply dipping layer of the Kef Eddour Fm., showing a similar configuration of bed-perpendicular and oblique conjugates but on a larger scale; c) Detail of (b) showing similar patterns on a smaller scale.

Northern flank

Bed-confined fractures are observed in gently dipping (i.e. 10°) layers along the northern flank of the fold. These fractures dip at a small angle with respect to bedding, with strike and dip towards the north and the south. Based on the consistent horizontal intersection angle, they are interpreted as conjugates with a sub-horizontal small angle bisector dipping towards the north, with the same dip as the beds (Figure 6.5c). No cement is observed in these fractures. No other fracture systems are observed along the northern flank (Figure 6.8), but we do observe E-W striking stylolites, dipping perpendicular to bedding with an E-W strike.

6.3.3. Fracturing synthesis

In summary, we have observed five types of deformation along the flanks of the fold, with three systems of conjugate pairs, with intersection angles between pairs of each conjugate system dipping perpendicular, parallel and oblique to bed-

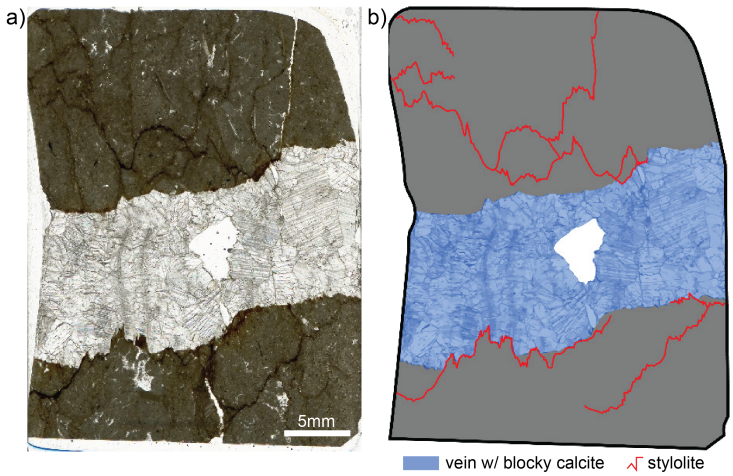


Figure 6.7: Thin section of a bed-perpendicular *Set II* vein with blocky cement that is partly aligned along a pre-existing bed-perpendicular E-W striking stylolite. Adapted from Vaughan (2015).

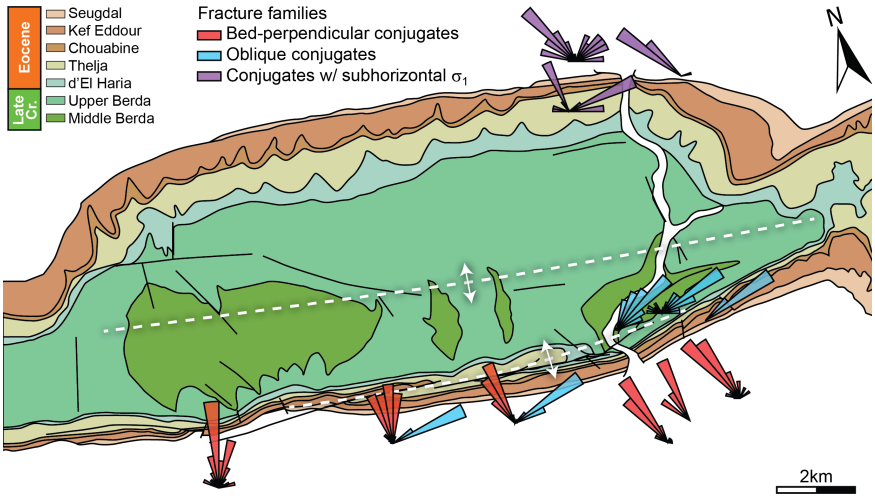


Figure 6.8: Geological map of the eastern part of the Alima fold, with rose plots showing the strike of back-rotated fracture measurements in different structural settings of the fold.

ding, and two systems of stylolites, dipping perpendicular and oblique to bedding. We investigate the large-scale mechanisms that potentially drove formation of these small-scale features, based on orientation, abutting relations, cement properties and isotope analysis.

Layer Parallel Shortening

We assume that the bed-perpendicular features are formed prior to folding, and rotate these back to their position in horizontal beds. The back-rotated bisector an-

gle of the bed-perpendicular conjugates is oriented approximately N-S (Figure 6.8), which corresponds to the regional maximum shortening direction prior to and during the onset of folding, during a phase of LPS. E-W striking bed-perpendicular tectonic stylolites are also compatible with this regional shortening phase.

The conjugates with a horizontal E-W striking intersection along the northern flank are also aligned with a regional N-S shortening phase prior to folding. However, although these conjugates have the same N-S oriented σ_1 as the bed-perpendicular conjugates along the southern flank, their σ_3 is vertical whereas σ_3 is horizontal and parallel to the fold axis for the bed-perpendicular conjugates. This indicates that these conjugate systems were formed at different depths. Assuming a tectonic stress of 20 MPa that increases with depth relating to the Poisson's effect, a vertical stress based on an overburden density of 2300 $kg\,m^{-3}$ and an average Poisson's ratio of 0.3, derived from the average of the analysed samples (Toby, 2013), bed-perpendicular conjugates likely formed at depths between 500–1100m (Figure 6.9a). The tectonic stress magnitude is an estimate, but variations in tectonic stress have only a minor impact on the upper limit of the domain where overburden stress becomes σ_2. Based on this model, the conjugates along the northern flank were formed at depths shallower than 500 m.

The first stage of folding of the Alima during late Paleogene has resulted in a height difference of several hundred meters between the northern and southern flanks (Bouaziz *et al.*, 2002; Riley *et al.*, 2011). We interpret that the conjugate systems were formed in the Neogene. The layers on the northern flank were at shallow depth, resulting in a vertical σ_3 creating conjugate pairs with a horizontal intersection (Figure 6.9b). Layers south of the crest were sufficiently deep to create bed-perpendicular conjugates under a vertical σ_2 (Figure 6.10a).

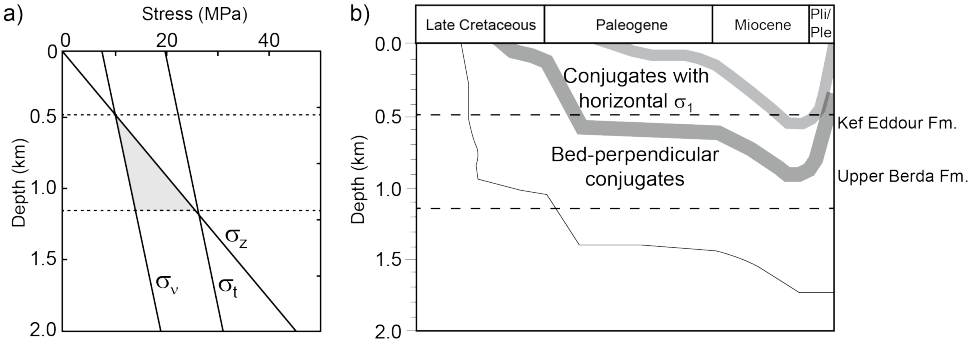


Figure 6.9: Analysis of the depth and timing of shortening-related fractures: a) Bed-perpendicular conjugates likely formed at a depth between 500–1100m; b) Depths of fracturing combined with a burial plot for formations in the Gafsa basin near the Alima fold, indicating the maximum depths of the Upper Berda and Kef Eddour Fms. prior to folding and exhumation. Adapted from (Zouaghi *et al.*, 2009).

Flexural slip during folding

Based on their dip, the oblique stylolites and fractures were likely formed during folding, when layers were already dipping (Figure 6.10b). The fracture strike of

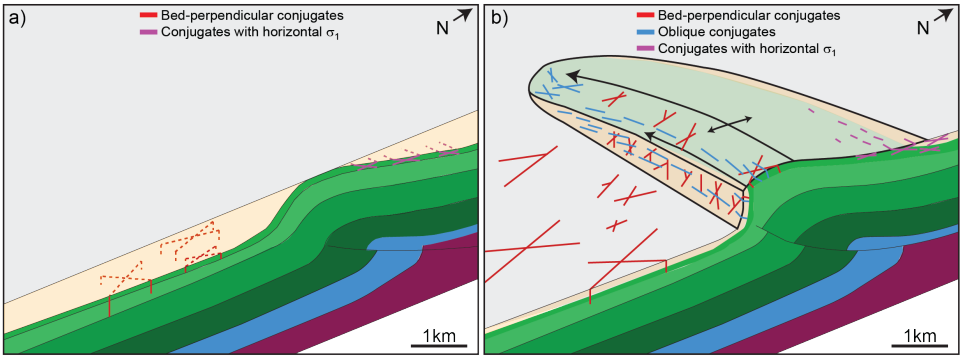


Figure 6.10: Conceptual model of the different fracture types and their distribution along the Alima fold during different stages of folding: a) Early onset of folding (Miocene), with bed-perpendicular conjugates along the southern flank and south of the fold and conjugates with a horizontal intersection in the shallower layers along the north flank; b) Present-day fold geometry with oblique conjugates on the southern flank. Formation colours are the same as those in the stratigraphic chart in Figure 6.1b.

the oblique conjugates, which is subparallel to the fold axis, is another indication of deformation associated with folding. The layers in which we find the oblique stylolites along the southern flank of the fold are nearly overturned because of the small superimposed fold along the south-east flank. Based on the orientation of the stylolites with respect to bedding, we relate these features to flexural slip during early folding, when layers were less steeply dipping (Geoff Tanner, 1989). These stylolites are exclusively found in the Upper Berda Fm., which, contrary to the Kef Eddour Fm., has no shale intervals separating the limestone beds. As a result, friction coefficients are high and this section of the Upper Berda Fm. is likely to act as a single mechanical unit, without slip along beds. During folding, strain in the dipping layers is directly accommodated by dissolution, creating tectonic stylolites that were vertical during their formation (Figure 6.11a,b).

In contrast, the shale layers in between the limestone units of the Kef Eddour Fm. do accommodate slip, such that flexural slip occurs along individual beds and principle stresses are perpendicular and parallel to the individual beds, creating predominantly bed-perpendicular features (Figure 6.11c). The oblique conjugate fractures are also associated with flexural slip, but the approximate E-W striking bisector angle, which indicates that σ_1 was parallel to the fold axis during fracturing, cannot be explained using the current dataset, as there is no evidence for a local or regional flip of σ_1 from N-S to E-W.

The analysis of veins from thin sections indicates small-scale E-W striking veins that have formed preferentially along the LPS-related tectonic stylolites, showing that these pre-folding features form mechanical weaknesses that control the spatial distribution of syn-folding fracturing (Figure 6.7).

The results of the isotope analysis suggest that bed-perpendicular veins associated with LPS were cemented by fluids of marine origin or mixed marine and meteoric, whereas oblique flexural slip related veins are associated with meteoric

waters (Vaughan, 2015). This corresponds to LPS-related fracturing at depth (Figure 6.10a), followed by continued folding and exhumation, during which flexural-slip related fractures were formed at shallower depths, were meteoric waters could enter the fracture system (Figure 6.10b). The cement composition confirms this relative trend, as the fibrous cement in LPS-veins combined with shear indicates cementation under horizontal compression, whereas we only find blocky cements in veins associated with flexural slip (Vaughan, 2015).

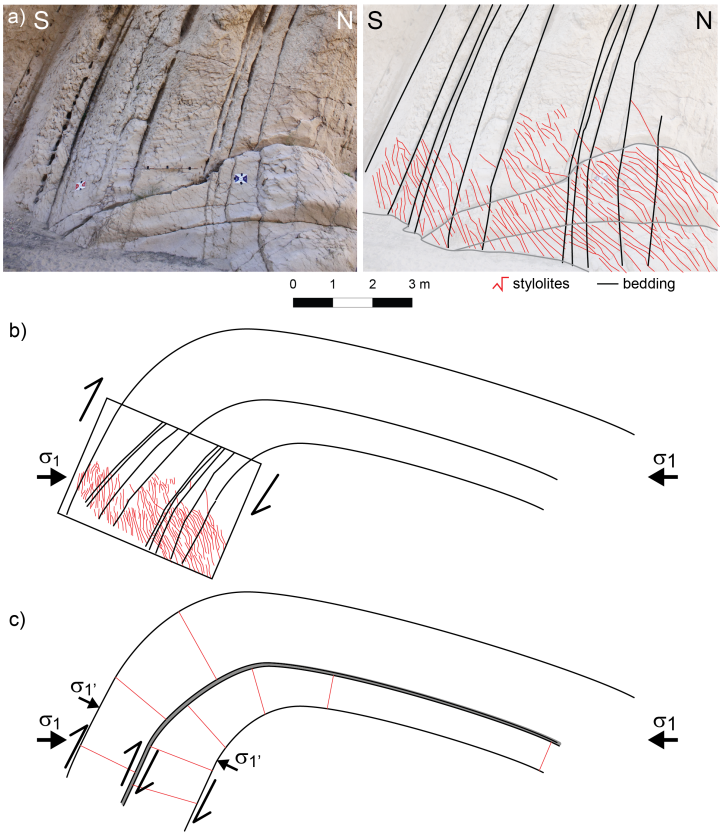


Figure 6.11: Wider view of the detail from Figure 6.5d illustrating the process of flexural slip in the Kef Eddour Fm. and the Upper Berda Fm.: a) Steeply dipping beds of the Upper Berda Fm. without any sediments in between the beds, and the oblique stylolites; b) A high friction coefficient for the interfaces between limestone units of the Upper Berda Fm. prevents slip, resulting in a high intensity of tectonic stylolites; c) Slip in between individual beds results in each bed acting as an individual mechanical unit with principle stress components perpendicular and parallel to bedding.

6.4. Fold-scale fracture distribution

We reconstruct the present-day fold geometry and mechanically restore this to pre-folding conditions to capture the strain distribution related to fold-

ing, which serves as a driver for the intensity of the oblique features associated with flexural slip during folding. Generally, the strain distribution during folding is modelled using 2-D and 3-D kinematic restorations, where cumulative strain is defined by step-by-step kinematic deformation (Sanders *et al.*, 2004; Midland Valley Exploration Ltd., 2014; Ukar *et al.*, 2016). The resulting strain is only related to horizontal regional shortening, which typically results in relatively small strain variations (e.g. Ukar *et al.*, 2016). The Alima fold, however, is formed by a combination of regional horizontal shortening and local vertical movements related to the underlying evaporites. Furthermore, spatial variations in fracture intensity are large compared to purely shortening-related folds. We use a geomechanical Finite Element (FE) approach that supports horizontal and vertical movements to restore the 3-D present-day geometry to pre-folding conditions (Durand-Riard *et al.*, 2012).

6.4.1. Methodology

Reconstruction of 3-D fold geometry

We reconstruct the pre-erosional fold structure of the Eocene and Upper Cretaceous formations. For these formations, we have a relatively high-density dataset with outcropping and subsurface data. The available data consists of:

- A Digital Elevation Model (DEM; 30 m resolution);
- Geological maps (1:100 000);
- 2-D seismic lines north and south of the fold (Figure 6.2a; Zouaghi *et al.*, 2007, 2009; Saïd *et al.*, 2011a);
- Digitised and georeferenced cross-sections from literature (Saïd *et al.*, 2011a; Riley *et al.*, 2011; Zouaghi *et al.*, 2011);
- Layer dips measured in the field;
- Unfolded formation depths and thicknesses from the well south of the fold (Figure 6.2a; Zouaghi *et al.*, 2009).

All data is georeferenced and loaded into SKUA/Gocad, which is used in combination with the implicit modelling plug-ins from the Gocad Research Consortium (RING, formerly GRG) to construct the 3-D fold geometry (Figure 6.12; Caumon *et al.*, 2009). This approach allows for reconstruction of folded geometries based on relatively sparse data (Caumon *et al.*, 2013). The formation boundaries, digitised from seismic, cross-sections and geological maps, and the measured dips are the main constraints for the 3-D modelling (Figure 6.12c,d). In areas with few or no data points, the implicit modelling method follows the trends from nearby areas with better constraints to construct a representative geometry, instead of trying to linearly interpolate between points, resulting in a realistic asymmetric fold geometry that honours the input data (Figure 6.12e,f).

3-D mechanical restoration

The RestorationLab plug-in (RING) for SKUA/Gocad is used for 3-D geomechanical restoration of the fold geometry to pre-folding conditions (Durand-Riard *et al.*, 2010). This tool restores folded and faulted bodies using FE models with Dirichlet boundary conditions, i.e. one or more boundaries of the meshed model are fixed,

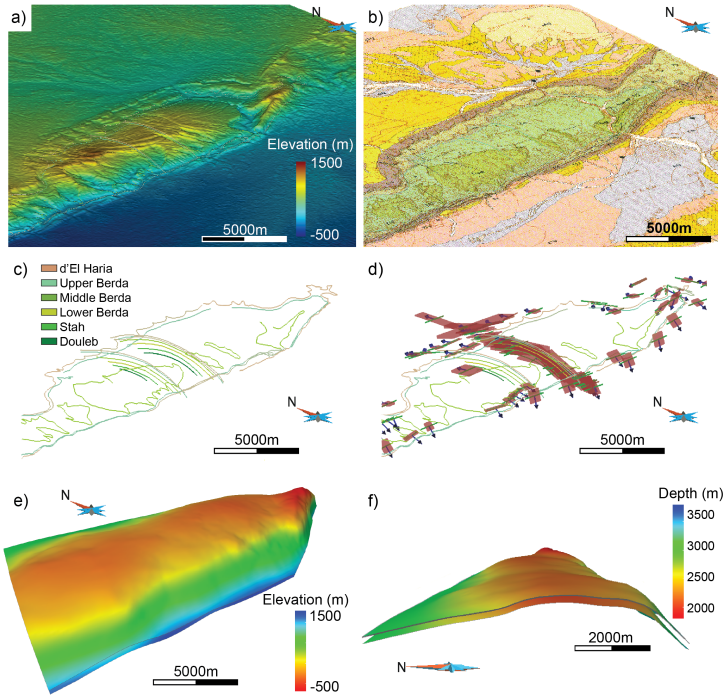


Figure 6.12: 3-D modelling of the Alima fold: a) 30 m resolution DEM of the present-day surface topography; b) georeferenced geological map; c) Digitised outcrop boundaries; d) Outcrop boundaries and measured layer dips; e) Reconstructed top of the Upper Berda Fm. in 3-D; f) N-S cross-section view of the base and top of the Berda Fm., showing the asymmetric shape of the fold.

and the model is restored based on a reference folded surface and pre-folding depth (Figure 6.13; Durand-Riard *et al.*, 2010). The restoration is based on preservation of mass (volume) and linear momentum, assuming homogeneous and isotropic elastic rock behaviour where we use a rock density of 2300 $\mathrm{kg\,m^{-3}}$, Young's modulus of 50 GPa and Poisson's ratio of 0.3 (Toby, 2013). It is possible to assign different mechanical properties to different formations, but as we have no in-situ measurements of mechanical rock properties we assume constant values. The impact of varying mechanical rock properties is investigated by Ranjan (2015), using 2-D and 3-D FE models of the Alima fold, which concludes that layer interactions and regional stresses have a larger impact compared to mechanical rock properties.

We perform the restoration on the 3-D fold with the Eocene and Upper Cretaceous horizons, which we restore to their maximum pre-folding depth, derived from the well south of the fold (Figure 6.2b). The minor syn-folding thickness variations in the uppermost section are negligible on the seismic scale of the model. We construct a tetrahedral meshed volume around the horizons, and fix the southern boundary in the y direction (N-S), as the horizons are at maximum burial depth in this domain. The meshed volume is $20 \times 14 \times 5.4\,\mathrm{km^3}$ and consists of 5.5×10^5 elements, which is the computational limit for RestorationLab supported by our

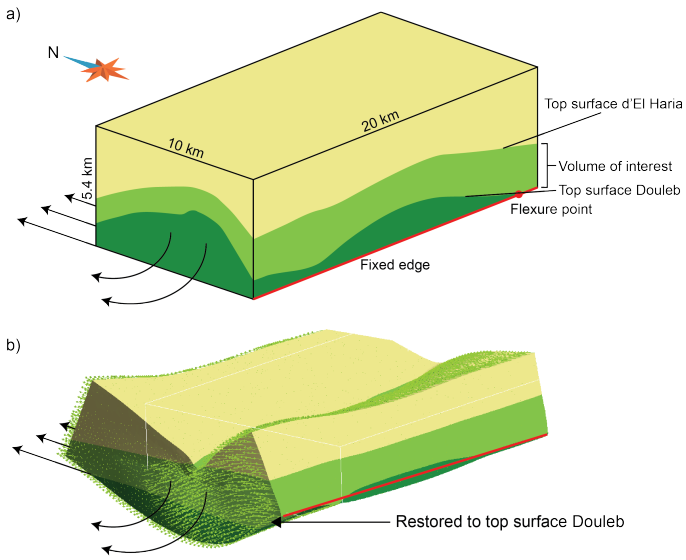


Figure 6.13: Geomechanical restoration: a) Meshed volume of the present-day 3-D fold geometry, with the volume of interest between the top of the d'El Haria Fm. and the top of the Douleb Fm.; b) Restored volume, using the top of the Douleb Fm. as the reference horizon. The arrows indicate the maximum displacement vector for each element in the mesh.

hardware. The mesh is unstructured and honours the geometry of the folded horizons. As burial has been relatively shallow (Figure 6.9) and the studied interval is relatively thin, we do not apply decompaction, and we restore all layers instantaneously rather than sequentially.

The mechanical restoration takes into account shear deformation and flexural slip within the volume (Durand-Riard *et al.*, 2010), but higher-resolution slip potential, i.e. along individual bedding planes, is not considered. We are therefore not able to represent the mechanical difference between the Kef Eddour Fm., which has a high probability for layer-parallel slip, and the Upper Berda Fm., which has no slip along beds, so these models cannot be used to make any statements regarding the formation of oblique stylolites.

6.4.2. Results

We calculate the strain eigenvector and maximum dilation from the geomechanical restoration for the Kef Eddour and Upper Berda Fms. (Figures 6.14 and 6.15). The dilation patterns in these formations are similar, with minor variations in magnitude (Figure 6.14b,c). The strain magnitude is slightly decreasing with increasing depth (Figure 6.14d). This may be indicative of bending stresses, increasing the probability of inner-arc compression in the deeper layers (Maerten and Maerten, 2006). Dilation is also strong along the eastern and western periclinal terminations of the fold. Negative dilation, i.e. compression, is localised along the steeply dipping southern flank, and decreases with increasing depth.

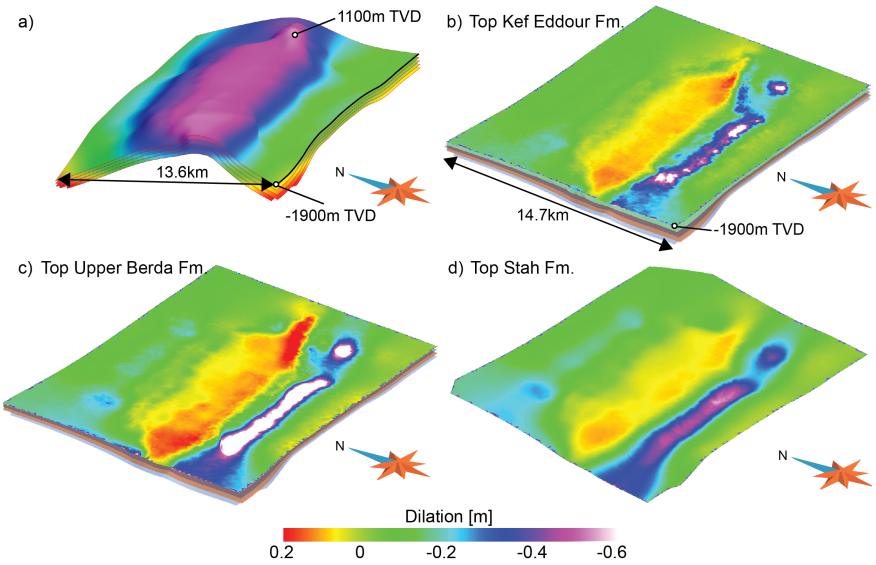


Figure 6.14: 3-D geomechanical restoration in SKUA/Gocad using RestorationLab: a) 3-D surfaces of the tops of the Kef Eddour, Upper, Middle and Lower Berda and Stah Fms. (colours indicate depth); b) Restored top surface of the Kef Eddour Fm., with the amount of dilation. Positive values indicate extension during folding, negative values represent shortening; c) The top of the Upper Berda Fm.; d) Top Stah Fm.

6

To quantify relative trends in strain in different domains of the fold, we plot folding-related strain onto the folded horizons (Figure 6.15). Strain is highest in the direction sub-parallel to regional shortening and lowest in the horizontal direction perpendicular to σ_1. Vertical strain is highest on the flanks, and scales with the flank dip.

The strain tensors illustrate the complex deformation patterns along the steeply dipping southern flank, as vertical strain is extensional in this domain, whereas horizontal strain is contractional. The overall strain in this domain of the fold is contractional. It is important to note, however, that we model only the cumulative strain of the folding process, and differences related to different folding stages are not considered. Contractional strains are likely highest during the initial phase of folding, when layers are sub-horizontal or gently dipping, creating first bed-perpendicular tectonic stylolites and conjugates. Increased folding leads to increased flexural slip acting on dipping layers, creating the oblique stylolites and conjugates. Extensional strain is more common during the final stage of folding and exhumation, related to bending stresses creating outer-arc extension.

Modelled strain versus outcrop observations

The strain distribution associated with folding indicates that the highest intensity of flexural slip and folding-related deformation is found along the crest and the steepest parts of the flanks, particularly near the periclinal terminations (Fig-

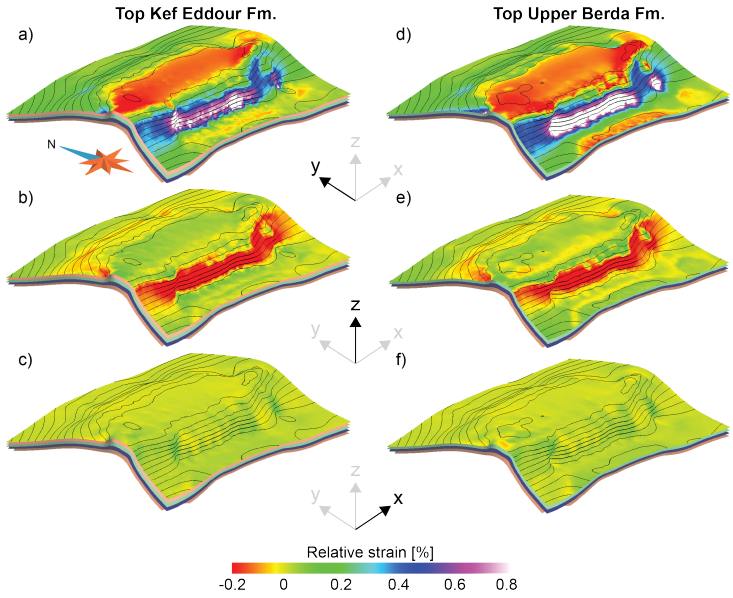


Figure 6.15: Relative strain eigenvalues in three dimensions for the top surfaces of the Kef Eddour Fm. (a-c) and the Upper Berda Fm. (d-f). Elevation contour lines have a spacing of 250 m.

ure 6.15). The southern flank also experiences contraction during part of the folding process, increasing the relative intensity of LPS features. The applied geomechanical restoration method only captures the total strain associated with folding, but does not show strain variations over time, so although the modelled strain is a driver for folding-related deformation, it does not show how fracture types and intensities changed during different stages of folding.

These model predictions correspond to the limited outcrop observations available throughout the fold, as the highest intensity of LPS-related deformation is found along the southern domain, which has the highest horizontal contraction (Figure 6.8). The highest intensity of flexural slip and folding-related deformation is found in outcrops closer to the crest, and in some outcrops along the southern flank. Unfortunately, there are no suitable outcrops closer to the crest of the main fold or along the northern flank to calibrate the model predictions. We do observe several E-W striking normal faults near the crest of the fold, indicative of high extensional strains during the latest stage of folding (Figures 6.3 and 6.8).

Geomechanical restoration versus kinematic analysis

The distribution of fold-related fractures is often studied using kinematic restorations combined with strain capturing (e.g. Sanders *et al.*, 2004; Roskam, 2016; Ukar *et al.*, 2016). However, this requires an accurate understanding of the kinematic evolution of a structure, which limits the application of this method to relatively simple geometries that are mainly the result of horizontal shortening (Sanders *et al.*, 2004; Vidal-Royo *et al.*, 2012). The Alima fold is formed by a combination of hori-

zontal shortening and vertical evaporite movements, but the relative contribution of each component is not known (Riley *et al.*, 2011).

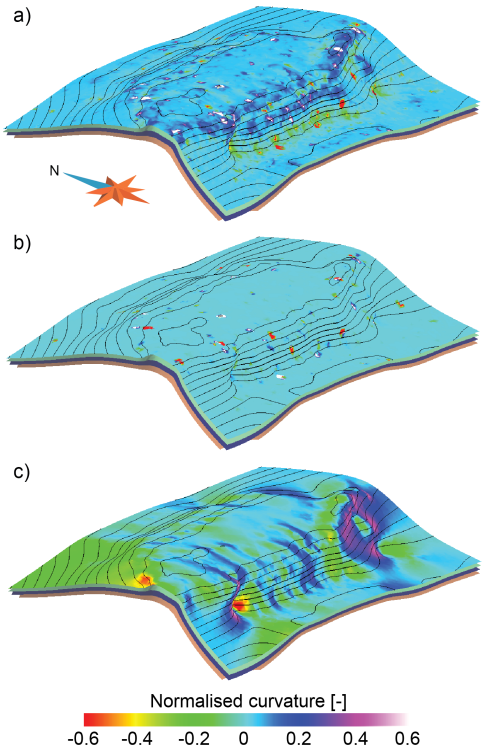


Figure 6.16: Surface curvature calculated for the top of the Upper Berda Fm.: a) Horizontal curvature; b) Vertical curvature; c) Normalised maximum curvature. Elevation contour lines have a spacing of 250 m.

Instead, we apply a geomechanical FE method, which has proven to be more accurate in capturing strain without requiring a full understanding of the kinematic evolution (Vidal-Royo *et al.*, 2012). The resulting variations in strain throughout the fold are larger and less sensitive to small-scale variations in surface geometry compared to strain patterns derived from kinematic restorations (e.g. Ukar *et al.*, 2016). The large contrast in modelled strain along the crest and flanks of the Alima fold is however more in line with the fracture intensity variations observed in outcrops. Moreover, the combination of vertical and horizontal movements to accommodate total strain corresponds to earlier qualitative and quantitative interpretations, where the present-day geometry of the fold is partly attributed to evaporite movement (Hlaiem, 1999; Riley *et al.*, 2011). Our models indicate that although there is a vertical strain component, horizontal strain is significantly larger, i.e. the main driver for deformation is regional shortening accommodated by the reactivated fault below the fold, and that evaporite movement only accentuated the fold geometry (Figure 6.15).

Curvature analysis is an alternative method for quantifying fracture intensity when the kinematic evolution of a structure is not known, as this analysis can be performed on outcropping structures and seismic data alike (e.g. Ericsson *et al.*, 1998; Sigismondi and Soldo, 2003; Makel, 2007). However, several outcrop-based studies have found that curvature is not representative of spatial fracture trends (e.g. Sanders *et al.*, 2004; Bergbauer, 2007). We also observe this for curvature maps of the Alima fold, which are not representative of the observed fracture patterns (Figure 6.16). Horizontal curvature does indicate a higher fracture intensity along the southern flank, but curvature along the crest and northern flank is as low as the non-folded areas away from the fold (Figure 6.16a). Vertical curvature shows no variation, and maximum curvature is mainly controlled by local variations in surface geometry whereas no larger-scale fold-related trends are observed (Figure 6.16b,c).

6.5. Pre-folding vs. syn-folding permeability

The strain distribution is a driver for relative trends in folding-related fracturing. Where extensional strain is low or absent, only LPS-related fractures are present, whereas relatively large extensional strains are indicative for high-intensity networks consisting of LPS- and folding-related deformation. We use a network of LPS-related bed-perpendicular fractures, defined as *Set I*, intersected by oblique flexural-slip related fractures (*Set II*) digitised from the steeply folded domain along the southern flank (Figure 6.17) to model permeability of the two end member networks. The present-day network is representative of post-folding, and by removing all E-W striking fractures we obtain a proxy for the pre-folding network. As the flow simulations assume fully saturated single-phase flow, gravity effects that impact flow in folded reservoirs have no impact, so we focus only on the change in permeability associated with changes in the fracture network, not taking into account the layer dip.

6.5.1. Network geometry

The fracture pattern is digitised from a 3-D outcrop model of a pavement of the Kef Eddour Fm. (Location C in Figure 6.2b), constructed using photogrammetry and interpreted using OpenPlot and SKUA/Gocad, resulting in a database of 345 barren fractures divided into two sets.

Set I

The digitised length of *Set I* in the Kef Eddour Fm. pavement ranges from 0.8–53.4m, where the upper limit is truncated by the outcrop dimensions (Table 6.1). Average digitised length is 22.9 m, based on 108 fractures. The length frequency distribution fits a power-law scaling function with an exponent of 1.2 covering two orders of magnitude not affected by censoring and truncation artefacts (Figure 6.18). This indicates that length on the observed scales is not scale-independent,

Fracture patterns used for permeability modelling are derived from the B.Sc. theses of Althuis (2014); Pengel (2014).

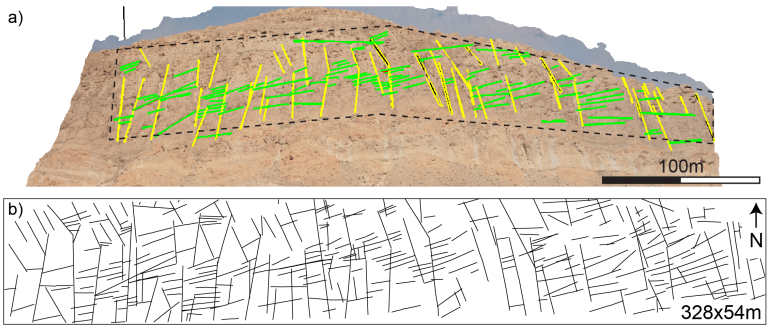


Figure 6.17: Fracture digitisation from the 3-D Kef Eddour Fm. model: a) Fracture digitisation in OpenPlot; b) 2-D tracemap extracted from the 3-D model, covering an area of 328 × 54 m with 345 digitised fracture lengths.

	Set I	Set II
# fractures	108	237
average spacing [m]	9.2	7.4
average length [m]	22.9	12.3
min. length [m]	0.8	2.2
max. length [m]	53.4	39.1
average orientation [°]	13.1	74.8
st. dev. orientation [°]	9.5	8.5
# intersections	278	

Table 6.1: Overview of the fracture geometry of *Set I* and *Set II* in the pavement.

lacking small fractures compared to the self-similar case (e.g. Odling, 1997; Bonnet *et al.*, 2001). Height is controlled by the thickness of the mechanical units of the different formations. Bed thickness in the Kef Eddour Fm. varies between 1–3m, and each bed is separated by up to a few cm of shale. The bed thickness of the Upper Berda Fm. is between 0.2–2m, with a direct limestone-limestone contact separating the individual beds.

The P_{21} intensity, calculated using the box-counting method (Chapter 2), is between 0.03–2.14m^{-1}. The frequency distribution fits a power-law function with an exponent of 1.2, which is identical to the power-law length exponent (Figure 6.18), as P_{21} intensity is defined by the cumulative fracture length in a given area. This is a more quantitative measure of fracture intensity compared to fracture count or spacing measured from a 1-D scanline (Dershowitz, 1985; Bisdom *et al.*, 2014).

Set II

The length of 237 digitised *Set II* fractures in the Kef Eddour Fm. pavement varies between 2.2–39.1m. The length domain that is free from sampling artefacts is relatively limited, but the frequency distribution within this domain best fits a power-law scaling trend with a scaling exponent of 3.8, indicating a lack of large fractures compared to the scale-independent distribution (Figure 6.18). Part of the *Set II* fractures are abutting against *Set I*, limiting their length. Height is generally equal to bed thickness. Fracture intensity of this set is between 0.09–1.56m^{-1} throughout the

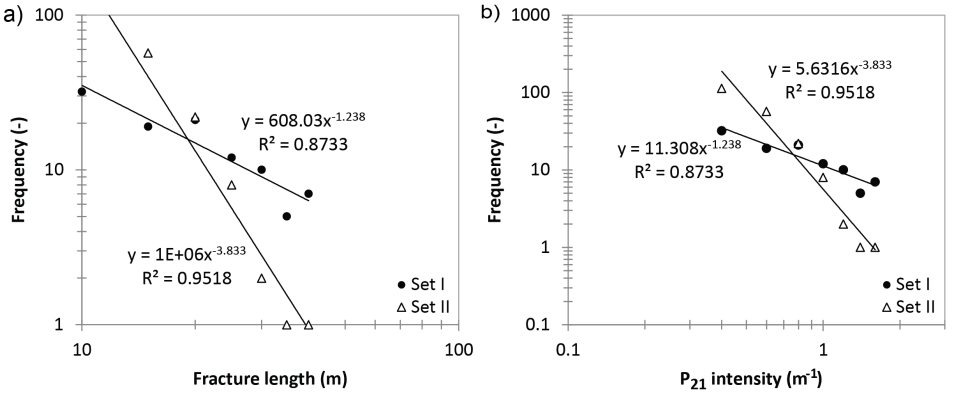


Figure 6.18: Geometrical frequency distributions for *Set I* and *Set II* fractures, digitised from the Kef Eddour Fm. pavement: a) Length frequency distributions with power-law scaling exponents of 1.2 (*Set I*) and 3.8 (*Set II*); b) P_{21} intensity distributions with power-law exponents of 1.2 and 3.8. These distributions are limited to the domain without censoring or truncation artefacts.

pavement (Table 6.1).

6.5.2. Permeability model set-up

We estimate the difference in equivalent permeability between domains with only LPS fractures versus domains with LPS- (*Set I*) and flexural-slip-related fractures (*Set II*) using 2-D equivalent permeability models with discrete fracture-matrix flow (Chapter 3). We only consider geometry as a variable, with a constant aperture of 1 mm and a constant matrix permeability of 10 mD. The relatively large constant aperture is used to generate large contrasts in permeability in the relatively low-intensity networks. The impact of heterogeneous apertures defined by a range of aperture models is quantified in Bisdom *et al.* (2016). Each network is discretised using 1-D line elements to represent the fractures, and fluid pressure and equivalent permeability are modelled using CSMP++ (Chapter 3).

Equivalent permeability is modelled in the directions parallel to *Set I* and *Set II* fractures as permeability is assumed highest in these directions. For each network, we model the fluid pressure gradient from left to right (Figure 6.19b,e) and bottom to top (Figure 6.19c,f).

6.5.3. Results

In the pre-folding network, E-W equivalent permeability increases marginally with respect to matrix permeability, as E-W connectivity is low (Figure 6.19b). In an impermeable matrix, there is no flow as there is no percolating network of fractures in this direction. In the direction parallel to the average *Set I* strike, the increase in equivalent permeability is significant, increasing from 10 mD matrix flow to more than 330 mD, as most fractures percolate the entire small dimension of the model (Figure 6.19c).

In the syn-folding network, the E-W striking fractures increase E-W equivalent

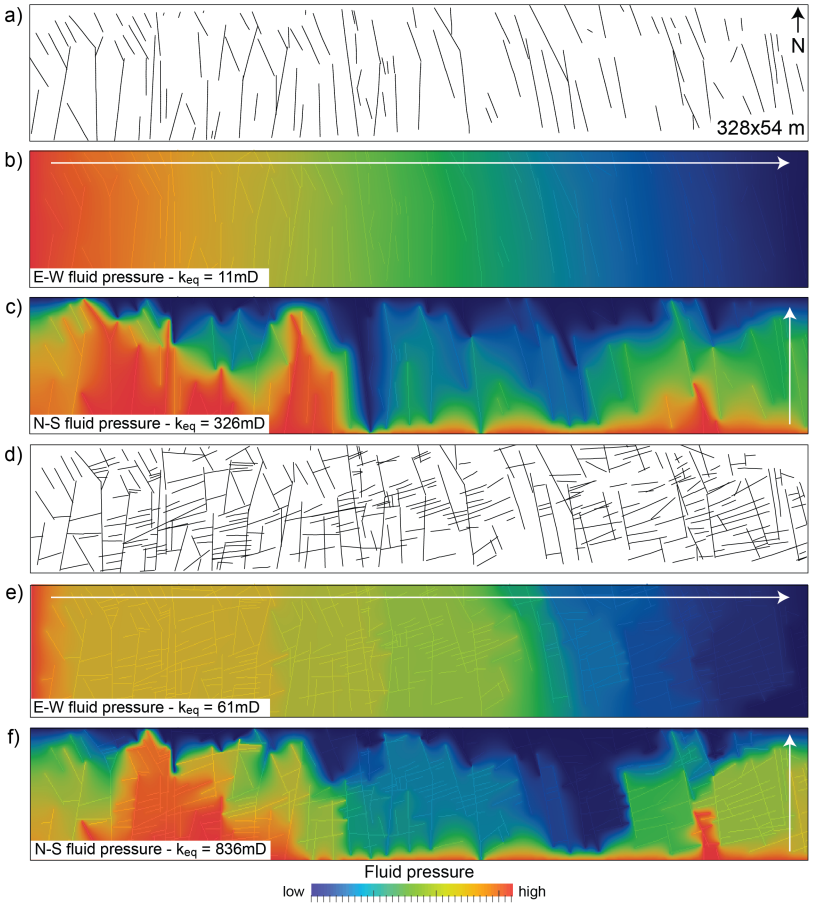


Figure 6.19: Network geometry and 2-D equivalent permeability for a section of burial-related fractures compared to a network with burial and folding-related fractures, derived from the Kef Eddour Fm. pavement from Figure 6.17: a) *Set I* network; b) Fluid pressure gradient for E-W flow; c) Fluid pressure gradient for N-S flow; d) Network consisting of *Set I* and *Set II* fractures; e) Fluid pressure gradient for E-W flow; f) Fluid pressure gradient for N-S flow. Matrix permeability in all networks is 10 mD, and the resulting equivalent permeability is listed in the lower-left corner for each model. White arrows indicate the direction of the fluid pressure gradient.

permeability sixfold with respect to matrix flow and the pre-folding flow models (Figure 6.19e). The E-W permeability remains however an order of magnitude lower compared to N-S permeability, which has increased to more than 800 mD (Figure6.19f). The E-W striking *Set II* fractures increase N-S equivalent permeability 2.5 times compared to the model with only *Set I* fractures, as *Set II* fractures connect previously isolated *Set I* fractures, which not only increases E-W permeability but also N-S permeability.

In contrast, the E-W permeability of the post-folding fracture network is relatively low, even though E-W striking fractures have a higher count and P_{21} in-

tensity compared to the N-S striking *Set I* fractures (Table 6.1). However, *Set II* fractures are smaller and hence their connectivity is lower, limiting the increase in equivalent permeability in the E-W direction.

6.6. Discussion

In the high-strain areas of the restored models, equivalent permeability related to open fractures can be up to several hundred millidarcy in the direction perpendicular to the fold axis and up to tens of millidarcy in the parallel direction (Figure 6.19). This observation is somewhat counter-intuitive, as typically the extensional folding-related fractures are interpreted to contribute more to permeability (e.g. Maffucci *et al.*, 2015), but we find that the pre-folding fractures related to LPS are larger than the syn-folding fractures (Table 6.1), resulting in a higher network connectivity in the direction of regional shortening, perpendicular to the fold axis.

P_{10} and P_{21} are not representative of these differences in connectivity, as density (P_{10}) and intensity (P_{21}) are higher for *Set II*. The P_{21} takes into account the cumulative length of fractures, but it does not distinguish between many short fractures or a few large fractures, whereas our permeability models indicate that fewer but longer fractures are preferential (Figure 6.19). Average length and the length domain should therefore also be taken into account when quantifying connectivity, for example by considering the amount of intersections within a single set through the percolation parameter defined by Robinson (1983, 1984).

The modelled permeabilities show relative trends, but likely overestimate permeability in subsurface folded reservoirs, as the impact of cementation and differential regional stresses on aperture is not taken into account. The networks studied in Brazil (Chapter 4) do take these effects into account, resulting in equivalent permeabilities that are only several times higher than matrix permeability, rather than orders of magnitude higher.

6.7. Conclusions

We have studied the impact of pre-folding regional fractures related to LPS on fold-related fracturing related to flexural slip in the outcropping Alima fold in central Tunisia. Fracture patterns were studied in different domains and separated into LPS- and flexural-slip-related fractures using 2-D and 3-D outcrop digitisation supported by isotope analysis of fracture cements (Vaughan, 2015). Based on this dataset we identify a regional set of pre-folding bed-perpendicular conjugates with a bisector angle striking parallel to the regional N-S to NW-SE shortening direction. Along the northern flank of the fold, which has experienced shallower burial, small conjugate fractures are found with a σ_2 parallel to the fold axis. These are interpreted to have formed in the same pre-folding stress field as a result of LPS, but at shallower depths where the overburden stress equals σ_3. Throughout the fold, we observe bed-perpendicular stylolites striking parallel to the fold axis, which were formed during regional shortening.

We observe conjugates and veins dipping oblique to bedding and striking par-

allel to the fold axis along the crest and steeply dipping southern flank. We interpret that these fractures are formed through flexural slip during early folding. The spatial distribution and length of these fractures are controlled by pre-folding stylolites and conjugate fractures. As a result, syn-folding fractures are shorter than pre-folding fractures.

Pre-folding fractures are observed in all studied outcrops throughout the fold, whereas syn-folding fractures are limited to the crest and steeply folded southern flank. To quantify the relative intensity of syn-folding fractures, we mechanically restore the fold to pre-folding conditions and use the resulting strain as a driver for syn-folding fracture intensity. The relative strain patterns derived from the geomechanical restoration predict large variations throughout the fold, with extensional features near the crest and a high intensity of compressional features along the southern flank. This corresponds to the observations from limited outcrop stations, but additional outcrops in different structural domains of the fold are required to further validate the strain model.

We use a network of pre- and syn-folding fractures digitised along a large dipping pavement on the southern flank of the fold to quantify relative differences in permeability associated with strain variations. In areas with high compressional strain and limited folding, permeability is controlled by pre-folding fractures. In these areas, equivalent permeability is up to 33 times higher than matrix permeability in the direction parallel to fracture strike, but there is no flow in the perpendicular horizontal direction.

In areas with high extensional strain, where pre- and syn-folding fractures are expected, permeability in the direction parallel to syn-folding fractures is up to six times higher than matrix permeability, whereas permeability in the direction parallel to pre-folding fractures is op to 83 times matrix permeability. This difference is mainly related to the larger average length and subsequent connectivity of pre-folding fractures.

In fracture modelling of folded structures, consideration and analysis of pre-folding fractures and their impact on the spatial distribution and length of syn-folding fractures may provide a more accurate quantification of permeability variations throughout the fold, rather than only considering fold-related fracturing.

References

B. J. Stephenson, A. Koopman, H. Hillgartner, H. McQuillan, S. Bourne, J. J. Noad, and K. Rawnsley, *Structural and stratigraphic controls on fold-related fracturing in the Zagros Mountains, Iran: implications for reservoir development*, Geological Society, London, Special Publications **270**, 1 (2007).

R. J. Dixon, J. K. S. Moore, M. Bourne, E. Dunn, D. B. Haig, J. Hossack, N. Roberts, T. Parsons, and C. J. Simmons, *Integrated petroleum systems and play fairway analysis in a complex Palaeozoic basin: Ghadames-Illizi Basin, North Africa*, Geological Society, London, Petroleum Geology Conference series **7**, 735 (2010).

G. Casini, P. a. Gillespie, J. Verges, I. Romaire, N. Fernandez, E. Casciello, E. Saura, C. Mehl, S. Homke, J.-C. Embry, L. Aghajari, and D. W. Hunt, *Sub-seismic frac-*

tures in foreland fold and thrust belts: insight from the Lurestan Province, Zagros Mountains, Iran, Petroleum Geoscience **17**, 263 (2011).

O. Lacombe, N. Bellahsen, and F. Mouthereau, *Fracture patterns in the Zagros Simply Folded Belt (Fars, Iran): constraints on early collisional tectonic history and role of basement faults*, Geological Magazine **148**, 940 (2011).

S. Tavani, F. Storti, B. Soleimany, M. Fallah, J. A. Muñoz, and R. Gambini, *Geometry, kinematics and fracture pattern of the Bangestan anticline, Zagros, SW Iran*, Geological Magazine **148**, 964 (2011).

N. J. Price, *Fault and Joint Development in Brittle and Semi-Brittle Rock* (Pergamon, 1966) p. 192.

P. J. Hudleston and S. H. Treagus, *Information from folds: A review*, Journal of Structural Geology **32**, 2042 (2010).

M. H. Anders, S. E. Laubach, and C. H. Scholz, *Microfractures: A review*, Journal of Structural Geology **69**, 377 (2014).

S. Bergbauer and D. D. Pollard, *A new conceptual fold-fracture model including prefolding joints, based on the Emigrant Gap anticline, Wyoming*, Geological Society of America Bulletin **116**, 294 (2004).

C. Sanders, M. Bonora, D. Richards, E. Kozlowski, C. Sylwan, and M. Cohen, *Kinematic structural restorations and discrete fracture modeling of a thrust trap: a case study from the Tarija Basin, Argentina*, Marine and Petroleum Geology **21**, 845 (2004).

G. H. Makel, *The modelling of fractured reservoirs: constraints and potential for fracture network geometry and hydraulics analysis*, Geological Society, London, Special Publications **292**, 375 (2007).

G. D. Couples and H. Lewis, *Lateral variations of strain in experimental forced folds*, Tectonophysics **295**, 79 (1998).

M. P. Fischer and P. B. Jackson, *Stratigraphic controls on deformation patterns in fault-related folds: a detachment fold example from the Sierra Madre Oriental, northeast Mexico*, Journal of Structural Geology **21**, 613 (1999).

N. Bellahsen, P. Fiore, and D. D. Pollard, *The role of fractures in the structural interpretation of Sheep Mountain Anticline, Wyoming*, Journal of Structural Geology **28**, 850 (2006).

H. M. Savage, J. Ryan Shackleton, M. L. Cooke, and J. J. Riedel, *Insights into fold growth using fold-related joint patterns and mechanical stratigraphy*, Journal of Structural Geology **32**, 1466 (2010).

A. Awdal, D. Healy, and G. I. Alsop, *Fracture patterns and petrophysical properties of carbonates undergoing regional folding: A case study from Kurdistan, N Iraq*, Marine and Petroleum Geology **71**, 149 (2016).

F. Salvini and F. Storti, *The distribution of deformation in parallel fault-related folds with migrating axial surfaces: comparison between fault-propagation and fault-bend folding*, Journal of Structural Geology **23**, 25 (2001).

M. Branellec, J. P. Callot, B. Nivière, and J. C. Ringenbach, *The fracture network, a proxy for mesoscale deformation: Constraints on layer parallel shortening history from the Malargüe fold and thrust belt, Argentina*, Tectonics **34**, 623 (2015).

J. C. Lorenz, L. W. Teufel, and N. R. Warpinski, *Regional fractures I: a mechanism for the formation of regional fractures at depth in flat-lying reservoirs*, (1991).

S. J. Roberts and J. A. Nunn, *Episodic fluid expulsion from geopressured sediments*, Marine and Petroleum Geology **12**, 195 (1995).

J. R. Shackleton, M. L. Cooke, J. Vergés, and T. Simó, *Temporal constraints on fracturing associated with fault-related folding at Sant Corneli anticline, Spanish Pyrenees*, Journal of Structural Geology **33**, 5 (2011).

A. Fall, P. Eichhubl, R. J. Bodnar, S. E. Laubach, and J. S. Davis, *Natural hydraulic fracturing of tight-gas sandstone reservoirs, Piceance Basin, Colorado*, Geological Society of America Bulletin **127**, 61 (2015).

G. Bertotti, S. de Graaf, K. Bisdom, H. Vonhof, J. Reijmer, F. Bezerra, and C. Cazarin, *Fracturing and flow during post-rift subsidence in carbonate rocks of the Jandaira Formation (NE Brazil)*, (subm).

L. Arlegui and J. Simón, *Geometry and distribution of regional joint sets in a nonhomogeneous stress field: case study in the Ebro basin (Spain)*, Journal of Structural Geology **23**, 297 (2001).

J. R. Shackleton, M. L. Cooke, and A. J. Sussman, *Evidence for temporally changing mechanical stratigraphy and effects on joint-network architecture*, Geology **33**, 101 (2005).

J. E. Olson, *Natural fracture pattern characterization using a mechanically-based model constrained by geologic dataMoving closer to a predictive tool*, International Journal of Rock Mechanics and Mining Sciences **34**, 171.e1 (1997).

J. B. Ericsson, H. C. McKean, and R. J. Hooper, *Facies and curvature controlled 3D fracture models in a Cretaceous carbonate reservoir, Arabian Gulf*, Geological Society, London, Special Publications **147**, 299 (1998).

C. J. Ormand and P. J. Hudleston, *Strain paths of three small folds from the Appalachian Valley and Ridge, Maryland*, Journal of Structural Geology **25**, 1841 (2003).

S. J. Wilkins, *Fracture intensity from geomechanical models: application to the Blue Forest 3D survey, Green River Basin, Wyoming, USA*, Geological Society, London, Special Publications **292**, 137 (2007).

E. Ukar, C. Ozkul, and P. Eichhubl, *Fracture abundance and strain in folded Cardium Formation, Red Deer River anticline, Alberta Foothills, Canada*, Marine and Petroleum Geology **76**, 210 (2016).

O. Vidal-Royo, N. Cardozo, J. A. Muñoz, S. Hardy, and L. Maerten, *Multiple mechanisms driving detachment folding as deduced from 3D reconstruction and geomechanical restoration: the Pico del Águila anticline (External Sierras, Southern Pyrenees)*, Basin Research **24**, 295 (2012).

S. Bouaziz, E. Barrier, M. Soussi, M. M. Turki, and H. Zouari, *Tectonic evolution of the northern African margin in Tunisia from paleostress data and sedimentary record*, Tectonophysics **357**, 227 (2002).

P. Riley, C. Gordon, J. a. Simo, B. Tikoff, and M. Soussi, *Structure of the Alima and associated anticlines in the foreland basin of the southern Atlas Mountains, Tunisia*, Lithosphere **3**, 76 (2011).

A. Saïd, P. Baby, D. Chardon, and J. Ouali, *Structure, paleogeographic inheritance, and deformation history of the southern Atlas foreland fold and thrust belt of Tunisia*, Tectonics **30** (2011a), 10.1029/2011TC002862.

A. Saïd, D. Chardon, P. Baby, and J. Ouali, *Active oblique ramp faulting in the Southern Tunisian Atlas*, Tectonophysics **499**, 178 (2011b).

F. Outtani, B. Addoum, E. Mercier, D. F. de Lamotte, and J. Andrieux, *Geometry and kinematics of the South Atlas Front, Algeria and Tunisia*, Tectonophysics **249**, 233 (1995).

A. Hlaiem, *Halokinesis and structural evolution of the major features in eastern and southern Tunisian Atlas*, Tectonophysics **306**, 79 (1999).

C. Swezey, *Structural controls on Quaternary depocentres within the Chotts Trough region of southern Tunisia*, Journal of African Earth Sciences **22**, 335 (1996).

R. Bekkers, *Discrete Fracture Networks in carbonate anticlines: an example from the Berda Anticline in Southern Tunisia*, M.sc. thesis, Delft University of Technology (2013).

S. Toby, *Rock properties and synthetic seismic modeling of anticlines in the Gafsa region, Tunisia*, Msc thesis, VU University Amsterdam (2013).

D. Boeser, *Fracture modelling based on kinematic evolution: Example of the Sehib anticline*, M.sc. thesis, Delft University of Technology (2014).

R. Vaughan, *Fracture and vein development in the Alima Anticline, Southern Tunisian Atlas*, M.sc. thesis, VU University Amsterdam (2015).

N. Hardebol and G. Bertotti, *DigiFract: A software and data model implementation for flexible acquisition and processing of fracture data from outcrops*, Computers & Geosciences **54**, 326 (2013).

K. Bisdom, B. Gauthier, G. Bertotti, and N. Hardebol, *Calibrating discrete fracture-network models with a carbonate three-dimensional outcrop fracture network: Implications for naturally fractured reservoir modeling*, AAPG Bulletin **98**, 1351 (2014).

S. Tavani, P. Granado, A. Corradetti, M. Girundo, A. Iannace, P. Arbués, J. Muñoz, and S. Mazzoli, *Building a virtual outcrop, extracting geological information from it, and sharing the results in Google Earth via OpenPlot and Photoscan: An example from the Khaviz Anticline (Iran)*, Computers & Geosciences **63**, 44 (2014).

A. Pengel, *Characterization of Natural Fractures in the Upper Berda Formation of the Alima Anticline, Tunisia*, B.sc. thesis, Delft University of Technology (2014).

K. Althuis, *Characterizing fractures and their relation with the structural setting in 3D using novel photogrammetry tools*, B.sc. thesis, Delft University of Technology (2014).

E. Bonnet, O. Bour, N. E. Odling, P. Davy, I. Main, P. Cowie, and B. Berkowitz, *Scaling of fracture systems in geological media*, Reviews of Geophysics **39**, 347 (2001).

T. Zouaghi, M. Bédir, H. Abdallah, and M. H. Inoubli, *Seismic sequence stratigraphy, basin structuring, and hydrocarbon implications of Cretaceous deposits (AlbianMaastrichtian) in central Tunisia*, Cretaceous Research **30**, 1 (2009).

P. Geoff Tanner, *The flexural-slip mechanism*, Journal of Structural Geology **11**, 635 (1989).

Midland Valley Exploration Ltd., *Move 2014.1*, (2014).

P. Durand-Riard, C. Guzofski, and J. H. Shaw, *Applying new restoration techniques to better understand the regional evolution of the outer fold-and-thrust belt, Niger Delta*, in *Proc. 32nd Gocad Meeting, Nancy* (Gocad Research Group, Nancy, France, 2012).

T. Zouaghi, M. H. Inoubli, and M. Bédir, *Contribution of seismic velocity studies to structural and lithostratigraphic reconstructions: Salt-intruded corridor ceiling and Lower Turonian Beida anhydrite deposits' outline in the centralsouthern Atlas of Tunisia*, Comptes Rendus Geoscience **339**, 13 (2007).

T. Zouaghi, I. Ferhi, M. Bédir, M. B. Youssef, M. Gasmi, and M. H. Inoubli, *Analysis of Cretaceous (Aptian) strata in central Tunisia, using 2D seismic data and well logs*, Journal of African Earth Sciences **61**, 38 (2011).

G. Caumon, J. Clement, D. Riffault, and C. Antoine, *Modeling of geological structures accounting for structural constraints: faults, fold axes and dip domains.* in *Proc. 29th Gocad Meeting, Nancy* (2009).

G. Caumon, G. Gray, C. Antoine, and M.-O. Titeux, *Three-Dimensional Implicit Stratigraphic Model Building From Remote Sensing Data on Tetrahedral Meshes: Theory and Application to a Regional Model of La Popa Basin, NE Mexico*, IEEE Transactions on Geoscience and Remote Sensing **51**, 1613 (2013).

P. Durand-Riard, G. Caumon, and P. Muron, *Balanced restoration of geological volumes with relaxed meshing constraints*, Computers and Geosciences **36**, 441 (2010).

S. Ranjan, *Mechanical modelling of the stress state in a reservoir-scale fold during and after folding*, M.sc. thesis, Delft University of Technology (2015).

L. Maerten and F. Maerten, *Chronologic modeling of faulted and fractured reservoirs using geomechanically based restoration: Technique and industry applications*, AAPG Bulletin **90**, 1201 (2006).

P. A. Roskam, *Sub-Seismic Deformation in the Sabria Oilfield, Central Tunisia*, M.sc. thesis, Delft University of Technology (2016).

M. E. Sigismondi and J. C. Soldo, *Curvature attributes and seismic interpretation: Case studies from Argentina basins*, The Leading Edge **22**, 1122 (2003).

S. Bergbauer, *Testing the predictive capability of curvature analyses*, Geological Society, London, Special Publications **292**, 185 (2007).

N. Odling, *Scaling and connectivity of joint systems in sandstones from western Norway*, Journal of Structural Geology **19**, 1257 (1997).

W. Dershowitz, *MIT*, Ph.d. thesis, Massachusetts Institue of Technology, Cambridge, MA. (1985).

K. Bisdom, G. Bertotti, and H. M. Nick, *The impact of different aperture distribution models and critical stress criteria on equivalent permeability in fractured rocks*, Journal of Geophysical Research: Solid Earth **121**, 4045 (2016).

R. Maffucci, S. Bigi, S. Corrado, A. Chiodi, L. Di Paolo, G. Giordano, and C. Invernizzi, *Quality assessment of reservoirs by means of outcrop data and discrete fracture network models: The case history of Rosario de La Frontera (NW Argentina) geothermal system*, Tectonophysics **647-648**, 112 (2015).

P. C. Robinson, *Connectivity of fracture systems-a percolation theory approach*, Journal of Physics A: Mathematical and General **16**, 605 (1983).

P. C. Robinson, *Numerical calculations of critical densities for lines and planes*, Journal of Physics A: Mathematical and General **17**, 2823 (1984).

7

Conclusion

In this Thesis, we have studied outcropping and subsurface regional fracture patterns that were formed during burial in compressional domains, to characterise their geometry, relation with regional and local stress conditions and potential impact on permeability in naturally fractured reservoirs.

Improved methodology for fractured reservoir flow modelling

Studying regional fractures in outcrops requires quantitative multiscale fracture datasets to derive representative distributions and to separate regional burial-related fractures from more recent deformation related to exhumation or folding. To acquire these datasets efficiently, we have developed a flexible outcrop digitisation workflow where we extract 2-D fracture patterns and attributes from 2-D and 3-D outcrop models (Chapter 2). This workflow combines high-resolution 3-D outcrop modelling techniques using an Unmanned Aerial Vehicle (UAV) and photogrammetry with 2-D fracture digitisation, the combination of which ensures fast but accurate extraction of all relevant parameters. In terms of effectiveness, this method is as fast as scanlines, as it provides results almost immediately during a fieldwork campaign, although the amount of relevant data and its accuracy are closer to what is typically obtained using LiDAR techniques.

We recognise that although outcrops provide fracture geometry, they are no proxy for fluid flow, as outcropping apertures are not representative for subsurface conditions. To assess the potential impact of regional fracture patterns digitised in outcrops on permeability in reservoirs, we develop a workflow for modelling stress-induced aperture and permeability, using estimated subsurface stress conditions (Chapter 3). The stress-induced aperture is defined using the Barton-Bandis model for conductive shear fractures, which considers apertures associated with the intrinsic roughness and strength of fractures that are not critically stressed as defined by Mohr-Coulomb. We consider this model representative for the mostly hybrid Mode I-Mode II regional fractures observed in the studied outcrops in Brazil and Tunisia (Chapters 4 and 6). Apertures predicted by this model are relatively small, i.e. less than 0.5 mm, but overall connectivity and subsequent equivalent permeability can be high as this model predicts that only a small subset of the network is fully closed at depth (Chapter 3). One limitation however is that the Barton-Bandis model requires the input of local stress and shear displacement, obtained from Finite Element (FE) models, but we derive an approximation based on far-field stresses and fracture network geometry to calculate aperture and permeability in networks for which FE modelling is not feasible (Appendix B).

To quantify the implications of realistic fracture patterns with heterogeneous stress-induced apertures on flow, we model permeability in discrete fracture networks, avoiding upscaling. We take into account matrix permeability to assess the relative impact of fracture versus matrix flow. This approach has been applied in other works, but the scale and complexity of fracture patterns in earlier studies were limited to tens of fractures in relatively small outcrops. By using an integrated approach combining our database of digitised high-resolution outcrops with the discrete permeability modelling approach, we model flow in networks containing more than a thousand discrete fractures, partly bridging the gap between outcrop-

scale and reservoir-scale fracture flow models.

Characterisation of burial-related fractures and implications for fractured reservoir modelling

We apply the methodology from Chapters 2 and 3 to quantify the permeability potential associated with regional fractures in three case studies:

i) Sub-horizontal outcropping carbonate pavements in the Potiguar basin, NE Brazil (Chapter 4);
ii) Sub-horizontal subsurface shales in the Neuquén basin, Argentina (Chapter 5);
iii) Folded outcropping carbonates in the Gafsa basin, Tunisia (Chapter 6).

Burial-related fractures in the Potiguar basin, Brazil

Sub-horizontal outcropping carbonate pavements in the Potiguar basin have experienced no major folding or faulting and relatively shallow maximum burial (Chapter 4). These rocks are nonetheless intensely fractured, as we observe high-intensity systems of bed-perpendicular joints and conjugate fractures with indications of opening and shear, and bed-perpendicular stylolites. Through combined interpretation of fracture geometry, cement composition, and fluid inclusion isotope analysis, we find that most of the fractures and stylolites were formed during burial, driven by regional N-S shortening at relatively shallow depths (i.e. less than 800 m). Most barren fractures, stylolites and veins are aligned to this stress field. However, we also observe E-W striking bed-perpendicular barren fractures, which are formed along pre-existing bed-perpendicular stylolites. These barren fractures are the result of stress relief during exhumation, and are not representative of the subsurface network. We separate exhumation-related effects, and quantify the horizontal reservoir permeability representative of subsurface conditions of the burial-related regional fracture networks. We show that regional fractures contribute to permeability at in-situ conditions, but when exhumation-related deformation is not accurately characterised, permeability is significantly overestimated. We further use our unique database of digitised fractures to quantify other uncertainties associated with naturally fractured reservoir modelling, which includes comparing the impact of different aperture methods and matrix permeabilities on equivalent permeability. We find that average aperture and fracture porosity without quantification of the spatial connectivity are insufficient as a proxy for equivalent permeability, and that aperture predicted by the investigated methods is more heterogeneous than what is typically considered in reservoir flow models.

Burial-related natural fractures versus induced fracturing in the Neuquén basin, Argentina

Even in situations where burial-related natural fractures do not contribute to fluid flow at in-situ conditions, they can impact reservoir development and hydrocarbon recovery. We present a case study of burial-related fractures in the shales of the Vaca Muerta Fm. in the Neuquén basin (Argentina) to illustrate the geomechanical impact of burial-related fractures on induced hydraulic fracturing (Chap-

ter 5). Within a pilot area, hydraulic fracturing of two horizontal wells and a vertical well indicates that mechanically, the Vaca Muerta Fm. is heterogeneous, as induced fracture height and the Stimulated Rock Volume (SRV) are highly variable. Within this pilot area, there is no seismic-scale faulting or folding, and the lithological interpretation is relatively homogeneous. Core data and borehole images indicate a high intensity of subseismic-scale natural fractures. These fractures are bed-perpendicular conjugates and joints, striking sub-parallel to the regional N070 shortening direction. Core analysis of fracture infill shows that part of these fractures are open, but the in-situ stress field prevents flow. We apply the Barton-Bandis method (Appendix B) to a discrete fracture network of natural fractures to quantify the equivalent permeability if the natural fractures are reactivated through shearing induced by water injection during hydraulic fracturing.

We use a coupled stress-pore pressure FE model to illustrate how these natural fractures can limit hydraulic fracture height and to model the distribution of the SRV, taking into account the potential for increased permeability associated with reactivated natural fractures and particularly fracture corridors. A relatively small increase in in-situ pore pressure is sufficient to reactivate fractures in these corridors, which results in an increase of equivalent permeability sub-parallel to the regional N070-striking σ_1 from nanodarcy to up to tens of millidarcy. The characterisation of regional natural fractures and their simulated impact on the SRV helps to optimise the hydraulic fracturing strategy of the Vaca Muerta shales.

Burial-related and folding-related fractures in the Gafsa basin, Tunisia

The study of the outcropping fold in the Gafsa basin (Tunisia) shows that part of the natural fractures across the fold are pre-folding, formed by Layer Parallel Shortening (LPS; Chapter 6). We separate these features from later syn-folding deformation associated with flexural slip through a combined study of fracture geometry and cement and isotope analyses. We find that the LPS-related fractures control the spatial distribution of syn-folding fractures, as the latter abut against LPS-fractures and preferentially form along pre-folding bed-perpendicular stylolites. Using strain patterns derived from a 3-D geomechanical restoration of the fold geometry, we define relative spatial trends in syn-folding fracture intensity and reactivation potential of LPS-fractures across the fold. We quantify fracture permeability for the different fold domains using our equivalent permeability modelling approach (Chapter 3). As pre-folding fractures are longer and more persistent throughout the fold, they contribute more to permeability than syn-folding fractures, although the combination of syn-and pre-folding fractures significantly increases connectivity and permeability in the direction parallel to the fold axis.

Synopsis

The three case studies show that regional burial-related fractures not only have a potentially large impact on subsurface permeability (Chapter 4), but that they mechanically control the geometry and distribution of more recent fracturing, both induced (Chapter 5) and natural (Chapter 6). Although the impact of regional fractures on permeability is sometimes considered, for example in the outcrops of the

Bristol Channel fracture systems and their subsurface analogue reservoirs, the mechanical role of burial-related fractures is less commonly recognised. We show however, that fracture development and aperture are strongly controlled by subsurface stresses, and that fractured reservoir permeability cannot be assessed without a detailed understanding of the relation between in-situ stress and fracturing.

The workflows and methodology presented in Chapters 2 and 3 help to further integrate detailed and realistic fracture patterns obtained from outcrops with stress and permeability distributions representative of subsurface conditions. The presented methods are fast and support large fracture systems with irregular geometries, although they are limited to 2-D and do not take into account the impact of (partial) cementation on fracture growth and permeability. We have successfully calibrated our methodology to correctly predict the aperture and permeability range of the natural fractures in the Vaca Muerta Fm., but further calibration and development toward 3-D is required to deploy our methods to predict fracture permeability in fractured reservoirs. This Thesis does, however, present an integrated and calibrated workflow that serves as a framework onto which further improvements and calibrations can be added.

A

Generating intersecting fracture seams in 2-D meshes

A

Throughout this Thesis we use ABAQUS ® (Dassault Systèmes®) to model stress and strain around natural fractures, which are represented as mechanical discontinuities by creating seams in the mesh. However, the user interface ABAQUS CAE® does not support intersecting seams, which is inconvenient as most natural fracture networks contain intersecting fractures. To overcome this limitation, we have created a tool that generates intersecting seams based on an input mesh with predefined fracture elements and nodes (Figure A.1). This tool, the *Intersecting Seams Generator* (ISG), is written in `Python` and reads any 2-D triangulated mesh.

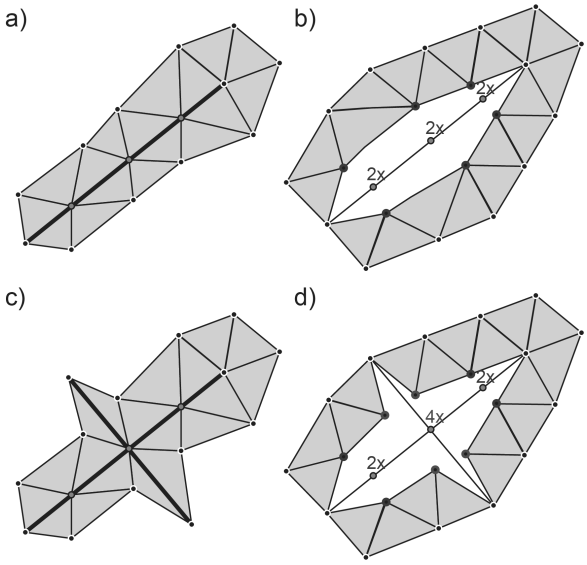


Figure A.1: Converting fractures into seams in a 2-D mesh: a-b) Converting a single fracture into a seam by duplicating the centre nodes of the fracture; c-d) Converting two intersecting fractures into seams, requiring one node to be duplicated four times. The latter is not supported by ABAQUS CAE.

Pre-processing: Building a 2-D fracture mesh

We generate a simulation input file for a 2-D fracture model using ABAQUS CAE. This simulation file is an `ASCII` file containing the mesh, material properties, boundary conditions and simulation steps. A simplified version of an input file is shown in Figure A.2. The fractures are created by partitioning the model. The internal geometry is considered during meshing, resulting in a mesh that is conformable to the fracture network, but these features are not recognised as mechanical discontinuities during simulations (Figure A.3a,b).

To avoid convergence issues, the mesh should be refined around the fractures, and particularly around the termination points. To avoid singularity effects, small circles can be generated around the tips of fractures to force further refinement. The ISG currently supports linear elements, i.e. each element is defined by three nodes. After generating the intersecting seams, the mesh can be read into ABAQUS CAE

and converted to quadratic elements. The intersections will be maintained during this conversion.



Figure A.2: Structure of an input file: 1) Node identifiers and node x and y coordinates; 2) Element identifiers, with the identifiers of the three nodes connected to each element; 3) Node identifiers that are part of fracture set 1; 4) Elements that are connected to two nodes from fracture set 1; 5) Node identifiers for fracture set 2; 6) Element identifiers for fracture set 2.

After meshing, the fractures need to be classified as geometry sets to identify which nodes and elements are part of a fracture. Each set can contain any number

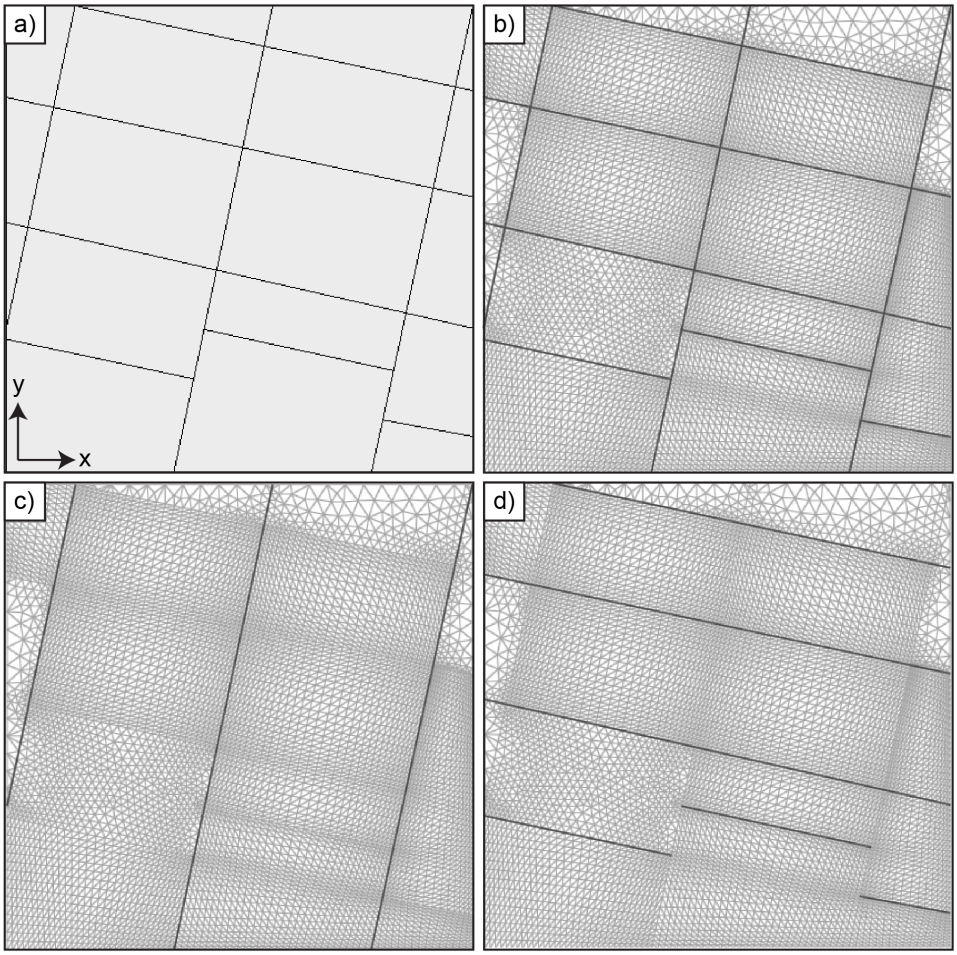


Figure A.3: Constructing a mesh for a synthetic fracture network: a) 50×50 m model with internal geometry representing the fractures; b) Meshed model with mesh refinements near the fractures; c) NNW-SSE striking fractures are defined as set 1; d) ESE-WNW striking fractures are defined as set 2.

of fractures, as long as there are no intersections or any two fractures that share a single element within a set. This means that for two intersecting fractures, two separate sets need to be defined (Figure A.3c-d and A.4). There is no limit to the amount of sets defined, and for fast processing it is preferential to define a large number of sets with a relatively small amount of fractures within each set, rather than a few sets with a large amount of fractures.

After generating the mesh and the sets, all other aspects of the model can be defined, such as interaction properties, loads and boundary conditions. Once all components of the model are added, the model is exported to a simulation input file (Figure A.1).

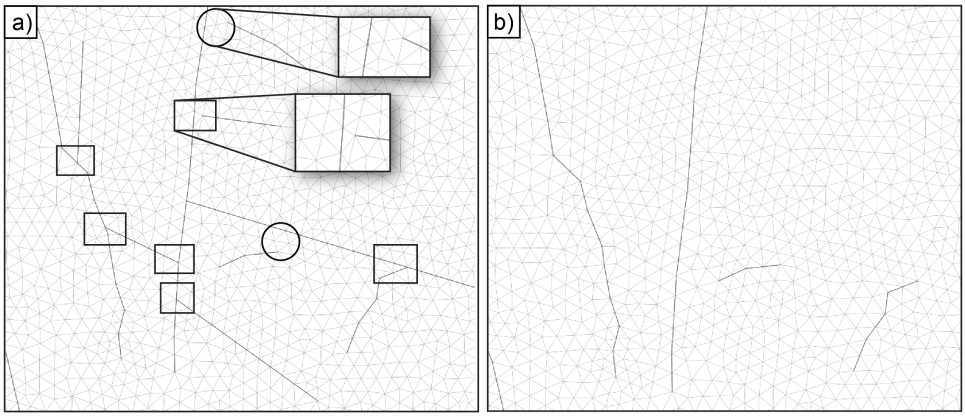


Figure A.4: To identify where one fracture stops and another continues, each element should only be connected to one fracture within a single fracture set: a) A fracture network with several connecting fractures or nearly connecting fractures, resulting in multiple fractures connecting to single elements, highlighted by the black boxes. The circles indicate areas where fractures are separated by at least two elements, preventing problems; b) A single fracture set is defined that consists only fractures that do not share single elements.

Generating intersecting fracture seams

The ISG reads the input file and identifies the nodes of the entire mesh and of the individual fracture sets, their coordinates and the elements to which they are connected. After generating intersecting seams, the updated mesh is written to a new input file that can be submitted directly to the simulator. The workflow explained in the following sections is also summarised in a flowchart (Figure A.5).

Generating seams for one fracture set

The first step is to create seams for non-intersecting fractures within a single set, duplicating the nodes along a fracture and reassigning them to the correct elements.

Identifying and duplicating fracture nodes

We start by identifying the number of fractures within a set, followed by identifying which nodes and elements belong to a single fracture. In addition, a distinction has to be made between nodes at the terminations of fractures and nodes along the centre part of fractures, as only the latter group needs to be duplicated to generate seams. To identify the *end-fracture-nodes*, we make use of the fracture elements obtained from the input file. For each given fracture node, we list the number of fracture elements it is connected to. If this number is larger than three, the node is somewhere along the middle of the fracture, and needs to be duplicated (*doubleFracNodes*; Figure A.6). If only two fracture elements are found for a given node, it is at the end of a fracture, and will be stored in a separate list (*endFracNodes*). Nodes in this list do not need to be duplicated, but are used to determine the amount of fractures contained within a set, which is the number of *endFracNodes* divided by

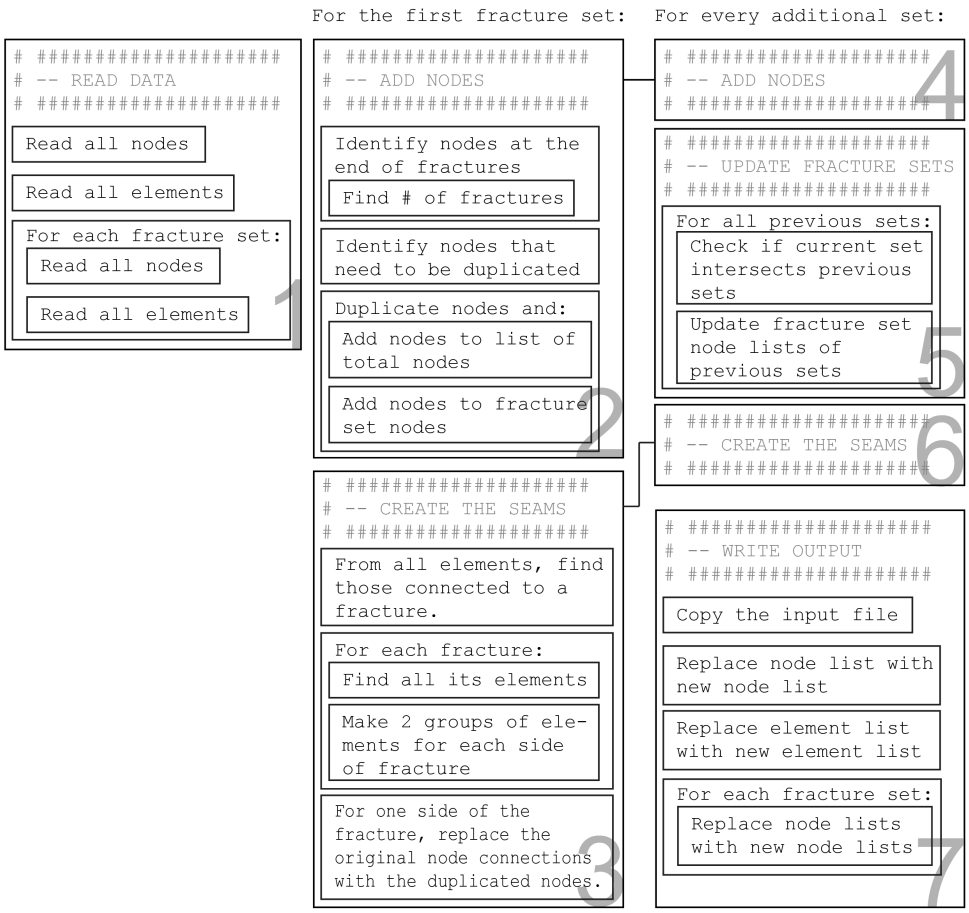


Figure A.5: The main functions if the ISG, used to read data (1), find and duplicate fracture nodes (2), reassign element-node connections to generate seams (3), generate seams for intersecting fracture sets (4-6) and write the updated mesh to an output file (7).

two. After all nodes are classified according to their position along a fracture, the *doubleFracNodes* are duplicated and added to the mesh.

Identifying fracture elements

In the input file, only elements that have two nodes connecting to the fracture are listed as fracture elements (Figure A.6). However, for generating seams, all elements that share at least one node with a fracture need to be processed. To identify these elements, we need to search through the entire mesh and identify elements that are linked to fracture nodes. Similar to the nodes, a distinction is made between elements that are at the end points of a fracture (*endFracElements*) versus those in the middle (*doubleFracElements*).

To generate seams, elements on one side of the fracture need to be connected

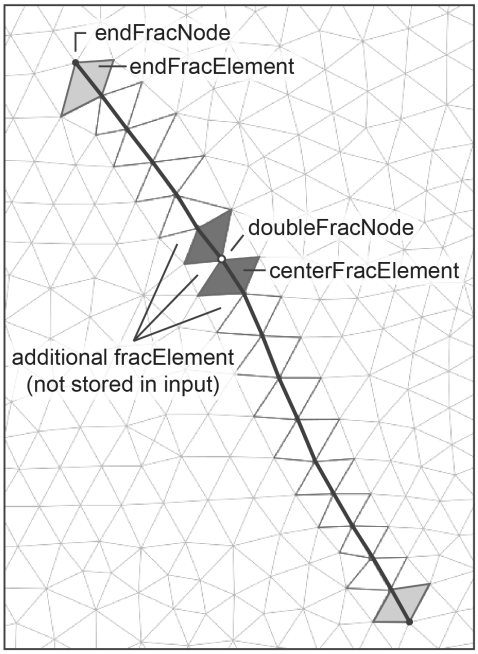


Figure A.6: Identifying fracture nodes and fracture elements. The fracture is defined by the black line. All nodes along this line are stored as fracture nodes in the input file, but for the fracture elements, only the red elements are stored. For each fracture, the ISG separates the nodes at the ends of the fracture (*endFracNodes*) from all other fracture nodes (*doubleFracNodes*) by looking at the number of (red) fracture elements connected to each node. Next, the fracture elements are found by collecting all elements that connect to one or more fracture nodes.

to the newly generated duplicate nodes, while elements on the other side need to remain connected to the original nodes. To identify all elements that are part of a single fracture, we start with a random fracture element, and search for the elements that are adjacent to this element and that are on the same side of the fracture (Figure A.7a). The shared nodes between the elements are used to identify these adjacent elements. If two elements share two nodes, and only one is a fracture node, then these elements must be adjacent and on the same side of a fracture (Figure A.7b). This process is repeated until the end of a fracture is reached, which we find using the *endFracElements* list. At this point, we return to the original element and start searching for adjacent elements in the other direction (Figure A.7b-c). The resulting group of elements is stored in a list of *adjacentElements*. After finding all elements on one side of a fracture, we can request all other elements that are connected to this fracture, based on the shared fracture nodes (Figure A.7d). These elements are stored in the list of *oppositeElements*. Using this method, all individual fractures and their corresponding nodes and elements are identified, without needing any a-priori information on fracture geometry. The trade-off, however, is that this process is computationally expensive, as for each element the entire list of

available fracture elements needs to be checked. For this reason, it is recommended to limit the number of fractures within each geometry set, and instead increase the number of sets.

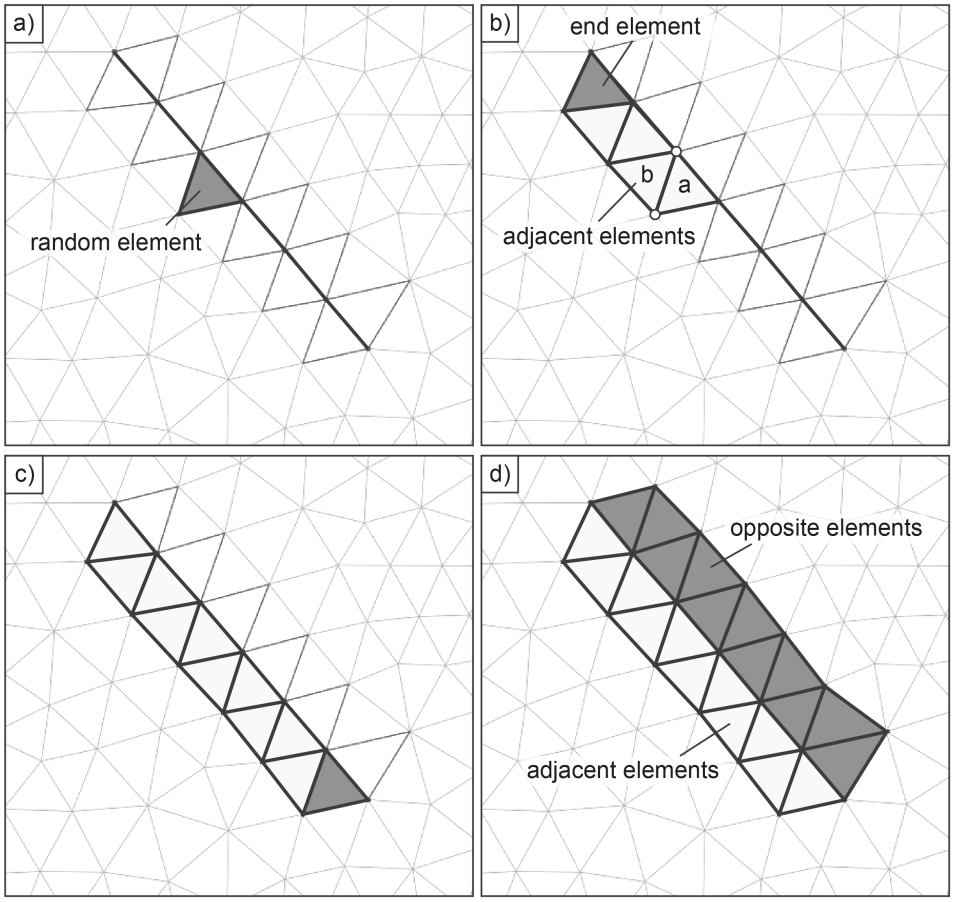


Figure A.7: Visual representation of identifying all elements connecting to one fracture, and separating them into two groups for both sides of the fracture: a) The ISG starts with a random fracture element; b) By looking at the number of shared nodes versus shared fracture nodes, element *b* adjacent to original element *a* is found. This process is repeated until we reach an *endFracElement*; c) The ISG returns to the original element and finds adjacent elements in the other direction, until all elements at one side of the fracture are found; d) all remaining elements of this fracture must then be on the other side of the fracture.

Reassigning nodes and elements

The last step for generating seams is to reassign the elements on one side of each fracture to the newly created duplicate nodes. All elements that need to be updated have been stored in *adjacentElements*, and for each original node, its duplicate node identifier is known. The seams are created by replacing the original node identifier

with its duplicate for all elements on one side of the fracture, which results in an updated list of elements with their new node connections. The result of the three steps of duplicating nodes, identifying fracture elements and reassigning the new nodes to part of the fracture elements is a list of nodes with their coordinates and a list of elements with their connections, which have the same format as the original mesh, with the exception of several added nodes and reassigned element-node connections.

Intersecting fracture sets

The process of creating multiple intersecting sets of seams is in principle simple, as it repeats mostly the steps used to generate a single set of seams. The main challenge is to properly duplicate and reorganise the nodes of a new seam that intersects an existing seam from a different fracture set, as the two nodes of the previous seam need to be duplicated to four nodes for the new set (Figure A.8). After processing one set, the fracture set nodes of all previously processed sets are checked to see if any nodes have been duplicated again, and the node connections are updated accordingly.

This process is illustrated for three intersecting fractures, which are stored in three sets that are processed one-by-one (Figure A.8a). After processing the first set, a duplicate node `101` of node `1` is created (Figure A.8b). For the second fracture set, nodes `1` and `101` are duplicated, to form nodes `201` and `202`, again at identical positions (Figure A.8c). For two intersecting fractures, all nodes at the position of the intersection simply need to be duplicated for each fracture.

For every additional fracture, only two additional nodes should be added (Figure A.8d). Nodes `201` and `202` are duplicated to form nodes `301` and `302`, while nodes `1` and `101` are not copied. To keep track of this process, a list is maintained and updated for each node duplication, containing pairs of original and duplicate nodes and statistics on how many times each node has been duplicated. Hence, fracture intersections are generated by making sure the node identifiers for each fracture set are always kept up to date after each processed set. The intersections are then generated step by step by adding and reassigning nodes.

T-intersections

In some fracture networks, one fracture abuts against another fracture, forming T-intersections (e.g. at the bottom in the model in Figure A.3). For these intersections, not four, but three nodes are needed to allow the fractures to open. These intersections are identified by checking whether any of the nodes that are part of the intersection, have been identified as nodes at the end of a fracture. In this case, this node will not be duplicated, resulting in a three-way intersection.

Output

After processing all fracture sets, the following sections are updated in the original input file, which can be imported in the model building and simulation tools of FE simulators for further processing:

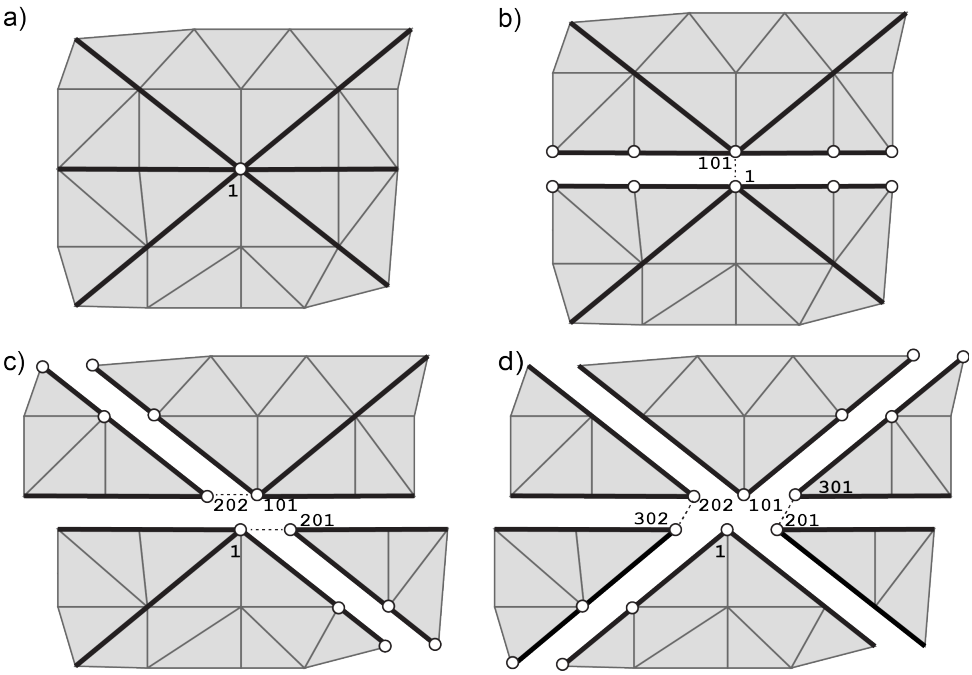


Figure A.8: Example illustrating the process of generating complex fracture intersections for three fractures that share a single intersection. The original node at this intersection, with identifier `1`, is duplicated several times to generate the intersecting seams. See text for more details.

i) The list of fracture nodes and their coordinates, extended with the newly created fracture nodes.
ii) The list of elements and their corresponding node connections, where for part of the fracture elements, the node connections are updated for the newly generated nodes.
iii) The list of fracture nodes for each fracture set, updated with the newly added fracture nodes.
iv) All other node sets, for example those used to define model boundaries, are checked to see if they contain any fracture nodes, and the corresponding duplicate nodes are added to these lists.

B

A geometrically-based method for predicting stress-induced fracture aperture and flow in Discrete Fracture Networks

This appendix is based on: K. Bisdom, G. Bertotti, H.M. Nick (2016). A geometrically-based method for predicting stress-induced fracture aperture and flow in Discrete Fracture Networks. AAPG Bulletin 100 (7), 1075-1097.

B

Relation between aperture and fracture geometry

Application of the Barton–Bandis method in Chapter 3 requires Finite Element (FE) models, which may not be feasible for application to reservoir-scale fracture models. We present a geometrical method for approximating Barton–Bandis aperture that does not require FE models. We analyse the relations between in-situ stress, fracture geometry and Barton–Bandis aperture using synthetic single-fracture and intersecting fracture models (Figure B.1). Geometrical properties including length, block size, spacing and orientation are varied for a range of stresses to analyse the impact on hydraulic fracture aperture.

Single-fracture FE models

The angle between fracture strike and the direction of σ_1, defined as stress angle α, is varied for the single-fracture FE model. We apply an initial maximum aperture of 0.3 mm at the centre of the fracture (Figure B.1a). The resulting mechanical and hydraulic apertures as a function of α, averaged along the length of the fracture, are shown in Figure B.2a.

Overall, mechanical aperture, averaged over the entire fracture, decreases from 0.2 mm to 0.18 mm at 30 MPa compression. Mechanical aperture is largest for fractures parallel to the direction of compression ($\alpha = 0°$), as the fracture opens in the direction of σ_3. For an increase in α, mechanical aperture decreases. At $\alpha = 90°$, the fracture is maximally closed. Maximum aperture, i.e. aperture at the centre of the fracture, follows the same distribution, starting at 0.3 mm for $\alpha = 0°$.

As only small amounts of shear occur on surfaces parallel or perpendicular to σ_1 (i.e. $\alpha = 0°$ and $\alpha = 90°$), it follows that the fracture is hydraulically closed at these angles. When α starts to increase, shear displacement increases, resulting in an increase in hydraulic aperture. At 15°, shear displacement exceeds peak shear displacement, resulting in the largest hydraulic aperture (Figure B.2b). For an increasing angle up to $\alpha = 45°$, the amount of shear displacement increases, but mechanical aperture decreases. For angles between 40–70°, the hydraulic aperture decreases with decreasing mechanical aperture. For $\alpha > 70°$, shear displacement and hydraulic aperture decrease to zero.

Hydraulic aperture is a function of shear displacement, which is controlled by α (Figure B.2b). We can describe this relation using:

$$\sigma_{n,\text{single}} = \sigma_1 \left(-0.33 \cos\left(\alpha\pi\right) + 0.65\right) \tag{B.1}$$

where $\sigma_{n,\text{single}}$ is the normal stress for a single fracture that is not intersected by any other fractures.

Multi-fracture models

We analyse mechanical and hydraulic aperture in multi-fracture FE models using a synthetic model (Figure B.1b), focusing on the five fractures belonging to orientation *set 1*. The length of all fractures in the model is 12 m, with a constant spacing of 2 m (i.e. block size $L = 2m$). To study the relation between α and hydraulic aperture, the entire system is rotated by α. The model dimensions are 150 × 150 m, i.e.

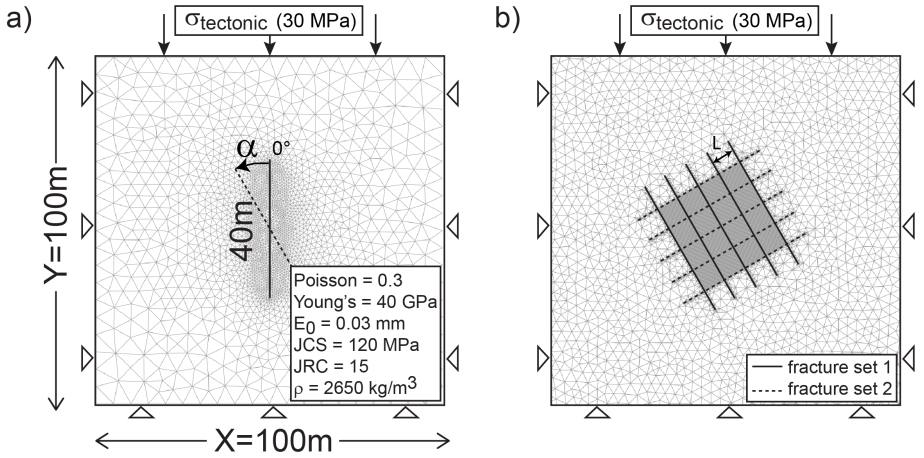


Figure B.1: Set-up for 2-D mechanical FE models. A tectonic stress (σ_1) is applied in one direction, resulting in a Poissons stress (σ_3) in the perpendicular direction: a) Single-fracture model where the angle between σ_1 and fracture strike is defined by α; b) System of two perpendicular fracture sets with a constant block size L. In all models the mesh around the fractures is locally refined, to capture in detail the stress distribution around the fractures.

large enough to avoid any boundary stress effects. The size of the elements around the fractures is refined to 0.1 m.

The resulting mechanical aperture, averaged for the entire set, is similar to that of single-fracture models (Figure B.2c). The average mechanical aperture per fracture changes only slightly, and is largest for $\alpha = 0°$. Compared to the single-fracture model, the trend of the distribution is slightly more irregular, as nearby fractures create a more heterogeneous stress field. This becomes clear when looking at normal stress and shear displacement (Figure B.2d). The shear displacement versus fracture orientation trend has a parabolic shape, similar to that of the single-fracture model in Figure B.2b, but the distribution is more irregular as the amount of shear varies per section of the different fractures. The relation between normal stress and α has changed, following a linear trend instead of the cosine function defined by equation B.1.

The irregular shear displacement profile of *set 1* has implications for the resulting hydraulic aperture (Figure B.2c). Similar to the single-fracture model, fractures are hydraulically closed when α is close to 0° and 90°, but the distribution is more irregular for the domain in between 5–85°. Furthermore, the shape of the distribution is stress-dependent. Increasing stress from 10 to 30 and 60 MPa yields a linear increase in normal stress, shear displacement, and mechanical aperture, whereas for hydraulic aperture, there is an increase for some values of α versus a decrease for other values (Figure B.2c-d). Specifically, for stresses of 10–30MPa, hydraulic aperture versus α follows a normal distribution, with aperture increasing for increasing stress. When σ_1 is 60 MPa, the normal distribution changes into a distribution with two peaks, with high apertures for $\alpha \approx 30°$ and $\alpha \approx 60°$, but a small

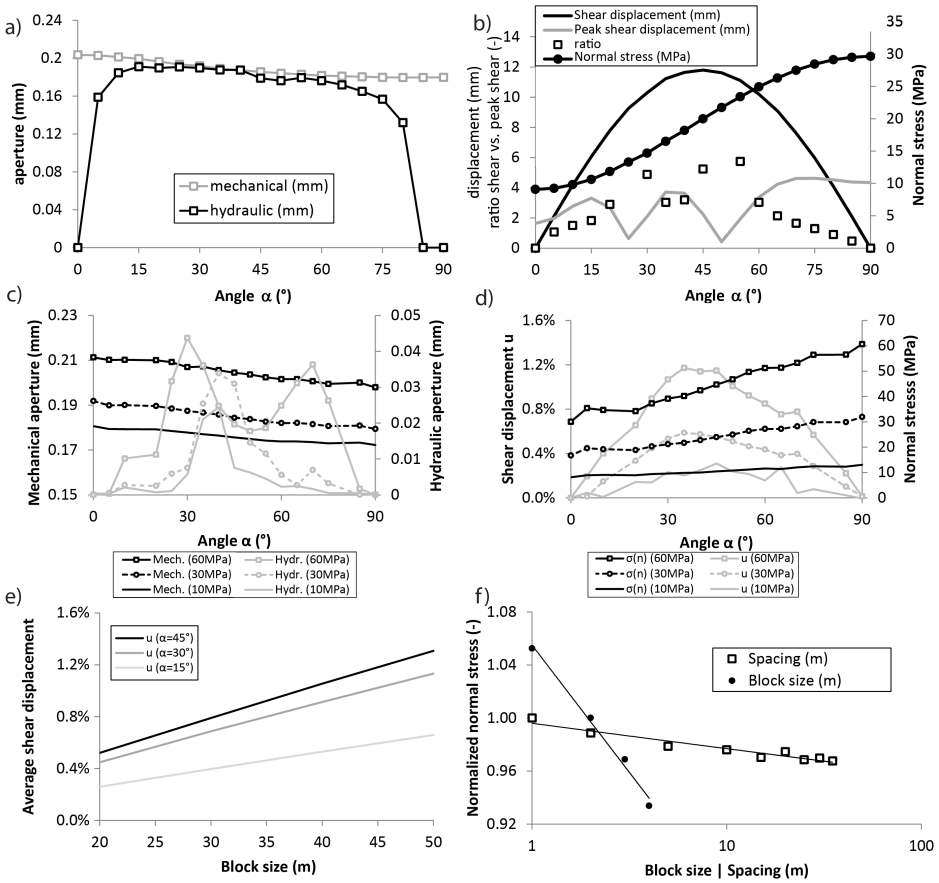


Figure B.2: Stress, shear displacement and aperture as a function of geometry for single- and multi-fracture FE models: a) Mechanical and hydraulic aperture of a single fracture as a function of α; b) Relation between α, shear displacement, peak shear displacement, normal stress and hydraulic aperture for a single fracture; c) Mechanical and hydraulic aperture as a function of α for ten fractures with $L = 2m$ for three tectonic stresses; d) Normal stress and shear displacement as a function of α for $L = 2m$; e): Normal stress and shear displacement as a function of fracture length for three different values of α; f) Normalised stress versus block size and spacing.

aperture for other values of α. This is the result of the stress-dependent cosine in the Barton–Bandis peak shear function, which changes the ratio between shear displacement and peak shear displacement, and the resulting hydraulic aperture.

Impact of block size and spacing

Normal stress and shear displacement increase with increasing block size. The increase in shear displacement is linear, as longer fracture segments can accommodate a larger shear displacement (Figure B.2e). The absolute values for the averaged hydraulic aperture of the multi-fracture models are smaller than those

of the single-fracture example as the impact of block size was not considered in the single-fracture model (Figure B.2b,c). Peak shear displacement increases block size, such that even if a fracture is ideally orientated with respect to the direction of maximum compression (i.e. $\alpha = 15°$), there still needs to be a sufficient amount of intersecting fractures to allow for a peak shear displacement that is smaller than the actual shear displacement.

The impact of block size on hydraulic aperture is taken into account through equation B.1, but changing the amount of intersecting fractures also changes the average value of normal stress acting on a fracture (Figure B.2f). An increase in block size results in a decrease in the average normal stress. We extend equation B.1 with a correction for block size. For normalised normal stress, this relation with block size L is a log-normal function:

$$\sigma_{n,L} = \sigma_n(-0.083 \ln L + 1.055) \tag{B.2}$$

In addition to changing the block size, fracture spacing changes the stress acting on a fracture as nearby fractures impact stresses locally. We quantify this relation using FE models with parallel fractures and variable spacing. Increasing spacing slightly decreases normal stress on the fracture of interest (Figure B.2f). This subsequently decreases fracture closing and increases aperture. The relation between normal stress acting on the fracture and its distance with respect to other fractures follows a negative exponential distribution, which is combined with the normalised correction for normal stress:

$$\sigma_{n,\text{spacing}} = \sigma_{n,L} \cdot 0.996 \cdot S^{-0.008} \tag{B.3}$$

where $\sigma_{n,L}$ is the calculated normal stress, corrected for block size in equation B.3, and S is the average fracture spacing (in m) near the fracture:

$$S = \frac{A}{\sum l + r} \tag{B.4}$$

where A is the analysed rock area (m), $\sum l$ is the total fracture length (in m) within A and r is a given radius around the fracture of interest, in which A and $\sum l$ are calculated.

Derivation of a geometrical description for aperture

Using the behaviour described in Figure B.2, we define relations between geometry, normal stress and shear displacement. These relations account for single and multiple interacting fractures.

Normal stress

For single fractures, the normal stress is accurately predicted by equation B.1. We use this function in combination with equations B.2 and B.3 for single fractures where block size equals total length. For intersecting fractures, the normal stress

remains relatively homogeneous, and can be partly described using a linear function relating normal stress to α. However, for increasing σ_1, the increase in normal stress is non-linear, described using a power-law function of the form:

$$\sigma_{n,angle} = 0.0054\sigma_1\alpha + 1.5186{\sigma_1}^{0.723} \tag{B.5}$$

The impact of block size is taken into account by the normalised stress correction factors from equations B.2 and B.3:

$$\sigma_{n,geom} = \sigma_{n,angle}(-0.083 \ln L + 1.055) \cdot 0.996 \cdot S^{-0.008} \tag{B.6}$$

Shear displacement

Average shear displacement as a function of α follows in all FE models a second-order polynomial function, irrespective of the number of fractures. For the multi-fracture model with different amounts of tectonic stress (Figure B.2d), this relation is defined as:

$$u_{geom} = \sigma_1(1.07 \cdot 10^{-8}\alpha^2 + 9.56 \cdot 10^{-7}\alpha) \tag{B.7}$$

The exact shape of the function depends on block size. Combining the linear relation between block size and shear displacement (Figure B.2e) with the polynomial function describing the relation with α yields the following geometrical description of shear displacement:

$$u_{geom} = L \cdot \sigma_1 \cdot \alpha\left(-9.07 \cdot 10^{-8}\alpha + 8.1 \cdot 10^{-6}\right) \tag{B.8}$$

where the resulting displacement is in meters.

Geometrically-based method

We consider two distinct situations:

i) Single fractures (i.e. length equals block size);
ii) Connected and intersecting fractures where block size is smaller than total length.

For single fractures, normal stress is defined by α in equation B.1. The resulting $\sigma_{n,\text{single}}$ is corrected for the small impact that block size (i.e. total length) has on normal stress through equation B.2. Lastly, the impact of nearby fractures on the local stress field is considered with a correction defined by equation B.3.

For intersecting fractures, the relation between normal stress and α is better described using equation B.5. Orientation has the strongest impact on normal stress, similar to the single fracture model. For intersecting fractures, the same corrections for block size and spacing are applied through equations B.2 and B.3, which can be combined with equation B.5 into equation B.6. Shear displacement is for all fractures defined using equation B.8.

The geometrically-based functions for normal stress and shear displacement are substituted into the Barton–Bandis equations for calculating mechanical and hydraulic aperture (Chapter 3), where either $\sigma_{n,\text{single}}$ (single fracture) or $\sigma_{n,\text{geom}}$ (intersecting fractures) is used in the equations for normal opening and peak shear

displacement and u_{geom} is used in the equation for hydraulic aperture. Using these functions and a constant far-field σ_1 and angle α for each fracture block segment, the mechanical and hydraulic apertures are calculated without the need for numerical FE simulations.

Method validation using simple models

We consider a system with two perpendicular sets of fractures with constant spacing of 2 m and a fracture length of 12 m (Figure B.3). Hydraulic aperture is shown for two stress angles, $\alpha = 30°$ (Figure B.3a-b) and $\alpha = 45°$ (Figure B.3c-d). For an angle of 30°, *set 1* has a larger hydraulic aperture than *set 2* in both the FE models (Figure B.3a) and the geometrical models (Figure B.3b). This is predicted by the relations in Figure B.2. The geometrical model correctly predicts the average apertures, but the difference in resolution between the two methods creates two different images. The FE model in this example has an element size of 0.1 m, whereas aperture in the geometrical model can only be calculated per segment of 2 m.

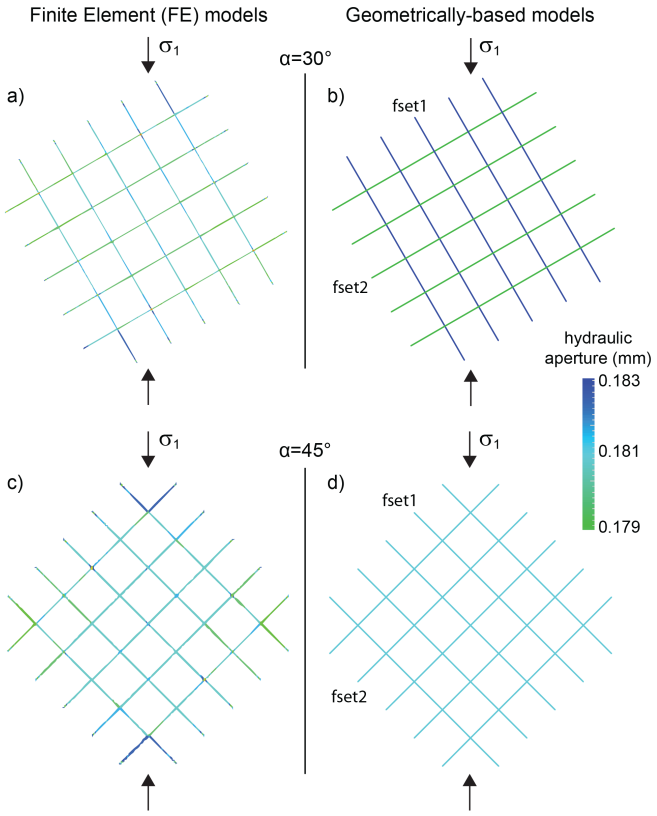


Figure B.3: Comparison of hydraulic aperture modelled using geomechanical FE models (a, c) versus geometrical equations (b, d). The stress angle α is indicated in each figure. Block size is 2 m.

For $\alpha = 45°$, the hydraulic aperture of *set 1* equals that of *set 2* in both the FE and

Pavement name	Formation and location (LAT/LON)	Spatial distribution	Fracturing
Tunisia I	Eocene Kef Eddour Fm. (carbonates), Gafsa basin, Central Tunisia (34.335626/ 8.330545)	2 conjugate families with bi-sections striking N-S and E-W	Bed-perpendicular conjugate fractures related to shortening at shallow depth
Tunisia II	50 × 50 m subset of Tunisia I		
Brazil I	Upper Cretaceous Jandaíra Fm. (carbonates), Potiguar basin, NE Brazil (-5.5610578/-37.661895)	Two main orientation families (NW-SE and SW-NE) with large scatter in size and orientation, no clear hierarchy, and a small N-S system.	Bed-perpendicular conjugates and joints related to shortening at shallow depth and karstification
Brazil II	(-5.536467/-37.639803)	Large conjugate family with N-S bisection, a N-S trending fracture system and small E-W trending fractures.	
Brazil III	(-5.495950/-37.549517)	Fractal system with chaotic orientations. Small high-intensity systems terminating against larger low-intensity systems.	

Table B.1: Summary of properties of the fractured pavements used for aperture modelling.

geometrical models (Figure B.3c-d). In the FE model, aperture is largest in the centre of the model and relatively small towards the left and right sides, related to the N-S orientation of σ_1 and the decrease in intensity at the outer edges of the model. These effects are not captured in the geometrical model, where all fractures have a constant aperture, but the average aperture of both sets is accurately predicted.

The geometrically-based functions for normal stress are based on average trends along each fracture. As a result, extreme values for normal stress and subsequent aperture are found in the FE models, but not in the geometrically-based models (Figure B.3). The mechanical aperture along a fracture in the FE model follows an elliptical shape with minimum aperture at the fracture terminations and maximum aperture at the centre. The geometrically-based models however have a constant aperture along any straight segment.

Hydraulic aperture in real-world networks

To further test the validity of the geometrically-based relations as alternative to FE models, we apply both methods to five large real-world fracture systems, digitised from outcropping pavements in Tunisia and Brazil (Chapters 4 and 6), and compare the resulting aperture. Each outcrop has a unique spatial distribution and topology, ranging from homogeneous systems with a clear hierarchical pattern to complex fractal systems (Figure B.4). A brief summary of the rock and fracture characteristics is supplied in Table B.1. The fractures dip perpendicular to bedding in all pavements.

The geometrical aperture analysis was applied to the digitised fractures by implementing the equations for normal stress and shear displacement into DigiFract. Curved or irregularly shaped fractures were divided into straight segments for which geometrical parameters were calculated. For the FE modelling, the fracture

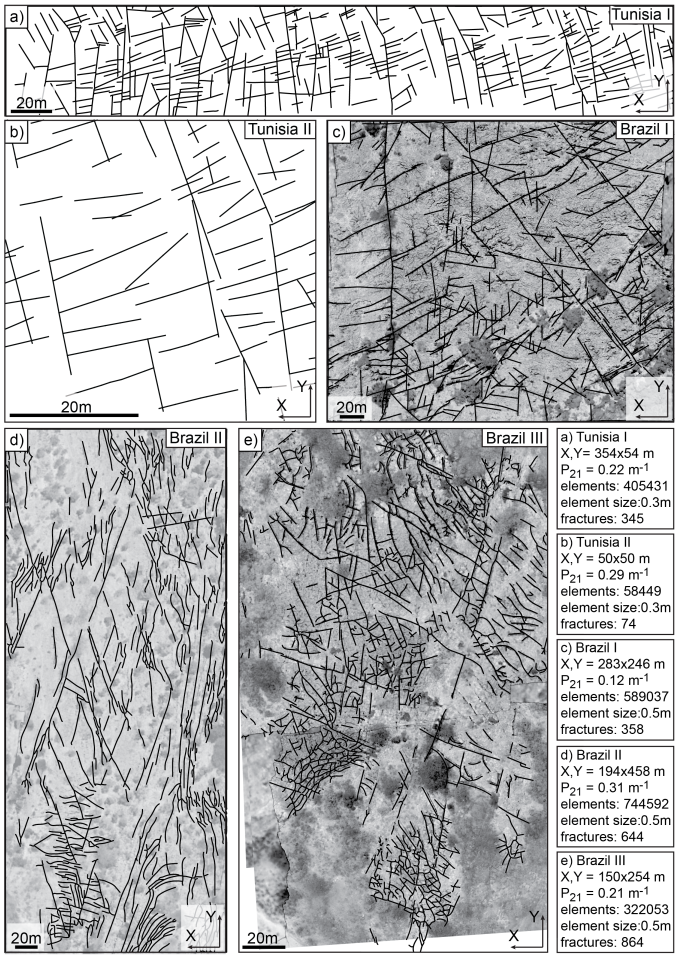


Figure B.4: The five real-world fracture patterns: a) Carbonate pavement from the Alima anticline, central Tunisia (Chapter 6); b) 50 × 50 m subset extracted from (a); c-e) Carbonate pavements from the Potiguar basin, Brazil (Chapter 4). The original orthophotos for the Potiguar basin outcrops are added to indicate areas affected by censoring (i.e. trees). For each model, the exact dimensions, fracture intensity P_{21} and number of elements, average element size and number of fractures are listed.

network was exported to the FE software and meshed. The network geometry was kept intact in this translation, ensuring that both methods for aperture modelling were performed on the exact same geometries. The resulting FE mesh size and resolution for each pavement is listed in Table B.1 and Figure B.4.

Aperture from FE models

We model the stress distribution in the numerical FE models for a constant 30 MPa far-field stress oriented N-S and calculate the hydraulic aperture (Figure B.5). All fractures have an initial aperture of 0.3 mm. No extension at the model edges is

allowed, and vertical stresses are not considered in these horizontal 2-D pavement models, as we only consider changes in aperture along the length of bed-perpendicular fractures.

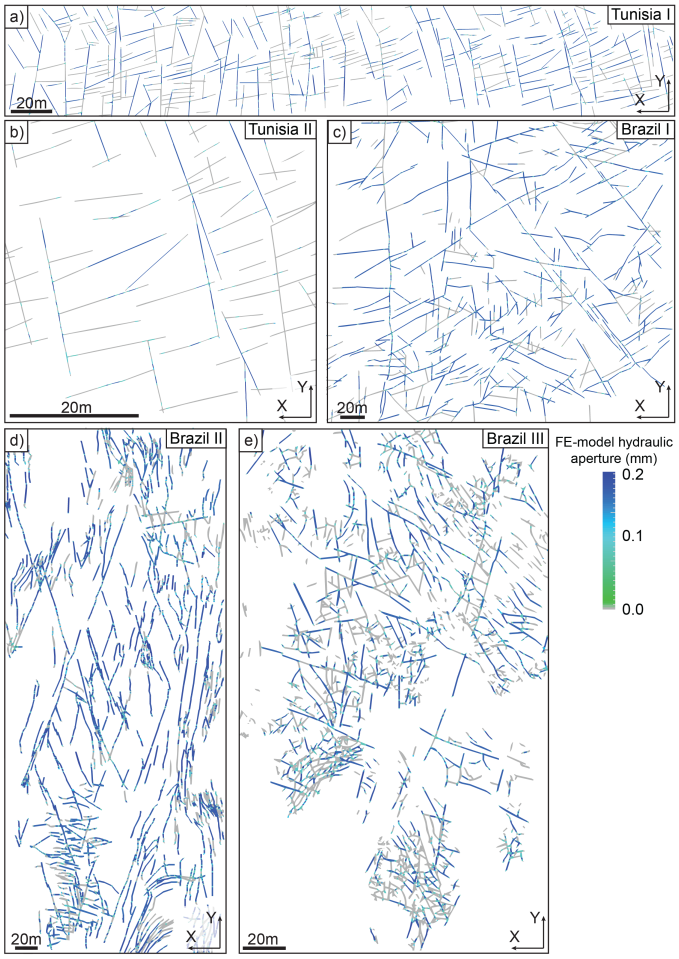


Figure B.5: Hydraulic aperture for all pavements, calculated using geomechanical FE simulations. Light grey indicates hydraulically closed fractures.

In most pavements, a large part of the fracture system is hydraulically open (Figure B.5). In most models, we observe that under N-S compression, aperture of fractures with an orientation close to the N-S axis is larger than that of fractures trending E-W. This contrast is particularly clear in the *Tunisia* pavements (Figure B.5a-b), which contain two fracture families with similar size distributions, striking on average N-S and E-W. The family that is almost parallel to the N-S σ_1 is experiencing sufficient shear to have more hydraulically open fractures compared to the E-W system. This behaviour is also observed in the *Brazil II* pavement, which

contains a large conjugate system with a N-S trending bisector. These fractures are ideally oriented with respect to σ_1, creating mostly hydraulically open fractures (Figure B.5d). In contrast, the smaller E-W trending set that is located in the southern half of the outcrop is mostly closed.

The closed E-W trending fractures in pavement *Brazil II* are related to orientation and to a lesser extent length and block size. In pavements *Brazil II* and *III*, where there is a contrast between large and small fractures, the smaller fractures are generally closed, irrespective of their orientation (Figure B.5d,e). Many of the small closed fractures have no intersections, resulting in relatively small shear displacement, as this is a function of length, in combination with a high peak shear displacement, resulting from the relatively large block size. Larger fractures have a higher probability of intersecting other fractures, which lowers their peak shear displacement. A lower peak shear displacement increases the likelihood of hydraulically open fractures.

Geometrically-based aperture

Workflow and intermediate steps

The calculation of hydraulic aperture as a function of geometry is done in a series of steps (Figure B.6). After calculating block size and stress angle, the normal stress is calculated, which is related to the stress angle (Figure B.6c-d). Shear displacement is mainly correlated to block size (Figure B.6b,e). Mechanical aperture is best described as an inverse function of normal stress, with low stress resulting in large apertures (Figure B.6d,f).

The geometrical aperture is close to the FE model aperture, with a similar ratio of open versus closed fractures (Figure B.6g,h). The average hydraulic aperture of the FE model is 0.182 mm, versus 0.186 mm in the geometrically-based model. However, the open fractures in the geometrically-based model are not always the same as in the FE model, as the impact of nearby fractures on normal stress of a given fracture is not fully captured in the geometrical model. This effect is approximated by equation B.3, which takes into account the presence of nearby fractures, but it does not take into account their exact positions and angles.

The minor overestimation of hydraulic aperture in the geometrically-based models is the result of the difference in resolution. The FE model has many small variations in aperture, varying between maximally and partially open, whereas aperture in the geometrical model is averaged towards maximum aperture per segment. This averaging effect occurs in the geometrical aperture models of all pavements (Figure B.7).

Aperture in real-world pavements

The geometrically-based hydraulic aperture for each pavement is heterogeneous, with variations in aperture along fractures (Figure B.7). However, there are some clear trends, as the largest aperture is often found along fractures that are nearly, but not perfectly, parallel to the N-S σ_1 direction. Large fractures in the *Brazil II* outcrop, which are striking at an angle of approximately 15-20° with respect to σ_1, have the largest hydraulic aperture, whereas the large approximately N-S striking

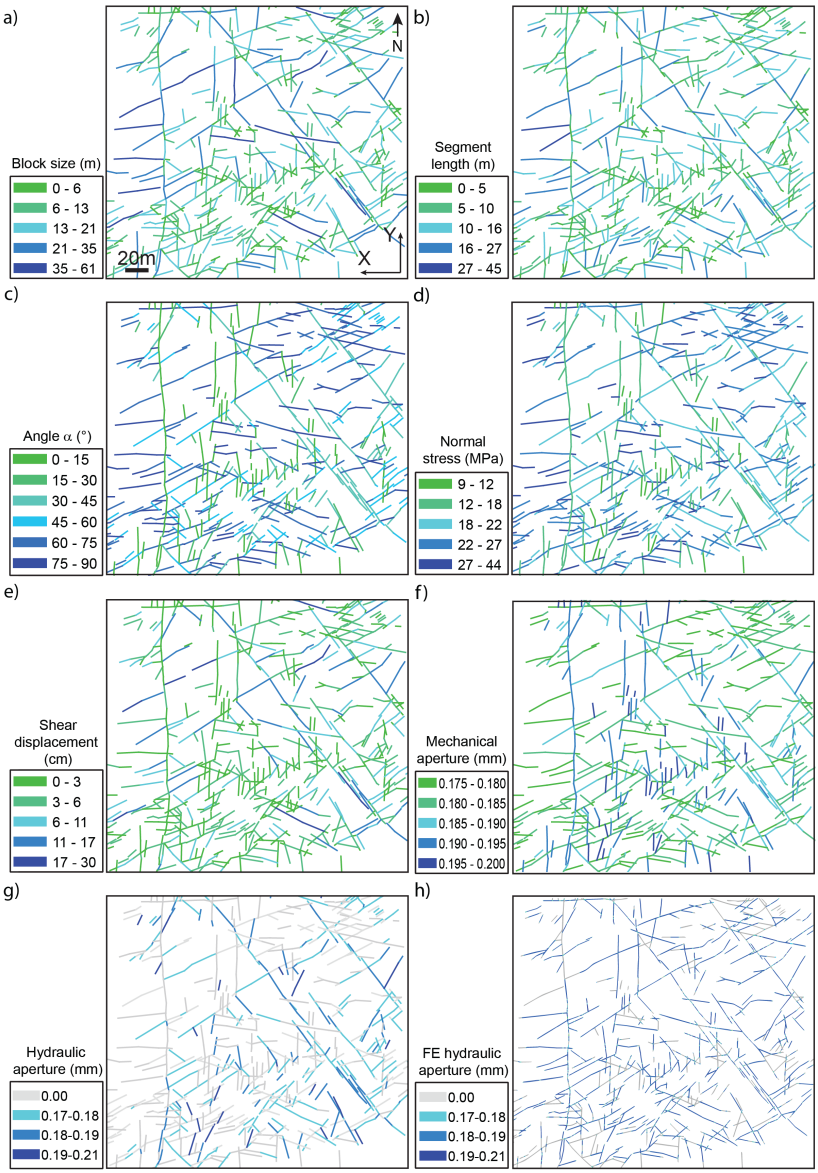


Figure B.6: Step-by-step calculation of geometrical aperture for pavement *Brazil I*: a) Block size (in m); b) Segment length; c) Stress angle α, assuming a N-S σ_1; d) Normal stress (in MPa); e) Average shear displacement along each fracture segment (in m); f) Mechanical aperture (in mm); g) Hydraulic aperture (in mm); h) Hydraulic aperture (in mm) from the FE model.

fractures in *Brazil I* and *II* are mostly hydraulically closed. This behaviour corresponds to what is found in the FE models and predicted by the relation between fracture orientation and aperture in Figure B.2.

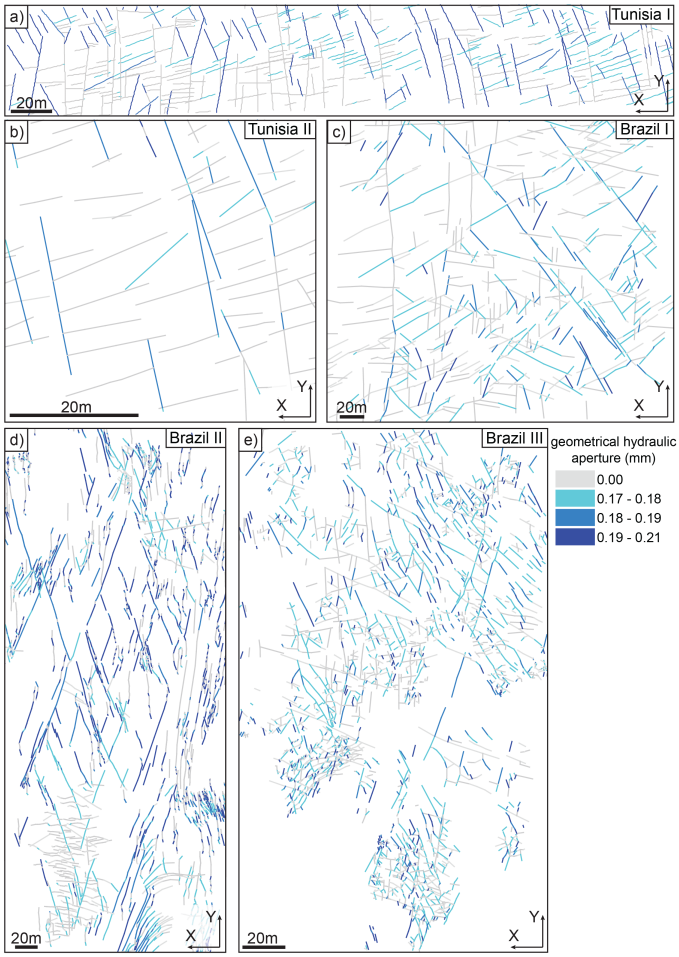


Figure B.7: Hydraulic aperture for all pavement models, calculated using the geometrical approach. Light grey indicates hydraulically closed fractures.

The relation between orientation and aperture predicts that fractures striking perpendicular to the direction of σ_1 are hydraulically closed. In the geometrically-based models this is observed in all pavements. The impact of orientation is most clear in the southern part of pavement *Brazil II*, where some fractures are seen that curve from a N-S strike towards an E-W strike. This change in orientation corresponds to a change from hydraulically open to hydraulically closed, as defined by equation B.5.

Comparison between geometrically-based and FE aperture

We compare the match between the FE models and the geometrically-based models through the aperture distribution of each pavement (Figure B.8). Mechanical and

hydraulic aperture follow (log)normal distributions, although this is not proven by quantitative statistics. These distributions are less apparent for geometrically-based aperture, as the orientation in equation B.5 has a large impact on aperture. In models with distinctive orientation sets, such as the *Tunisia* pavements and the *Brazil II* pavement, this results in several peaks corresponding to the different orientation sets.

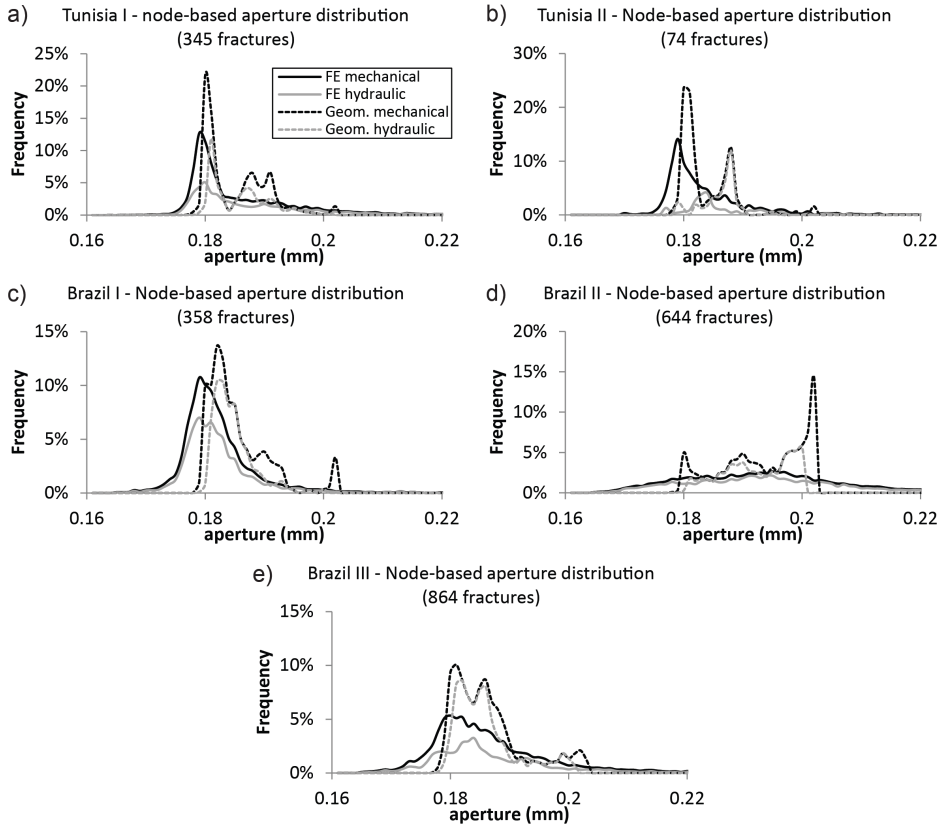


Figure B.8: Mechanical and hydraulic aperture distributions from the FE models (FE) and the geometrical calculations (Geom.) for all pavements. The frequency indicates the percentage of open fracture nodes compared to the total number of fracture nodes.

More fractures are mechanically and hydraulically open in the geometrically-based models compared to the FE models (Figure B.8). The spread in mechanical and hydraulic aperture is larger for the FE models, whereas the aperture of the geometrically-based model is limited to 0.18–0.2mm. This is related to the averaging of normal stress and subsequent aperture along the fracture, removing extreme values from the geometrically-based distribution.

Although the geometrically-based distributions are narrower than those of the FE models, there is a good match for the average hydraulic aperture (Figure B.9a).

At most, the difference between the two methods is 2.5%. The difference in mechanical aperture is slightly larger, up to 5%. The error in hydraulic aperture is smaller because these averages only take into account the fraction of open fractures. A comparison of the amount of mechanically and hydraulically open nodes show an error of 8% for the mechanically open fracture ratio, but an error of up to 29% for the amount of hydraulically open fractures (Figure B.9b). On average, the error in the ratio of open versus closed is 4% for mechanical aperture and 7% for hydraulic aperture. Accuracy is lowest for the *Brazil III* pavement, which is also the most heterogeneous model in terms of geometry, with several very large fractures that control aperture, whereas most of the high-intensity small fractures are closed. This results in a heterogeneous normal stress pattern that is not fully captured by the geometrically-based method.

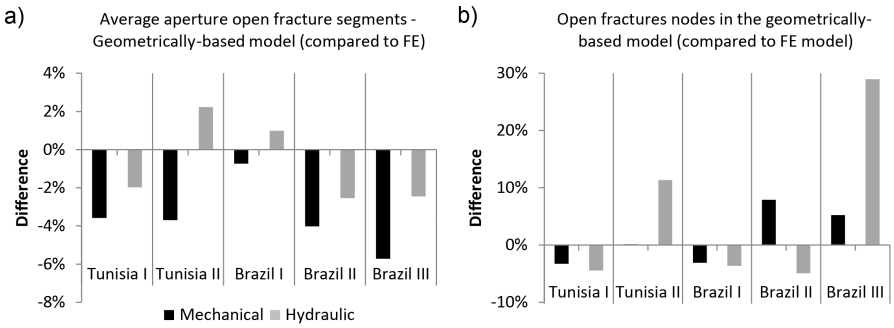


Figure B.9: Overview of mechanical (black bars) and hydraulic (grey bars) aperture per pavement: a) Difference between the geometrically-based model compared to the FE models, considering only open fracture segments. Negative differences indicate that the geometrically-based method underestimates aperture; b) Difference in the amount of open versus closed fracture nodes, comparing the geometrically-based method with the FE models. Negative values indicate an underestimation of the amount of mechanically or hydraulically open nodes in the geometrically-based model, compared to the FE model.

Implications for fluid flow

Small changes in aperture form either bottle-necks or pathways for flow through fracture networks, especially in low-intensity networks with large fractures such as *Tunisia II* (Figure B.5b and Figure B.7b). Although the hydraulically open network in both models looks similar, the geometrically-based aperture in Figure B.7b has several large fractures that are entirely open, resulting from the averaged normal stress, whereas parts of these fractures are closed in the FE model, forming flow bottle-necks (Figure B.5b). To quantify the impact of the differences in the aperture distributions, we calculate the equivalent permeability of these networks using the flow modelling approach presented in Chapter 3, using a range of matrix permeabilities.

In models with 10 mD matrix permeability, the heterogeneous aperture from the FE and geometrically-based models results in an increase from 10 mD to a max-

imum of 20 mD (Figure B.10a). This is a relatively small increase, but in most of the models, fracture intensity is relatively low.

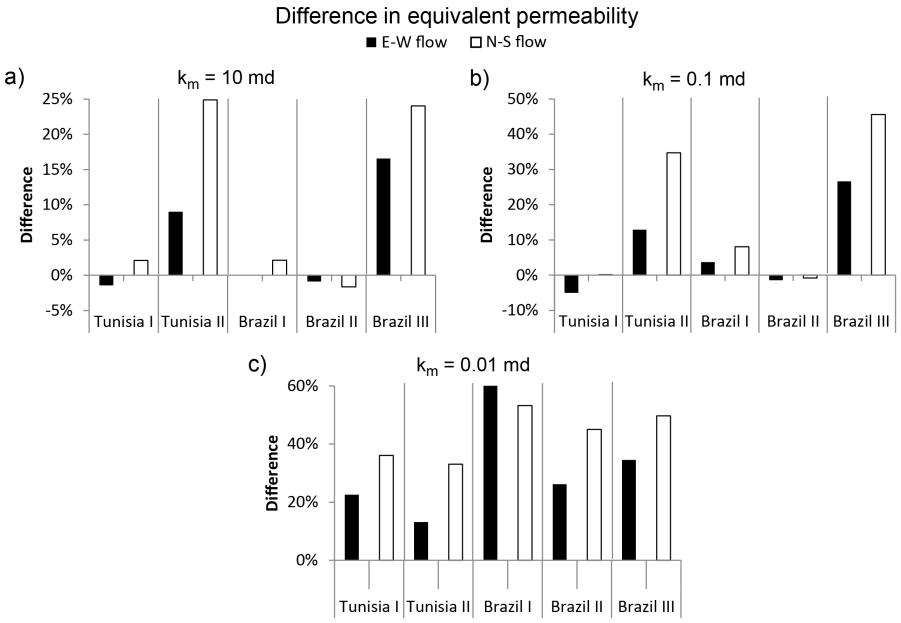


Figure B.10: Geometrically-based equivalent permeability per pavement in E-W (black bars) and N-S (white bars) directions, expressed as the difference between geometrically-based and FE-based permeability, considering a matrix permeability of: a) 10 mD; b) 0.1 mD and c) 0.01 mD. Negative differences indicate an underestimation of the geometrically-based method with respect to the FE method.

In most pavements, the difference in permeability resulting from the FE and geometrically-based models is less than 2%, with the exception of *Tunisia II* and *Brazil III*, where the error is up to 25%. The error in *Brazil III* is related to the relatively large error in hydraulic aperture. The geometrically-based aperture of *Tunisia II*, however, is relatively close to the FE distribution. In this pavement, the error in equivalent permeability is large in N-S direction but small in E-W direction. This pavement contains several large fractures that are striking approximately N-S, and form a pathway through the model. In the geometrically-based model, these fractures are mostly hydraulically open (Figure B.7b). In the FE model, the terminations and intersections of these fractures are closed, forming flow bottlenecks that lower the effective permeability in N-S direction.

In models where flow is not controlled by a percolating path or a small sub-set of very large fractures, the permeability is accurately predicted by the geometrically-based method. These findings hold for a matrix permeability down to 0.1 mD, for which the maximum error in permeability is 46% in *Brazil III*, but the average error for the other pavements is 3% (Figure B.10b). The error increases for a matrix permeability of 0.01 mD (Figure B.10c). The low matrix permeability increases the relative impact of closed fracture sections acting as flow bottlenecks.

C

Fracture networks in the Jandaíra Fm.

Interpretation of these datasets is partly done by M. van Eijk, E. van der Voet and C. Paulides.

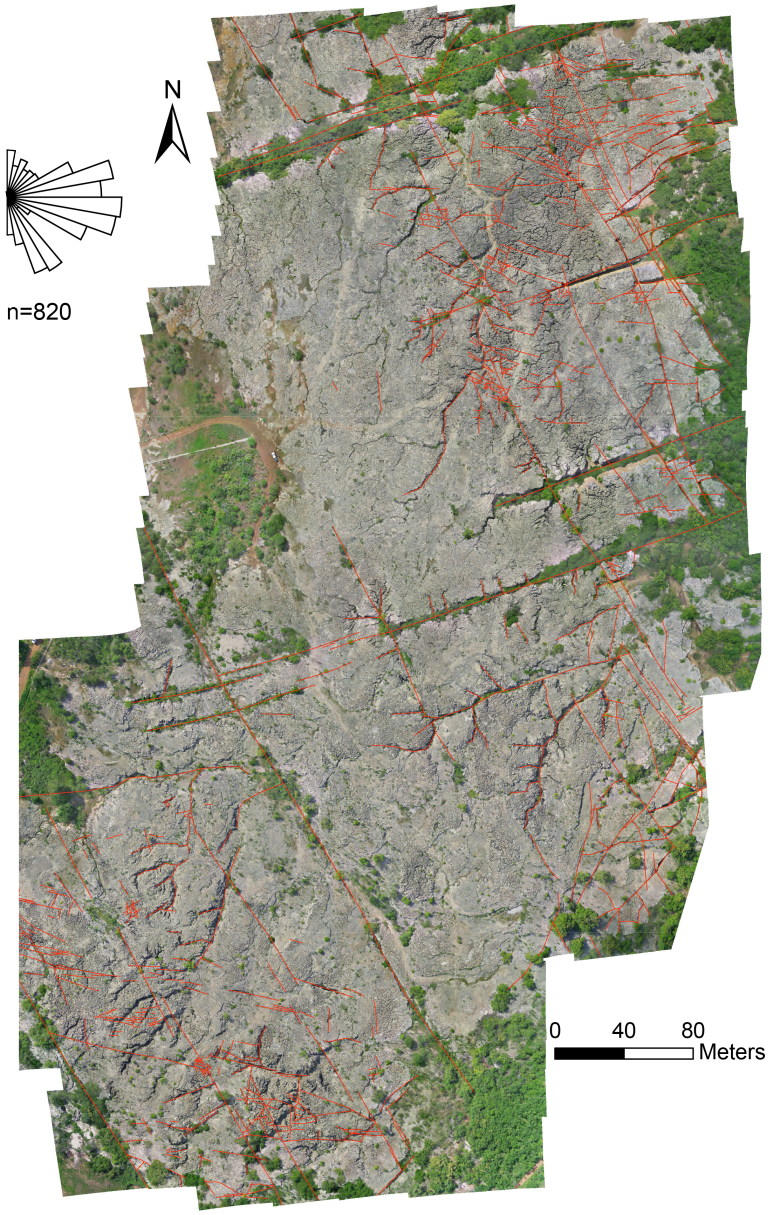


Figure C.1: Pavement *Apodi 1*.

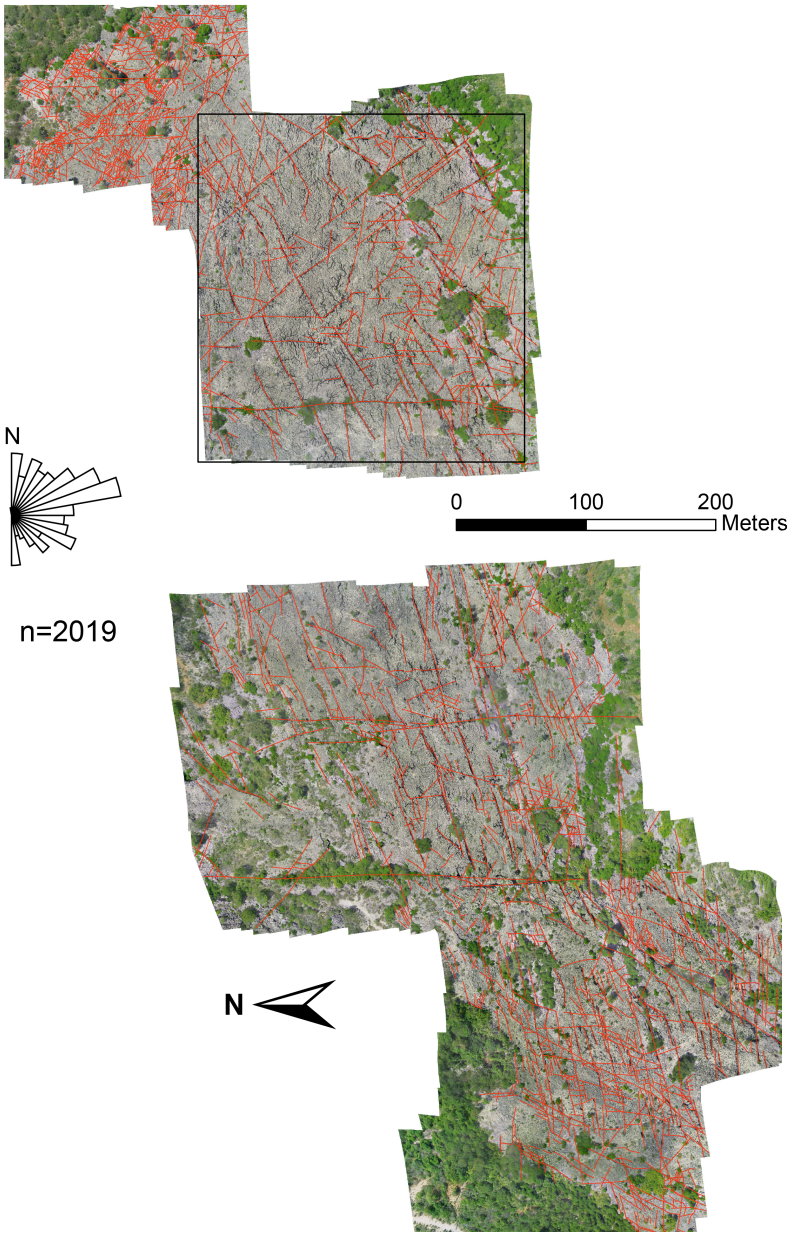


Figure C.2: Pavement *Apodi 2*. The area within the black rectangle is used for permeability modelling (Chapter 4).

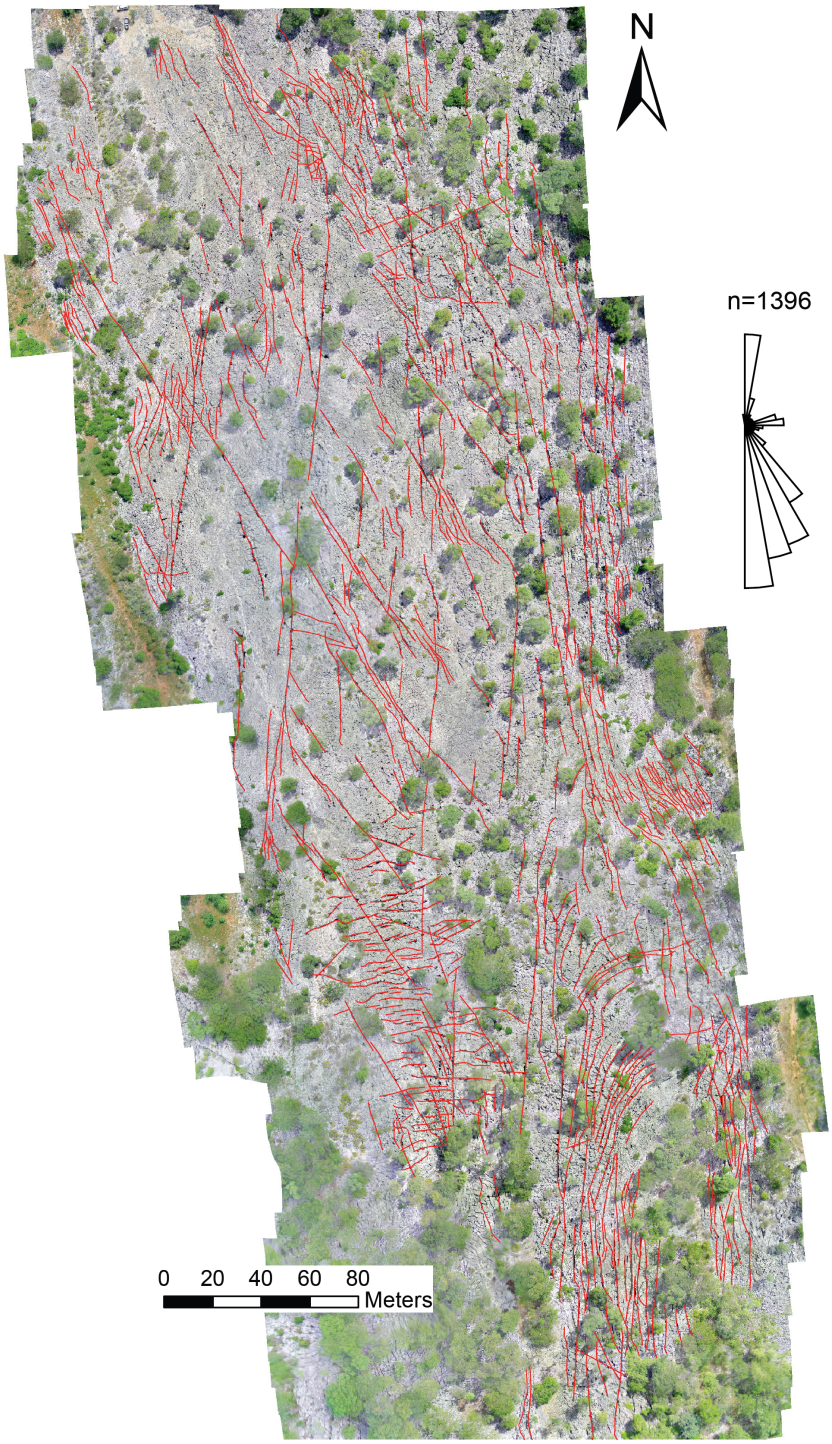


Figure C.3: Pavement *Apodi 3*.

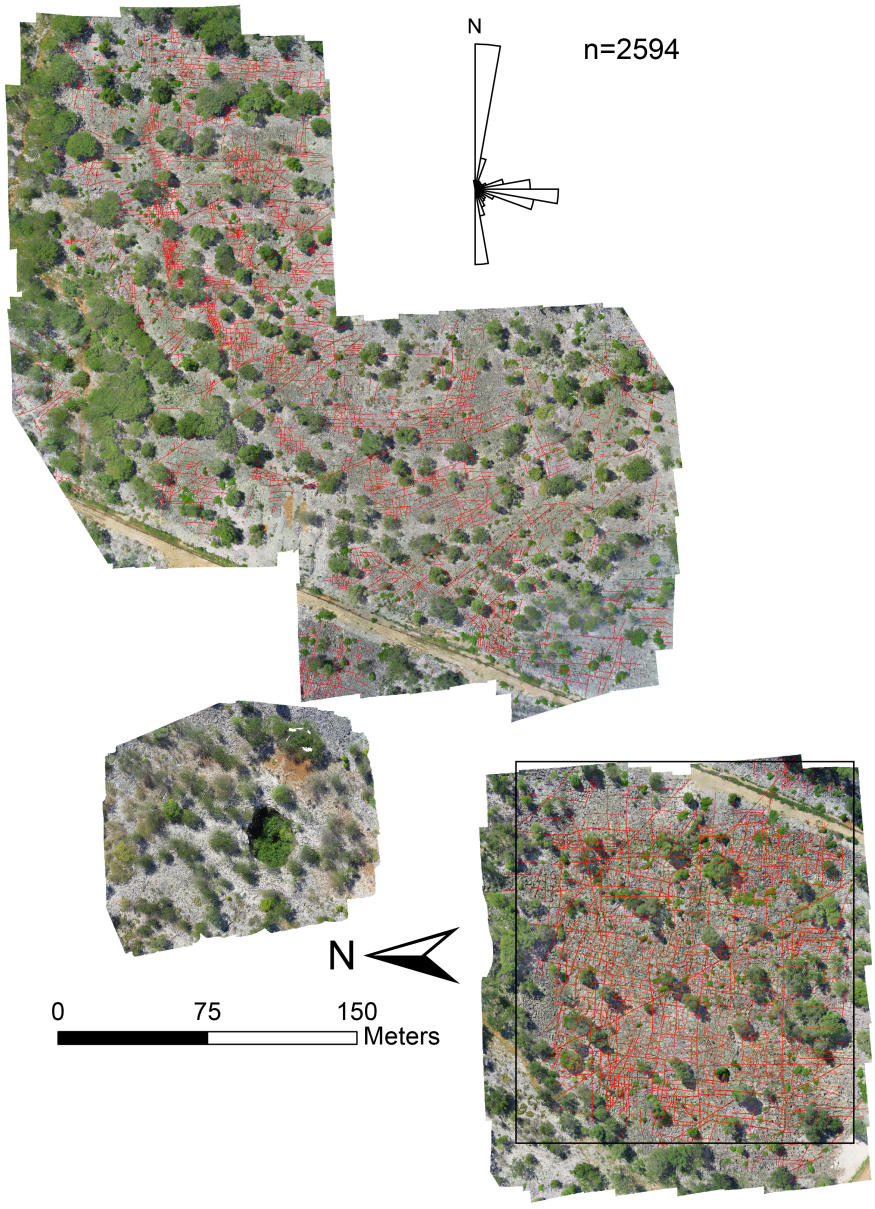


Figure C.4: Pavement *Apodi 4*. The area within the black rectangle is used for permeability modelling (Chapter 4).



Figure C.5: Pavement *Apodi 5*.

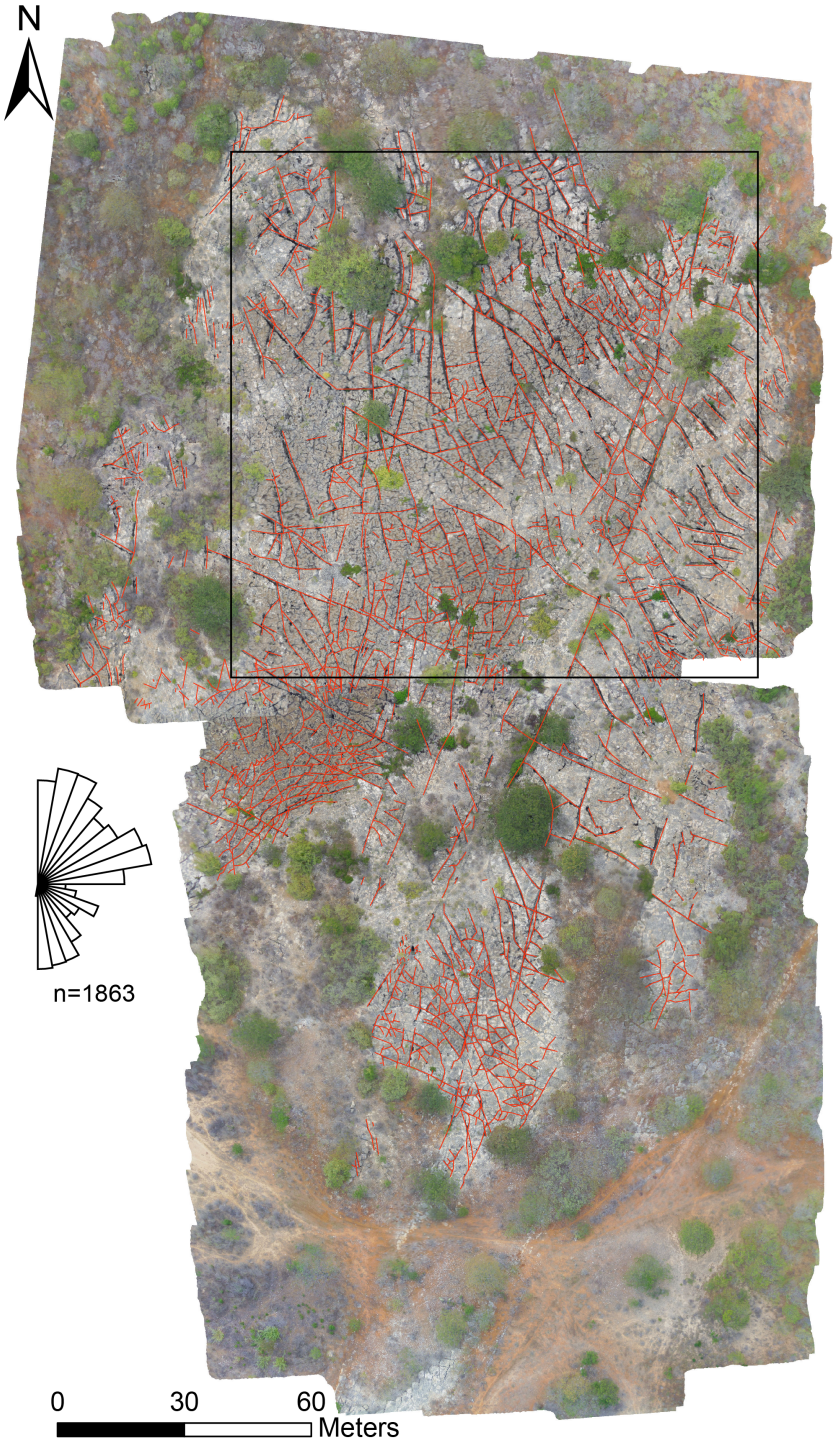


Figure C.6: Pavement *Dix-sept 1*. The area within the black rectangle is used for permeability modelling (Chapter 4).

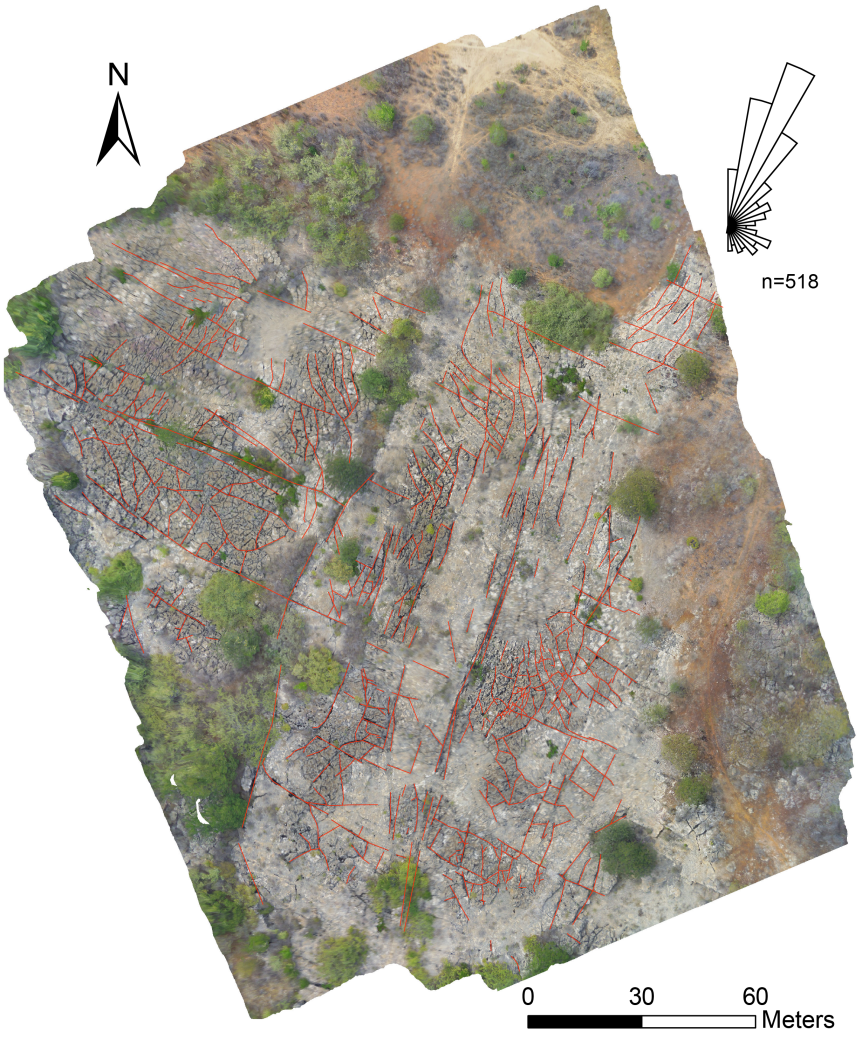


Figure C.7: Pavement *Dix-sept 2*.

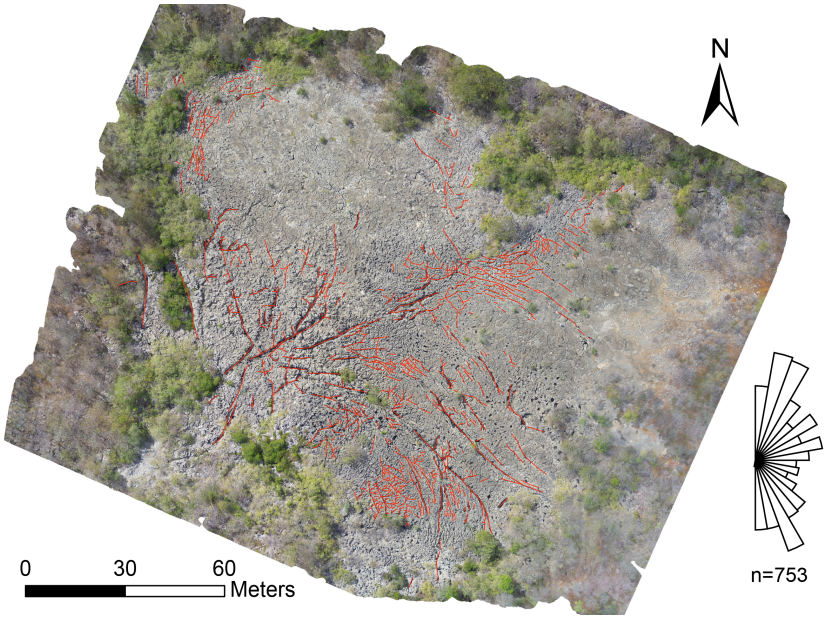


Figure C.8: Pavement *Mossoró 1*.

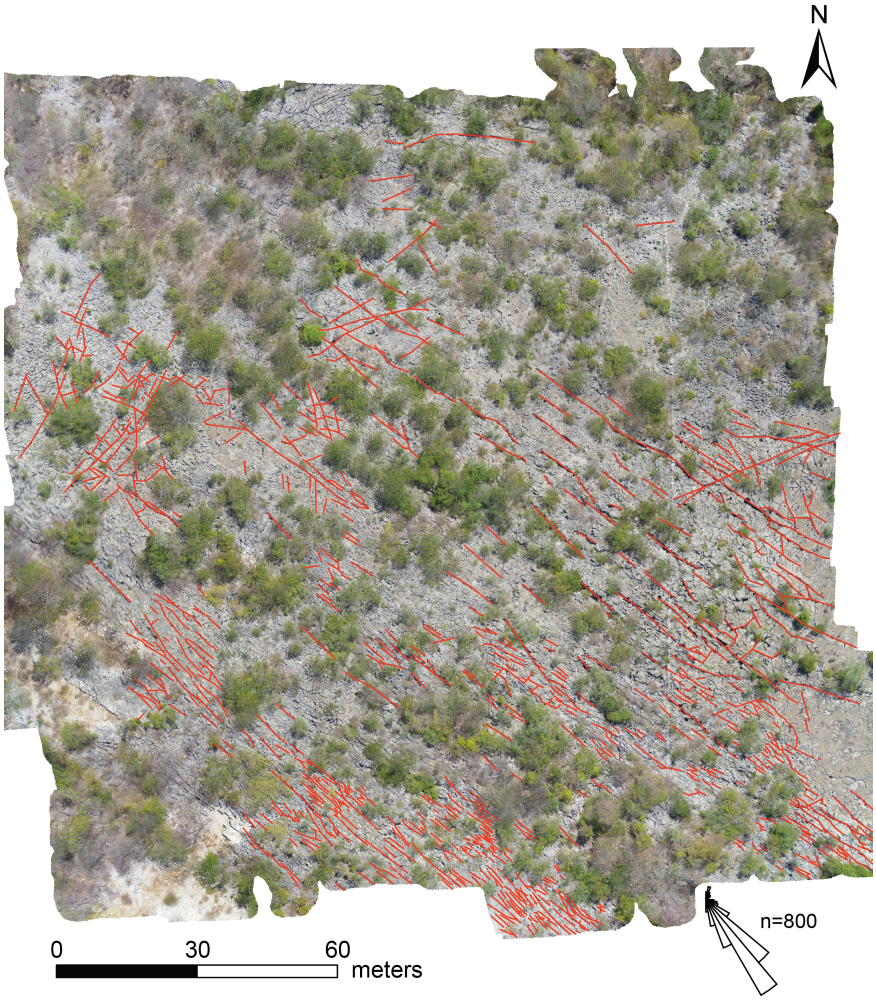


Figure C.9: Pavement *Mossoró 2*.

Acknowledgements

This PhD is funded by Total S.A., with additional support from Agência Nacional de Petróleo (ANP), Petrobras (through the POROCARSTE project) and the Molengraaff fund for the fieldworks in Brazil. I am indebted to Bertrand Gauthier for recognising the value of this project and for generating support by Total S.A., as well as his guidance during the past years, particularly during the two internships in Pau. Others from Total S.A. have also contributed greatly, particularly Arjan Kamp and Yves-Marie Leroy, who have taught me a great deal about the reservoir engineering and geomechanical aspects of fractured reservoirs, and the people who supported me during my stay in Pau: Sebastian Estrada, Emmanuelle Baud, Sandrine Vidal-Gilbert, Yonatan Sanz-Perl, Paul Froydenlund, Camille Ben-Miloud, Stefano Denetto, Chris Wibberley, Alain Lejay, Jonatan Pelettier and the interns. I am particularly grateful to Emmanuelle Baud for enabling me to apply my research to a real reservoir study and allowing for publication of results.

The work in Brazil would not have been possible without the collaboration with Universidade Federal do Rio Grande do Norte (UFRN), driven by Hilario Bezerra, who set up the POROCARSTE project funded by Petrobras and ANP. I very much enjoyed the multicultural and multidisciplinary collaboration with Hilario, David, Cézar, Narendra, Uilson, Lorenna, Alanny, Suelen, Keyla, Christiane, Franklyn, Pedro, Fernando and the other students and staff from UFRN and UFCG (Universidade Federal de Campina Grande) and John Reijmer and his students from the VU University in Amsterdam: Annelieke, Frida, Mariska, Eva, Brigit, Stefan, Robin and Mathijs. I am also grateful to Caroline, Aline, Vitor and Orildo from Petrobras for their active participation in the project.

In Tunisia I have enjoyed great scientific and logistical support from Samir Bouaziz and his PhD students Ayman Hammami and Safwen Makni from Ecole Nationale d'Ingénieurs de Sfax (ENIS). Students from TU Delft (Rob, Damien and Þórey) and VU University (Rubio) have also contributed significantly to acquisition and analysis of outcrop data.

This Thesis has benefited greatly from satellite projects executed by BSc and MSc students from TU Delft and VU University: Rob Bekkers, Damien Boeser, Gatien de Callatay, Mariska van Eijk, Stefan de Graaf, Frida Hameka, Brigit Oskam, Sanjeev Ranjan, Paul Roskam, Stephan Toby, Rubio Vaughan, Annelieke Vis and Eva van der Voet; BSc projects by Kaj Althuis, Jelmer Doff, Eelco Mechelse, Coen Paulides, Alisha Pengel and Esther Wever. Many other students and staff from the departments of Geoscience & Engineering and Geoscience & Remote Sensing supported me throughout the years. Thanks in particular to Bill Rossen, Hadi Hajibeygi, Denis Vostok, Sandra Verhagen, Roderik Lindenbergh and Auke Barnhoorn and their postdocs and PhD students Jiakun, Matei, Beril and Swej. I am also grateful to the supporting staff: Ralf, Marlijn, Margot, Lydia, Anke, Marja, Marijke

and Hannie.

In the last four years, a fruitful collaboration has developed with Heriot Watt, and I am very grateful to Sebastian Geiger and Patrick Corbett and their students, particularly David Egya and Faisal Aljuboori, whose work supplemented and extended the work presented in this Thesis. I very much enjoyed my visits to Edinburgh, thanks to David, Daniel, Simeon, Alessandro and the other students.

The wide range of geological, geomechanical and flow models have been created with support from the following companies and individuals: Paradigm (Gocad/SKUA); RING (Gocad plugins), with special thanks to Guillaume Caumon, Guillaume Rongier and François Bonneau; Baker Hughes (JewelSuite) with special thanks to Wouter van der Zee and Marc Holland for the excellent discussions regarding geomechanics and Ade Nasution and Jeremy Brown for software support; Golder Associates (FracMan), with special thanks to Bill Dershowitz and Neal Josephson; Michel Garcia from Kidova for support with GoFraK, and of course I thank Guus Lohlefink for being incredibly patient with me during the many times I needed help with licenses or when I was overloading the servers again with my simulations.

Thanks to Hamid Maghami Nick I have been able to close the loop of our fracture geometry, geomechanics and fluid flow workflow. Hamid, your support was essential for the fluid flow modelling aspects of this Thesis. Your enthusiasm and creativity were the driving force that pushed me to further develop our numerical approach, resulting in several joint publications.

Since *day 1* of my 'career' in fractures nearly six years ago, Nico Hardebol has been a great colleague and friend, who introduced me to the world of fractures, DigiFract, Python and geomechanics. I learned a lot from our joint DigiFract development sessions and endless discussions. Your critical second opinion has strengthened this Thesis significantly.

This Thesis would never have existed if it was not for Giovanni Bertotti, who as my MSc Thesis supervisor managed to make me enthusiastic for fractures and a PhD, two things I had never considered before. Since the very beginning I have always appreciated your advice, honesty, guidance and patience. I am grateful for everything you have taught me, from structural geology to how to present my work, manage my research and improve my communication and writing skills.

While all these collaborations were essential for the contents of this Thesis, getting this far would have been impossible without support from my friends and family. I thank my friends in the Applied Geology section: Andrea, Cees, Helena, Menno, Koen, Liang, Navid, Quinten, Rémi, Rodolfo, Runhai, Siddarth, Thaís, as well as those in the other sections of our department. Without the playful elements introduced into the office by Rémi and Koen I might have finished my PhD somewhat earlier. However, "The journey is more important than the destination", and you guys ensured a fantastic and fun journey. Rahul, thanks for wanting to be friends with a geoscientist.

My greatest appreciation goes to my parents, for always having given me the freedom to make my own choices and mistakes, and to Laurie: Thank you for your endless patience, love, more patience, support, care, and patience.

Curriculum Vitæ

Kevin BISDOM

05-09-1987 Born in Alphen aan den Rijn, Netherlands.

Education

1999–2005 Grammar School
Groene Hart Lyceum, Alphen aan den Rijn

2005–2008 BSc in Applied Earth Sciences
Delft University of Technology

2009–2011 MSc in Petroleum Engineering & Geosciences
Delft University of Technology

2012–2016 PhD. Applied Geology
Delft University of Technology

List of Publications

Journal publications

8. **K. Bisdom**, H.M. Nick, G. Bertotti, *An integrated workflow for stress and permeability modelling using inter-well scale outcrop-derived fracture networks*, **Submitted**.

7. **K. Bisdom**, G. Bertotti, F.H. Bezerra, *Inter-well scale natural fracture geometry and permeability variations in low-deformation carbonate rocks*, **Submitted**.

6. G. Bertotti, S. de Graaf, **K. Bisdom**, B. Oskam, H.B. Vonhof, F.H. Bezerra, J.J.G. Reijmer, C. Cazarin, *Fracturing and fluid flow during post-rift subsidence in carbonate of the Jandaíra Formation, Potiguar Basin, NE Brazil*, **Submitted**.

5. S. de Graaf, G. Bertotti, J.J.G. Reijmer, F.H. Bezerra, C. Cazarin, **K. Bisdom**, H.B. Vonhof, *Fracture-controlled fluid circulation and calcite vein cementation during early burial in shallow water carbonates (Jandaíra Formation, northeast Brazil)*, **Submitted**.

4. **K. Bisdom**, G. Bertotti, H.M. Nick, *The impact of in-situ stress and outcrop-based fracture geometry on hydraulic aperture and upscaled permeability in fractured reservoirs*, Tectonophysics, **In Press**.

3. **K. Bisdom**, G. Bertotti, H.M. Nick, *The impact of different aperture distribution models and critical stress criteria on equivalent permeability in fractured rocks*, Journal of Geophysical Research: Solid Earth **121** (5), 4045-4063 (2016).

2. **K. Bisdom**, G. Bertotti, H.M. Nick, *A geometrically based method for predicting stress-induced fracture aperture and flow in discrete fracture networks*, AAPG Bulletin **100** (7), 1075-1097 (2016).

1. **K. Bisdom**, B.D.M. Gauthier, G. Bertotti, N.J. Hardebol, *Calibrating discrete fracture-network models with a carbonate three-dimensional outcrop fracture network: Implications for naturally fractured reservoir modeling*, AAPG Bulletin **98** (7), 1351-1376 (2014).

Conference proceedings

23. N.J. Hardebol, B. Sirmacek, **K. Bisdom**, G. de Callatay, R. Lindenbergh and G. Bertotti, *Fracture network characterization using multi-scale UAV imagery, line extraction and stochastic simulation tools*, Second Virtual Geoscience Conference, 21-23 September, Bergen, Norway (2016).

22. **K. Bisdom**, G. Bertotti, H.M. Nick, *A Different Perspective on Critically Stressed Fractures and Their Impact on Fluid Flow*, AAPG Annual Conference & Exhibition, 19-22 June, Calgary, Canada (2016).

21. **K. Bisdom**, G. Bertotti, H.M. Nick, *The Great Unknown in Fractured Reservoirs - The Impact of Three Models for Aperture and Flow in Fractured Reservoirs*, 78th EAGE Conference and Exhibition, 30 May - 2 June, Vienna, Austria (2016).

20. **K. Bisdom**, E. Baud, S. Estrada, Y. Sanz-Perl, B.D.M. Gauthier, G. Bertotti, *Coupled Stress-fluid Pressure Modelling of Stimulated Rock Volume in Shale - Impact of Natural Fractures and Beef*, 78th EAGE Conference and Exhibition, 30 May - 2 June, Vienna, Austria (2016).

19. G. Bertotti, **K. Bisdom**, J.J.G. Reijmer, F.H. Bezerra, C. Cazarin, *Wholesale Fracturing of Carbonate Rocks during Subsidence - Tectonics, Geometry and Implications for Reservoir Studies*, 78th EAGE Conference and Exhibition, 30 May - 2 June, Vienna, Austria (2016).

18. D. Egya, S. Geiger, P. Corbett, **K. Bisdom**, G. Bertotti, F.H. Bezerra, *Assessing the Validity and Limitations of Dual-porosity Models Using Geological Well Testing for Fractured Formations*, 78th EAGE Conference and Exhibition, 30 May - 2 June, Vienna, Austria (2016).

17. G. Bertotti, **K. Bisdom**, F.H. Bezerra, J.J.G. Reijmer, C. Cazarin, *Distributed deformation structures in shallow water carbonates subsiding through a simple stress field (Jandaira Formation, NE Brazil)*, EGU General Assembly Vol. 18. Geophysical Research Abstracts, 17-22 April, Vienna, Austria (2016).

16. **K. Bisdom**, G. Bertotti, *Natural fracturing and fluid flow in carbonate rocks from surface to reservoir*, 13th Nederlands Aardwetenschappelijk congress (NAC13), 7-8 April, Veldhoven, Netherlands (2016).

15. **K. Bisdom**, G. Bertotti, H.M. Nick, *A different perspective on critically stressed fractures and their impact on fluid flow*, The Geological Society - The Geology of Geomechanics), 28-29 October, London, UK (2015).

14. F. Aljuboori, P. Corbett, **K. Bisdom**, G. Bertotti, S. Geiger, *Using Outcrop Data for Geological Well Test Modelling in Fractured Reservoirs*, 77th EAGE Conference and Exhibition, 1 June, Madrid, Spain (2015).

13. F.H. Bezerra, C. Cazarin, F. Nogueira, J. Rabelo, G. Bertotti, **K. Bisdom**, C. Silva, R. Maia, *Dissolution along fracture systems in Turonian-Campanian carbonates in Brazil*, EGU General Assembly Vol. 17. Geophysical Research Abstracts, 12-17 April, Munich, Germany (2015).

12. **K. Bisdom**, G. Bertotti, H.M. Nick, *Outcrop-based Geomechanical Fracture Aperture and Flow Modeling: The Importance of Shear on Flow*, AAPG Geoscience Technology Workshop, Carbonate Plays around the World Analogs to Support Exploration and Development, 4-5 February, New Orleans, Louisiana, USA (2015).

11. F.H. Bezerra, G. Bertotti, J. Rabelo, A.T. Silva, M.A. Carneiro, C.L. Cazarin, C.C. Silva, M.M. Vieira, **K. Bisdom**, A. Moraes, *Shallow properties of faults in carbonate rocks - The Jandaira Formation, Potiguar Basin, Brazil*, AGU fall meeting, 15-19 December, San Francisco, USA (2014).

10. **K. Bisdom**, G. Bertotti, B.D.M. Gauthier, *Lessons for Subsurface Fractured Reservoir Studies from an Outcrop-based 3-D Model of Fluid Flow in a Fractured Carbonate Fold*, AAPG International Conference & Exhibition, 14-17 September, Istanbul, Turkey (2014).

9. G. Bertotti, **K. Bisdom**, M. van Eijk, F. Hameka, A. Vis, F.H. Bezerra, J.J.G. Reijmer, *Fractures and Fracture Networks in Carbonate Reservoirs: A Geological Perspective*, AAPG International Conference & Exhibition, 14-17 September, Istanbul, Turkey (2014).

8. **K. Bisdom**, G. Bertotti, B.D.M. Gauthier, *Predicting Multi-scale Deformation and Fluid Flow Patterns in Folds Using 3D Outcrop Models and Mechanical Modelling*, 76th EAGE Conference and Exhibition, 16 June, Amsterdam, Netherlands (2014).

7. **K. Bisdom**, G. Bertotti, *A modern bird's eye perspective on quantitative geological fieldworks: using a drone to capture 3D structural deformation in complex outcrops*, 12th Nederlands Aardwetenschappelijk congress (NAC12), 8-9 April, Veldhoven, Netherlands (2014).

6. G. Bertotti, N.J. Hardebol, **K. Bisdom**, *Predicting Multiscale Fracture Patterns in Buried Reservoirs: the Importance of Outcrop Data in a Coherent Workflow*, Second EAGE Workshop on Naturally Fractured Reservoirs, 8 December, Muscat, Oman (2013).

5. **K. Bisdom**, G. Bertotti, B.D.M. Gauthier, N.J. Hardebol, *A Geologically Consistent Permeability Model of Fractured Folded Carbonate Reservoirs: Lessons from Outcropping Analogue*, Second EAGE Workshop on Naturally Fractured Reservoirs, 8 December, Muscat, Oman (2013).

4. G. Bertotti, F.H. Bezerra, **K. Bisdom**, C. Cazarin, J.J.G. Reijmer, *Outcropping Analogs and Multiscale Fracture Patterns in the Jandaíra Formation*, First EAGE/SBGf Workshop, Fractures in Conventional and Unconventional Reservoirs, 5 November, Rio de Janeiro, Brazil (2013).

3. **K. Bisdom**, G. Bertotti, B.D.M. Gauthier, N.J. Hardebol, *Quantifying Fracture Heterogeneity in Different Domains of Folded Carbonate Rocks to Improve Fractured Reservoir Analog Fluid Flow Models*, AAPG European Regional Conference & Exhibition, 8-10 April, Barcelona, Spain (2012).

2. B.D.M. Gauthier, **K. Bisdom**, G. Bertotti, *Modeling 3D Fracture Network in Carbonate NFR: Contribution from an Analogue Dataset, the Cante Perdrix Quarry, Calvisson, SE France*, AAPG Hedberg Conference, Fundamental Controls on Flow in Carbonates, 8-13 July, Saint-Cyr sur Mer, France (2012).

1. A. Faisal, **K. Bisdom**, B. Zhumabek, A. Mojaddam Zadeh, W.R. Rossen, *Injectivity and Gravity Segregation in WAG and SWAG Enhanced Oil Recovery*, SPE Annual Technical Conference and Exhibition, 4-7 October, New Orleans, Louisiana, USA (2009).

Datasets

2. **K. Bisdom**, *Natural fracture patterns in carbonate rocks*, Delft University of Technology (2015).

1. G. Bertotti, **K. Bisdom**, *Fracture patterns in the Jandaíra Fm. (NE Brazil)*, Delft University of Technology (2013).